

UNIVERSITA' VITA-SALUTE SAN RAFFAELE

CORSO DI DOTTORATO DI RICERCA INTERNAZIONALE IN
MEDICINA MOLECOLARE

CURRICULUM IN NEUROSCIENZE E NEUROLOGIA
SPERIMENTALE

EXPLORING THE PLEOMORPHIC
PHENOMENOLOGY OF NEUROMYELITIS
OPTICA SPECTRUM DISORDERS WITH MRI

DoS: Prof. Massimo Filippi

Second Supervisor: Prof. Sean J. Pittock



Tesi di DOTTORATO di RICERCA di:

Laura Cacciaguerra matr. 015518

Ciclo di dottorato: XXXV

SSD: MED 26

Anno Accademico 2021/2022

THESIS CONSULTATION AUTHORISATION

La sottoscritta / I
Matricola / *Registration number*
nata a / *born at*
il / *on*

Laura Cacciaguerra
015518
Pordenone (PN)
30/06/1990

autore della tesi di Dottorato dal titolo / *Author of the PhD Thesis titled*

EXPLORING THE PLEOMORPHIC PHENOMENOLOGY OF NEUROMYELITIS OPTICA SPECTRUM DISORDERS WITH MRI

AUTORIZZA la Consultazione della tesi / *AUTHORIZES the public release of the thesis*

NON AUTORIZZA la Consultazione della tesi per 12 mesi / *DOES NOT AUTHORIZES the public release of the thesis for 12 months*

a partire dalla data di conseguimento titolo e precisamente / *from the PhD thesis date, specifically*

Dal / *from* 20/12/2022 Al / *to* 19/12/2023

Poiché / *because*:

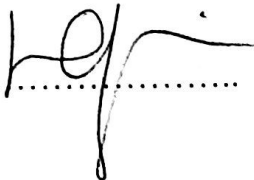
l'intera ricerca o parti di essa sono potenzialmente soggette a brevettabilità / *The whole project or part of it might be subject to patentability;*

ci sono parti della tesi che sono già state sottoposte a un editore o sono in attesa di pubblicazione / *Parts of the thesis have been or are being submitted to a publisher or are in press;*

la tesi è finanziata da enti esterni che vantano dei diritti su di esse o sulla loro pubblicazione / *the thesis project is financed by external bodies that have rights over it and on its publication.*

E' fatto divieto di riprodurre, in tutto o in parte, quanto in essa contenuto / *Copyright the contents of the thesis in whole or in part is forbidden*

Data/Date... 18/11/2022.....

Firma/Signature... .....

DECLARATION

This thesis has been composed by myself and has not been used in any previous application for a degree. Throughout the text I use both 'I' and 'We' interchangeably.

The thesis has been written according to the editing guidelines approved by the University.

Permission to use images and other material covered by copyright has been sought and obtained.

- The present work “Spinal Cord Atrophy in Neuromyelitis Optica Spectrum Disorders Is Spatially Related to Cord Lesions and Disability” (*Section 4.1*) was performed by Laura Cacciaguerra in partial fulfilment of the requirements for obtaining the PhD degree at Vita-Salute San Raffaele University, Milano, Italy. The present work has already been published in Radiology (PMID: 32720869, DOI: 10.1038/s41380-021-01085-2).
- The present work “Volume of hippocampal subfields and cognitive deficits in neuromyelitis optica spectrum disorders” (*Section 4.2*) was performed by Laura Cacciaguerra in partial fulfilment of the requirements for obtaining the PhD degree at Vita-Salute San Raffaele University, Milano, Italy. The present work has already been published in European Journal of Neurology (PMID: 34415660, DOI: 10.1111/ene.15073).
- The present work “Time-varying connectivity of the precuneus and its association with cognition and depressive symptoms in neuromyelitis optica: A pilot MRI study” (*Section 4.3*) was performed by Laura Cacciaguerra in partial fulfilment of the requirements for obtaining the PhD degree at Vita-Salute San Raffaele University, Milano, Italy. The present work has already been published in Multiple Sclerosis Journal (PMID: 35796514, DOI: 10.1177/13524585221107125).
- The present work “Mapping white matter damage distribution in neuromyelitis optica spectrum disorders with a multimodal MRI approach” (*Section 5.1*) was performed by Laura Cacciaguerra in partial fulfilment of the requirements for obtaining the PhD degree at Vita-Salute San Raffaele University, Milano, Italy.

- The present work has already been published in *Multiple Sclerosis Journal* (PMID: 32672089, DOI: 10.1177/1352458520941493).
- The present work “MR T2-relaxation time as an indirect measure of brain water content and disease activity in NMOSD” (*Section 5.2*) was performed by Laura Cacciaguerra in partial fulfilment of the requirements for obtaining the PhD degree at Vita-Salute San Raffaele University, Milano, Italy. The present work has already been published in *Journal of Neurology Neurosurgery and Psychiatry* (PMID: 35483915, DOI: 10.1136/jnnp-2022-328956).
 - The present work “Magnetic Resonance Imaging Evaluation of Perivascular Space Abnormalities in Neuromyelitis Optica” (*Section 5.3*) was performed by Laura Cacciaguerra in partial fulfilment of the requirements for obtaining the PhD degree at Vita-Salute San Raffaele University, Milano, Italy. The present work has already been published in *Annals of Neurology* (PMID: 35596582, DOI: 10.1002/ana.26419).
 - The present work “Application of deep-learning to the seronegative side of the NMO spectrum” (*Section 6.1*) was performed by Laura Cacciaguerra in partial fulfilment of the requirements for obtaining the PhD degree at Vita-Salute San Raffaele University, Milano, Italy. The present work has already been published in *Journal of Neurology* (PMID: 34328544, DOI: 10.1007/s00415-021-10727-y).
 - Clinical, laboratory and MRI data used for the projects entitled “Tumefactive demyelination in MOG antibody-associated disease versus other demyelinating disorders” (*Section 6.2*) and “Timing and Predictors of T2-Lesion Resolution in MOGAD” (*Section 6.3*) were collected by Laura Cacciaguerra at the Mayo Clinic, Rochester, Minnesota in the context of her PhD course under the guidance of Prof. Eoin P. Flanagan.

All sources of information are acknowledged by means of reference.

Acknowledgements

To Prof. Rocca, Prof. Flanagan, Prof. Pittock, and Prof. Filippi, who gave me good advice for my career and good examples for my life.

ABSTRACT

Neuromyelitis optica spectrum disorders (NMOSD) is an autoimmune disorder of the central nervous system (CNS) characterized by primary astrocytes damage and secondary demyelination. An antibody targeting the aquaporin-4 (AQP4) water channel is the pathogenetic element and elicits tissue damage by triggering the complement cascade.

Although the pathophysiology of the disease has been already clarified, several aspects are yet to be clarified.

Despite the well-established association between clinical attacks and motor disability, there is a growing body of literature indicating a high prevalence of cognitive issues in NMOSD patients, which are not justifiable based on the inflammatory activity and likely rely on different mechanisms. Moreover, conventional magnetic resonance imaging (MRI), was proven useful for the differential diagnosis of this disease, but not relevant for its monitoring, since was unable to underpin subclinical disease activity. The identification of MRI correlates of NMOSD pathogenesis might therefore help patient management. Finally, AQP4-IgG cannot be detected in a minority of patients, that can be still diagnosed with NMOSD if presenting typical clinical and MRI features. However, the inclusion of these patients under the umbrella of NMOSD is a question highly debated due to controversial clinical and immunological findings. Furthermore, a significant proportion of these patients test positive to an antibody targeting the myelin-oligodendrocyte glycoprotein (MOG), but a growing body of evidence indicates that they are a separate disease entity with a different pathophysiology, now known as MOG antibody-associated disease (MOGAD).

Therefore, in this PhD project we used conventional and advanced MRI, together with artificial intelligence algorithms and newly available tools such as brain gene expression atlases to explore the different substrates of attack-dependent and attack-independent disability, identify the MRI correlates of NMOSD pathophysiology, and enhance the understanding of seronegative patients and MOGAD.

TABLE OF CONTENTS

ACRONYMS AND ABBREVIATIONS	1
LIST OF FIGURES AND TABLES	4
1. PREFACE	9
2. INTRODUCTION: NEUROMYELITIS OPTICA SPECTRUM DISORDERS	11
2.1. EPIDEMIOLOGY	11
2.2. CLINICAL FEATURES AND DIAGNOSIS	11
2.3. KEY ELEMENTS OF NMOSD PATHOGENESIS AND AQP4 FUNCTIONS	13
2.3.1. Pathophysiology of NMOSD	13
2.3.2. AQP4 functions	14
2.3.3. The issue of AQP4-seronegative patients	15
2.4. TAILORED TREATMENTS AND DISEASE MONITORING	16
2.4.1. Eculizumab	17
2.4.2. Inebilizumab	17
2.4.3. Satralizumab	18
2.4.4. Treatment monitoring	19
2.5. TISSUE OBSERVATIONS IN NMOSD: WHY MRI CAN CONTRIBUTE TO THE FIELD	20
2.6. QUANTITATIVE AND ADVANCED MRI IN NMOSD	21
2.6.1. Volumetric measures and atrophy	21
2.6.2. Microstructural tissue abnormalities	22
2.6.3. Functional abnormalities	24
2.6.4. Artificial Intelligence	24
3. AIMS OF THE WORK	26
3.1. PECULIARITIES OF NMOSD RESEARCH AND OPEN QUESTIONS	26
3.2. AIMS OF THE WORK	26
4. MRI SUBSTRATES OF MOTOR AND COGNITIVE DISABILITIES	27
4.1. SPINAL CORD ATROPHY ON MRI IN NEUROMYELITIS OPTICA SPECTRUM DISORDERS IS SPATIALLY RELATED TO CORD LESIONS AND DISABILITY	27
4.2. VOLUME OF HIPPOCAMPAL SUBFIELDS AND COGNITIVE DEFICITS IN NEUROMYELITIS OPTICA SPECTRUM DISORDERS	46
4.3. TIME-VARYING CONNECTIVITY OF THE PRECUNEUS AND ITS ASSOCIATION WITH COGNITION AND DEPRESSIVE SYMPTOMS IN NEUROMYELITIS OPTICA: A PILOT MRI STUDY	69
5. UNTRAVELING NMOSD PATHOPHYSIOLOGY WITH MRI	88

5.1 MAPPING WHITE MATTER DAMAGE DISTRIBUTION IN NEUROMYELITIS OPTICA SPECTRUM DISORDERS WITH A MULTIMODAL MRI APPROACH	88
5.2 MR T2-RELAXATION TIME AS AN INDIRECT MEASURE OF BRAIN WATER CONTENT AND DISEASE ACTIVITY IN NMOSD	111
5.3. MAGNETIC RESONANCE IMAGING EVALUATION OF PERIVASCULAR SPACE ABNORMALITIES IN NEUROMYELITIS OPTICA	130
5.4. SPATIAL ASSOCIATION BETWEEN GENE EXPRESSION AND BRAIN DAMAGE IN NEUROMYELITIS OPTICA SPECTRUM DISORDERS	150
6. SERONEGATIVE PATIENTS AND MOGAD	177
6.1. APPLICATION OF DEEP-LEARNING TO THE SERONEGATIVE SIDE OF THE NMO SPECTRUM	178
6.2. TUMEFACTIVE DEMYELINATION IN MOG ANTIBODY-ASSOCIATED DISEASE VERSUS OTHER DEMYELINATING DISORDERS	196
6.3. TIMING AND PREDICTORS OF T2-LESION RESOLUTION IN MOGAD	229
7. DISCUSSION	236
8. CONCLUSIONS	244
9. ADDITIONAL PUBLICATIONS OF THE PHD COURSE	245
10. REFERENCES	248

ACRONYMS AND ABBREVIATIONS

a	Automated
AD	Axial diffusivity
AHBA	Allen Human Brain Atlas
AI	Artificial intelligence
AQP4	Aquaporin-4
AQP4+NMOSD	Aquaporin-4 seropositive neuromyelitis optica spectrum disorders
BBB	Blood-brain barrier
BDI	Beck Depression Inventory-II
BOLD	Blood-oxygen-level dependent
BRB-N	Brief Repeatable Battery of Neuropsychological Tests
C	Cervical
CA	Cornus Ammonis
CBA	Cell-based assay
CI	Cognitively impairment
CIS	Clinically isolated syndrome
CNS	Central nervous system
CP	Cognitively preserved
CSA	Cross-sectional area
CSF	Cerebrospinal fluid
DIR	Double inversion recovery
DL	Deep learning
DG	Dentate gyrus
DTI	Diffusion tensor imaging
DTI-ALPS index	Diffusion along perivascular spaces index
EDSS	Expanded disability status scale
FA	Fractional anisotropy
FC	Functional connectivity
FDA	Food and Drug Administration
FLAIR	Fluid attenuated inversion recovery
fMRI	Functional magnetic resonance imaging
GFAP	Glial fibrillary acidic protein
GM	Grey matter
IGF	Insulin-like growth factor
IGFBPs	Insulin-like growth factor binding proteins
IL	Interleukin
IPS	Information processing speed
IRM	Idiopathic recurrent myelitis
IRON	Idiopathic recurrent optic neuritis

LETM	Longitudinally-extensive transverse myelitis
LV	Lesion volume
MD	Mean diffusivity
ML	Machine learning
MNI	Montreal National Institute
MOG	Myelin-oligodendrocyte glycoprotein
MOGAD	Myelin-oligodendrocyte glycoprotein antibody-associated disease
MPRAGE	Magnetization-prepared rapid gradient-echo imaging
MRI	Magnetic resonance imaging
MS	Multiple sclerosis
MUCCA	Mean upper cervical cord area
NAWM	Normal-appearing white matter
NBV	Normalized brain volume
NDGMV	Normalized deep grey matter volume
NGMV	Normalized grey matter volume
NMDA-R	N-methyl-D-aspartate receptor
NMOSD	Neuromyelitis optica spectrum disorders
NWMV	Normalized white matter volume
PASAT	Paced Auditory Serial Addition Test
PLB	Percentage of lesioned band
OCBs	Oligoclonal bands
RD	Radial diffusivity
ROI	Region of interest
RR	Relapsing-remitting
RS	Resting-state
S100B	S100 calcium-binding protein B
SCWT	Stroop Color Word Test
SDMT	Symbol Digit Modalities Test
SFC	Static FC
SPART	10/36 Spatial Recall Test
SRT	Selective Reminding Test
SWI	Susceptibility weighted imaging
T	Thoracic
T1/T2-w	T1/T2-weighted ratio
T2rt	T2-relaxation time
TBSS	Tract-based spatial statistics
TVC	Time-varying connectivity
VBM	Voxel-based morphometry
VF	Verbal fluency
VL	Verbal learning
VSL	Visuospatial learning

WM	White matter
----	--------------

LIST OF FIGURES AND TABLES

Figures	
Figure 4.1.1	Schematic representation of the spinal cord analysis, modified from Cacciaguerra et al., Radiology 2020.
Figure 4.1.2	T1-hypointense lesion probability maps and regional atrophy, modified from Cacciaguerra et al., Radiology 2020.
Figure 4.1.3	Correlations between regional spinal cord damage and clinical and MRI measures, modified from Cacciaguerra et al., Radiology 2020.
Figure 4.2.1	Coronal view of the left-hippocampus and of the FreeSurfer 6.0 segmentation of subfields (a) in a patient with NMOSD and a HC (anatomical convention), modified from Cacciaguerra et al., European Journal of Neurology 2021.
Figure 4.2.2	Scattered boxplots of volumes (z-scores) of the hippocampus and its subfields in patients with NMOSD, according to domain-specific cognitive impairment, modified from Cacciaguerra et al., European Journal of Neurology 2021.
Figure 4.2.3	Significant bivariate associations between the neuropsychological performance (domain-specific z-scores, y-axis) and hippocampal volumes atrophy (z-scores, x-axis), combined with marginal boxplot in NMOSD patients, stratified according to the presence (red dots) or absence (blue dots) of verbal memory impairment. Modified from Cacciaguerra et al., European Journal of Neurology 2021.
Figure 4.2.4	Significant bivariate associations between the neuropsychological performance (domain-specific z-scores, y-axis) and hippocampal volumes atrophy (z-scores, x-axis), combined with marginal boxplot in NMOSD patients, stratified according to the presence (red dots) or absence (blue dots) of visuo-spatial memory impairment. Modified from Cacciaguerra et al., European Journal of Neurology 2021.
Figure 4.3.1	Distribution of BDI scores, cognitive impairment index and information processing speed index among patients' groups.
Figure 4.3.2	Resting state static functional connectivity of the precuneus.
Figure 4.3.3	Resting state time-varying functional connectivity of the precuneus.
Figure 5.1.1	WM abnormalities in HC (blue line), MS (green line) and NMOSD (red line) patients.
Figure 5.2.1	T2-relaxation time map and tissue segmentation.
Figure 5.2.2	Barcharts of T2rt in NMOSD and HC.
Supplementary Figure 5.2.1	Scatterplot of the bivariate correlation between the T2rt z-score in the grey matter and steroid dose in treated patients (n=10).
Figure 5.3.1	DTI-ALPS index measurement in the two datasets.

Figure 5.4.1	Brain damage distribution in AQP4+NMOSD patients in terms of lesion location, grey and white matter atrophy, and microstructural abnormalities.
Figure 5.4.2	Spatial association between gene expression and brain damage in AQP4+NMOSD patients.
Figure 5.4.3	Network of enriched biological processes. Nodes size represents the size of the pathway, while edges width represents the number of genes shared by the connected pathways (i.e., nodes).
Figure 5.4.4	Enrichment analysis of biological processes associated with brain damage in AQP4+NMOSD.
Figure 6.1.1	Schematic representation of the study design.
Figure 6.1.2	Model performance and MRI images of the two AQP4-seronegative patients misclassified by the DL algorithm.
Figure 6.2.1	Pictorial overview of the MRI features evaluated in the study, with corresponding definitions.
Figure 6.2.2	Long-term outcomes of patients with tumefactive lesions.
Figure 6.2.3	Examples of tumefactive brain lesions and relevant MRI features for the differential diagnosis of patients with MOGAD, MS, and AQP4+NMOSD.
Supplementary Figure 6.2.1	Examples of tumefactive lesions with similar MRI features at first and subsequent tumefactive attacks.
Figure 6.3.1	Forest plot of patient and lesion factors associated with T2-lesion resolution at 12 months in MOGAD.
Tables	
Table 2.2.1	Diagnostic criteria for NMOSD, adapted from Wingerchuk et al., Neurology 2015.
Table 2.4.1	Summary of the three phase-III clinical trials of FDA-approved treatments for AQP4+NMOSD, modified from Cacciaguerra et al., Neurotherapeutics 2021.
Table 4.1.1	Demographic, clinical, and conventional MRI characteristics of healthy controls and participants with neuromyelitis optica spectrum disorders.
Table 4.1.2	Regional distribution between gray matter and white matter of T1-hypointense lesion volumes among vertebral segments.
Table 4.1.3	Significant clusters of spinal cord atrophy in participants with neuromyelitis optica spectrum disorders compared to healthy controls.
Table 4.2.1	Demographic, clinical, and neuropsychological variables of study population.
Table 4.2.2	MRI variables of NMOSD patients and HC.
Supplementary Table 4.2.1	MRI variables of NMOSD patients according to the impairment in the verbal memory domain.

Supplementary Table 4.2.2	MRI variables of NMOSD patients according to the impairment in the visuo-spatial memory domain.
Supplemental Table 4.2.3	MRI variables of NMOSD patients according to the impairment in the attentive domain.
Supplemental Table 4.2.4	MRI variables of NMOSD patients according to the impairment in the executive domain (Stroop test).
Table 4.3.1	Demographic, clinical, neuropsychological and structural MRI features of NMOSD patients and HC.
Table 4.3.2	Clusters of abnormal RS static functional connectivity (SFC) of the precuneus between healthy controls (HC) and neuromyelitis optica spectrum disorder (NMOSD) patients ($p < 0.001$ uncorrected, cluster extent threshold $k_E = 10$).
Table 4.3.3	Clusters of abnormal time-varying RS functional connectivity (TVC) between healthy controls (HC) and neuromyelitis optica spectrum disorder (NMOSD) patients ($p < 0.001$ uncorrected, cluster extent threshold $k_E = 10$).
Table 4.3.4	Bivariate Pearson's correlations between neuropsychological variables and resting state static and time-varying functional connectivity (FC) of the precuneus (z-scores) in patients with neuromyelitis optica spectrum disorder (NMOSD).
Table 4.3.5	Linear regression models between neuropsychological variables and time-varying functional connectivity (TVC) of the precuneus (z-scores) in patients with neuromyelitis optica spectrum disorder (NMOSD).
Table 5.1.1	Main demographic, clinical and brain MRI features of HC, NMOSD and MS patients.
Table 5.1.2	Microstructural intra-lesional measures in NMOSD and MS patients at global level and in each concentric band (the lower the number, the nearer to the CSF).
Table 5.1.3	NAWM measures in HC, NMOSD and MS patients at global level and in each concentric band (the lower the number, the nearer to the CSF).
Table 5.1.4	Periventricular (bands 1-5) and deep (bands 6-10) microstructural gradients of intralesional damage in NMOSD and MS patients.
Table 5.1.5	Periventricular (bands 1-5) and deep (bands 6-10) microstructural gradients of damage in the NAWM of HC, NMOSD and MS patients.
Table 5.1.6	Significant age- and sex-adjusted partial correlations between periventricular (bands 1-5) and deep (bands 6-10)

	microstructural gradients of intralésional and NAWM damage in MS patients.
Table 5.2.1	Demographic, clinical and MRI features of the study population.
Table 5.2.2	T2rt values of NMOSD patients and HC.
Table 5.2.3	Demographic, clinical and MRI features of active and stable NMOSD patients.
Table 5.2.4	T2rt in active and stable NMOSD patients.
Table 5.2.5	Univariate logistic regressions between the T2rt (z-score) and disease activity in NMOSD patients.
Supplementary Table 5.2.1	Between-group comparison of active patients having vs. not having received high-dose steroids.
Supplementary Table 5.2.2	Bivariate Pearson's correlations between T2rt z-scores and steroid dose in treated patients (n=10).
Supplementary Table 5.2.3	Between-group comparison of patients relapsing before and after the MRI acquisition.
Table 5.3.1	Demographic and clinical variables in the two datasets.
Table 5.3.2	Between-group comparison of MRI variables and Virchow-Robin space enlargement score distribution.
Table 5.3.3	Between-group comparison of aDTI-ALPS index.
Table 5.3.4	Regression models, p values refer to age-, sex-, and scanner-adjusted binomial logistic regression (NMOSD diagnosis) or linear regression models (EDSS).
Table 5.4.1	Demographic, clinical, and conventional MRI features of the study population.
Table 5.4.2	Clusters of significant atrophy in AQP4-IgG+NMOSD patients compared to HC.
Supplementary Table 5.4.1	Detailed description of the standardized MRI protocol at each participating center and scanner.
Supplementary Table 5.4.2	List of candidate genes analyzed in the study with the overall association score (i.e., degree of association with AQP4+NMOSD according to the Open Target Platform).
Table 6.1.1	Main demographic, clinical, and MRI data of the studied populations.
Table 6.1.2	Main demographic, clinical and MRI data of AQP4-seronegative patients.
Table 6.1.3	Main demographic, clinical, and MRI data of the training and validation sets.
Table 6.1.4	DL-estimated classification of AQP4-seronegative NMOSD patients and unclassified AQP4-seronegative patients with NMOSD-like manifestations.

Table 6.2.1	Demographic, clinical and cerebrospinal fluid attributes of tumefactive demyelination across the three groups.
Table 6.2.2	Comparison of MRI features of tumefactive demyelination across the three groups.
Table 6.2.3	Multivariable binary logistic regression analysis between clinical/MRI variables and MOGAD diagnosis.
Table 6.2.4	MRI features of subsequent tumefactive demyelination across the three groups.
Supplementary Table 6.2.1	Demographic, clinical and cerebrospinal fluid attributes of tumefactive demyelination in MOGAD patients with adult- and pediatric-onset.
Supplementary Table 6.2.2.	MRI features of tumefactive demyelination in MOGAD patients with adult- and pediatric-onset.
Supplementary Table 6.2.3	Univariable binary logistic regression analysis between clinical/MRI variables and MOGAD diagnosis.
Table 6.3.1	Demographic and clinical features of the study population.

1. PREFACE

When I studied Neurology at medical school, I was taught that neuromyelitis optica was an aggressive variant of multiple sclerosis and no effective treatments were available.

When I started my PhD course, the notion that autoantibodies targeting the aquaporin-4 (AQP4) water channel were pathogenetic in this disease was fully established, and phase III clinical trials demonstrated that drugs specifically targeting the key steps of neuromyelitis optica spectrum disorders (NMOSD) pathogenesis were highly effective in controlling disease activity, hence being approved by the Food and Drugs Administration later.

At that time, the diagnostic criteria had already moved towards the different terminology of neuromyelitis optica “spectrum disorders”, and allowed also seronegative patients (i.e., patients with a negative AQP4-IgG testing) to be diagnosed with NMOSD if presenting with typical clinical and magnetic resonance imaging (MRI) features. Antibodies targeting the myelin-oligodendrocyte glycoprotein (MOG) were suggested as possible biomarkers of seronegative NMOSD, to the point that MOG-IgG-positive patients were also recruited in NMOSD clinical trials. However, treatments were less effective in these patients, raising doubts about their inclusion into the neuromyelitis optica spectrum.

As I am writing now, I was told that the first diagnostic criteria for MOG antibody-associated disease (MOGAD) as a separate disease entity, have just been accepted for publication.

This is to say that Autoimmune Neurology is a young and dynamic research field, and the knowledge on these disorders was very different when this PhD course started. Several choices, such as the inclusion of seronegative NMOSD and anti-MOG-IgG positive patients in a few of my studies are nowadays questionable but were in line with the latest diagnostic criteria available. I think this underlines the need of faster official guidelines updates, to keep pace with the evolution of knowledge.

Therefore, as you may notice while reading, this thesis is written by a person whose opinions on NMOSD and MOGAD had the chance to change over time, in the light

of novel evidence in literature and of the possibility of listening to the words of experts in this field.

2. INTRODUCTION: NEUROMYELITIS OPTICA SPECTRUM DISORDERS

Dear Reader,

Please be aware that we are herein using the term of NMOSD to improve homogeneity. When referring to studies specifically including only AQP4-seropositive patients, the terminology AQP4+NMOSD will be applied.

2.1. Epidemiology

According to latest esteems, AQP4+NMOSD is a rare disease, with a worldwide prevalence ranging between 1/100,000 and 10/100,000. The lowest prevalence is encountered among White people (~1/100,000 population), increases to ~3.5/100,000 population in East Asians, and peaks to 10/100,000 population in Black people (Hor, Asgari et al., 2020).

The disease usually affects middle-aged individuals, with an average age at onset around 40 years, although extremes ages (i.e., pediatric or elderly) are not spared. There is a significant predominance of female sex, with a female-to-male ratio of 9:1 (Hor et al., 2020).

Among risk factors, evidence is less striking than in multiple sclerosis (MS), with a substantial lack of association with viral infections such as Ebstein Barr virus and Herpes simplex virus, or vitamin D deficits (Graves, Grandhe et al., 2014, Simon, Schmidt et al., 2015).

2.2. Clinical features and diagnosis

NMOSD is a relapsing-remitting disease in over 80% of cases (Wingerchuk, Hogancamp et al., 1999), with relapses usually occurring relatively early in disease history (55% at 1 year from onset, 90% at 5 years from onset) (Wingerchuk et al., 1999).

Core clinical features are transverse myelitis (85% of patients, typically involving at least three contiguous vertebral segments), optic neuritis (65%) (Hyun, Jeong et al., 2016), and the area postrema syndrome (16%-43%) (Filippi & Rocca, 2020), but also other manifestations including brainstem, diencephalic or cerebral involvement

(Wingerchuk, Banwell et al., 2015). The presence of at least one of the core clinical manifestations together with AQP4-IgG detection in serum define the diagnosis of AQP4+NMOSD (**Table 2.2.1**) (Wingerchuk et al., 2015).

Table 2.2.1. Diagnostic criteria for NMOSD, adapted from Wingerchuk et al., Neurology 2015 (Wingerchuk et al., 2015).

NMOSD with AQP4-IgG	NMOSD without AQP4-IgG or with unknown AQP4-IgG status
<p>At least 1 core clinical characteristic among:</p> <ol style="list-style-type: none"> 1. Optic neuritis 2. Acute myelitis 3. Area postrema syndrome: episode of otherwise unexplained hiccups or nausea and vomiting 4. Acute brainstem syndrome 5. Symptomatic narcolepsy or acute diencephalic clinical syndrome with NMOSD-typical diencephalic MRI lesions 6. Symptomatic cerebral syndrome with NMOSD-typical brain lesions 	<p>At least 2 core clinical characteristics as a result of ≥ 1 clinical attack and meeting the following requirements:</p> <ol style="list-style-type: none"> 1) At least 1 core clinical characteristic must be optic neuritis, acute myelitis with LETM, or area postrema syndrome 2) Dissemination in space (2 or more different core clinical characteristics) 3) Fulfillment of additional MRI requirements, as applicable: <p>Acute optic neuritis: requires brain MRI showing normal findings or only nonspecific white matter lesions, OR optic nerve MRI with T2-hyperintense lesion or T1-weighted gadolinium-enhancing lesion extending over 1/2 optic nerve length or involving optic chiasm;</p> <p>Acute myelitis: requires associated intramedullary MRI lesion extending over 3 contiguous segments OR ≥ 3 contiguous segments of focal spinal cord atrophy in patients with history compatible with acute myelitis;</p> <p>Area postrema syndrome: requires associated dorsal medulla/area postrema lesions;</p> <p>Acute brainstem syndrome: requires associated periependymal brainstem lesions</p>
Positive test for AQP4-IgG using best available detection method*	Negative test for AQP4-IgG using best available detection method*
Exclusion of alternative diagnoses	

*Cell-based assay recommended.

Abbreviations: NMOSD=neuromyelitis optica spectrum disorders; AQP4=aquaporin-4; LETM=longitudinally extensive transverse myelitis; MRI=magnetic resonance imaging.

Clinical attacks are usually severe and full recovery of visual or motor deficits occurs in 15-36% of cases (Kleiter, Gahlen et al., 2016), hence disability is driven by relapses (i.e., attack-related disability). Deaths in the setting of cervical myelitis have also been reported, leading to a 68% 5-year survival according to the natural history of the disease (Wingerchuk et al., 1999).

Secondary progression unrelated to disease activity, common in MS, is in contrast extremely rare in NMOSD (Wingerchuk, Pittock et al., 2007).

However, there is growing interest on cognitive issues in patients with NMOSD, which mainly affect the attentive and memory domains. They have been reported in 30-70% of patients (Oertel, Schliesseit et al., 2019) and have been described as attack-independent symptoms of NMOSD, possibly due to the interaction between AQP4-IgG and astrocytes eventually leading to synaptic plasticity dysfunction (Saji, Arakawa et al., 2013), although this is still controversial.

Additional systemic or organ-specific autoimmune comorbidities are common in NMOSD patients, with Sjogren's syndrome and systemic lupus erythematosus described as the most frequent systemic autoimmune associated disorders (Wingerchuk et al., 2015). Among organ-specific disease, autoimmune thyroiditis are also common (Wingerchuk & Weinshenker, 2012), and anti-thyroid antibodies are present in approximately 38% of patients (Wang, Yi et al., 2016).

Association with neurological autoimmune disorders has also been described, with the strongest association found with myasthenia gravis. More recently, coexistence of anti-N-methyl-D-aspartate receptor (NMDA-R) encephalitis (Zoccarato, Saggi et al., 2013), and glial fibrillary acidic protein (GFAP, especially in the context of ovarian teratoma) (Flanagan, Hinson et al., 2017) was reported.

2.3. Key elements of NMOSD pathogenesis and AQP4 functions

2.3.1. Pathophysiology of NMOSD

NMOSD is an autoimmune astrocytopathy with secondary demyelination (Lucchinetti, Mandler et al., 2002). The pathogenesis of the disease relies on the presence of autoantibodies, targeting AQP4 (Lennon, Wingerchuk et al., 2004), which is the main water channel of the central nervous system (CNS) (Nagelhus, Veruki et al., 1998, Oshio, Binder et al., 2004, Papadopoulos, Manley et al., 2004), and is

mainly expressed on the plasma membrane of astrocytes, at interface between brain parenchyma and water-containing structures (i.e., at the blood-brain barrier, BBB) (Nielsen, Nagelhus et al., 1997).

The binding between antibodies and their target activates the complement cascade through the classical pathway, leading to astrocytes damage or loss by complement-dependent cytotoxicity (Bennett, Lam et al., 2009) and antibody-dependent cell-mediated cytotoxicity (Zhang & Verkman, 2013). The consequent release of anaphylatoxins such as C5a locally recruits granulocytes (i.e., neutrophils and eosinophils), which exert a non-selective damage on the standby tissue, including both grey matter (GM) and white matter (WM). Although pathology studies initially investigated tissue abnormalities within lesions (Lucchinetti, Mandler et al., 2002), more recent investigations suggested that astrocyte damage may be diffuse (Guo, Lennon et al., 2022).

Beside the direct effect of complement and granulocytes, indirect sources of tissue injury have also been hypothesized: given the role of AQP4 in maintaining water homeostasis, vasogenic edema with increased vascular permeability may also contribute to tissue damage and possibly lead to secondary ischemia (Lucchinetti, Mandler et al., 2002).

Although the disease specifically targets the CNS, antibody production occurs in the periphery, as suggested by the higher sensitivity for antibody testing in serum than cerebrospinal fluid (CSF) (Majed, Fryer et al., 2016). Interleukin (IL) 6 appears particularly relevant, since it stimulates T cell differentiation into T helper17, B cell survival, and plasma cell synthesis of anti-AQP4-IgG. The secretion of IL6 by T helper17 and of B-cell activating factor by B cells furtherly reinforces the circuit (Cacciaguerra, Tortorella et al., 2021b).

2.3.2. AQP4 functions

AQP4 is the main water channel of the CNS and regulates water homeostasis, hence being involved in edema formation and resolution (Saadoun & Papadopoulos, 2010). Recent studies also suggested a role of AQP4 in the transport of CSF from the perivascular spaces to the brain parenchyma in the context of the glymphatic system functioning (Iliff & Nedergaard, 2013). Finally, according to pre-clinical studies,

AQP4 might be also involved in synaptic plasticity and memory formation by acting on long-term potentiation and long-term depression (Hubbard, Szu et al., 2018, Szu & Binder, 2016), although the mechanisms have not been fully clarified yet.

2.3.3. The issue of AQP4-seronegative patients

As mentioned before, current diagnostic criteria allow NMOSD diagnosis also in patients with no evidence of AQP4-IgG, if they have typical disease manifestations and MRI features (Wingerchuk et al., 2015). Studies in different cohorts estimated that a percentage of AQP4-seronegative patients, ranging between 30 to 70%, test positive to the myelin-oligodendrocyte glycoprotein (MOG) antibody (Sechi, Cacciaguerra et al., 2022). These patients are characterized by significant differences such as younger age at presentation, lower female-to-male ratio, and better prognosis (Sechi et al., 2022), suggesting their inclusion into a separate disease entity, nowadays known as MOGAD (MOG-antibody associated disease) (Marignier, Hacoheh et al., 2021). Although official diagnostic criteria have not been published yet, there is growing consensus in literature to consider these patients separated from NMOSD.

MOG is a glycoprotein expressed on the external myelin layer of oligodendrocytes, whose functions have not been fully elucidated but are thought to include cell adhesion, microtubule stability, and regulation of the interaction between myelin and the complement cascade (Johns & Bernard, 1999). Based on pathology findings, it is likely that the pathophysiology of MOGAD includes antibody deposition, complement activation, but also CD4 T cells and granulocytes (Hoftberger, Guo et al., 2020, Takai, Misu et al., 2020).

In addition to MOGAD, double-seronegative NMOSD patients (i.e., AQP4- and MOG-IgG negative patients) have also been described, but literature is controversial, suggesting a clinical and MRI overlap with AQP4+NMOSD in some studies (Cacciaguerra, Meani et al., 2019b, Gibbons, Campagna et al., 2022) and lower female-to-male ratio (almost 1:1), frequent concomitant optic neuritis and myelitis at onset (around 30%), and better visual outcomes in others (Jiao, Fryer et al., 2013, Marignier, Bernard-Valnet et al., 2013). Additional evidence arguing against the inclusion of AQP4-seronegative NMOSD come from the results of the phase III clinical trial of biologics in NMOSD, where treatment efficacy seemed lower in these

patients (Cree, Lamb et al., 2005, Traboulsee, Greenberg et al., 2020, Yamamura, Kleiter et al., 2019).

From my personal standpoint, it is likely that double-seronegative NMOSD patients are a heterogeneous population, possibly including AQP4+NMOSD patients whose testing was for some reasons initially negative but later on seroconvert to positive (for instance due to initial steroids or plasma exchange administration) (Cacciaguerra, Storelli et al., 2022d), AQP4+NMOSD patients with AQP4-IgG detectable only in the CSF (Majed et al., 2016), and patients with other known (i.e., MS) or unknown CNS autoimmune disorders.

However, the growing availability of antibody-testing strongly supports a classification of antibody-mediated disorders based on antibody identification rather than relying on phenotypes.

2.4. Tailored treatments and disease monitoring

Beside the well-known acute treatment of NMOSD, including high-dose intravenous corticosteroids, immunoglobulins, and plasma-exchange (which are not discussed in this section), the pathophysiological understanding of the disorder has allowed the development of tailored treatments aimed at preventing relapses by targeting the complement cascade, B cells, and the IL6 pathway.

In this section we will discuss the three drugs recently approved for the treatment of AQP4+NMOSD by the Food and Drug Administration (FDA) following the results of phase-III clinical trials: eculizumab (C5 inhibitor), inebilizumab (anti-CD19) and satralizumab (IL6-receptor inhibitor). The main features of the phase-III trials are summarized in **Table 2.4.1**. For all trials, the primary endpoint was time-to-first relapse.

Table 2.4.1 Summary of the three phase-III clinical trials of FDA-approved treatments for AQP4+NMOSD, modified from Cacciaguerra et al., Neurotherapeutics 2021 (Cacciaguerra et al., 2021b).

Trial Name	Drug	AQP4-seronegative patients	Control group	Concomitant therapies*
PREVENT	Eculizumab (900 mg per week for the first four	No	Placebo	Corticosteroids, AZA, MMF, other (76%), also in association

	weeks, followed by 1200 mg every two weeks)			
N-Momentum	Inebilizumab (300 mg at day 1 and 15)	Yes	Placebo	20 mg prednisolone (day 1-14), tapered to day 21
SAkuraStar	Satralizumab	Yes	Placebo	None
SAkuraSky	Satralizumab+add (120 mg at weeks 0, 2, 4, then and every four weeks)	Yes	Placebo	Corticosteroids, AZA, MMF; pediatric patients could associate AZA or MMF plus corticosteroids

*Both groups.

Abbreviations: NMOSD=neuromyelitis optica spectrum disorders; AQP4=aquaporin-4; AZA=azathioprine; MMF= mycophenolate mofetil.

2.4.1. Eculizumab

The first FDA-approved medication for AQP4+NMOSD is eculizumab, which is a humanized monoclonal antibody that blocks C5 and stops its cleavage, preventing the development of the membrane attack complex.

The efficacy and safety of eculizumab was tested in the PREVENT trial, a double-blind, randomized phase III trial (NCT01892345) that demonstrated a relapse-risk reduction by 94% (Pittock, Berthele et al., 2019). Inclusion criteria were at least two relapses in the previous year or three relapses in the previous two years (at least one of which occurring in the last year). At the end of the trial, a significantly higher percentage of patients was relapse-free in the eculizumab-treated arm (97%) compared to the placebo group (57%, $p=0.001$) (Pittock et al., 2019).

The prevalence of adverse events was similar between eculizumab and placebo (92 and 91%, respectively). Upper respiratory tract infections (29%), headaches (23%), and nasopharyngitis (21%), which were the most frequent side events in the eculizumab group, were mild (108/100 patients per year) to moderate (620/100 patients per year). Notably, all patients received the N. meningitidis vaccine before study initiation due to the 2000-fold increase in capsulate bacteria infection risk (McNamara, Topaz et al., 2017). During the open-labeled extension of the research, one patient in the eculizumab group receiving additionally azathioprine died from a pulmonary empyema (Cacciaguerra et al., 2021b).

2.4.2. Inebilizumab

The surface antigen CD19 is present on all B-lineage cells, including several plasmacells and antibody-secreting plasmablasts (LeBien & Tedder, 2008, Otero, Anzelon et al., 2003, Scheuermann & Racila, 1995). Inebilizumab, a humanized IgG1 kappa monoclonal antibody, targets this protein to induce antibody-dependent cellular cytotoxicity, ensuing B-cell depletion. Inebilizumab showed a 73% reduction in the risk of relapse in the double-blind, randomized, placebo-controlled phase II/III trial N-Momentum (NCT02200770), which led to FDA approval (Cree, Bennett et al., 2019). Patients who had at least one or two relapses that required rescue therapy in the preceding one or two years, respectively, were eligible.

At study end, 88% of treated patients and 61% of untreated patients were relapse-free ($p < 0.0001$). According to serostatus, relapses occurred in 12% of AQP4-IgG-positive treated patients (42% of placebo) and 23% of AQP4-IgG-negative treated patients, of which one was anti-MOG-positive.

Urinary tract infections (11%), arthralgia (10%), and infusion-related responses (9%) were the most prevalent adverse events, which were similarly frequent in treated (72%) and untreated patients (73%). No patients died during the randomized-controlled period, but two did during the open-label extension (Cacciaguerra et al., 2021b).

2.4.3. Satralizumab

Satralizumab, which was specifically developed for the treatment of NMOSD, can bind to both soluble and membrane IL6 receptors, inhibiting the activation of its signaling pathways. In two phase III randomized placebo-controlled clinical trials, subcutaneous satralizumab was administered to NMOSD patients as add-on therapy (Yamamura et al., 2019) or as monotherapy (Traboulsee et al., 2020).

In NMOSD patients with at least two relapses in the previous two years (at least one in the most recent year), the SAKuraSky trial (NCT02028884) (Yamamura et al., 2019) demonstrated the efficacy and safety of satralizumab as an add-on therapy to stable-dosed background immunosuppressants, while the SAKuraStar trial demonstrated the efficacy and safety of satralizumab as monotherapy in NMOSD patients who had at least one relapse in the year prior to study allocation (Traboulsee et al., 2020).

At the study end, 72% of treated patients (*vs.* 51% of placebo) in the SakuraStar trial and 78% of treated patients (*vs.* 59% of patients receiving immunosuppressants only) in the SakuraSky trial were relapse-free among the intent-to-treat population (including both AQP4-seropositive and AQP4-seronegative patients).

Efficacy was even higher in AQP4-seropositive patients, where it decreased the probability of relapses by 79% (combination therapy) and 74% (monotherapy). However, results were weaker in AQP4-seronegative NMOSD.

Patients receiving satralizumab, placebo, or immunosuppressants had similar rates of adverse events (injection-related reactions was the most common), serious adverse events, and infections (especially upper respiratory and urinary tract infections). No deaths or anaphylactic reactions occurred (Cacciaguerra et al., 2021b).

2.4.4. Treatment monitoring

Given its sensitivity to new (even asymptomatic) lesions, conventional MRI (i.e., T2- and pre- and post-contrast T1-weighted sequences) represents a fundamental tool for treatment monitoring in multiple sclerosis (MS), hence being one of the criteria for the evidence of disease activity (Giovannoni, Tomic et al., 2017) and representing one of the secondary outcome measure of most clinical trials (Sormani & Bruzzi, 2013, Wattjes, Steenwijk et al., 2015).

However, MRI monitoring of the disease is not a good approach in NMOSD, since asymptomatic brain lesions have been observed in only 3.4% (Lee, Yong et al., 2020) and overall new lesions are rare (Matthews, Kolind et al., 2015). Asymptomatic lesions or gadolinium enhancement have been reported in the spinal cord (Solomon, Paul et al., 2021) and optic nerve (Shah, Morris et al., 2022), but studies are still scanty and their clinical significance is unclear. Similarly, sequential monitoring of AQP4-IgG titers in serum was demonstrated unsuccessful for relapses prediction (Rocca, Cacciaguerra et al., 2020a).

In contrast, a recent study demonstrated that serial levels of GFAP, a biomarker of astrocytes damage, can be useful for disease monitoring, since levels increased one week before relapses and correlated with the associated clinical disability (Aktas, Smith et al., 2021). However, this type of test is not yet available in most clinical facilities.

2.5. Tissue observations in NMOSD: why MRI can contribute to the field

The first description of the pathophysiological cascade anticipated the discovery of the anti-AQP4 antibody and was based on the observation of pathological tissue obtained from spinal cord lesions in patients (Lucchinetti et al., 2002). Tissue was characterized by vasulocentric deposition of IgG, co-localized complement activation, astrocytes loss, and infiltrates of granulocytes, lymphocytes, and plasma cells, leading to the hypothesis that the primary mechanism of damage could be an antibody targeting perivascular structures and triggering the complement cascade and local recruitment of inflammatory cells (Lucchinetti et al., 2002)(Kawachi & Lassmann, 2017). Tissue damage in NMOSD encompasses astrocyte abnormalities (from the AQP4 loss in an otherwise healthy tissue to astrocytes apoptosis or vacuolar degeneration), demyelination, and tissue loss (necrosis or secondary Wallerian degeneration) (Misu, Hoftberger et al., 2013).

MRI has become a fundamental tool in the diagnostic work-up of inflammatory CNS disorders. In NMOSD, the detection of typical lesions on conventional T2-weighted images is a supportive or mandatory element for the diagnosis (see **Table 2.2.1**) (Wingerchuk et al., 2015).

In the clinical setting, the use of MRI is mainly limited to conventional sequences for the identification of lesions, and several groups proposed MRI-based algorithms for the differential diagnosis of AQP4+NMOSD, MS (Cacciaguerra et al., 2019b, Matthews, Marasco et al., 2013a), and MOGAD (Carnero Contentti, Rojas et al., 2022, Jurynczyk, Geraldles et al., 2017a) based on lesion location and qualitative features, with a sensitivity of approximately 91% and a specificity of up to 96%.

However, in a research setting, the application of more advanced techniques or the acquisition of advanced MRI sequences has the advantage of affording quantitative data, thus enabling the detection of the pathological features described above, such tissue loss (i.e., through atrophy measurement), and demyelination (i.e., with diffusion tensor imaging, magnetic transfer ratio, etc.) *in vivo*. In addition, functional MRI techniques may allow the detection of functional changes and cortical reorganization associated with the disease.

2.6. Quantitative and advanced MRI in NMOSD

2.6.1. Volumetric measures and atrophy

Volumetric measures are assessed on 3D-T1-weighted sequences.

Brain atrophy

WM and GM volumes can be assessed individually, and both contribute to brain volume. According to Pfefferbaum, et al. (Pfefferbaum, Mathalon et al., 1994), physiological brain volume loss in healthy individuals is 0.1-0.3% per year. Among neuroinflammatory diseases, a worsening of atrophy rates is seen in MS, reaching values of 0.46-1% per year (Bermel & Bakshi, 2006, De Stefano, Stromillo et al., 2016, Grassiot, Desgranges et al., 2009). Recently, similar results were found in patients with NMOSD (0.47%), with higher GM atrophy rates in case of long spinal cord lesions (Masuda, Mori et al., 2022).

SIENAx (Structural Image Evaluation, Using Normalization, of Atrophy - Cross Sectional) (Battaglini, Smith et al., 2008) and VBM (voxel-based morphometry)(Whitwell, 2009) analyses have both been used to confirm the presence of brain atrophy in NMOSD compared to healthy controls (HC).

No agreement has been reached regarding the extent of WM atrophy in NMOSD, as some Authors found more widespread WM damage than anticipated by pure secondary degeneration (Chanson, Lamy et al., 2013), whereas others provided evidence of regional atrophy at the level of the corticospinal and optic tracts, which could indicate secondary degeneration following spinal cord and optic nerve lesions (Duan, Liu et al., 2014, Pichiecchio, Tavazzi et al., 2012).

The presence of GM atrophy in NMOSD is controversial and was not observed in all NMOSD cohorts (Blanc, Noblet et al., 2012, Duan, Liu et al., 2012). Most of the evidence indicates a minimal amount of cortical injury and a stronger involvement of deep GM structures, although milder than in MS. For instance, using the FreeSurfer software, two separate studies found cortical anomalies limited to the visual cortex, suggesting a mechanism of damage consequent to Wallerian degeneration (Calabrese, Oh et al., 2012, Liu, Xie et al., 2014). Thalamic and hippocampal atrophy were also observed in NMOSD patients with cognitive impairment (Chanson et al., 2013, Liu, Fu et al., 2015a).

To conclude, in NMOSD there is evidence of brain atrophy, but further investigations are needed to understand if it represents a diffuse or regional process, and if it is led by primary or secondary neurodegeneration.

Spinal cord atrophy

Damage to the spinal cord is a specific feature of NMOSD (Wingerchuk et al., 1999). Clinical evidence suggests that NMOSD patients have spinal cord atrophy on conventional MRI (Cassinotto, Deramond et al., 2009, Krampla, Aboul-Enein et al., 2009), although at the beginning of this PhD course no quantitative information was available. At that time, only a few studies used a semi-automated volumetric method that could measure the mean upper cervical cord area (MUCCA) on the brain magnetization-prepared rapid gradient-echo imaging (MPRAGE) sequence, disclosing severe spinal cord atrophy in NMOSD compared to MS, which was correlated with disability measures and the number of prior myelitis (Chien, Scheel et al., 2019, Liu, Duan et al., 2018, Liu, Wang et al., 2015b).

2.6.2. Microstructural tissue abnormalities

With various approaches, microstructural alterations in inflammatory CNS diseases have been documented. The primary methods employed in research settings to assess occult damage to brain tissue in the so-called normal-appearing WM (NAWM) are summarized in this paragraph.

Diffusion tensor imaging (DTI)

The motion of water molecules in space is measured using diffusion imaging. Each water molecule can migrate in any direction due to the Brownian diffusion law that governs free water movement (i.e., isotropic pattern of diffusion).

In the brain, this scenario matches with the properties of liquid compartments like the CSF but differs from the brain parenchyma where water transport is controlled by physically defined trajectories represented by neural fibers, so water movement follows a preferred direction (i.e., anisotropic pattern of diffusion).

By incorporating at least six extra encoding gradients into a fast-imaging sequence, the DTI is able to record the 3D directionality of water diffusion.

The following parameters are identified from DTI: mean diffusivity (MD, i.e., average diffusivity of water molecules regardless of direction, that increases in case of demyelination), fractional anisotropy (FA, i.e., degree of diffusivity anisotropy, used to assess the integrity of fibre tracts in the WM and their structural alignment), radial diffusivity (RD, i.e., diffusivity perpendicular to axons), and axial diffusivity (AD, i.e., diffusivity parallel to axons) (O'Donnell & Westin, 2011).

At the time of this PhD course most investigations showed that NAWM occurs in NMOSD, but again with conflicting findings about its distribution. Several studies demonstrated microstructural damage restricted to the motor and visual networks (supporting the hypothesis of secondary degeneration) (Jeantroux, Kremer et al., 2012, Pichiecchio et al., 2012, Yu, Lin et al., 2008, Yu, Lin et al., 2006), whereas other found a widespread distribution of microstructural abnormalities (Kimura, Doring et al., 2014, Liu, Duan et al., 2012a, Liu, Duan et al., 2012b, Rueda Lopes, Doring et al., 2012, Zhao, Zhou et al., 2012).

Other techniques

Additional techniques considered sensitive to myelin content have been described, mainly in the setting of MS. One is magnetization transfer imaging (Wolff & Balaban, 1994), which assesses the tissue healthiness by examining the protons' capacity to exchange energy with tissues close by. The effectiveness of this exchange can be inferred if scans with and without the magnetic-transfer (MT)-pulse are compared by calculating a ratio between the two (MT ratio [MTR]). Low MTR values thus indicate damage to macromolecules such as myelin and axonal membranes, with consequent little exchange of magnetization.

Only a few research on NMOSD patients have been performed so far and involved small cohorts (Filippi, Rocca et al., 1999, Pichiecchio et al., 2012, Rocca, Agosta et al., 2004).

Another measure was gathering attention at the time of the PhD course, which was the T1/T2-weighted ratio, which was investigated in MS (Nakamura, Chen et al., 2017, Righart, Biberacher et al., 2017) as a measure of myelin content (Nakamura et al., 2017), but later found also correlated with dendrite density (Righart et al., 2017).

2.6.3. Functional abnormalities

Functional MRI (fMRI) during resting conditions (resting-state, RS) is an advanced imaging technique able to underpin spontaneous (i.e., not task-related) interactions among different brain regions (Buckner, Krienen et al., 2013) based on the blood-oxygen-level dependent (BOLD) signal fluctuations associated with brain activity (DeYoe, Bandettini et al., 1994).

Only a few studies explored this in NMOSD, and overall suggested that cortical reorganization involves the networks mainly hampered by the disease (i.e., visual and sensory-motor) (Backner, Ben-Shalom et al., 2020, Bigaut, Achard et al., 2019, Finke, Zimmermann et al., 2018), with a potential compensatory role of cross-modal plasticity (Rocca, Savoldi et al., 2019).

2.6.4. Artificial Intelligence

As previously mentioned, MRI-based algorithms were proposed to improve NMOSD diagnosis based on radiological features present on conventional sequences (Cacciaguerra et al., 2019b, Carnero Contentti et al., 2022, Juryneczyk, Tackley et al., 2017c, Matthews, Marasco et al., 2013b).

However, all these approaches may be biased by (i) the a priori selection of the classification features, (ii) the inclusion of a limited number of candidate predictors, and (iii) by inter-rater variability in the interpretation of MRI scans and the identification of classification elements.

The term artificial intelligence (AI) refers to the application of digital computers to perform tasks commonly associated with human intelligence (Muthukrishnan, Maleki et al., 2020) such as decision-making or classification.

It includes two main approaches: machine learning (ML), which learns from specific data features, and deep learning (DL), that learns directly from data, without any external (i.e., human) intervention on features selection. This methodology was demonstrated particularly useful in the radiological field, where it can assist the diagnostic work-up and provide information on disease prognosis.

Only a few investigations applied artificial intelligence to NMOSD, and mainly focused on the differential diagnosis with MS, revealing milder atrophy (Eshaghi, Wottschel et al., 2016) and different radiomic features in the GM (Yan, Liu et al.,

2021). The diagnostic performance of these algorithms was demonstrated to outperform experienced neuroradiologists, supporting their application (Rocca, Anzalone et al., 2021).

3. AIMS OF THE WORK

3.1. Peculiarities of NMOSD research and open questions

All that said, NMOSD represents a unique research scenario where the pathogenesis of the disease is known and proven but we still lack MRI biomarkers able to underpin the pathophysiological process and its dynamic in-vivo. Among them, the recognition of early biomarkers or predictors of disease activity would have direct practical implications since disability worsening is usually due to clinical attacks.

Open questions in this research field are: (i) the different substrates of attack-dependent and attack-independent disability; (ii) the MRI correlates of NMOSD pathophysiology and how they can be relevant for disease monitoring and (iii) if MRI can be a useful tool for the characterization and pathophysiological understanding of seronegative patients, and the differentiation between NMOSD and the newly defined entity of MOGAD.

3.2. Aims of the work

1. To examine the MRI substrates of attack-related (i.e., motor) and attack-independent (i.e., cognitive impairment) clinical disability in NMOSD, in order to understand the relationship between mechanisms of inflammation and neurodegeneration;
2. To identify the MRI correlates of NMOSD pathogenesis through the study of brain micro and macro-structural alterations and assess whether they can be useful in the diagnosis or monitoring of the disease;
3. To characterize seronegative patients and MOGAD with a focus on differences and similarities with AQP4+NMOSD.

4. MRI SUBSTRATES OF MOTOR AND COGNITIVE DISABILITIES

In this Chapter we investigated the MRI substrates of motor (i.e., attack-dependent) and cognitive (i.e., attack-independent) disabilities, to clarify whether CNS damage occurs following focal inflammatory injury, primary neurodegenerative mechanisms, or a combination of the two.

We chose the spinal cord, one of the target structures of NMOSD, to study the spatial association between the presence of focal lesions, atrophy, and motor disability.

Then, we tried to identify the correlation between cognitive impairment, structural and functional abnormalities by analyzing the global and regional hippocampal volume and the dynamics of RS functional connectivity.

4.1. Spinal cord atrophy on MRI in neuromyelitis optica spectrum disorders is spatially related to cord lesions and disability

Cacciaguerra *et al.*, Radiology 2020

This chapter describes the work published in Radiology (PMID: 32720869, DOI: 10.1148/radiol.2020192664).

Spinal Cord Atrophy in Neuromyelitis Optica Spectrum Disorders Is Spatially Related to Cord Lesions and Disability

Laura Cacciaguerra, MD • Paola Valsasina, MSc • Sarlota Mesaros, MD, PhD • Vittorio Martinelli, MD • Jelena Drulovic, MD • Massimo Filippi, MD • Maria A. Rocca, MD

From the Neuroimaging Research Unit, Institute of Experimental Neurology, Division of Neuroscience (L.C., P.V., M.F., M.A.R.) and Neurology Unit (L.C., V.M., M.F., M.A.R.), IRCCS San Raffaele Scientific Institute, via Olgettina 60, Milan 20132, Italy; Vita-Salute San Raffaele University, Milan, Italy (L.C., M.F.); and Clinic of Neurology, Faculty of Medicine, University of Belgrade, Belgrade, Serbia (S.M., J.D.). Received December 5, 2019; revision requested February 5, 2020; final revision received May 18; accepted May 26. Address correspondence to M.A.R. (e-mail: rocca.maria@hsr.it).

Supported in part by the Ministry of Science, Republic of Serbia (project no. 175031).

Conflicts of interest are listed at the end of this article.

Radiology 2020; 297:154–163 • <https://doi.org/10.1148/radiol.2020192664> • Content codes: **MR** **NR**

Background: The spinal cord is commonly involved in patients with neuromyelitis optica spectrum disorders (NMOSDs). However, the relationship between inflammation and atrophy remains unclear.

Purpose: To characterize the spatial distribution of T1-hypointense lesions in the spinal cord at MRI, its association with cord atrophy, and its correlation with disability in participants with NMOSDs.

Materials and Methods: This prospective study evaluated three-dimensional T1-weighted spinal cord MRI scans in seropositive participants with NMOSDs and in age-matched healthy control participants acquired between February 2010 and July 2018. Binary masks of T1-hypointense lesions and lesion probability maps were produced. Cross-sectional area of the cervical and upper thoracic cord (down to T3 level) was calculated with the active-surface method. Full factorial models were used to assess cord atrophy in participants with NMOSDs. Correlations between cord atrophy and clinical and brain MRI measures were investigated with multiple regression models.

Results: A total of 52 participants with NMOSDs (mean age \pm standard deviation, 44 years \pm 15; 45 women) and 28 age-matched healthy control participants (mean age, 44 years \pm 13; 16 women) were evaluated. Thirty-eight of 52 (73%) participants with NMOSDs had T1-hypointense cord lesions. No cord lesions were detected in the healthy control participants. Lesion probability maps showed a predominant involvement of the upper cervical (C2–C4) and upper thoracic (T1–T3 level) cord. The greater involvement of C1–C4 survived Bonferroni correction (P value range, .007–.04), with a higher percentage lesion extent in the gray matter ($P < .001$). Atrophy colocalized with focal cord lesions and correlated with pyramidal subscore (r ranging from -0.53 to -0.40 ; $P < .001$) and sensitive subscore (r ranging from -0.48 to -0.46 ; $P = .001$) of the Expanded Disability Status Scale. Participants without cord lesions had no cord atrophy.

Conclusion: In participants with neuromyelitis optica spectrum disorders, focal areas of spinal cord atrophy at MRI were topographically associated with lesions and correlated to motor and sensory disability. Participants without visible cord lesions had no atrophy.

© RSNA, 2020

Introduction

Spinal cord involvement is a core feature of NMOSD (Wingerchuk et al., 2015). Classically, acute spinal cord lesions involve at least three contiguous vertebral segments (long transverse myelitis (Kim, Paul et al., 2015)), but also shorter lesions can be observed (Asgari, Skejoe et al., 2013, Cacciaguerra, Meani et al., 2019a, Flanagan, Weinshenker et al., 2015a). Lesions involve both cervical and thoracic levels (Tatekawa, Sakamoto et al., 2018), preferentially with a central location (Ciccarelli, Cohen et al., 2019, Nakamura, Miyazawa et al., 2008). The area postrema, which is also affected by NMOSD (Wingerchuk et al., 2015), can be damaged by lesions extending cranially from the spinal cord (Iorio, Damato et al., 2013) or by isolated abnormalities (Popescu, Lennon et al., 2011).

In contrast to MS, asymptomatic cord lesions are uncommon in NMOSD (Flanagan, Weinshenker et al., 2015b). Myelitis typically lead to a rapidly evolving complete spinal cord syndrome (Wingerchuk et al., 1999), followed by residual clinical disability in up to 80% of patients (Kleiter et al., 2016). Outside these acute disabling manifestations, only a few NMOSD patients experience a subtle disability progression (Wingerchuk et al., 2007), suggesting that there is a prominent (though not exclusively so) inflammatory-driven mechanism accounting for clinical impairment.

Nevertheless, in NMOSD patients, evidence of significant atrophy (and, therefore, neurodegeneration) of the spinal cord has also been observed (Liu et al., 2018, Liu et al., 2015b). Although cord atrophy has been shown to correlate with the number of myelitis episodes (Liu et al., 2015b), to our knowledge innovative analysis exploring the voxel-wise spatial relationship between focal lesions and atrophy has not been performed in this condition. Recently, optimized three-dimensional T1-weighted MRI sequences have shown a similar performance in lesion identification compared to short-tau inversion recovery sequences, with the advantage of enabling volumetric measures of both spinal cord lesion load and atrophy (Valsasina, Aboulwafa et al., 2018).

Because of the association between acute myelitis and clinical disability, we hypothesized that an evaluation of the voxel-wise correspondence between lesions and atrophy on three-dimensional T1-weighted MR images would help to clarify the relationship between cord injury and clinical disability in NMOSD. In this study, we aimed to characterize the spatial distribution of T1-hypointense lesions in the spinal cord, its association with spinal cord atrophy and the correlation with clinical disability in a sample of seropositive participants with NMOSD. A group of participants without cord lesions was also included, to establish whether cord atrophy may be attributable to a peculiar susceptibility to damage of the cord independent of focal damage.

Material and methods

Ethical committee approval. Approval was received from the local ethical standards committees on human experimentation and written informed consent was obtained from all participants prior to study participation. The study was partially supported by a grant from the Ministry of Science, Republic of Serbia (Project number: 175031).

Participants. Fifty-two consecutive participants with NMOSD in the chronic disease phase and 28 HC were prospectively enrolled at two European tertiary centers from February 2010 to July 2018. Twenty-three/52 NMOSD participants (44.2%) had been included in a previous study aimed at identifying the MRI features of brain and spinal cord lesions that differentiate NMOSD from MS (Cacciaguerra et al., 2019a). Inclusion criteria for NMOSD participants were the achievement of NMOSD diagnosis according to 2015 criteria (Wingerchuk et al., 2015), the presence of seral anti-aquaporin4-IgG on a cell-based assay (Waters, McKeon et al., 2012) and a complete brain MRI protocol. Exclusion criteria were any movement artifacts on brain and spinal cord MRI, the administration of corticosteroids in the previous month, history of cervical spine trauma, severe cord compression, drug/alcohol abuse, or other diseases involving the spinal cord.

Clinical assessment. Within 48 hours from the MRI, all participants underwent a complete neurological examination, including disability assessment through the expanded disability status scale (EDSS) (Kurtzke, 1983) and its functional scores. For each subject, the number of previous clinical myelitis episodes (defined as inflammatory spinal cord syndromes characterized by a nadir between four and 21 days after symptoms onset (Transverse Myelitis Consortium Working, 2002)) and disease duration were reported.

MRI acquisition. Using two Philips Achieva scanners (Philips Medical Systems, Best, The Netherlands, 3.0 T [Center A] and 1.5 T [Center B]), the following MR images were acquired in the cervical cord: sagittal 3D T1-weighted gradient-echo (Center A: repetition time [TR]/echo time [TE]=8/3.6 ms, inversion time [TI]=”shortest”, flip angle [FA]=8°, field of view [FOV]=250x250 mm², voxel size=1x1x1 mm³, 64 slices; Center B: TR/TE=25/9.2 ms, FA=30°, FOV=220x220 mm², reconstructed voxel size=0.86x0.86x1.1 mm³, 96 slices) and sagittal short-tau inversion recovery (Center A: TR/TE=2463/70 ms, TI=200 ms, FOV=130x250 mm², voxel size=0.49x0.49x2.5 mm³, 14 slices; Center B: TR/TE=2500/70 ms, TI=165 ms, FA=90°, FOV=250x250 mm², voxel size=0.78x0.78x3.0 mm³, 11 slices). Spinal cord images included the entire cervical segment and the thoracic segment (down to T3) in all participants. Axial dual-echo turbo spin-echo and 3D T1-weighted gradient-echo scans of the brain were also acquired.

Qualitative and quantitative assessment of MRI lesions. Lesions in the region from the area postrema to the inferior border of T3 were analyzed. Lesions limited to the area postrema were included. T1-hypointense lesions were consensually identified on the 3D T1-weighted scans by two physicians blinded to the participants' clinical data (L.C. and M.A. R., four and 25 years experience in neuroimaging, respectively). Sagittal short-tau inversion recovery images were used to increase confidence in lesion identification and when counting T2-hyperintense lesions. The presence of long and short transverse myelitis (involving, respectively, at least three or less than three contiguous vertebral segments (Wingerchuk et al., 2015)) was evaluated. On sagittal planes, lesions were defined as cervical or thoracic. White matter and gray matter involvement was assessed according to the PAM50 template (included in the Spinal Cord Toolbox, version 3.2.2 (De Leener, Levy et al., 2017)) overlaid on individual T1-weighted images. WM was divided into anterior, lateral and posterior having the GM as anatomical reference. T1-hypointense cord lesion volume (LV) was calculated using a local thresholding segmentation technique (Jim software package, version 7, Xinapse Systems, Colchester, UK).

Spinal cord lesion maps and atrophy assessment. **Figure 4.1.1** summarizes the spinal cord analysis.

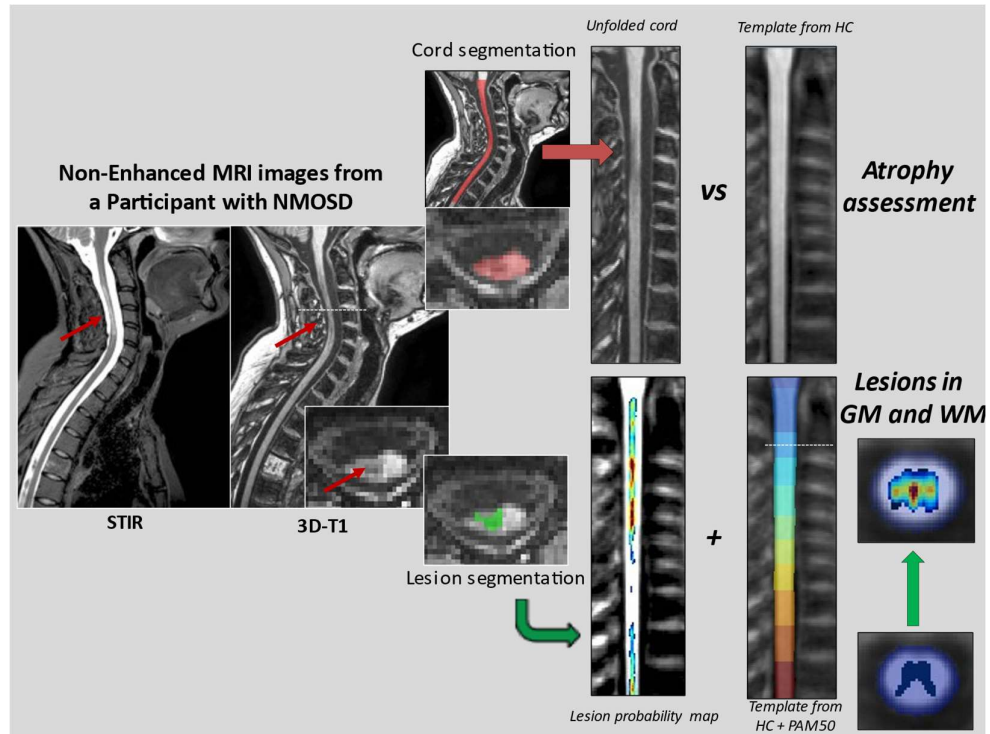
Atrophy was estimated from the area postrema to the inferior border of T3 by measuring cord cross-sectional area (CSA) using the active surface method (Horsfield, Sala et al., 2010) implemented in Jim (see above), and normalized by scaling according to the head size (Horsfield et al., 2010). This approach is able to quantify spinal cord atrophy, although the intra-cord source of volume reduction cannot be identified when it is applied to images with poor GM/WM contrast.

Straightened cord, binary cord masks and lesion images for each participant were obtained (Valsasina, Horsfield et al., 2012). Neck length variability and inter-center scan geometry differences were taken into account. Scans were coregistered to the mean cord image of the HC which served as cord template, and smoothed (Supplementary Materials and Methods) (Valsasina et al., 2012). A custom tissue/label template, obtained by warping the *a priori* gray matter probability map (thresholded at 25%) and cord levels from the PAM50 template (included in the Spinal Cord Toolbox, version 3.2.2 (De Leener

et al., 2017)) into our template space, was overlaid on individual T1-weighted lesion masks to quantify both the raw and fractional LV in the gray and white matter (obtained by dividing the GM and WM -LV by the total GM and WM volumes at each level).

Figure 4.1.1. Schematic representation of the spinal cord analysis, modified from Cacciaguerra et al., Radiology 2020 (Cacciaguerra, Valsasina et al., 2020).

Sagittal view of a native short tau inversion recovery MR image and sagittal/axial view of 3D T1-weighted MR image acquired from an example participant with neuromyelitis optica spectrum disorders (NMOSD), showing a cervical lesion with associated spinal cord atrophy (red arrows). The spinal cord was segmented using the active surface method from the area postrema to the inferior border of T3 (top row, in red). Unfolded spinal cord masks of NMOSD participants were compared to the spinal cord template obtained from healthy controls (HC), in order to detect spinal cord atrophy voxel-wise. Spinal cord lesion segmentation (bottom row, in green) was performed on the 3D T1-weighted images from each NMOSD participant, and an unfolded T1-hypointense lesion probability map was obtained. A custom tissue/label template (colors in the figure correspond to spinal cord levels and gray/white matter), obtained by warping the gray matter probability map and cord level maps from the PAM50 template into our template space, was overlaid on the T1-weighted lesion masks from each participant to quantify raw and fractional lesion volume in the gray and white matter. Author's reuse as per Journal pre-approved permission (<https://pubs.rsna.org/page/policies#license>).



Abbreviations: STIR=short tau inversion recovery sequence; 3D T1=3D T1-weighted sequence; HC=healthy controls; GM=gray matter; WM=white matter.

Statistical analysis. Between-group comparisons of continuous variables were performed using the two-sample t-test or Mann-Whitney U- test. Pearson χ^2 and Fisher's exact tests were used for categorical variables and to compare MRI outcomes between participants acquired at 3.0 T (Center A) and 1.5 T (Center B), and lesion characteristics between T1- and T2-weighted scans. Correlations between clinical and MRI variables were tested using age-, sex- and center-adjusted partial correlation coefficients (r) (SPSS software, version 23.0, IBM, Armonk, NY), $p < 0.05$ was considered significant.

Mean T1-hypointense lesion probability maps were produced by averaging coregistered lesion masks, and these were then thresholded at 30%. The voxel-wise analysis of T1-hypointense cord lesions and atrophy distribution was performed using Statistical Parametric Mapping (SPM), version 12 (Functional Imaging Laboratory, London, UK). Full factorial models (sex-, age-, center- and total cord volume-corrected) were used to assess differences in cord atrophy between HC and NMOSD. Results are reported as clusters (i.e., regions of contiguous significant voxels) and the corresponding cluster extent (i.e., number of voxels in each cluster).

Correlations (r) of cord atrophy with clinical and brain MRI variables were assessed using multiple regression models corrected for sex, age, center and total cord volume. A $p < 0.05$, family-wise error (FWE) corrected for multiple comparisons, was applied to all analyses; uncorrected results for $p < 0.001$ are also reported.

Center-adjusted linear mixed-effect models, with raw LV as the dependent variable and subject as the grouping factor, were used to test the effect of tissue (i.e., GM vs WM) and cord level on lesion distribution. Pair-wise *post hoc* contrasts were Bonferroni-adjusted for multiple comparisons. A tissue \times level interaction term tested whether lesion extent was different between gray and white matter across levels. This analysis was repeated using fractional LV as the dependent variable.

Results

Demographic and clinical features. 52 participants with NMOSD (44 +/- 15 years, 45 women) and 28 age-matched HC (44 +/- 13 years, 16 women) were evaluated (**Table 4.1.1**). Thirty-eight/52 (73%) participants with NMOSD had at least one clinical episode of myelitis (median number=2.0, range 0-14). Participants did not differ in demographic or clinical variables according to the site of acquisition: NMOSD (age: Center A=46 +/- 11 years, Center B=43 +/- 16 years, $p=0.42$; men/women: Center A=2/9, Center B=5/36, $p=0.6$; mean disease duration: Center A=5.9 years, Center B=6.5 years, $p=0.85$), HC (age: Center A=46 +/-10 years, Center B=42 +/- 15 years, $p=0.38$; men/women: Center A=7/10, Center B=5/6, $p=0.82$).

Table 4.1.1. Demographic, clinical, and conventional MRI characteristics of healthy controls and participants with neuromyelitis optica spectrum disorders.

Characteristic	Clinical measures		
	NMOSD (n=52)	HC (n=28)	p
Mean age (SD) [years]	44 (15)	44 (13)	0.82 ^a
Men/Women	7/45	12/16	0.005 ^b
Median disease duration (IQR) [years]	3.9 (2-11)	-	-
Median EDSS (IQR)	4.5 (2.5-8.0)	-	-
Median number of myelitis (range)	2.0 (0-14)	-	-

Median time from last relapse (IQR) [days]	801 (53-1095)	-	-
Brain MRI measures			
Median brain T2 LV (IQR) [ml]	0.37 (0.07-2.12)	0.00 (0.0-0.2)	<0.001 ^c
Median brain T1 LV (IQR) [ml]	0.08 (0.0-0.8)	0.00 (0.0-0.0)	0.001 ^c
Mean NBV (SD) [ml]	1462 (93)	1532 (96)	0.002 ^a
Spinal cord MRI measures			
	T1-w	T2-w	p
N° of patients with spinal cord lesions (%)	38 (73.1)	38 (73.1)	>0.99 ^b
N° of patients with LTM (%)	30 (78.9)	31 (81.6)	0.77 ^b
Median n° of spinal cord lesions (IQR)	1 (0-3)	1 (0-3)	0.32 ^c
N° of patients with cervical cord lesions (%)	24 (63.1)	25 (65.8)	0.81 ^b
N° of patients with thoracic cord lesions (%)	12 (31.6)	12 (31.6)	>0.99 ^b
N° of patients with cervical-thoracic cord lesions (%)	7 (18.4)	7 (18.4)	>0.99 ^b
Median T1 LV (IQR) [ml]	0.43 (0.0-0.1)		-
Mean CSAn (SD) [mm ²]	98 (16)		101 (11)

^at-test; ^bPearson's χ^2 test; ^cMann-Whitney test.

Abbreviations: NMOSD=neuromyelitis optica spectrum disorders; HC=healthy controls; SD=standard deviation; IQR=interquartile range; EDSS=expanded disability status scale; LV=lesion volume; NBV=normalized brain volume; CSAn=normalized cord cross-sectional area; T1-w=T1-weighted sequence; T2-w=T2-weighted sequence; LTM=long transverse myelitis.

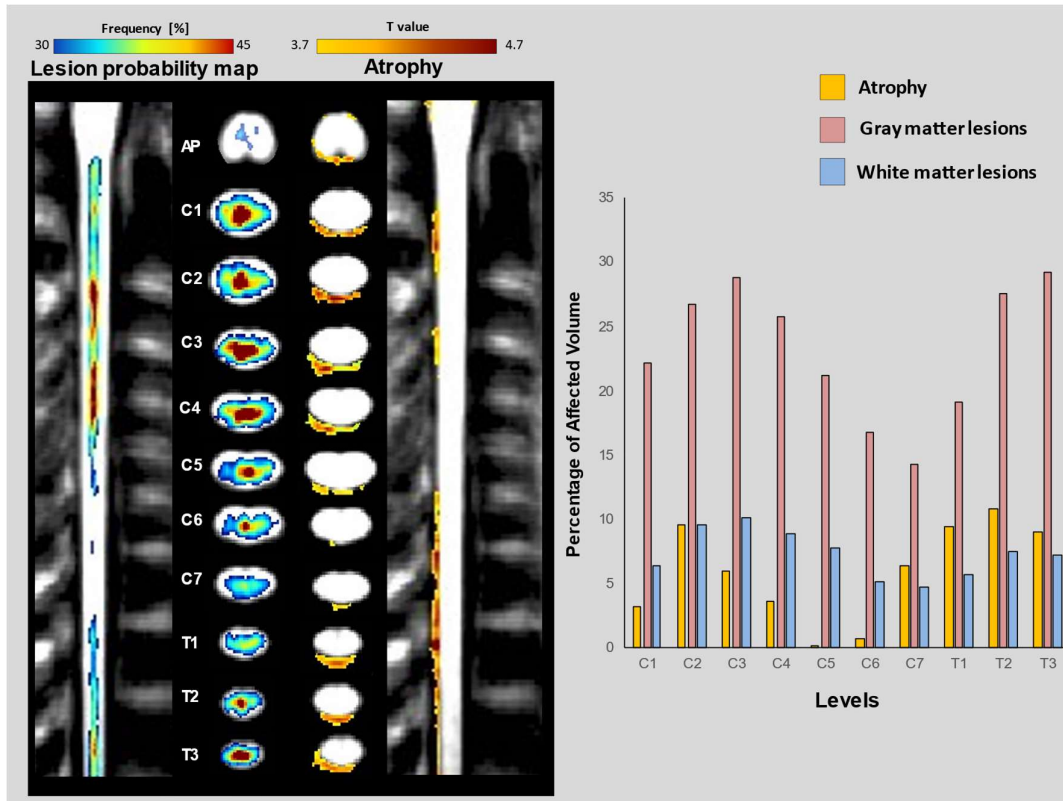
Brain MRI analysis. 40/52 (76.9%) participants with NMOSD showed T2-hyperintense brain lesions and 11/28 (39.3%) HC had small, nonspecific lesions. Higher brain T2 (0.37 vs 0.00 ml, $p<0.001$) and T1 LV (0.08 vs 0.00 ml, $p<0.001$) and reduced normalized brain volume (1462 +/- 93 vs 1532 +/- 96 ml, $p=0.002$) were observed in NMOSD (**Table 4.1.1**).

Spinal cord analysis. No spinal cord lesions were detected in HC and in 14/52 (27%) participants with NMOSD. In the remaining participants, 11/52 (21.1%) had short myelitis, 20/52 (38.5%) had long transverse myelitis and 7/52 (13.5%) had both. Lesions detected on short tau inversion recovery and 3D T1-weighted images were highly overlapping (**Table 4.1.1**).

No difference in the mean normalized cord CSA was found between HC and participants with NMOSD (101 +/- 11 vs 98 +/- 16 mm² respectively, p=0.70, see **Table 4.1.1**) or between NMOSD participants with and without spinal cord lesions (with lesions=99 +/- 19, without lesions=94 +/- 19 mm², p=0.40).

Regional distribution of T1-hypointense cord lesions. At a visual inspection of T1-hypointense lesion probability map, lesions were located centrally, and showed a greater involvement of cervical levels between C2 and C4 and of the thoracic segments between T1 and T3, whereas between C6 and C7 the spinal cord was relatively spared (**Figure 4.1.2**).

Figure 4.1.2. T1-hypointense lesion probability maps and regional atrophy, modified from Cacciaguerra et al., Radiology 2020 (Cacciaguerra et al., 2020). Sagittal and axial views showing the T1-hypointense lesion probability map at each spinal cord level plus area postrema (left side, thresholded in order to retain only pixels having a probability $\geq 30\%$ of including lesions, rainbow colour scale represents frequency values) and sagittal and axial views showing clusters of significant cord atrophy vs healthy controls at each spinal cord level plus area postrema (right side, colour scale from yellow to brown indicates t value). Bar graphs report the percentage of T1 lesion volume in the gray matter and white matter at each cord level (normalized with respect to the total gray matter and white matter volumes at that level) and the percentage reduction in cord area (atrophy) at each spinal cord level. Author's reuse as per Journal pre-approved permission (<https://pubs.rsna.org/page/policies#license>).



Abbreviations: AP=area postrema; C=cervical; T=thoracic.

Thirty-three and 19 lesions were detected in the cervical and thoracic segments of the spinal cord, respectively. Among them, four (12.1%) cervical lesions were limited to the WM, two to the GM (6.1%) and 27 were mixed (81.8%). WM involvement in mixed lesions was anterior (3/27, 11.1%), lateral (6/27, 22.2%), posterior (4/27, 14.8%) or combined (lateral-anterior [4/27, 14.8%], lateral-posterior [8/27, 29.6%], lateral-anterior-posterior [2/27, 7.4%]). Among thoracic lesions, nine involved only the GM (47.4%) and the remaining were mixed (anterior [2/10, 20.0%], lateral [1/10, 10.0%], posterior [1/10, 10.0%], lateral-anterior [1/10, 10.0%] and lateral-posterior [5/10, 50.0%]). When lesions involved both the cervical and the thoracic segments, regional extents were analyzed separately in each segment.

Statistical analysis of the LV distribution across tissue types and levels was largely in line with visual inspection. When analyzing raw LV, lesions were found to be heterogeneous across spinal cord levels ($p < 0.001$), with higher involvement of the C1, C3 and C4 segments vs C6 and C7 (p ranging between 0.007 and 0.04, **Table 4.1.2**). Although raw

LV was higher in the T2 and T3 segments than in the C6 and C7 segments, this did not survive Bonferroni correction.

When assessed using raw volumes, the WM was more involved than the GM ($p < 0.001$, **Table 4.1.2**). Conversely, when using fractional LV, only a trend towards heterogeneity of lesion location across levels was found ($p = 0.07$, **Table 4.1.2**), and fractional LV was significantly higher in the gray than in the white matter ($p < 0.001$, **Table 4.1.2**). No significant tissue \times level interaction was found either for raw LV ($p = 0.99$), or for fractional LV ($p = 0.83$).

Table 4.1.2. Regional distribution between gray matter and white matter of T1-hypointense lesion volumes among vertebral segments. Lesion volumes are expressed as raw lesion volumes, and as fractional lesion volumes [FLV] with respect to the total gray matter and white matter volumes at each spinal cord level.

	Mean raw lesion volume (SD) [ml]				FLV [%] (SD)				
	GM	WM	p ^a	p ^b	p ^c	GM	WM	p ^a	p ^b
C1	0.109 (0.14)	0.164 (0.23)	<0.001	<0.001	0.04 (vs C6) 0.007 (vs C7)	22.16 (29.0)	6.42 (8.9)	0.07	<0.001
C2	0.082 (0.08)	0.136 (0.18)			-	26.74 (27.5)	9.61 (12.7)		
C3	0.101 (0.11)	0.160 (0.22)			0.02 (vs C7)	28.80 (32.2)	10.06 (14.1)		
C4	0.102 (0.12)	0.154 (0.23)			0.03 (vs C7)	25.82 (29.6)	8.92 (13.1)		
C5	0.063 (0.08)	0.108 (0.17)			-	21.21 (27.4)	7.74 (12.13)		
C6	0.051 (0.08)	0.064 (0.13)			-	16.81 (25.6)	5.17 (10.2)		
C7	0.034 (0.07)	0.06 (0.13)			-	14.23 (28.6)	4.75 (10.5)		
T1	0.051 (0.09)	0.084 (0.15)			-	19.11 (32.3)	5.73 (10.4)		
T2	0.065 (0.09)	0.107 (0.18)			-	27.61 (37.6)	7.53 (12.8)		
T3	0.070 (0.09)	0.103 (0.16)			-	29.26 (38.0)	7.20 (11.3)		

^aCenter-adjusted linear mixed-effect model, main effect of level; ^blinear mixed-effect model, main effect of tissue; ^cpost hoc pair-wise comparison between levels (Bonferroni corrected), only significant p values are reported.

Abbreviations: SD=standard deviation; C=cervical; T=thoracic, GM=gray matter; WM=white matter; FLV=fractional lesion volumes.

Regional distribution of spinal cord atrophy. The voxel-wise analysis of spinal cord atrophy showed two clusters of tissue loss in NMOSD vs HC, from C2 to C4 ($p<0.001$, FWE-corrected) and from T1 to T3 ($p=0.004$, FWE-corrected in **Figure 4.1.2** and **Table 4.1.3**). A smaller atrophy cluster was observed in the area postrema ($p<0.001$, uncorrected). In the axial plane, voxels indicating atrophy were located posteriorly (**Figure 4.1.2**). When the analysis was restricted to participants with NMOSD without spinal cord lesions, no statistically significant regions of cord atrophy were observed.

Table 4.1.3. Significant clusters of spinal cord atrophy in participants with neuroyelitis optica spectrum disorders compared to healthy controls. Full factorial model adjusted for age, sex, total cord volume and center, $p<0.001$, uncorrected, cluster extent $k=50$). Clusters that survived the family-wise error (FWE) correction for multiple comparisons are marked with * and the corresponding FWE corrected p value is reported.

Spinal cord level	Cluster extent	t value		p
AP	137	4.05		<0.001
C2-C4	2196	C2	5.04	0.04*
		C3	5.49	0.01*
		C4	4.69	<0.001
T1-T3	2698	T1	5.11	0.03*
		T2	5.73	0.004*
		T3	4.55	<0.001

Abbreviations: AP=area postrema; C=cervical; T=thoracic.

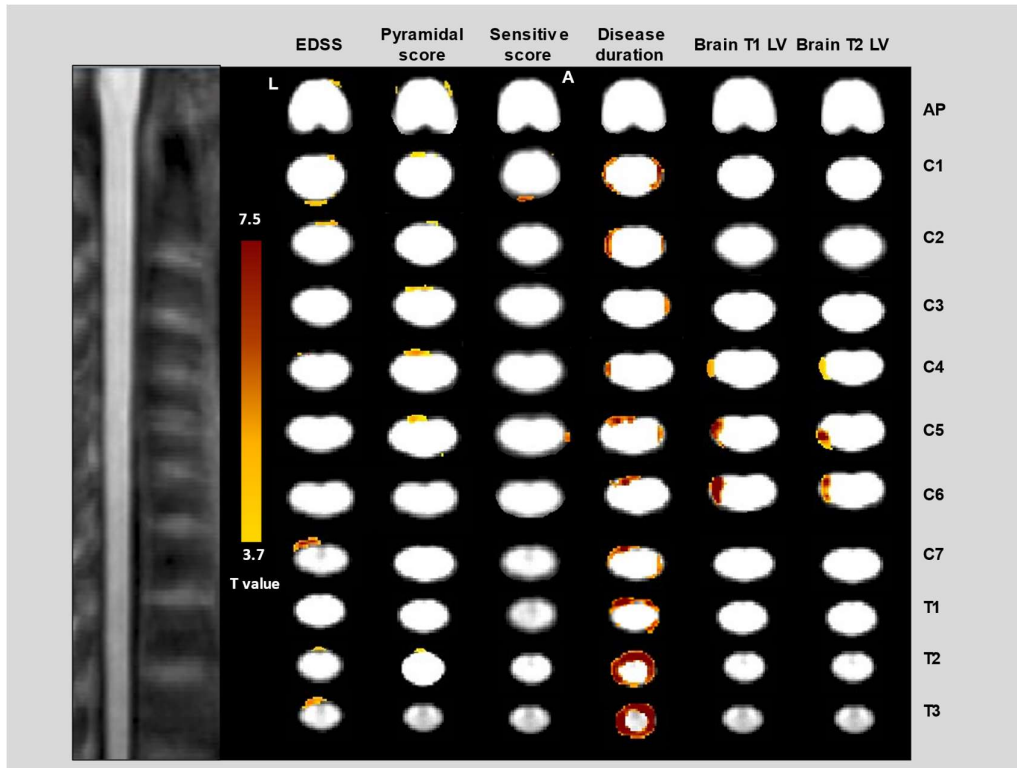
Correlations between clinical and MRI measures. In participants with NMOSD, no correlation emerged between EDSS and disease duration ($r=0.064$, $p=0.67$), brain T2 LV ($r=0.24$, $p=0.11$), brain T1 LV ($r=0.067$, $p=0.65$), spinal cord LV ($r=0.20$, $p=0.18$), cord lesion number ($r=0.10$, $p=0.07$) or normalized brain volume ($r=-0.14$, $p=0.34$). Similarly, normalized-CSA was not correlated with brain T2 LV ($r=-0.21$, $p=0.15$), brain T1 LV ($r=-0.005$, $p=0.97$) or normalized brain volume ($r=0.22$, $p=0.11$).

The voxel-wise analysis showed a correlation between EDSS and atrophy of the area postrema ($r=-0.38$, $p<0.001$ uncorrected) and of the spinal cord between C7 and T1 ($r=-$

0.39, $p < 0.001$ uncorrected). When considering EDSS functional systems, the pyramidal score correlated with atrophy in the area postrema and with anterior cervical atrophy between C3 and C5 (r ranging from -0.53 to -0.40, $p < 0.001$ uncorrected), while the sensitive score correlated with atrophy at C4, C5 and the area postrema (r ranging from -0.48 to -0.46, $p = 0.001$ uncorrected). Disease duration correlated with atrophy of the cervical cord between C2 and C3 ($r = -0.64$, $p = 0.001$, FWE-corrected) and of the thoracic segment ($r = -0.69$, $p < 0.001$, FWE-corrected).

The number of T1-hypointense lesions did not correlate with clinical variables. Cervical cord LV correlated with brain T2 ($r = 0.71$, $p = 0.006$, FWE-corrected) and T1 ($r = 0.84$, $p < 0.001$ FWE-corrected) LV. The results of the correlation analysis are shown in **Figure 4.1.3**.

Figure 4.1.3. Correlations between regional spinal cord damage and clinical and MRI measures, modified from Cacciaguerra et al., Radiology 2020 (Cacciaguerra et al., 2020). From left to right, axial view at each spinal cord level plus area postrema of significant correlations between regional spinal atrophy and: EDSS, pyramidal functional score, sensitive functional score, disease duration, brain T1 LV and brain T2 LV (colour scale from yellow to brown indicates t value, $p < 0.001$). Spinal cord levels are shown on the left. Author's reuse as per Journal pre-approved permission (<https://pubs.rsna.org/page/policies#license>).



Abbreviations: AP=area postrema; C=cervical, T=thoracic; EDSS=Expanded disability status scale; LV=lesion volume; A=anterior; L=left.

Discussion

The spinal cord is involved in NMOSD with both of focal lesions (Kim et al., 2015) and atrophy (Liu et al., 2015b) being associated with clinical disability (Kleiter et al., 2016). In this work, we performed a voxel-wise analysis of spinal cord lesions, atrophy and their correlations to clinical features, in a sample of 52 seropositive participants with NMOSD. Accordingly, the lesion probability map showed a greater involvement of cervical levels between C2 and C4 and of the thoracic segments between T1 and T3, while quantitative analysis revealed a higher fractional LV in the gray than in the white matter. Although raw LV were higher in the upper thoracic than in the lower cervical cord, only higher raw LV in C1, C3 and C4 vs C6 and C7 survived Bonferroni correction.

Mean normalized CSA was similar between NMOSD participants and HC, but regional atrophy was evident in the area postrema, between C2 and C4 and between T1 and T2 and correlated with EDSS measure of clinical disability, its pyramidal and sensitive scores and with disease duration.

Gray matter involvement was in line with previous studies applying visual inspection (Filippi et al., 1999, Pekcevik, Mitchell et al., 2016) and semi-quantitative methods (Nakamura et al., 2008).

Recently, the regional distribution of cervical cord lesions was assessed in a large cohort of participants with MS (Eden, Gros et al., 2019) and mirrored the cranio-caudal gradient observed in our study, with relative sparing of C6-C7. Lower cervical segments are likely to have a lower histological myelin and fiber content, as supported by lower magnetization transfer ratio and fractional anisotropy values (Taso, Girard et al., 2016), which may explain their sparing in both disorders.

However, quantitative analysis of fractional LV previously revealed a preferential white matter location of MS lesions, which differs from what we observed here in NMOSD participants. One possible explanation is that spinal cord aquaporin4 expression is prominent in the dorsal horns of the gray matter and around the central canal (Okłinski, Skowronski et al., 2016). This may also help to explain the preferential posterior localization of atrophy observed in NMOSD participants.

High levels of AQP4 expression in the spinal cord and in several brain areas could also be responsible for the correlation disclosed between cervical and brain lesion volumes, as an epiphenomenon of the inflammatory activity due to anti-AQP4 antibodies.

Currently, only a few studies have explored cord atrophy in NMOSD. The active surface method was tested at the cervical level and, similar to our results, showed a higher frequency of spinal cord lesions, longer disease duration and more severe disability in NMOSD patients with cord atrophy (Wang, Wu et al., 2014). Similarly, the mean upper cervical cord area (between C1 and C2) was reduced in NMOSD participants compared to HC (Liu et al., 2018, Liu et al., 2015b), giving further evidence of atrophy at the C2 level.

Voxel-wise techniques revealed the presence of focal atrophy that co-localized with spinal cord lesions, and no focal atrophy in those participants with NMOSD but without visible focal spinal cord lesions.

The importance of the topography of focal tissue damage for regional atrophy accrual was also underlined by the lack of correlation between global measures of spinal cord involvement and clinical disability, in contrast with the significant voxel-wise correlations between EDSS, disease duration and spinal cord atrophy. Disability measures

better correlated with focal area postrema and spinal cord atrophy when pyramidal and sensitive subscores of the EDSS were considered. This is conceivable, since spinal cord damage is likely to be mostly associated with motor and sensitive scoring, while spinal cord-independent functional systems (i.e., visual) also contribute to global EDSS calculation (Kurtzke, 1983).

These findings are different from what is observed in MS, where only mild to moderate correlations have been found between spinal cord lesions and disability, and spinal cord atrophy was only partially related to the presence of local lesions (Valsasina et al., 2018). Since MS lesions are preferentially located in the dorsal columns (Eden et al., 2019) and spinal cord atrophy is largely confined to the white matter (Gilmore, DeLuca et al., 2005), it is tempting to speculate that lesion location may play a role in the different association between focal lesions and atrophy in NMOSD and MS.

Finally, we must discuss several limitations of our study. First, our scans did not include the entire cord, preventing an exhaustive interpretation of results. Second, as a constraint of the active surface method and the images we acquired, we could not determine whether atrophy is driven by a loss of gray or of white matter. Third, our sample was limited to 52 participants with NMOSD (14 of whom were without spinal cord lesions) and 28 HC, reducing the statistical power and possibly hiding several findings, especially after Bonferroni correction. However, to our knowledge, neither a quantitative analysis of gray matter and white matter LV nor thoracic cord involvement in NMOSD have previously been performed and, in view of the rarity of the disease, this is one of the largest samples described in this disorder.

Our study suggests that, in NMOSD, spinal cord lesions on MRI were mainly distributed in the upper cervical cord and in the gray matter, and were spatially associated with atrophy and correlated to disability. Future studies should focus on the temporal evolution of atrophy and its microstructural substrates, by acquiring longitudinal data using advanced MRI pulse sequences.

Supplemental Materials and Methods

MRI acquisition protocol

Brain: a) axial dual-echo turbo spin-echo (Center A: repetition time[TR]/echo time [TE]=2599/16-80 ms, echo train length [ETL]=6, flip angle [FA]=90°, matrix=256x256, field of view [FOV]=240x240 mm², 44 3-mm-thick slices; Center B: TR/TE=3141/20-100 ms, ETL=6, FA=90°, matrix=256x256, FOV=240x240 mm², 44 3-mm-thick slices); and b) axial 3D T1-weighted gradient-echo scans (Center A, fast field echo [FFE]: TR/TE=25/4.6 ms, FA=30°, matrix=256x256; FOV=230x230 mm², 220 0.8-mm-thick slices; Center B, turbo field echo [TFE]: TR/TE=7.2/3.2 ms; TI=1000 ms; FA=8°, matrix=256x256, FOV=256x256 mm², 180 1-mm-thick slices).

Brain MRI analysis. Brain T2-hyperintense and T1-hypointense lesion volumes (LV) were quantified using a local thresholding segmentation technique implemented in the Jim software package (version 7, Xinapse Systems, Colchester, UK). After T1-hypointense lesion refilling (Battaglini, Jenkinson et al., 2012), normalized brain volumes were assessed using FSL Structural Image Evaluation with Normalization of Atrophy (SIENAX) version 2.6 (<http://fsl.fmrib.ox.ac.uk/fsl/fslwiki/SIENA>).

Spinal cord lesion maps and atrophy assessment. Sagittal T1-weighted cord images and the corresponding T1-hypointense lesion masks were reformatted to the axial plane and resampled to 1-mm slice thickness. The cross-sectional area (CSA) of the spinal cord was measured (from the area postrema to the inferior border of T3) using the active surface method (Horsfield et al., 2010) implemented in the Jim software package. Landmarks were manually placed in the center of the cord between the above mentioned boundaries, at intervals of approximately 10 mm. The cord center line and cord outlines were automatically estimated for each slice and results were reviewed to exclude possible failure of cord outlining. The mean CSA was calculated as the total cord volume divided by the cord length and was normalized (CSAn) by multiplying the raw values by the head scaling factor obtained when transforming to standard space provided by the FSL SIENAX version 2.6 software, which is inversely proportional to the total intracranial volume and not influenced by brain atrophy (Horsfield et al., 2010). Unfolded cord and lesion images of each participant were obtained by reformatting the input images and the

corresponding T1-weighted lesion masks in planes perpendicular to the estimated cord center-line (Horsfield et al., 2010). Binary cord masks were also straightened using the same procedure. We corrected interparticipant neck length variability by rescaling unfolded cord and mask images in the through-slice direction to the median cord length of healthy controls (HC) (i.e., 190 mm), and corrected inter-center geometry differences by cropping all images to the common inner FOV (i.e., 106 x 220 mm²). Then, all scans were coregistered to a cord template obtained by averaging straightened HC cord images from both centers. The transformation between straightened cord images, cord masks and lesion masks from each participant and the HC template consisted of a scaling factor applied along the cranio-caudal direction (Valsasina et al., 2012). Finally, cord masks and T1-weighted lesion masks were smoothed using an anisotropic Gaussian kernel filter with a full width at half maximum of 1x1x2 mm³ (Valsasina et al., 2012).

4.2. Volume of hippocampal subfields and cognitive deficits in neuromyelitis optica spectrum disorders

Cacciaguerra *et al.*, *European Journal of Neurology* 2021

This chapter describes the work published in *European Journal of Neurology* (PMID: 34415660, DOI: 10.1111/ene.15073).

Received: 3 April 2021 | Accepted: 17 August 2021

DOI: 10.1111/ene.15073

European Journal
of Neurology

ORIGINAL ARTICLE

Volume of hippocampal subfields and cognitive deficits in neuromyelitis optica spectrum disorders

Laura Cacciaguerra^{1,2,3} | Paola Valsasina¹ | Alessandro Meani¹ |
Gianna C. Riccitelli¹ | Marta Radaelli² | Maria A. Rocca^{1,2,3} | Massimo Filippi^{1,2,3,4,5}

¹Neuroimaging Research Unit, Division of Neuroscience, IRCCS San Raffaele Scientific Institute, Milan, Italy

²Neurology Unit, IRCCS San Raffaele Scientific Institute, Milan, Italy

³Vita-Salute San Raffaele University, Milan, Italy

⁴Neurorehabilitation Unit, IRCCS San Raffaele Scientific Institute, Milan, Italy

⁵Neurophysiology Service, IRCCS San Raffaele Scientific Institute, Milan, Italy

Correspondence

Massimo Filippi, IRCCS San Raffaele Scientific Institute, Neuroimaging Research Unit, Division of Neuroscience, Via Olgettina 60, 20132 Milan, Italy.
Email: filippi.massimo@hsr.it

Abstract

Background: Aquaporin-4 (AQP4) water channel is involved in hippocampal plasticity and is the target of neuromyelitis optica spectrum disorders (NMOSD) autoimmunity. We measured volumes of hippocampal subfields and their association with cognitive performance in AQP4-seropositive NMOSD patients.

Methods: Global and regional hippocampal volumes were derived from 28 AQP4-seropositive NMOSD patients and 101 healthy controls (HC) from 3D-T1-weighted images. Normalized brain volumes were also calculated. A neuropsychological evaluation, including the Brief Repeatable Battery of Neuropsychological Tests, was performed in patients. Based on HC data, we estimated mean z-scores of volumes in the whole NMOSD group and compared them according to the status of global and domain-selective cognitive impairment.

Results: Global cognitive impairment was detected in 46.4% of NMOSD patients, with attentive (60.7%) and executive (21.4%) domains being the most affected. NMOSD patients had left hippocampal atrophy at global ($p = 0.012$) and regional level (fimbria, Cornu Ammonis [CA] 3, molecular layer, dentate gyrus [DG], and subicular complex, p values ranging between 0.033 and <0.001). On the right side the fimbria and hippocampal tail were atrophic ($p = 0.024$ for both). Cognitively impaired patients showed atrophy in the left CA3 and CA4 ($p = 0.025$ – 0.028), while patients presenting verbal and visual memory impairment had significant CA3 and DG atrophy. Those patients with attentive or executive impairment had preserved brain and hippocampal volumes.

Conclusions: NMOSD patients showed hippocampal atrophy associated with verbal and visual memory impairment. Such damage did not explain attention and executive function alterations, which were the most common cognitive deficits in this population.

Introduction

In NMOSD, cognitive impairment has been reported in up to 70% of patients and is characterized by multidomain deficits similar to MS (Oertel *et al.*, 2019). Although their

underlying structural substrates are still debated (Oertel et al., 2019), one of the largest studies identified hippocampal atrophy as the best predictor of CI in NMOSD (Liu et al., 2015a).

In line with this observation, AQP4 water channel is involved in cognition by favoring hippocampal synaptic plasticity (Skucas, Mathews et al., 2011). The “trisynaptic circuit”, the main hippocampal path (Stepan, Dine et al., 2015), comprises three hippocampal subfields (the dentate gyrus [DG], the Cornus Ammonis [CA] 3 and the CA1) and two projective connections (the perforant path-DG pathway, between entorhinal cortex and DG and the Schaffer collaterals, between CA3 and CA1) (Stepan et al., 2015).

In translational models lacking AQP4 expression, both these connections showed increased synaptic long-term depression and reduced long-term potentiation resulting in defective spatial memory formation and consolidation (Skucas et al., 2011).

AQP4-seropositive NMOSD patients represent an in-vivo, disease-related model of AQP4 water channel autoimmunity (Wingerchuk et al., 2015), where the distribution of hippocampal damage might involve similar subfields (DG, CA3, and CA1) and lead to cognitive impairment.

Hence, here we assessed regional hippocampal volumes in AQP4+NMOSD patients and their association with cognitive performance.

Methods

Ethic committee approval. Approval was received from the local ethical standards committee (IRCCS San Raffaele Scientific Institute) on human experimentation. The study conforms to the Declaration of Helsinki, and all subjects signed informed consent.

Subjects. MRI scans were acquired from 28 clinically stable and steroid-free (for at least one month) AQP4+NMOSD (Wingerchuk et al., 2015) patients and 101 healthy controls (HC). AQP4 serostatus was assessed by cell-based assay (Wingerchuk et al., 2015). Exclusion criteria were history of drug/alcohol abuse, psychiatric comorbidities, and head trauma.

Clinical and neuropsychological evaluation. On the same day of MRI, all patients received a neurological examination, including the EDSS, and a neuropsychological

evaluation, with the Brief Repeatable Battery of Neuropsychological Tests (BRB-N) and a short version of the Stroop Color Word Test (SCWT). Verbal and visual memory were assessed with the Selective Reminding Test (SRT) and the 10/36 Spatial Recall Test (SPART); attention with the Symbol Digit Modalities Test (SDMT) and the Paced Auditory Serial Addition Test (PASAT) 2” and 3”. According to normative data, z-scores were obtained from BRB-N raw scores correcting for demographic variables (Amato, Portaccio et al., 2006), and were averaged to obtain the domain-specific z-scores. Patients with at least two abnormal tests ($z\text{-score} < -1.64$, corresponding to the normal distribution 5% lower quantile) were considered cognitively impaired (CI). Impairment in each domain (attention, verbal, and visual memory) was also assessed (at least one abnormal test). Patients with a SCWT time or error interference effect equivalent score of zero were considered impaired in executive functioning.

MRI acquisition. Brain MRI was acquired on a 3.0 T scanner (Intera, Philips Medical Systems, Best, the Netherlands) and included: axial dual-echo turbo spin-echo (repetition time [TR]/echo time [TE]=2599/16-80 milliseconds [ms], echo train length [ETL]=6, flip angle [FA]=90°, matrix=256x256, field of view [FOV]=240x240 mm², 44 3-mm-thick slices), axial 3D T1-weighted fast-field echo (TR/TE=25/4.6 ms, FA=30°, matrix=256x256; FOV=230x230 mm², 220 0.8-mm-thick slices) and axial double inversion recovery (DIR) (TR/TE =18146/125 ms, TI=3000 ms, delay=100 ms, ETL=27, matrix=256x192, FOV=240x180 mm², 44 3 mm-thick slices, number of excitations= 2).

MRI analysis. Brain lesions were segmented on T2- and T1-weighted sequences (Jim 8.0 Xinapse Systems Ltd) to calculate LV. The double inversion recovery (DIR) sequence was used to assess the presence of hippocampal lesions (Roosendaal, Moraal et al., 2008). After lesion refilling,(Chard, Jackson et al., 2010) normalized brain volume (NBV), GM volume (NGMV), and white matter (WM) volume (NWMV) were measured on T1-weighted sequences (FSL SIENAx software).

The automatic cortical and hippocampal subfield segmentation analysis of the FreeSurfer 6.0 software suite was run on lesion-refilled, bias-field-, intensity non-uniformity- and contrast-corrected T1-weighted sequences, obtaining global and regional hippocampal volumes including: hippocampal tail, subiculum, presubiculum, parasubiculum, CA1,

CA3, CA4, hippocampal molecular layer, granule cell and molecular layer of the DG (GC-ML-DG), hippocampal fissure, fimbria, hippocampal-amygdaloid transition area (HATA) (Iglesias, Augustinack et al., 2015). We inspected the output surfaces, and if necessary, images were manually corrected (e.g., by removing skull structures from brain image, modifying the WM mask, or adding control points).

To optimize the number of variables to the sample size, we combined the volumes of subiculum, presubiculum and parasubiculum in a variable named “subicular complex”.

Statistical analysis. Clinical and conventional MRI variables were compared using two-sample t-test/Mann-Whitney U-test (continuous variables) or Pearson χ^2 (categorical variables).

To overcome the issue of the limited cohort of NMOSD patients, we regressed out the NMOSD-independent effects of age and sex on MRI volumes by running linear models on a large cohort of HC covering a wide range of ages (18-63 years) and with a balanced sex distribution (female/male: 44/57). The SIENAx inverse V-scaling factor was included as additional covariate in models for global and regional hippocampal volumes, to correct for head-size. Predicted residuals for NMOSD patients were divided by the HC error term and converted into z-scores. Mean z-scores were estimated by one-sample t-tests in the whole patients' group and compared according to the status of global and domain-selective impairment by Wilcoxon rank-sum exact tests.

The associations between MRI measures and domain-specific cognitive z-scores/equivalent scores were explored with Pearson's/Spearman's correlation analysis and bivariate scatterplots.

Benjamini-Hochberg False Discovery Rate (FDR) correction was applied. FDR-corrected p values are reported as p_{FDR} and survival is specified in text and table. Due to the exploratory nature of the study, also significant results not surviving the correction are reported.

Data availability. The dataset analyzed is available on reasonable request.

Results

Table 4.2.1 reports clinical and neuropsychological features of the study subjects. Cognitive impairment was detected in 46.4% NMOSD patients, with the attentive domain being the most affected (60.7%), followed by executive functions (21.4%), verbal (17.9%), and visuo-spatial (14.8%) memory. Visual memory impairment was not assessed in a patient who refused to perform the SPART test.

Table 4.2.1. Demographic, clinical, and neuropsychological variables of study population. Unless otherwise specified, data are reported as median and interquartile range. Results of the executive domain (Stroop test) are expressed as frequencies (percentages) of equivalent scores (0=impaired) of time delay and errors.

Clinical variables						
	HC (n=101)	NMOSD (n=28)	p HC vs NMOSD	CP NMOSD (n=15)	CI NMOSD (n=13)	p CI vs CP
Mean age (SD) [years]	37.6 (12.9)	43.6 (12.4)	0.03^a	37.4 (8.3)	50.9 (12.6)	0.01^b
Female/Male	44/57	22/6	0.03^c	11/4	11/2	0.47 ^c
Education [years]	13 (12-15)	13 (12-14)	0.99 ^b	13 (13-17)	11 (7-13)	0.050 ^b
EDSS	-	5.0 (2.5-6.0)	-	3.5 (1.5-6.5)	5.5 (3.5-6.5)	0.03^b
Disease duration [years]	-	3.5 (2.9-7.5)	-	4.1 (2.9-11.9)	4.6 (2.3-12.0)	0.25 ^b
Neuropsychological variables						
Domain	-	NMOSD (n=28)	-	CP NMOSD (n=15)	CI NMOSD (n=13)	p CI vs CP
Verbal memory [z-scores]	-	-0.57 (-1.03; 0.11)	-	-0.17 (-0.90; 0.38)	-0.85 (-1.7; -0.48)	0.041 ^d
Visuo-spatial memory [z-scores]	-	-0.02 (-1.00; 0.56)	-	0.24 (-0.36; 0.87)	-0.90 (-1.5; 0.08)	0.021 ^d
Attentive [z-scores]	-	-1.20 (-2.16; -0.44)	-	-0.50 (-0.83; -0.12)	-2.18 (-2.50; -1.77)	<0.001 ^d
Executive (Stroop test)						
Time delay (%)						
0	-	2 (7.1)	-	0 (0.0)	2 (7.1)	0.55 ^c
1	-	4 (14.3)	-	2 (7.1)	2 (7.1)	
2	-	3 (10.7)	-	1 (3.6)	2 (7.1)	
3	-	4 (14.3)	-	3 (10.7)	1 (3.6)	
4	-	15 (53.6)	-	9 (32.1)	6 (21.4)	
Error (%)						
0	-	5 (17.9)	-	0 (0.0)	5 (17.9)	0.027 ^e

1	-	1 (3.6)	--	0 (0.0)	1 (3.6)
2	-	9 (32.1)	-	6 (21.4)	3 (10.7)
3	-	2 (7.1)	-	1 (3.6)	1 (3.6)
4	-	11 (39.3)	-	8 (28.6)	3 (10.7)

^aTwo-sample t test; ^bMann-Whitney U-test; ^cPearson χ^2 ; ^dWilcoxon Rank Sum test; ^eFisher's Exact test.

Abbreviations: HC=healthy controls; NMOSD=neuromyelitis optica spectrum disorders; EDSS=expanded disability status scale; CP=cognitively preserved; CI=cognitively impaired; SD=standard deviation.

The Freesurfer 6.0 pipeline ran successfully in all subjects. We found no hippocampal lesions on DIR sequences in patients or HC.

Structural MRI measures of NMOSD and HC are reported in **Table 4.2.2**. NMOSD patients had a significant reduction from healthy population age- and sex-expected values (i.e., z-score=0) of NBV ($p_{FDR}=0.002$), NGMV ($p_{FDR}<0.001$), and left-hippocampal volume ($p_{FDR}=0.012$), with atrophy of its fimbria, CA3, molecular layer, GC-ML-DG and subicular complex (p_{FDR} -values range: 0.033-<0.001). The right-hippocampus showed atrophy of tail and fimbria ($p_{FDR}=0.024$, **Figure 4.2.1**).

Table 4.2.2. MRI variables of NMOSD patients and HC. MRI volumes are reported as z-scores, obtained from age-, sex- and head-size-adjusted linear models estimated in the HC cohort, for the whole NMOSD group, and according to the global cognitive status. When specified, p-values are false-discovery rate corrected. Except where specified, data are reported as means (standard deviation).

Brain MRI variables (mL)							
	HC* (n=101)	NMOSD* (n=28)	Mean estimated z- score (95% CI) in NMOSD	P_{FDR}^a	Median z- score (IQR) in CP NMOSD (n=15)	Median z- score (IQR) in CI NMOSD (n=13)	Uncorrected p^b CI vs CP
Median brain T2 LV (IQR)	-	0.16 (0.0-0.8)	-	-	0.11 (0.0; 0.5)	0.21 (0.1; 1.3)	0.27
Median brain T1 LV (IQR)	-	0.10 (0.0-0.4)	-	-	0.06 (0.0; 0.3)	0.14 (0.0; 0.6)	0.31
NBV	1600 (81)	1541 (55)	-0.70 (-1.01; -0.39)	0.002	-0.52 (-1.52; -0.19)	-0.69 (-1.08; 0.04)	0.99

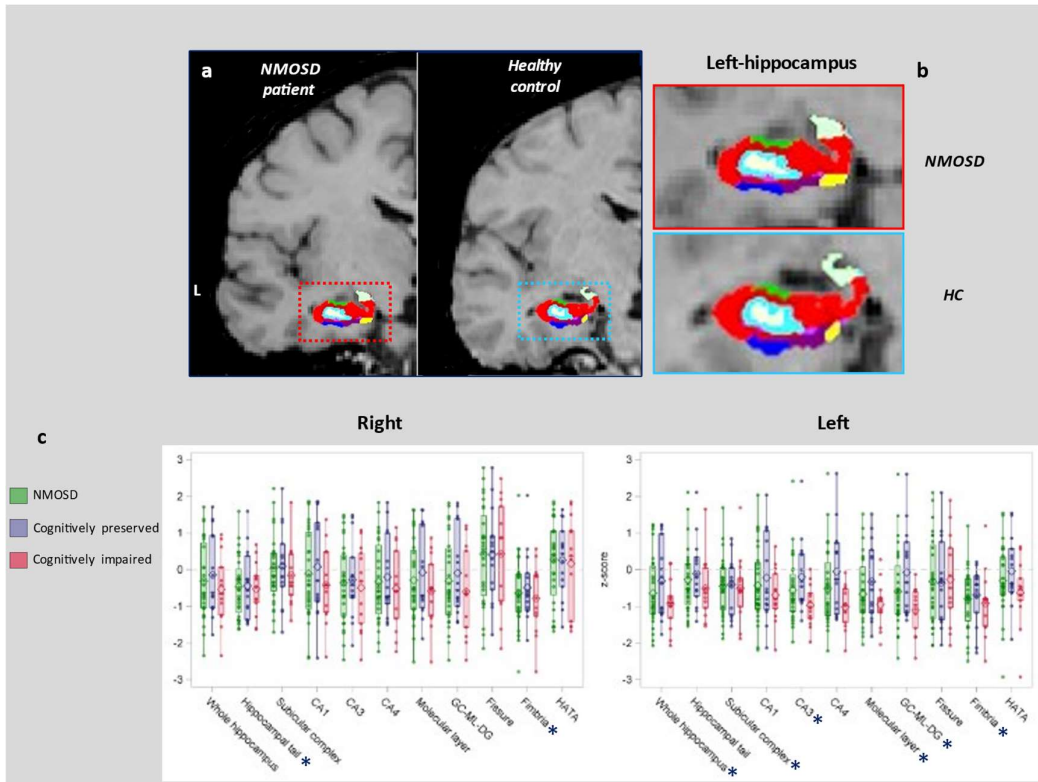
NGMV	751 (51)	700 (39)	-0.99 (-1.31; -0.67)	<0.001	-1.05 (-1.98; -0.47)	-0.71 (-1.27; -0.21)	0.20
NWMV	849 (46)	840 (34)	-0.24 (-0.57; 0.10)	0.35	0.1 (-1.15; 0.49)	-0.41 (-0.87; 0.24)	0.62
Hippocampal volumes [mL *1000]							
Whole hippocampus							
Left	3452 (341)	3188 (333)	-0.64 (-1.02; -0.26)	0.012	-0.35 (-1.19; 0.98)	-0.91 (-1.31; -0.71)	0.27
Right	3461 (341)	3267 (342)	-0.31 (-0.77; 0.15)	0.24	-0.63 (-1.04; 0.94)	-0.66 (-1.24; 0.06)	0.44
Hippocampal tail							
Left	554 (69)	525 (64)	-0.27 (-0.62; 0.08)	0.20	-0.21 (-0.73; 0.34)	-0.64 (-1.04; 0.05)	0.16
Right	555 (72)	511 (59)	-0.46 (-0.79; -0.14)	0.024	-0.56 (-1.37; 0.38)	-0.48 (-0.9; -0.16)	0.96
Subicular complex							
Left	796 (94)	732 (73)	-0.45 (-0.77; -0.12)	0.025	-0.3 (-1.23; 0.06)	-0.56 (-1.02; -0.22)	0.59
Right	738 (81)	715 (74)	-0.06 (-0.40; 0.27)	0.83	0.04 (-0.46; 0.7)	-0.34 (-0.69; 0.43)	0.59
CA1							
Left	633 (74)	589 (75)	-0.44 (-0.86; -0.01)	0.10	-0.61 (-1.09; 1.06)	-0.8 (-1.06; -0.11)	0.36
Right	649 (77)	617 (84)	-0.10 (-0.58; 0.37)	0.67	-0.3 (-0.87; 1.28)	-0.42 (-1.16; 0.48)	0.34
CA3							
Left	207 (27)	190 (25)	-0.56 (-0.90; -0.21)	0.012	-0.45 (-0.85; 0.44)	-1.02 (-1.33; -0.65)	0.025
Right	228 (28)	212 (30)	-0.36 (-0.82; 0.10)	0.20	-0.41 (-0.76; 0.34)	-0.31 (-1.47; 0.45)	0.65
CA4							
Left	257 (28)	240 (32)	-0.51 (-0.94; -0.08)	0.053	-0.26 (-1.21; 0.74)	-0.98 (-1.44; -0.52)	0.028
Right	270 (28)	256 (31)	-0.33 (-0.80; 0.15)	0.23	-0.73 (-0.92; 1)	-0.58 (-1.33; 0.51)	0.62
Molecular layer							
Left	572 (60)	525 (57)	-0.66 (-1.04; -0.29)	0.012	-0.55 (-1.17; 0.54)	-0.84 (-1.17; -0.76)	0.20
Right	574 (60)	542 (64)	-0.28 (-0.74; 0.18)	0.25	-0.71 (-1.04; 1.25)	-0.52 (-1.26; 0.15)	0.44
GC-ML-DG							
Left	301 (32)	278 (38)	-0.59 (-1.05; -0.14)	0.033	-0.35 (-1.17; 0.76)	-0.96 (-1.59; -0.61)	0.052
Right	313 (32)	296 (36)	-0.31 (-0.80; 0.19)	0.25	-0.56 (-0.99; 1.39)	-0.66 (-1.57; 0.51)	0.34
Fissure							
Left	149 (27)	145 (31)	-0.32 (-0.78; 0.14)	0.24	-0.35 (-1.37; 0.76)	-0.50 (-1.03; 0.6)	0.96
Right	143 (26)	158 (34)	0.42 (-0.10; 0.95)	0.20	0.49 (-0.54; 0.92)	0.86 (-0.86; 1.73)	0.82
Fimbria							
Left	74 (18)	55 (15)	-0.79 (-1.12; -0.47)	<0.001	-0.41 (-1.17; -0.17)	-0.8 (-1.54; -0.78)	0.18

Right	75 (16)	61 (14)	-0.64 (-1.08; -0.19)	0.024	-0.7 (-1.11; -0.1)	-0.78 (-1.27; -0.14)	0.68
HATA							
Left	58 (9)	54 (8)	-0.30 (-0.65; 0.06)	0.19	-0.37 (-0.61; 0.57)	-0.53 (-0.84; -0.23)	0.10
Right	58 (10)	57 (11)	0.28 (-0.21; 0.77)	0.28	0.43 (-0.46; 1.04)	0.38 (-1.41; 1.06)	0.96

^aOne-sample t-test for the nullity (i.e. healthy population expected value) of the mean estimated z-score; ^bWilcoxon rank-sum exact test.

Abbreviations: HC=healthy controls; NMOSD=neuromyelitis optica spectrum disorders; CP=cognitively preserved; CI=cognitively impaired; LV=lesion volume; IQR=interquartile range; NBV=normalized brain volume; NGV=normalized gray matter volume; NWMV=normalized white matter volume; CA=Cornus Ammonis; GC-ML-DG=granule cell and molecular layer of the dentate gyrus; HATA=hippocampal-amygdaloid transition area.

Figure 4.2.1. Coronal view of the left-hippocampus and of the FreeSurfer 6.0 segmentation of subfields (a) in a patient with NMOSD and a HC (anatomical convention). Modified from Cacciaguerra et al., European Journal of Neurology 2021 (Cacciaguerra, Valsasina et al., 2021c), reused with permission (license 5431680771865). A zoomed image of the left-hippocampus is provided in (b). Panel (c) represents the scattered boxplots of volumes (z-scores) of the hippocampus and its subfields in patients with NMOSD (whole group=green dots; cognitively preserved patients=blue dots; cognitively impaired patients=red dots). Boxes represent the median and interquartile range of distribution. *Indicates significant results ($p_{FDR}<0.05$).



Abbreviations: NMOSD=neuromyelitis optica spectrum disorders; HC=healthy controls; L=left; CA=Cornus Ammonis; GC-ML-DG=granule cell and molecular layer of the dentate gyrus; HATA=hippocampal-amygdaloid transition area.

Compared to cognitively preserved, CI NMOSD patients had atrophy in left-CA3 ($p=0.025$), left-CA4 ($p=0.028$), and a trend in left-GC-ML-DG ($p=0.052$), although results did not survive FDR correction. Differences in hippocampal global and regional measures are reported in **Table 4.2.2** and **Figure 4.2.1**.

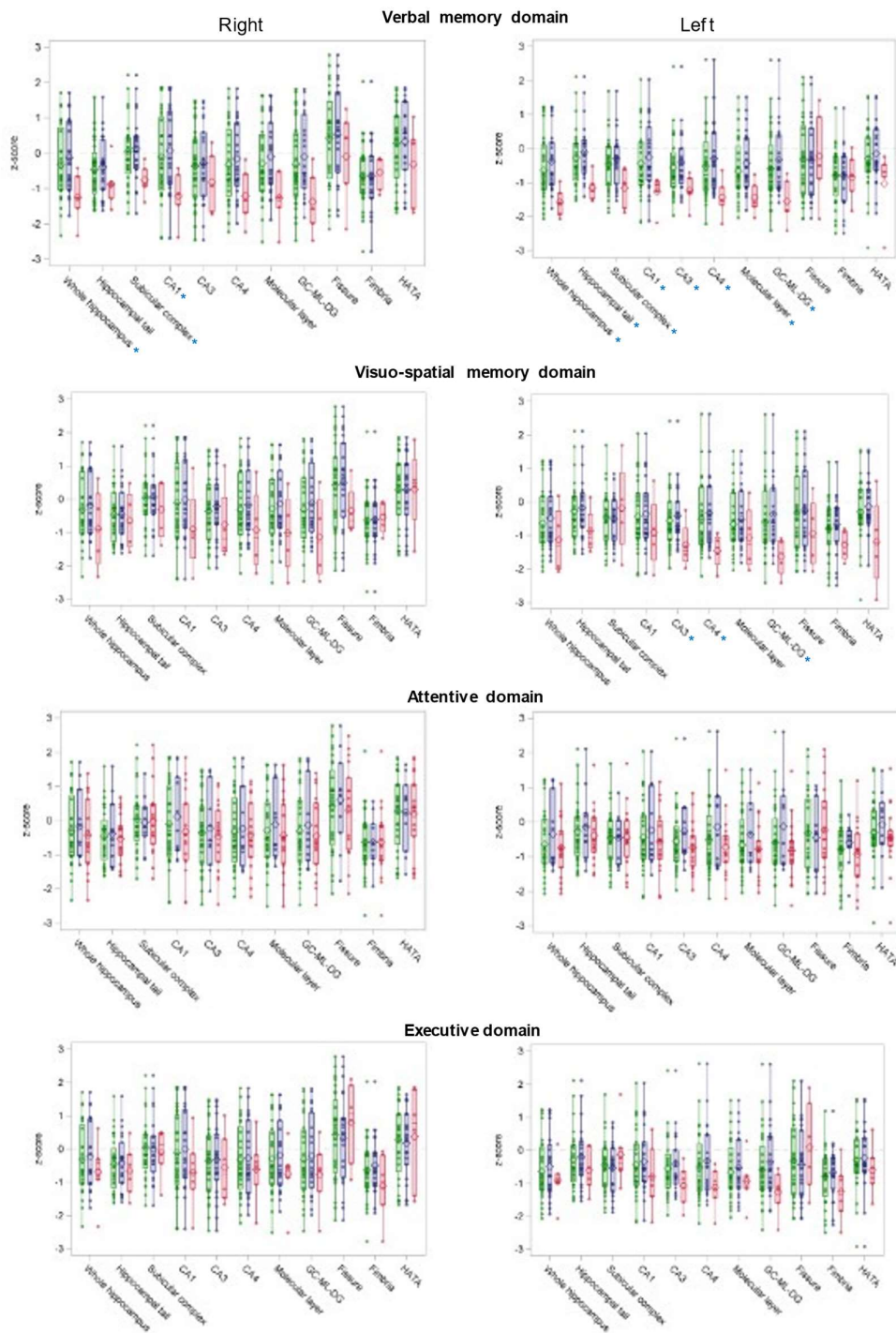
Patients presenting verbal memory impairment had median (IQR) atrophy of the left-hippocampus (-1.60 [-1.93; -1.31] vs -0.71 [-1.07; 0.19], $p_{FDR}=0.033$), left-subicular complex (-1.02 [-1.75; -0.62] vs -0.3 [-1.04; 0.08], $p_{FDR}=0.048$), left-molecular layer (-1.59 [-1.70; -1.08] vs -0.79 [-1.12; 0.32], $p_{FDR}=0.048$), left-GC-ML-DG (-1.82 [-1.84; -0.96] vs -0.61 [-1.17; 0.41]), $p_{FDR}=0.048$) and left-CA3 (-1.27 [-1.33; -0.87] vs -0.65 [-1.02; 0.01], $p=0.045$). All, but CA3, survived FDR correction (Supplementary Table 1). In patients with visuo-spatial memory impairment, left-GC-ML-DG was atrophied (-1.51 [-2.12; -1.15] vs -0.61 [-1.17; 0.41], $p=0.022$) and a trend was observed in left-CA3 (-

1.45 [-1.77; -0.79] vs -0.72 [-0.91; 0.01], $p=0.058$), although results did not survive FDR correction (**Supplementary Table 4.2.1**).

NMOSD participants with memory impairment also had additional hippocampal damage in subfields not atrophied at group level. Those with abnormal verbal memory had reduced volumes of the right-hippocampus, left-hippocampal tail, right-subicular complex, bilateral CA1, left-CA4, and right-DG ($p<0.045$, see Supplemental Table 1 for further details). Patients with visuo-spatial memory impairment also had atrophy in the left-CA4 ($p=0.04$, see **Supplementary Table 4.2.1**).

Patients with abnormal attention or executive functions had neither worse brain nor hippocampal atrophy compared to patients without such deficits (see Supplementary Tables 3 and 4). Hippocampal volumes (z-scores) in NMOSD patients, according to domain-specific cognitive impairment are reported in **Figure 4.2.2**.

Figure 4.2.2. Scattered boxplots of volumes (z-scores) of the hippocampus and its subfields in patients with NMOSD, according to domain-specific cognitive impairment. Modified from Cacciaguerra et al., European Journal of Neurology 2021 (Cacciaguerra et al., 2021c), reused with permission (license 5431680771865). Legend: whole group=green dots; cognitively preserved patients=blue dots; cognitively impaired patients=red dots). Boxes represent the median and interquartile range of distribution. *Indicates significant results (uncorrected $p<0.05$).



No significant correlations between MRI measures and neuropsychological z-scores were found (**Supplementary Tables 4.2.1-4**). The significant volume reduction disclosed in several hippocampal subfields in patients impaired in verbal and visuo-spatial memory

compared to the preserved ones is represented in **Figure 4.2.3 and 4.2.4**, which combines bivariate scatterplots with marginal boxplots.

Figure 4.2.3. Significant bivariate associations between the neuropsychological performance (domain-specific z-scores, y-axis) and hippocampal volumes atrophy (z-scores, x-axis), combined with marginal boxplot in NMOsD patients, stratified according to the presence (red dots) or absence (blue dots) of verbal memory impairment. Modified from Cacciaguerra et al., *European Journal of Neurology* 2021 (Cacciaguerra et al., 2021c), reused with permission (license 5431680771865).

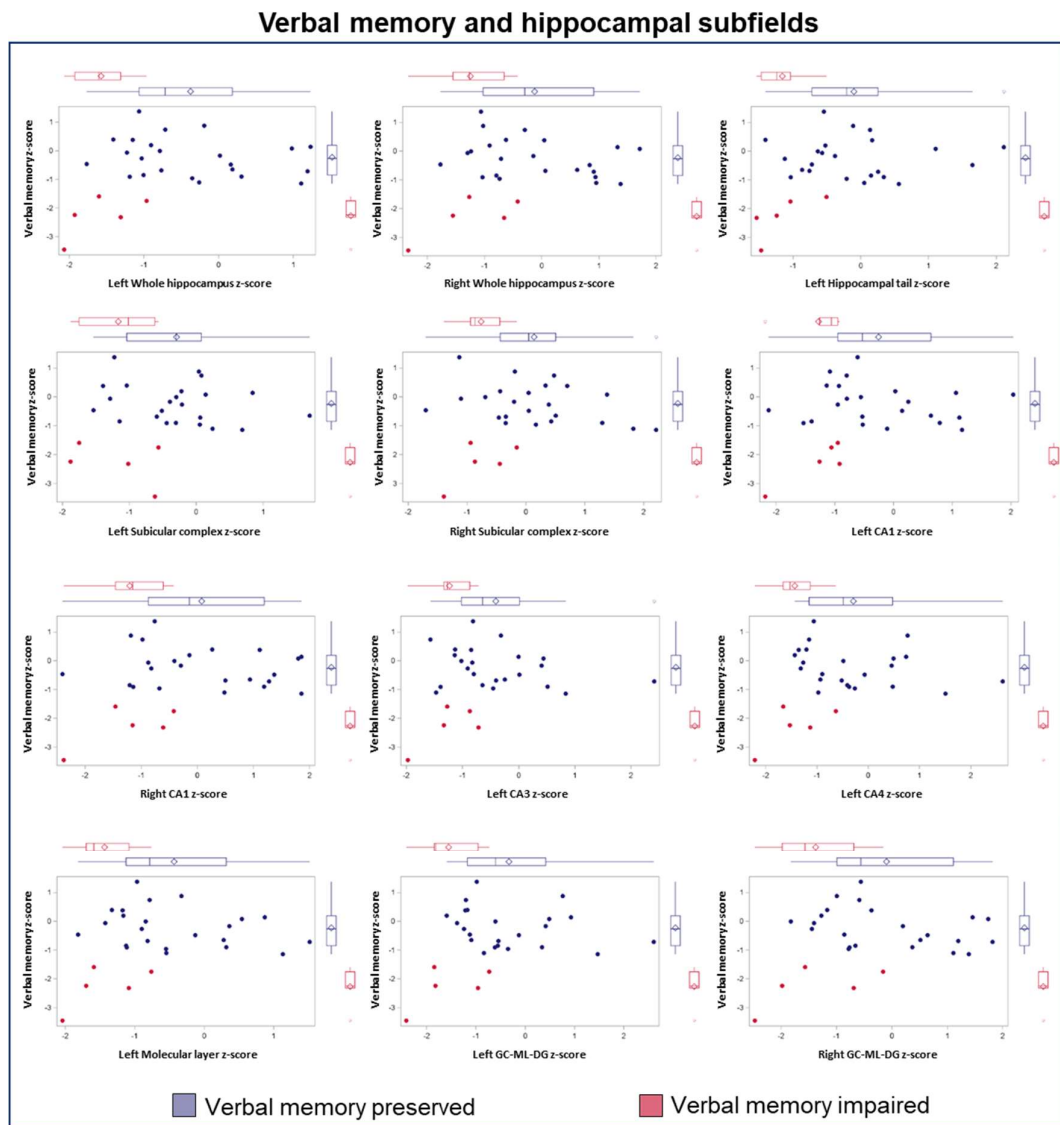
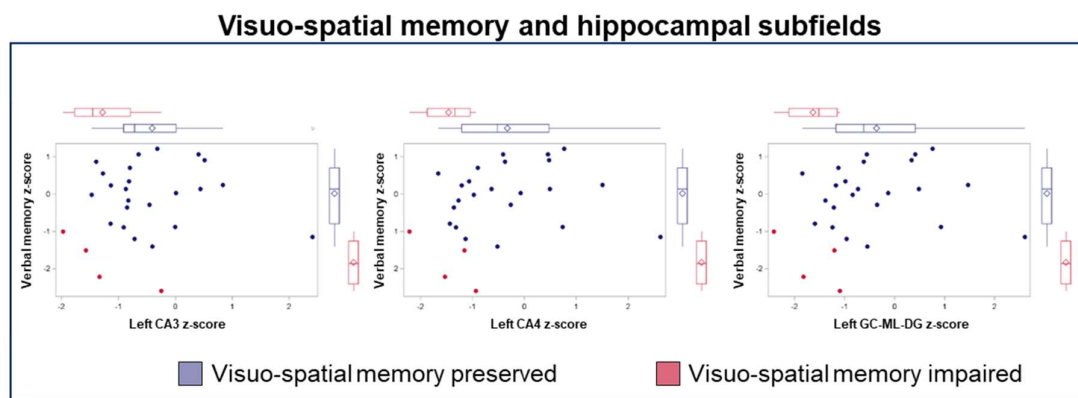


Figure 4.2.4. Significant bivariate associations between the neuropsychological performance (domain-specific z-scores, y-axis) and hippocampal volumes atrophy (z-scores, x-axis), combined with marginal boxplot in NMOSD patients, stratified according to the presence (red dots) or absence (blue dots) of visuo-spatial memory impairment. Modified from Cacciaguerra et al., *European Journal of Neurology* 2021 (Cacciaguerra et al., 2021c), reused with permission (license 5431680771865).



Discussion

Hypothesizing that anti-AQP4-IgG might trigger hippocampal damage by affecting specific hippocampal pathways, we investigated volumetric alterations of hippocampal subfields in NMOSD patients.

NMOSD patients had hippocampal atrophy, with CA3 and GC-ML-DG atrophy associated with poor verbal and visual memory. However, atrophy did not explain attentive domain impairment, which was the most common deficit.

Hippocampal atrophy was preferentially left-sided, similarly to neurodegenerative disorders (Lindberg, Walterfang et al., 2012, Thompson, Hayashi et al., 2003). Among neuroinflammatory diseases, hippocampal damage was mainly investigated in MS, where studies have detected both bilateral (Sicotte, Kern et al., 2008) and asymmetric damage (right-(Roosendaal, Hulst et al., 2010) or left-sided) (Preziosa, Pagani et al., 2017). However, over a five-year follow-up, MS patients showed a worse atrophy progression in the left- hemisphere despite symmetrical WM lesions accumulation (Preziosa et al., 2017). This finding aligns with longitudinal observations of faster GM volume loss in the

left-hemisphere (Thompson et al., 2003), including the hippocampus (Nobis, Manohar et al., 2019), in HC with aging. Possible explanations rely on the left-hemispheric dominance for language (Knecht, Dräger et al., 2000), potentially conditioning an asymmetrical use of the cerebral hemispheres and consequent metabolic unbalance in the course of life (Preziosa et al., 2017). The likelihood of this lateralization increases with the degree of right-handedness (Knecht et al., 2000). However, given the lack of data in support or against asymmetric susceptibility to damage in NMOSD, future studies are needed to confirm or refute our observation.

CA1, CA3, and GC-ML-DG, the three core synaptic stations of the “trisynaptic circuit”, (Stepan et al., 2015) were the most atrophic subfields in patients with verbal (all subfields) and visual memory impairment (GC-ML-DG). In line with this, histopathological studies on temporal lobe epilepsy suggested a prominent role of CA3 and DG in declarative memory acquisition (Coras, Pauli et al., 2014), whereas pathology in Alzheimer’s disease disclosed CA1 decreased hippocampal neuronal density and dendritic abnormalities (Dorostkar, Zou et al., 2015, Padurariu, Ciobica et al., 2012). Similarly, the selective damage of the DG in the Kabuki syndrome is associated with prominent visuo-spatial abnormalities (Harris, Mahone et al., 2019). This is a rare genetic disorder mainly due to mutations in the lysine-specific methyltransferase 2D (KMT2D) gene, whose clinical manifestations include facio-skeletal abnormalities and cognitive deficits. In translational models, the mutation was associated with reduced volume of the granule cell layer in the DG (Bjornsson, Benjamin et al., 2014), and this observation was confirmed in a MRI study documenting a decreased volume of the hippocampus and its DG in these patients (Boisgontier, Tacchella et al., 2019).

However, CA1 atrophy was detected only in the subgroup of patients with verbal memory impairment, while it was not atrophied at group level in NMOSD. Although this finding might be due to the small number of patients with verbal memory impairment in our sample, it seems in contrast with previous observations of its peculiar, etiology-independent, susceptibility to damage (Coras et al., 2014, Lindberg et al., 2012). Aside from sample-size or technical limitations, the different vascularization of CA3 and CA1 might explain their vulnerability. Since AQP4 water channels are located at blood-brain barrier, a poorer vascular supply, as suggested by the hippocampal watershed area in CA1

and its propensity to ischemia, might determine a lower AQP4 expression in this subfield, hence preventing its involvement in AQP4-seropositive NMOSD patients.

In our work, the correlation analysis between hippocampal subfields and cognitive scores did not identify any significant result. Bivariate scattered boxplots confirmed a significant regional hippocampal atrophy in several subfields in patients impaired in verbal or visuo-spatial memory domains. Unfortunately, the number of cognitively impaired patients in each domain was too small to identify significant correlations. In fact, we do not expect a linear association with hippocampal volumes in cognitive preserved patients, similarly to what is observed in healthy individuals, who often show intersubject variability (Van Petten, 2004).

Despite these remarks, hippocampal atrophy was unrelated to attentive and executive impairment, which were the most common cognitive alterations in our patients, suggesting that other features, like brain microstructural or functional alterations, might contribute to cognitive deterioration in NMOSD (Oertel et al., 2019). In line with this, diffusion tensor imaging studies (Cho, Han et al., 2018, Liu et al., 2012a) disclosed an association between poor performance in attention, information processing speed and working memory, and disruption in networks including the precuneus, a hub of the default-mode network involved in highly-integrated cognitive tasks. These results align with those of a functional MRI study revealing an adaptive role of higher resting-state functional connectivity in the precuneus, correlating with better attentive and executive scores in NMOSD patients (Savoldi, Rocca et al., 2020).

This work is not without limitations, including the small sample-size, the lack of functional MRI measures, and the absence of AQP4-seronegative NMOSD patients. Also, CI and CP patients had a tendency (although not statistically significant) towards lower education levels in the former, which could have worsened the effect of age-related hippocampal volume loss (Noble, Grieve et al., 2012).

However, it suggested that AQP4-seropositive NMOSD patients have global and regional hippocampal atrophy, which is associated with verbal and visual memory impairment, but does not explain alterations of attention and executive functions.

Supplemental Material

Supplementary Tables 4.2.1-4. MRI variables of NMOSD patients according to the impairment in each cognitive domain. MRI volumes are reported as z-scores, obtained from age-, sex- and head-size-adjusted linear models estimated in the HC cohort. All variables are reported as median (interquartile range). Pearson's/Spearman's correlations were run between MRI measures and domain-specific cognitive z-scores/equivalent scores. Significant results are shown bold.

Supplementary Table 4.2.1. MRI variables of NMOSD patients according to the impairment in the verbal memory domain.

Verbal Memory	CP (n=23)	CI (n=5)	p ^a	r ^b	p ^b
Brain MRI variables					
T2 LV [ml]	159 (55; 1296)	0 (0; 352)	0.38	0.03	0.85
T1 LV [ml]	104 (0; 589)	0 (0; 234)	0.48	0.02	0.90
NBV	-0.5 (-1.04; 0.07)	-1.08 (-1.47; -0.77)	0.22	-0.01	0.95
NGMV	-1.03 (-1.53; -0.21)	-1.42 (-1.48; -0.71)	0.45	0.05	0.81
NWMV	0.06 (-1.08; 0.45)	-0.75 (-0.93; -0.41)	0.38	-0.06	0.78
Hippocampal volumes					
Whole hippocampus					
Left	-0.71 (-1.07; 0.19)	-1.60 (-1.93; -1.31)	0.003	0.28	0.14
Right	-0.3 (-1.02; 0.91)	-1.27 (-1.56; -0.66)	0.045	0.21	0.28
Hippocampal tail					
Left	-0.21 (-0.73; 0.26)	-1.24 (-1.47; -1.04)	0.005	0.36	0.06
Right	-0.34 (-1.04; 0.38)	-0.90 (-1.28; -0.81)	0.24	0.29	0.20
Subicular complex					
Left	-0.3 (-1.04; 0.08)	-1.02 (-1.75; -0.62)	0.02	0.15	0.43
Right	0.05 (-0.44; 0.5)	-0.87 (-0.94; -0.44)	0.03	0.13	0.52
CA1					
Left	-0.53 (-0.95; 0.64)	-1.06 (-1.26; -0.95)	0.02	0.25	0.20
Right	-0.14 (-0.87; 1.19)	-1.16 (-1.46; -0.61)	0.04	0.25	0.19
CA3					
Left	-0.65 (-1.02; 0.01)	-1.27 (-1.33; -0.87)	0.045	0.16	0.41
Right	-0.31 (-1.21; 0.6)	-0.93 (-1.66; -0.08)	0.32	-0.01	0.93
CA4					
Left	-0.49 (-1.16; 0.47)	-1.53 (-1.66; -1.13)	0.01	0.21	0.29
Right	-0.48 (-0.92; 0.87)	-1.33 (-1.68; -0.58)	0.09	0.11	0.58
Molecular layer					
Left	-0.79 (-1.12; 0.32)	-1.59 (-1.7; -1.09)	0.03	0.23	0.24
Right	-0.49 (-0.88; 0.86)	-1.26 (-1.53; -0.52)	0.06	0.19	0.32

GC-ML-DG					
Left	-0.61 (-1.17; 0.41)	-1.82 (-1.84; -0.96)	0.02	0.24	0.21
Right	-0.56 (-0.99; 1.11)	-1.57 (-1.98; -0.69)	0.04	0.19	0.34
Fissure					
Left	-0.35 (-1.37; 0.6)	-0.5 (-0.89; 0.93)	0.91	-0.01	0.95
Right	0.65 (-0.54; 1.73)	0.43 (-0.86; 0.86)	0.45	-0.03	0.89
Fimbria					
Left	-0.73 (-1.54; -0.24)	-0.8 (-1.25; -0.33)	0.82	0.05	0.81
Right	-0.73 (-1.27; -0.08)	-0.19 (-1.04; -0.17)	0.82	-0.03	0.89
HATA					
Left	-0.39 (-0.63; 0.57)	-0.69 (-0.84; -0.47)	0.12	0.26	0.18
Right	0.57 (-0.46; 1.45)	0.28 (-1.57; 0.38)	0.19	0.12	0.52

^aWilcoxon rank-sum exact test; ^bPearson's correlations.

Abbreviations: HC=healthy controls; NMOSD=neuromyelitis optica spectrum disorders; CP=cognitively preserved; CI=cognitively impaired; LV=lesion volume; NBV=normalized brain volume; NGV=normalized gray matter volume; NWMV=normalized white matter volume; CA=Cornus Ammonis; GC-ML-DG=granule cell and molecular layer of the dentate gyrus; HATA=hippocampal-amygdaloid transition area.

Supplementary Table 4.2.2. MRI variables of NMOSD patients according to the impairment in the visuo-spatial memory domain.

Visuo-spatial Memory	CP (n=23)	CI (n=4)	p ^a	r ^b	p ^b
Brain MRI variables					
T2 LV [ml]	147 (0; 628)	725.5 (77.5; 1759)	0.63	-0.03	0.89
T1 LV [ml]	102 (0; 301)	362.5 (68; 1114.5)	0.48	-0.08	0.70
NBV	-0.5 (-1.08; 0.07)	-0.77 (-1.22; -0.33)	0.49	0.01	0.94
NGMV	-1.03 (-1.57; -0.24)	-0.98 (-1.33; -0.46)	0.92	-0.05	0.81
NWMV	0.06 (-0.93; 0.45)	-0.56 (-1.05; 0.2)	0.58	0.06	0.75
Hippocampal volumes					
Whole hippocampus					
Left	-0.91 (-1.19; 0.16)	-1.32 (-2; -0.26)	0.34	0.03	0.87
Right	-0.63 (-1.02; 0.91)	-0.93 (-1.95; 0.16)	0.30	-0.05	0.81
Hippocampal tail					
Left	-0.38 (-0.76; 0.26)	-1.06 (-1.36; -0.37)	0.13	0.19	0.35
Right	-0.56 (-1.04; 0.2)	-0.72 (-1.44; 0.16)	0.87	-0.07	0.73
Subicular complex					
Left	-0.44 (-1.15; 0.05)	-0.27 (-1.25; 0.89)	0.82	-0.25	0.21
Right	-0.16 (-0.44; 0.43)	-0.19 (-1.13; 0.49)	0.77	0.09	0.65
CA1					
Left	-0.61 (-1.06; 0.25)	-1.03 (-1.73; -0.08)	0.34	-0.09	0.64
Right	-0.3 (-0.87; 1.19)	-1.07 (-1.77; -0.02)	0.19	-0.13	0.52
CA3					
Left	-0.72 (-0.91; 0.01)	-1.45 (-1.77; -0.79)	0.058	0.09	0.66
Right	-0.29 (-0.76; 0.45)	-1.2 (-1.57; 0.04)	0.24	-0.20	0.32
CA4					
Left	-0.52 (-1.21; 0.47)	-1.34 (-1.87; -1.05)	0.04	0.25	0.21
Right	-0.48 (-0.92; 0.87)	-1.14 (-1.96; 0.11)	0.21	-0.04	0.86
Molecular layer					
Left	-0.82 (-1.17; 0.32)	-1.24 (-1.87; -0.25)	0.30	0.00	0.98
Right	-0.52 (-0.88; 0.86)	-1.01 (-2.02; -0.01)	0.30	-0.01	0.97
GC-ML-DG					
Left	-0.61 (-1.17; 0.41)	-1.51 (-2.12; -1.15)	0.02	0.24	0.23
Right	-0.56 (-0.99; 1.11)	-1.28 (-2.23; -0.04)	0.22	-0.01	0.97
Fissure					
Left	-0.35 (-1.3; 0.93)	-1.05 (-1.83; -0.05)	0.30	0.11	0.58
Right	0.65 (-0.54; 1.68)	-0.65 (-0.89; 0.21)	0.27	0.06	0.77
Fimbria					
Left	-0.55 (-1.17; -0.17)	-1.22 (-1.69; -0.85)	0.07	0.19	0.33
Right	-0.70 (-1.12; -0.1)	-0.46 (-0.98; -0.11)	0.82	0.05	0.82
HATA					
Left	-0.39 (-0.61; 0.38)	-1.23 (-2.27; -0.11)	0.15	0.24	0.22
Right	0.43 (-0.46; 1.06)	0.47 (-0.59; 1.18)	>0.99	-0.05	0.81

^aWilcoxon rank-sum exact test; ^bPearson's correlations.

Abbreviations: HC=healthy controls; NMOSD=neuromyelitis optica spectrum disorders; CP=cognitively preserved; CI=cognitively impaired; LV=lesion volume; NBV=normalized brain volume; NGV=normalized gray matter volume; NWMV=normalized white matter volume; CA=Cornus Ammonis; GC-ML-DG=granule cell and molecular layer of the dentate gyrus; HATA=hippocampal-amygdaloid transition area.

Supplemental Table 4.2.3. MRI variables of NMOSD patients according to the impairment in the attentive domain.

Attentive	CP (n=11)	CI (n=17)	p ^a	r ^b	p ^b
Brain MRI variables					
T2 LV [ml]	55 (0; 472)	175 (143; 1296)	0.23	0.11	0.59
T1 LV [ml]	27 (0; 301)	134 (12; 589)	0.30	0.14	0.49
NBV	-0.39 (-1.52; 0.27)	-0.69 (-1.08; -0.27)	0.55	0.14	0.48
NGMV	-1.05 (-1.92; -0.47)	-1.03 (-1.42; -0.24)	0.64	0.06	0.78
NWMV	0.10 (-1.08; 0.49)	-0.41 (-0.93; 0.29)	0.40	0.15	0.44
Hippocampal volumes					
Whole hippocampus					
Left	-1.03 (-1.19; 0.98)	-0.79 (-1.31; -0.26)	0.61	0.35	0.07
Right	-0.63 (-1.04; 0.91)	-0.66 (-1.24; 0.62)	0.85	0.20	0.31
Hippocampal tail					
Left	-0.38 (-1.03; 0.26)	-0.52 (-0.87; 0.14)	0.55	0.36	0.06
Right	-0.56 (-1.37; 0.48)	-0.48 (-1; -0.16)	0.93	0.19	0.32
Subicular complex					
Left	-0.39 (-1.23; 0.06)	-0.52 (-1.02; 0.05)	0.85	0.01	0.94
Right	-0.19 (-0.46; 0.39)	-0.16 (-0.69; 0.48)	0.96	0.08	0.70
CA1					
Left	-0.80 (-1.09; 1.06)	-0.56 (-1.06; 0.03)	0.75	0.20	0.31
Right	-0.30 (-0.87; 1.28)	-0.42 (-1.16; 0.5)	0.46	0.21	0.28
CA3					
Left	-0.81 (-0.91; 0.41)	-0.8 (-1.27; -0.4)	0.35	0.36	0.06
Right	-0.58 (-1.29; 1.28)	-0.31 (-1.21; 0.3)	0.64	0.05	0.78
CA4					
Left	-0.37 (-1.27; 0.74)	-0.90 (-1.16; -0.41)	0.33	0.24	0.22
Right	-0.75 (-1.34; 1)	-0.58 (-1.07; 0.51)	>0.99	0.15	0.44
Molecular layer					
Left	-0.90 (-1.17; 0.54)	-0.82 (-1.17; -0.55)	0.46	0.33	0.08
Right	-0.71 (-1.04; 1.25)	-0.52 (-1.26; 0.47)	0.61	0.24	0.22
GC-ML-DG					
Left	-0.61 (-1.22; 0.76)	-0.84 (-1.2; -0.54)	0.33	0.39	0.05
Right	-0.56 (-1.17; 1.46)	-0.66 (-1.28; 0.51)	0.55	0.22	0.25
Fissure					
Left	-0.35 (-1.43; 0.76)	-0.50 (-1.03; 0.6)	0.78	-0.18	0.36
Right	0.74 (-0.36; 1.68)	0.43 (-0.86; 1.26)	0.58	-0.04	0.83
Fimbria					
Left	-0.41 (-0.73; -0.24)	-0.80 (-1.58; -0.33)	0.16	0.28	0.15
Right	-0.70 (-1.11; -0.1)	-0.73 (-1.18; -0.14)	>0.99	0.12	0.55
HATA					
Left	0.13 (-0.63; 0.57)	-0.47 (-0.69; -0.23)	0.31	0.18	0.36
Right	0.60 (-0.9; 1.04)	0.38 (-0.46; 1.06)	0.85	-0.05	0.81

^aWilcoxon rank-sum exact test; ^bPearson's correlations.

Abbreviations: HC=healthy controls; NMOSD=neuromyelitis optica spectrum disorders; CP=cognitively preserved; CI=cognitively impaired; LV=lesion volume; NBV=normalized brain volume; NGV=normalized gray matter volume; NWMV=normalized white matter volume; CA=Cornus Ammonis; GC-ML-DG=granule cell and molecular layer of the dentate gyrus; HATA=hippocampal-amygdaloid transition area.

Supplemental Table 4.2.4. MRI variables of NMOSD patients according to the impairment in the executive domain (Stroop test).

Executive	CP (n=22)	CI (n=6)	p ^a	r _T ^b	r _E ^b	p _T ^b	p _E ^b
Brain MRI variables							
T2 LV [ml]	130 (0; 472)	490 (155; 1296)	0.15	0.03	-0.08	0.87	0.69
T1 LV [ml]	42 (0; 301)	185 (126; 589)	0.12	0.00	-0.08	0.99	0.67
NBV	-0.51 (-1.42; -0.19)	-0.73 (-0.85; 0.09)	>0.99	0.08	-0.03	0.70	0.88
NGMV	-1.04 (-1.57; -0.47)	-0.36 (-1.25; -0.13)	0.14	0.04	-0.21	0.84	0.28
NWMV	0 (-1.08; 0.49)	-0.5 (-0.87; 0.24)	0.57	0.13	0.11	0.51	0.56
Hippocampal volumes							
Whole hippocampus							
Left	-0.78 (-1.23; 0.16)	-0.94 (-1.01; -0.71)	0.72	0.14	0.12	0.47	0.55
Right	-0.64 (-1.06; 0.91)	-0.61 (-0.91; -0.3)	0.57	0.16	0.06	0.41	0.74
Hippocampal tail							
Left	-0.45 (-0.76; 0.26)	-0.7 (-1.04; 0.14)	0.36	0.21	0.12	0.28	0.54
Right	-0.45 (-1.04; 0.2)	-0.69 (-1.28; -0.16)	0.68	0.13	0.05	0.52	0.80
Subicular complex							
Left	-0.42 (-1.23; 0.05)	-0.39 (-0.62; 0.08)	0.57	0.12	0.03	0.56	0.89
Right	-0.19 (-0.69; 0.39)	0.14 (-0.44; 0.48)	0.76	0.18	0.02	0.36	0.93
CA1							
Left	-0.59 (-0.95; 0.25)	-0.93 (-1.4; 0.03)	0.34	0.07	0.09	0.74	0.63
Right	-0.35 (-0.87; 1.19)	-0.7 (-1.21; -0.14)	0.26	0.20	0.20	0.32	0.31
CA3							
Left	-0.76 (-1.02; 0.01)	-1 (-1.57; -0.65)	0.12	-0.09	0.21	0.65	0.27
Right	-0.35 (-0.93; 0.45)	-0.76 (-1.47; 0.3)	0.57	-0.12	0.02	0.48	0.94
CA4							
Left	-0.50 (-1.21; 0.47)	-1.05 (-1.44; -0.64)	0.14	0.01	0.17	0.95	0.38
Right	-0.66 (-1.33; 0.87)	-0.5 (-1.07; -0.18)	0.72	-0.06	-0.01	0.77	0.98
Molecular layer							
Left	-0.83 (-1.17; 0.32)	-0.95 (-1.17; -0.76)	0.46	0.10	0.12	0.61	0.56
Right	-0.61 (-1.1; 0.86)	-0.55 (-0.88; -0.49)	0.60	0.07	0.07	0.70	0.73
GC-ML-DG							
Left	-0.61 (-1.17; 0.41)	-1.15 (-1.59; -0.73)	0.10	0.01	0.14	0.96	0.48
Right	-0.62 (-1.17; 1.11)	-0.62 (-1.28; -0.16)	0.57	0.00	0.04	0.99	0.84
Fissure							
Left	-0.45 (-1.37; 0.6)	-0.05 (-1.03; 1.42)	0.46	0.03	-0.11	0.87	0.56
Right	0.46 (-0.86; 0.92)	1.06 (-0.44; 1.92)	0.43	0.23	-0.15	0.24	0.44
Fimbria							
Left	-0.61 (-1.17; -0.24)	-1.22 (-1.84; -0.78)	0.16	0.15	0.14	0.44	0.46
Right	-0.67 (-1.11; -0.1)	-0.98 (-1.68; -0.17)	0.31	0.30	0.26	0.12	0.19

HATA							
Left	-0.42 (-0.63; 0.38)	-0.69 (-1.01; -0.23)	0.28	0.15	0.19	0.44	0.33
Right	0.33 (-0.46; 1.04)	0.8 (-1.41; 1.79)	0.57	-0.05	-0.08	0.79	0.68

^aWilcoxon rank-sum exact test; ^bSpearman's correlations.

Abbreviations: HC=healthy controls; NMOSD=neuromyelitis optica spectrum disorders; T=time delay; E= error; CP=cognitively preserved; CI=cognitively impaired; LV=lesion volume; NBV=normalized brain volume; NGV=normalized gray matter volume; NWMV=normalized white matter volume; CA=Cornus Ammonis; GC-ML-DG=granule cell and molecular layer of the dentate gyrus; HATA=hippocampal-amygdaloid transition area.

4.3. Time-varying connectivity of the precuneus and its association with cognition and depressive symptoms in neuromyelitis optica: A pilot MRI study

Cacciaguerra *et al.*, *Multiple Sclerosis Journal* 2022

This chapter describes the work published in *Multiple Sclerosis Journal* (PMID: 35796514, DOI: 10.1177/13524585221107125).

MULTIPLE
SCLEROSIS
JOURNAL

MSJ

Original Research Paper

Time-varying connectivity of the precuneus and its association with cognition and depressive symptoms in neuromyelitis optica: A pilot MRI study

Laura Cacciaguerra, Damiano Mistri, Paola Valsasina, Vittorio Martinelli, Massimo Filippi  and Maria A Rocca 

Abstract

Background: The precuneus is involved in cognition and depression; static functional connectivity (SFC) abnormalities of this region have been observed in neuromyelitis optica spectrum disorders (NMOSD). Time-varying functional connectivity (TVC) underpins dynamic variations of brain connectivity.

Objective: The aim of this study was to explore precuneus SFC and TVC in NMOSD patients and their associations with neuropsychological features.

Methods: This retrospective study includes 27 NMOSD patients and 30 matched healthy controls undergoing resting state functional magnetic resonance imaging (MRI) and a neuropsychological evaluation of cognitive performance and depressive symptoms. A sliding-window correlation analysis using bilateral precuneus as seed region assessed TVC, which was quantified by the standard deviation of connectivity across windows. Mean connectivity indicated SFC.

Results: Compared to controls, patients had reduced SFC between precuneus, temporal lobe, putamen and cerebellum, and reduced TVC between precuneus and prefronto-parietal-temporo-occipital cortices and caudate. Patients also had increased intra-precuneal TVC and increased TVC between the precuneus and the temporal cortex. More severe depressive symptoms correlated with increased TVC between the precuneus and the temporal lobe; worse cognitive performance mainly correlated with higher TVC between the precuneus and the parietal lobe.

Conclusion: TVC rather than SFC of the precuneus correlates with NMOSD neuropsychological features; different TVC abnormalities underlie depressive symptoms and cognitive impairment.

Introduction

NMOSD is an autoimmune disease caused by an autoantibody targeting the AQP4 water channel on astrocytes, with consequent astrocyte damage and secondary demyelination (Wingerchuk et al., 2015). Although the main clinical manifestations are recurrent optic neuritis, myelitis, and area postrema syndrome (Wingerchuk et al., 2015), the high prevalence of depressive symptoms and multi-domain cognitive impairment in NMOSD is gathering clinical attention, since their underlying substrates are yet to be clarified (Chavarro, Mealy et al., 2016, Oertel et al., 2019).

Several MRI studies suggested a contribution of the precuneus, an associative cortex involved in highly integrated cognitive tasks (Cavanna & Trimble, 2006), in the development of cognitive abnormalities in NMOSD (Cho et al., 2018, Han, Liu et al., 2020, Liu et al., 2012a, Savoldi et al., 2020). Functional MRI (fMRI) investigations showed that NMOSD patients have increased RS functional connectivity (FC) of the precuneus within the default-mode network and the working-memory network compared to healthy subjects (Han et al., 2020, Savoldi et al., 2020), which correlated with better performance in terms of attention/information processing speed and executive functions, suggesting an adaptive role of these functional changes to preserve cognitive efficiency (Savoldi et al., 2020).

On the other hand, precuneal damage has been associated with cognitive deficits in several neurological disorders. For instance, in patients with Alzheimer's disease or mild cognitive impairment, glucose hypometabolism in the precuneus precedes the involvement of the parietotemporal cortices and the development of atrophy (Bailly, Destrieux et al., 2015). Similarly, precuneus functional or structural abnormalities were associated with cognitive impairment in patients with stroke (Kumral, Bayam et al., 2021), Parkinson's disease (Jia, Li et al., 2018) and MS (Rocca, Absinta et al., 2014).

Functional changes in precuneal connectivity seem to be relevant for the development of depression as well, as increased FC with the prefrontal and temporo-parietal cortices were detected in treatment-naïve depressed patients and were restored after antidepressant treatment start (Cheng, Rolls et al., 2018).

RS FC abnormalities in NMOSD have been investigated so far using a static FC (SFC) approach. SFC assumes that FC is stationary across the entire fMRI acquisition, and reflects the architecture of stable brain functional connections (i.e., networks). However,

there is growing evidence that the analysis of variability of RS FC within small temporal segments is complementary to the static approach, since it might underpin fast inter- and intra-network cross-talk and coordination (Kaiser, Whitfield-Gabrieli et al., 2016). Dynamic FC, also known as time-varying connectivity (TVC), can be measured by performing a seed-region correlation analysis over short segments of RS fMRI time-series, and calculating the standard deviation (SD) of FC over these so-called “sliding-windows” (Valsasina, Hidalgo de la Cruz et al., 2019).

TVC was already investigated in other inflammatory neurological disorders such as MS, where it detected changes in brain functional reorganization since the earliest phases of the disease (Rocca, Hidalgo de La Cruz et al., 2020b), underlined the existence of heterogeneous patterns of connectivity at different disease stages (i.e., relapsing remitting vs. progressive MS) (Carotenuto, Valsasina et al., 2022), and showed that slower inter-network connectivity (d'Ambrosio, Valsasina et al., 2020) and inefficient maintenance of stable intra-network connections (Carotenuto et al., 2022) contributed to cognitive impairment.

Here, we hypothesize that patients with NMOSD might have abnormal RS FC of the precuneus in terms of both SFC and TVC, and that, based on the experience in other neurological disorders, these alterations could be associated with cognitive impairment and depressive symptoms. To test this, we investigated SFC and TVC of the precuneus at RS, and their correlations with cognitive performance and depressive symptoms in NMOSD patients.

Materials and methods

Standard protocol approvals, registration, and patient consent. Approval was received from the local ethical standards committee on human experimentation. Written informed consent was obtained from all participants prior to enrolment.

Subjects. This retrospective study included 27 right-handed patients and 30 age-, sex- and education-matched right-handed HC enrolled between February 2012 and August 2015. Patients satisfied the 2015 International Panel diagnostic criteria for aquaporin-4-seropositive NMOSD diagnosis (Wingerchuk et al., 2015). All patients were evaluated during the remission phase of the disease (i.e., at least one month apart acute relapses,

intravenous steroid administration, and treatment changes). Twenty-five NMOSD patients and all HC were included in our previous study by Savoldi et al., investigating SFC abnormalities in the main cognitive networks of NMOSD patients and their associations with neuropsychological performances (Savoldi et al., 2020). For all participants, exclusion criteria were history of drug or alcohol abuse, head trauma, other neurological/psychiatric conditions, a formal diagnosis of major depressive disorder, and any contraindication to MRI.

Clinical and neuropsychological assessment. On the same day of the MRI acquisition patients underwent a neurological evaluation including the Expanded Disability Status Scale (EDSS) (Kurtzke, 1983) assessment and a neuropsychological examination.

Verbal learning (VL) was tested with the Selective Reminding Test and its subsections (long-term storage, consistent long-term retrieval and delayed recall tested) (Amato et al., 2006); visuospatial learning (VSL) was assessed with the 10/36 Spatial Recall Test and its delayed recall (Amato et al., 2006); attention/IPS were evaluated through the Symbol Digit Modalities Test and the Paced Auditory Serial Addition Test-2” and -3” (Amato et al., 2006); verbal fluency (VF) was examined with the phonemic and semantic fluency tests (Novelli, Papagno et al., 1986).

For each test, a grading system dependent on the number of standard deviations below normative values was applied. Grade 0 corresponded to scores \geq normative values; grade 1 to scores at 1 or between 0 and 1 standard deviations below normative values; grade 2 to scores at 2 or between 1 and 2 standard deviations below normative values, etc (Camp, Stevenson et al., 1999). Grades of each test were summed up to provide global and domain-specific indexes of cognitive impairment (CI, the higher the index, the worse the impairment) (Camp et al., 1999): CI-index, VL-index, VSL-index, IPS-index, and VF-index. Patients with at least two abnormal tests (performance below the 5th percentile of the normative sample) in different domains were considered cognitively impaired (Portaccio, Goretti et al., 2009).

To investigate subclinical depressive symptoms, subjects were administered the Beck Depression Inventory-II (BDI) (Beck, Ward et al., 1961), which quantifies the intensity of depressive symptoms (a score ≥ 10 corresponding to at least mild depression symptoms) (Beck & Steer, 1987, Beck et al., 1961).

MRI acquisition. All participants underwent a 3.0 T brain MRI scan (Philips Intera, Best, The Netherlands), following a standardized protocol: (1) T2*-weighted single-shot echo-planar imaging sequence for RS fMRI acquisition (repetition time [TR]=3000 ms; echo time [TE]=35 ms; flip angle [FA]=90°; matrix=128x128; field of view [FOV]=240x240 mm²; 30 4-mm-thick slices; total acquired images=200); (2) dual-echo turbo spin-echo (TR=2599 ms; TE=16/80 ms; FA=90°; matrix=256x256; FOV=240x240 mm²; 44 3-mm-thick slices) and (3) three-dimensional (3D) T1-weighted fast field echo (TR=25 ms; TE=4.6 ms; FA=30°; matrix=256x256; FOV=230x230 mm²; 220 0.8-mm-thick slices). RS fMRI scans positioning included the whole cerebellum/pons regions, and RS fMRI acquisition required about 10 minutes. During acquisition, subjects were asked to keep their eyes closed, remain motionless, and not to focus on specific thoughts. A questionnaire was administered immediately after the MRI session ensure participants had not fallen asleep during scanning.

Structural MRI analysis. Brain T2-hyperintense and T1-hypointense lesions were segmented using a local thresholding segmentation technique (Jim 7; Xinapse Systems Ltd, Colchester, UK) and T2-, and T1-lesion volume were calculated. After T1-hypointense lesion refilling, normalized brain volume, white matter volume, and grey matter volume were measured using the FSL SIENAX software (Smith, Zhang et al., 2002).

Resting-state FC analysis.

Images preprocessing: The main pre-processing steps were performed using SPM12 and REST software (<http://resting-fmri.sourceforge.net/>). After discarding the first two timepoints, RS fMRI scans were rigid-body realigned to the mean of each session. After rigid registration to the lesion-filled 3D T1-weighted scan, RS fMRI images were non-linearly normalized to the Montreal Neurological Institute template. Linear detrending and band-pass filtering (0.01-0.08 Hz) were performed to partially remove low-frequency drifts and high-frequency physiological noise. The six motion parameters estimated by SPM12, along with the mean white matter and ventricular CSF fluid signals (extracted from 2-mm eroded masks to be conservative), were regressed to minimize non-neuronal

sources of synchrony between RS fMRI time series and motion-related artifacts. Finally, smoothing was performed using a 3D 6-mm isotropic Gaussian kernel.

SFC and TVC analysis: A mask of the bilateral precuneus was obtained by merging the left and right precuneal masks in the WFU PickAtlas toolbox (<http://fmri.wfubmc.edu/software/PickAtlas>). Using a rectangular window of $22 \times TR$ time points (convolved with a Gaussian of $\sigma = 3 \times TR$ and shifted along the fMRI time series in steps of $1 \times TR$, as previously suggested) (d'Ambrosio et al., 2020), FC between the precuneus and any other voxel of the brain was calculated, and r-to-z Fisher transformed. This allowed obtaining a series of 178 RS FC maps of the precuneus across the whole fMRI session.

SFC of the precuneus was assessed by producing a mean map of FC across all sliding windows (Carotenuto et al., 2022, d'Ambrosio et al., 2020). The standard deviation of the FC map across all windows was chosen as a measure of TVC (Carotenuto et al., 2022, Choe, Nebel et al., 2017).

Statistical analysis. Between-group comparisons of demographic, neuropsychological and structural MRI variables were performed using two-sample t-test/non-parametric Mann-Whitney U-test, according to normality assumption. Categorical variables, including frequency of mild depressive symptoms between cognitively impaired and preserved patients, were compared by Pearson χ^2 test. Finally, the median test for independent samples with Fisher's exact test and Bonferroni correction for *post hoc* comparisons, was used to compare depressive and cognitive scores among NMOSD patients, grouped according to the presence/absence of depression and/or cognitive impairment (SPSS software, version 23.0).

Voxel-wise comparisons of RS SFC and TVC of the precuneus between HC and NMOSD patients were performed using SPM12 and age- and sex-adjusted full factorial models. Given the exploratory design of the study, voxel-wise results of between-group comparisons were tested at $p < 0.001$ (uncorrected, cluster extent threshold $k_E = 10$ voxels). Using such cluster-forming threshold, we also identified results surviving at $p < 0.05$, cluster-wise family-wise error corrected for multiple comparisons. (Friston, Holmes et al., 1996)

In NMOSD patients, we extracted average z-scores of abnormal RS SFC and TVC from clusters surviving family-wise-error threshold using REX ([NITRC: REX: Tool/Resource Info](#)). These z-scores were used in bivariate correlation analyses to assess the association of functional abnormalities with BDI scores and cognitive indexes in all patients.

Multiple linear regression models were then used to identify the set of SFC and TVC z-scores independently associated with cognitive impairment indices and BDI, using a stepwise variable selection (p value=0.10 for entry and =0.05 to remain in the multivariate model). Demographic variables such as age and sex were not included since they were already used to obtain the functional z-scores. The proportion of variance explained by each model was expressed by the R² index.

Data availability. The dataset used and analyzed during the current study are available from the corresponding author on reasonable request.

Results

Clinical, neuropsychological, and structural MRI findings (Table 4.3.1). 27 NMOSD patients (mean age, 44 years +/- 12; 21 women) and 30 HC (mean age 41 +/- 12, 21 women) were evaluated. Cognitive impairment was observed in 12 patients (44.4%) and depressive symptoms in 17 patients (63.0%). Concomitant cognitive impairment and depressive symptoms were detected in 9 patients (33.3%), isolated depressive symptoms were present in 8 patients (29.6%) and isolated cognitive impairment was present in 3 patients (11.1%). Frequency of depression was not different between cognitively impaired and preserved patients (p=0.25). The median test for independent samples showed a significant difference in terms of median values of BDI score (p=0.001), CII (p=0.01) and IPS-index (p<0.001) among patients divided according to the presence of cognitive impairment/depressive symptoms, in combination or alone.

Table 4.3.1. Demographic, clinical, neuropsychological and structural MRI features of NMOSD patients and HC. Significant p values are highlighted in bold.

	NMOSD (n=27)	HC (n=30)	p
Demographic and clinical variables			

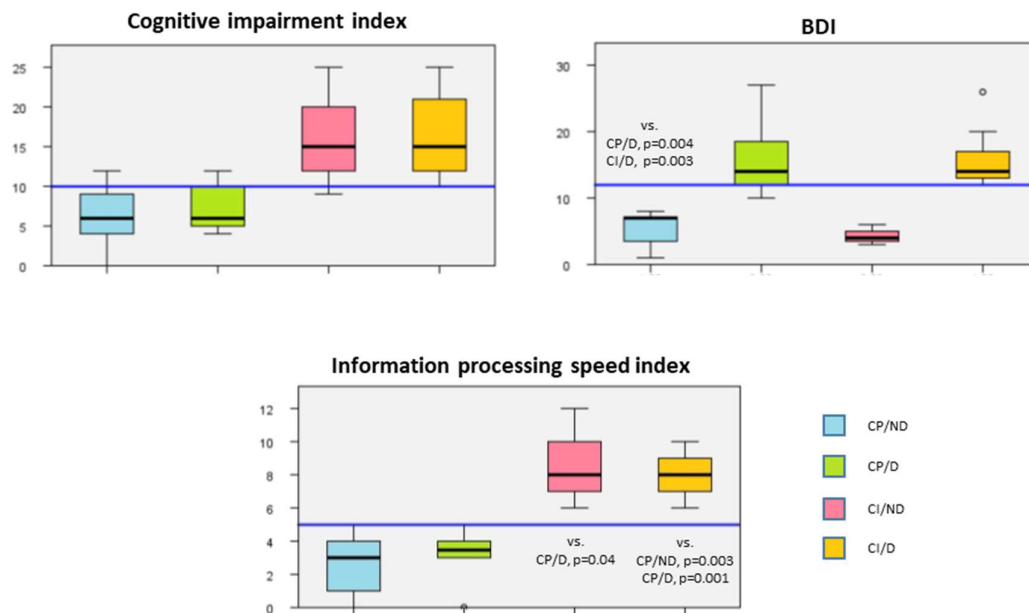
Female/male	21/6	21/9	0.71 ^a
Mean age (SD) [years]	44.1 (12.4)	41.2 (11.6)	0.37 ^b
Mean education (SD) [years]	12.6 (3.8)	13.2 (3.5)	0.54 ^b
Median EDSS (IQR)	4.0 (3.0-6.0)	-	-
Mean decimal high-contrast bilateral visual acuity (SD)	0.81 (0.32)	-	-
Median number of optic neuritis (range)	1 (0-9)	.	.
Median number of myelitides (range)	2 (0-15)	.	.
Median disease duration (IQR) [years]	3.4 (2.8-8.0)	-	-
Neuropsychological variables			
Mean cognitive impairment index (SD)	11.0 (6.7)	-	-
Mean verbal learning index (SD)	3.4 (2.8)	-	-
Mean visuospatial learning index (SD)	1.8 (1.7)	-	-
Mean information processing speed index (SD)	5.2 (3.1)	-	-
Mean verbal fluency index (SD)	0.7 (0.8)		
Mean BDI (SD)	11.8 (6.8)	-	-
N° of cognitively impaired subjects (%)	12 (44.4)	-	-
N° of patients with depressive symptoms (%)	17 (63.0)	-	-
N° of patients with both depressive symptoms and cognitive impairment (%)	9 (33.3)	-	-
Structural MRI variables			
Median T2 LV (IQR) [ml]	0.16 (0.0-0.8)	-	-
Median T1 LV (IQR) [ml]	0.10 (0.0-0.4)	-	-
Mean NBV (SD) [ml]	1541 (55)	1568 (95)	0.21 ^b
Mean NGMV (SD) [ml]	700 (39)	726 (46)	0.03^b
Mean NWMV (SD) [ml]	840 (34)	841 (52)	0.93 ^b

^aPearson χ^2 , ^bindependent-sample t-test.

Abbreviations: NMOSD=neuromyelitis optica spectrum disorders; HC=healthy controls; SD=standard deviation; IQR=interquartile range; EDSS=expanded disability status scale; CII=cognitive impairment index; VLI=verbal learning index; VSLI=visuospatial learning index; IPSI=information processing speed index; BDI-II=Beck depression inventory-II; LV=lesion volume; NBV=normalized brain volume; NGMV=normalized grey matter volume; NWMV=normalized white matter volume.

However, patients with both cognitive impairment and depressive symptoms did not show worse cognitive performance or more severe depressive symptoms compared to those with cognitive impairment or depression alone (**Figure 4.3.1**).

Figure 4.3.1. Distribution of BDI scores, cognitive impairment index and information processing speed index among patients' groups. Data represent boxplots of BDI, CII and IPS-I scores of NMOSD patients, grouped according to the presence/absence of cognitive impairment and depressive symptoms, combined or in isolation. Not specified pairwise comparisons did not survive Bonferroni correction. The blue line represents the median value of the study population (i.e., all NMOSD patients). A scatterplot of the correlation analysis between BDI score and CII is also reported. Author's reuse as per Journal pre-approved permission (<https://us.sagepub.com/en-us/nam/pre-approved-permission-requests-journals>).



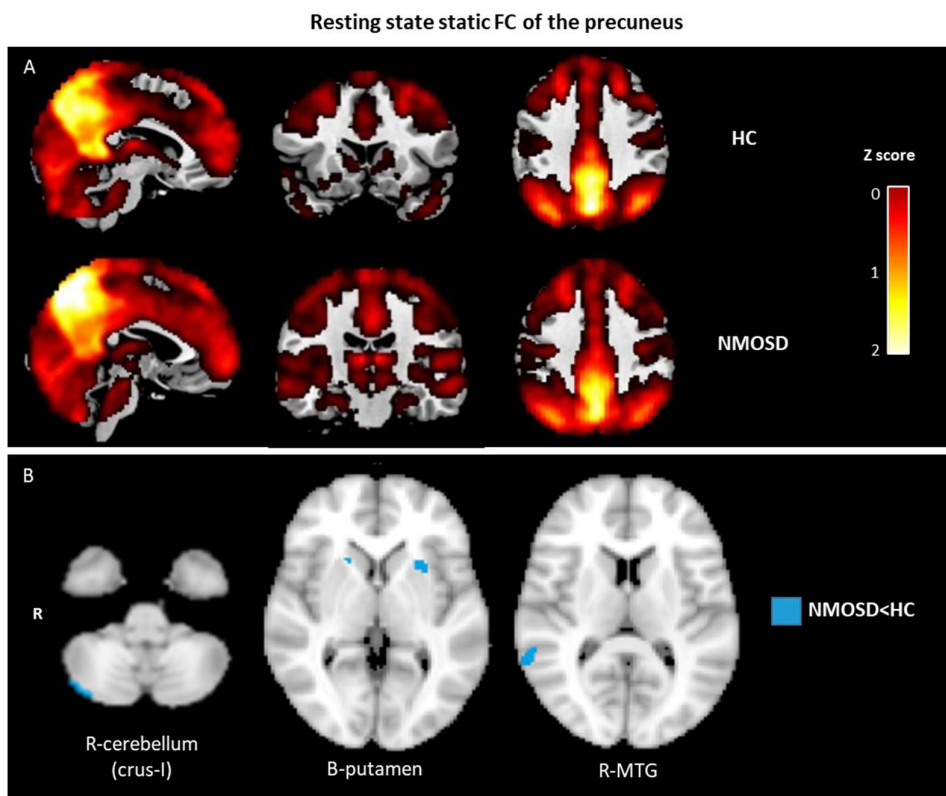
Abbreviations: CP/ND=cognitively preserved/not depressed; CP/D=cognitively preserved/depressed; CI/ND=cognitively impaired/not depressed; CI/D=cognitively impaired/depressed.

Structural MRI variables were similar between patients and HC, except for lower normalized grey matter volume in patients.

Voxel-wise between-group comparisons of RS FC of the precuneus.

SFC analysis (Figure 4.3.2 and Table 4.3.2): Compared to HC, NMOSD patients had decreased SFC between the precuneus and the right middle temporal gyrus, bilateral putamen and right cerebellum (crus I).

Figure 4.3.2. Resting state static functional connectivity of the precuneus. Panel A: Static resting state functional connectivity (TVC) of the precuneus across windows in healthy controls (HC) and neuromyelitis optica spectrum disorder (NMOSD) patients. Panel B: Voxel-wise comparisons of SFC of the precuneus between NMOSD and HC (age- and sex-adjusted full factorial models; only results surviving at $p < 0.05$, clusterwise FWE corrected are retained). Author's reuse as per Journal pre-approved permission (<https://us.sagepub.com/en-us/nam/pre-approved-permission-requests-journals>).



Abbreviations: B=bilateral; FC=functional connectivity; HC=healthy controls; MTG=middle temporal gyrus; NMOSD=neuromyelitis optica spectrum disorders; R=right.

Table 4.3.2. Clusters of abnormal RS static functional connectivity (SFC) of the precuneus between healthy controls (HC) and neuromyelitis optica spectrum disorder (NMOSD) patients ($p < 0.001$ uncorrected, cluster extent threshold $k_E = 10$). Clusters surviving family-wise error (FWE)-correction ($p < 0.05$) are marked with * and highlighted in bold.

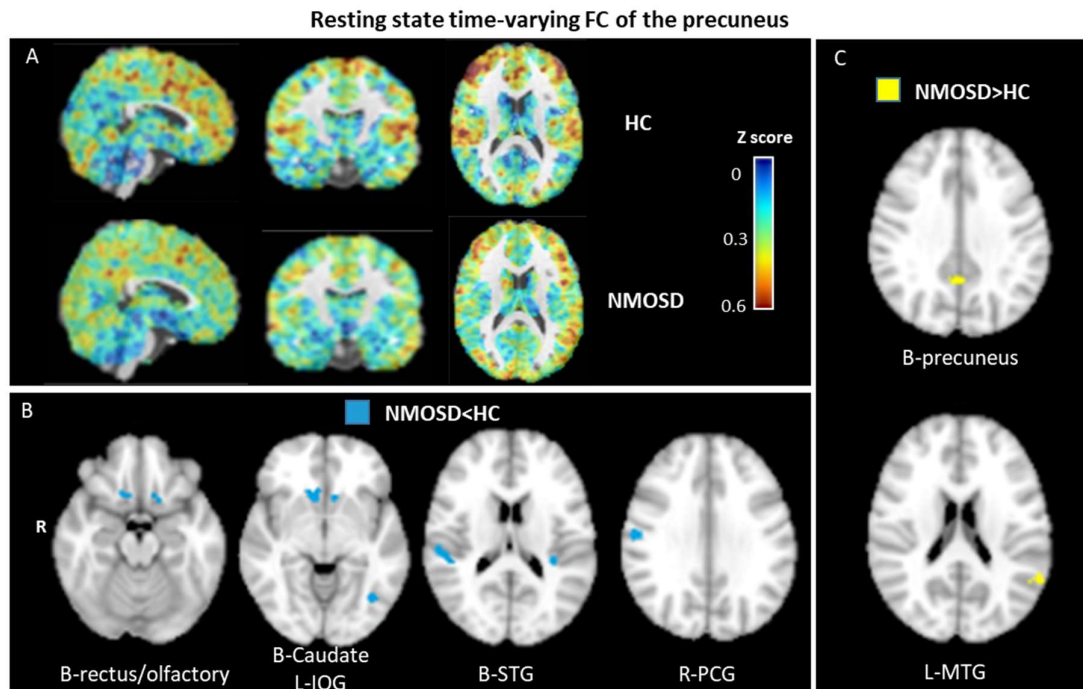
HC>NMOSD				
Brain lobes/structures	Region	k_E	MNI space coordinates (x, y, z)	t-value
Frontal lobe	Right superior frontal gyrus	32	14,58,12	3.85
	Left orbitofrontal gyrus	23	-30,54,-8	3.41
Temporal lobe	Right middle temporal gyrus*	49	62,54,-46	3.22
		12	-2, 12, -26	3.09
	Bilateral inferior temporal gyrus	34	46,-54,4	3.60
		12	0, -34, -34	2.97
Occipital lobe	Left lingual gyrus	33	-6,-66,0	3.21
	Left calcarine sulcus	22	-8,-66,10	3.71
Deep grey matter	Bilateral putamen*	49	-26,22,14	4.32
		12	18, 0, 4	3.02
	Right thalamus	21	16,-24,14	3.70
	Left caudate nucleus	19	-14, 8,16	3.13
	Posterior fossa	Right cerebellum (crus-I)*	93	44,-80,-34
NMOSD>HC				
Brain lobes/structures	Region	k_E	MNI space coordinates (x y z)	t-value
Parietal lobe	Right precuneus	14	22, -54, 44	3.66

Abbreviations: MNI=Montreal Neurological Institute.

TVC analysis (Figure 4.3.3 and Table 4.3.3): Compared to HC, NMOSD patients exhibited a widespread decrease of the TVC between the precuneus and the frontal lobes (especially the prefrontal cortex, including bilateral rectus gyrus and left olfactory bulb), parietal lobe (right postcentral gyrus), temporal lobe (bilateral superior temporal gyrus), occipital lobes (left inferior occipital gyrus and bilateral lingual gyrus), and deep grey matter (bilateral caudate nuclei). Patients also had increased intra-precuneal TVC, as well as increased TVC between the precuneus and the left-middle temporal gyrus.

Figure 4.3.3. Resting state time-varying functional connectivity of the precuneus.

Panel A: Time-varying resting state functional connectivity (TVC) of the precuneus across windows in healthy controls (HC) and neuromyelitis optica spectrum disorder (NMOSD) patients. Panel B: Voxel-wise comparisons of TVC of the precuneus between NMOSD and HC (NMOSD<HC, age- and sex-adjusted full factorial models; only results surviving at $p<0.05$, clusterwise FWE corrected are retained). Panel C: Voxel-wise comparisons of TVC of the precuneus between NMOSD and HC (NMOSD>HC, age- and sex-adjusted full factorial models; only results surviving at $p<0.05$, clusterwise FWE corrected, are retained). Author's reuse as per Journal pre-approved permission (<https://us.sagepub.com/en-us/nam/pre-approved-permission-requests-journals>).



Abbreviations: B=bilateral; FC=functional connectivity; HC=healthy controls; IOG=inferior occipital gyrus; MTG=middle temporal gyrus; NMOSD=neuromyelitis optica spectrum disorders; PCG=postcentral gyrus; R=right; STG=superior temporal gyrus.

Table 4.3.3. Clusters of abnormal time-varying RS functional connectivity (TVC) between healthy controls (HC) and neuromyelitis optica spectrum disorder

(NMOSD) patients ($p < 0.001$ uncorrected, cluster extent threshold $k_E = 10$). Clusters surviving family-wise error (FWE)-correction ($p < 0.05$) are marked with * and highlighted in bold.

HC>NMOSD				
Brain lobes/structures	Region	k_E	MNI space coordinates (x, y, z)	t-value
Frontal lobe	Bilateral rectus gyri*	75	-12, 10, 20	3.71
		24	20, -16, -18	4.09
	Left olfactory bulb*	75	-16, 12, -14	3.94
	Right supplementary motor area	39	10, 18, 68	4.11
	Bilateral superior frontal gyrus	20	16, -28, -2	3.81
		17	58, 62, 62	3.80
		10	34, 22, 40	3.93
	Left paracentral lobule	19	-2, -12, 74	3.23
	Left middle frontal gyrus	17	-34, 56, 28	3.34
	Left orbitofrontal gyrus	12	-24, -16, -12	3.47
Parietal lobe	Right postcentral gyrus*	42	58, -12, 30	4.19
		15	30, -40, 66	3.41
Temporal lobe	Bilateral superior temporal gyrus*	83	52, -30, 16	4.33
		83	46, -36, 20	3.46
		21	58, -36, 22	4.11
		26	-34, -36, 16	4.11
	Right superior temporal gyrus (pole)	21	30, 6, -20	3.92
	Left hippocampus	15	-22, -36, 4	3.36
Occipital lobe	Left inferior occipital gyrus*	42	-38, -64, -8	3.65
	Bilateral posterior fusiform gyrus*	40	-36, -80, 8	3.78
		42	-42, -62, 2	2.91
		14	34, -54, -18	3.34
	Bilateral lingual gyrus	36	10, -32, -6	3.03
20		-16, -70, 0	3.87	
Cingulate lobe	Bilateral anterior cingulate cortex	22	2, 42, 16	3.61
		14	4, 16, 30	3.24
	Left midcingulate cortex	11	-12, -34, 54	4.05
Deep grey matter	Bilateral caudate nucleus*	75	-8, 18, -6	3.25
		60	8, 20, -4	4.25
Posterior fossa	Left cerebellum (VII b)	36	-18, -72, -42	3.43
	Right cerebellum (VIII)	28	12, -58, -42	3.68
	Right cerebellum (VI)	22	42, -40, -30	4.10
	Periaqueductal grey	36	6, -24, -12	3.89
NMOSD>HC				
Brain lobes/structures	Region	k_E	MNI space coordinates (x, y, z)	t-value
Frontal lobe	Right premotor cortex	27	32, -10, 44	4.13
	Right primary motor cortex	18	14, -26, 58	3.74
Parietal lobe	Bilateral precuneus*	46	4, -52, 34	4.21

		31	-24, -78, 44	3.49
		10	-12, -64, 50	2.86
Temporal lobe	Left middle temporal gyrus* Left insula	43	-60, -52, 22	3.52
		16	-46, -2, 18	3.50
Occipital lobe	Left calcarine sulcus	14	-8, -56, 8	3.70
Deep grey matter	Bilateral thalamus	14	-16, -12, 6	3.82
		10	16, -16, 2	3.53
	Left putamen	17	-18, 12, -2	3.84
Posterior fossa	Left cerebellum (IV-V)	15	-20, -46, -22	4.90
	Bilateral cerebellum (crus-I)	11	-50, -68, -30	3.84
		10	52, 64, 30	3.49

Abbreviations: MNI=Montreal Neurological Institute.

Correlation analysis and regression models in NMOSD patients (Tables 4.3.4 and 4.3.5).

Depressive symptoms (Table 4.3.4): No correlations were found between abnormal SFC and BDI scores. Higher BDI scores correlated with increased TVC between the precuneus and the superior temporal gyrus, bilaterally.

Cognitive performance (Table 4.3.4): Higher VL-index correlated with decreased SFC between the precuneus and the right cerebellar crus-I. Increased TVC between the precuneus and the right postcentral gyrus correlated with higher CI-index, IPS-index, and VSL-index. Decreased TVC between the precuneus and the left inferior occipital gyrus correlated with higher VL-index.

Table 4.3.4. Bivariate Pearson’s correlations between neuropsychological variables and resting state static and time-varying functional connectivity (FC) of the precuneus (z-scores) in patients with neuromyelitis optica spectrum disorder (NMOSD). Values represent rho (p value).

	BDI	CII	IPSI	VSLI	VLI	VFI
Static functional connectivity						
Right Middle temporal gyrus	-0.11 (0.59)	0.02 (0.92)	-0.05 (0.80)	-0.08 (0.72)	0.08 (0.70)	0.15 (0.45)
Bilateral putamen	-0.02 (0.94)	0.03 (0.88)	0.01 (0.95)	-0.03 (0.88)	0.06 (0.77)	0.00 (0.98)
Right cerebellum (crus-I)	0.18 (0.38)	-0.30 (0.13)	-0.14 (0.48)	-0.27 (0.18)	-0.38 (0.05)	-0.06 (0.76)
Time-varying functional connectivity						

Bilateral rectus gyrus	0.31 (0.12)	-0.05 (0.79)	-0.06 (0.78)	-0.02 (0.93)	-0.13 (0.51)	0.29 (0.15)
Left olfactory bulb	0.28 (0.16)	0.05 (0.80)	0.05 (0.79)	0.02 (0.92)	-0.05 (0.81)	0.32 (0.10)
Right postcentral gyrus	0.05 (0.81)	0.49 (0.009)	0.47 (0.02)	0.61 (0.001)	0.19 (0.35)	0.34 (0.08)
Bilateral superior temporal gyrus	0.48 (0.01)	0.11 (0.59)	0.15 (0.46)	0.07 (0.73)	-0.00 (0.99)	0.18 (0.38)
Left inferior occipital gyrus	-0.09 (0.67)	-0.23 (0.26)	-0.10 (0.63)	-0.08 (0.71)	-0.41 (0.04)	0.11 (0.60)
Bilateral posterior fusiform gyrus	0.08 (0.70)	-0.22 (0.28)	-0.14 (0.50)	-0.15 (0.50)	-0.36 (0.07)	0.26 (0.20)
Bilateral caudate nucleus	0.22 (0.27)	0.24 (0.23)	0.20 (0.32)	0.08 (0.71)	0.19 (0.33)	0.37 (0.06)
Bilateral precuneus	-0.14 (0.49)	-0.19 (0.34)	-0.23 (0.25)	0.08 (0.72)	-0.25 (0.20)	0.06 (0.78)
Left middle temporal gyrus	-0.08 (0.68)	0.04 (0.83)	0.05 (0.82)	-0.06 (0.76)	0.06 (0.79)	0.17 (0.38)

Abbreviations: BDI=Beck depression inventory-II; CII=global cognitive impairment index; IPSI=information processing speed index; VLI=verbal learning index; VSLI=visuospatial learning index; VFI=verbal fluency index.

In the multivariate linear regression analysis, a higher TVC between the precuneus and the bilateral superior temporal gyrus was the only variable retained as independent predictor of a higher BDI score. Higher CI-index, IPS-index and VSL-index were independently associated with a higher TVC between the precuneus and the right postcentral gyrus, while a higher VL-index was independently predicted by decreased TVC between the precuneus and the left inferior occipital gyrus. No predictors of VF-index were identified (**Table 4.3.5**).

Table 4.3.5. Linear regression models between neuropsychological variables and time-varying functional connectivity (TVC) of the precuneus (z-scores) in patients with neuromyelitis optica spectrum disorder (NMOSD).

	Independent variable	Standardized beta	p	Adjusted R²
BDI	TVC Bilateral superior temporal gyrus	0.48	0.01	0.20
CII	TVC Right postcentral gyrus	0.49	0.009	0.21
IPSI	TVC Right postcentral gyrus	0.46	0.02	0.18
VSLI	TVC Right postcentral gyrus	0.61	0.001	0.35

VLI	TVC Left inferior occipital gyrus	-0.41	0.04	0.13
VFI	-	-	-	-

Abbreviations: BDI=Beck depression inventory-II; CII=global cognitive impairment index; IPSI=information processing speed index; VLI=verbal learning index; VSLI=visuospatial learning index; VFI=verbal fluency index.

Discussion

We explored static and time-varying RS FC of the precuneus in patients with NMOSD, and their associations with depressive symptoms and cognitive performance. Compared to HC, NMOSD patients had a few clusters of reduced SFC between the precuneus, the temporo-cerebellar cortices and the putamen, and a diffuse TVC reduction with the prefronto-parieto-temporo-occipital cortices and caudate nuclei, together with increased TVC within the precuneus and between the precuneus and the temporal lobe. More severe depressive symptoms were associated with increased TVC between the precuneus and temporal cortex, while worse cognitive performance was associated with higher TVC between the precuneus and the parietal cortex and, to a lesser extent, the occipital lobe.

These results suggest that TVC is more sensitive than SFC to detect brain functional reorganization in patients with NMOSD, and that it better contribute to explain cognitive and mood abnormalities. Although a concomitant evaluation of static and time-varying connectivity was never performed before in this disease, former studies suggested that TVC can underpin functional changes since the earliest stages of both inflammatory and degenerative neurological disorders (Valsasina et al., 2019). For instance, patients with clinically isolated syndrome suggestive of MS showed an initial decrease of TVC within the brain network involved by the first demyelinating attack, followed by a progressive increase of TVC over the next two years (Rocca et al., 2020b) and TVC was more sensitive than SFC in identifying MS patients with very mild disability (i.e., EDSS \geq 2) (Tozlu, Jamison et al., 2021). Similarly, compared with HC, patients with early mild cognitive impairment were characterized by increased TVC (Jie, Liu et al., 2018).

These observations suggest that TVC could be sensitive to functional changes associated with neurological conditions characterized by mild or absent structural damage (i.e., early stages) or in the presence of only mild clinical symptoms. This might explain why TVC abnormalities exceeded those of SFC in patients with NMOSD, where structural MRI

abnormalities are usually milder than those observed in other neuroinflammatory conditions such as MS.

In NMOSD, a higher burden of depressive symptoms correlated with higher TVC between the precuneus and the superior temporal gyrus, suggesting an adaptive role of its reduced dynamism in these patients. This aligns with another work, which found that the deactivation of the superior temporal gyrus was one of the physiological mechanisms contrasting a constant emotional arousal in HC compared to depressed subjects. The superior temporal gyrus is involved in social cognition (Bigler, Mortensen et al., 2007), and functional abnormalities of this region were detected in patients with major depressive disorder (Helm, Viol et al., 2018). Interestingly enough, atrophy of the superior temporal gyrus was found since the earliest phases of depression (Ramezani, Johnsrude et al., 2014), therefore, it is reasonable to speculate that functional changes might be evident even earlier, and be sensitive to mild symptoms, such as in our cohort. When we explored correlations between RS FC of the precuneus and cognitive functions, higher TVC in the postcentral gyrus and lower TVC in the inferior occipital gyrus were correlated with worse cognitive performance. Although this might seem surprising, the contribution of the sensorimotor system to cognition aligns with the emerging evidence that motor and cognitive functions are interrelated, as shown in MS patients with concomitant involvement of physical and cognitive disability, but also in patients with Alzheimer's disease (Allali, Assal et al., 2008, Mistri, Cacciaguerra et al., 2022). Our hypothesis is that the increased TVC in the sensorimotor system, which occurs after the demyelinating attack in NMOSD (possibly as an attempt of adaptive functional reorganization, as shown in other disorders) (Carotenuto et al., 2022) might interfere with the cognitive processes intermingled with the motor functions. Conversely, the involvement of the occipital cortex in high-cognitive functions was already described in blind people (Tomasello, Wennekers et al., 2019), suggesting that a similar phenomenon of cross-modal plasticity might occur in neurological disorders characterized by severe visual loss such as NMOSD. Although not selected by the final predicted model, we also found that lower SFC in the cerebellar crus I correlated with poorer performance at the verbal learning task, supporting the evidence that posterior cerebellar regions are involved in non-motor functions including language and verbal working memory, due to their connections with the prefrontal cortex (Stoodley & Schmahmann, 2009).

In a previous study using network RS FC analysis, we found that patients with higher SFC in the precuneus within the default-mode network and working memory network had better cognitive performance (Savoldi et al., 2020). In the current work, which uses a seed-based approach with the precuneus as seed region, we detected a higher intra-precuneal TVC in NMOSD patients, which did not correlate with cognitive scores. In contrast, TVC between the precuneus and parieto-occipital and cerebellar regions was relevant, suggesting that dynamism of long-range precuneus RS FC rather than the functional activity of the precuneus itself acts as a modulator of cognitive processes.

Finally, in line with our clinical data, where a clear association between depressive symptoms and cognitive impairment was not found, precuneal TVC seems to be involved in both these neuropsychological features, but through different circuits, involving the temporal lobe for depressive symptoms and the parieto-occipital and cerebellar regions for cognition.

Moving to limitations, we must acknowledge the cross-sectional retrospective design and the small sample-size, since the former prevented an evaluation of SFC and TVC abnormalities over time, and the latter might have hindered subtle effects on brain functional reorganization associated with the disease or with its neuropsychological features. In addition, our RS fMRI acquisitions were performed using a relatively long TR, possibly introducing aliasing effects in our data and not complete removal of physiological noise artefacts, leading to an underestimation of between-group TVC differences. Also, enrolled HC did not undergo an extensive neuropsychological evaluation; so, we could not assess whether cognitive and depression scores were correlated with TVC in HC. Finally, we cannot exclude an “a priori” sample bias, since we focused on the seed-based FC of the precuneus only, and functional changes in other functionally unrelated regions might be associated with depressive symptoms and worse cognitive performance as well. However, since the analysis of TVC is still novel and the interpretation of findings is challenging, we preferred to start this pilot study with a seed-based approach applied to a seed region which has an established centrality in the RS FC of the main cognitive networks, including the default-mode network and the parietal-memory network.

Future studies should include NMOSD patients with a secondary diagnosis of major depressive disorders, since we expect that TVC abnormalities would be more evident than

in our cohort and will clarify whether these functional abnormalities are specific of NMOSD or only the epiphenomenon of depression.

To conclude, our findings suggest that NMOSD patients have both static and time-varying abnormalities in the RS FC of precuneus, but TVC changes are more diffuse and better explain neuropsychological features. Different patterns of TVC contribute to depressive symptoms and cognition, the first through the connections with the temporal lobe, and the latter mainly involving the parieto-occipital areas.

5. UNTRAVELING NMOSD PATHOPHYSIOLOGY WITH MRI

In this Chapter we analyzed brain structural damage, mainly using advanced MRI techniques, to get insights on potential correlates of NMOSD pathophysiology.

Starting from the pattern and distribution of microstructural WM abnormalities in NMOSD patients, we hypothesized that astrocytes damage and AQP4 loss may lead to water unbalance (i.e., increased water content) in the CNS.

We tested this hypothesis by measuring the T2-relaxation time, an MRI proxy of water content in NMOSD patients and HC. Then, we compared the T2-relaxation time between active and clinically stable patients, to test its sensitivity to disease activity.

Astrocytes damage and AQP4 loss may also alter the anatomy and microstructural integrity of perivascular spaces, which are limited by astrocytes endfeet. Together with water homeostasis, recent evidence suggests that AQP4 may be also involved in the functioning of the glymphatic system, a CNS clearance system which runs along the perivascular spaces and brain parenchyma. Therefore, we analyzed macroscopic and microscopic perivascular spaces abnormalities in NMOSD patients.

Finally, we matched the distribution of brain lesions, microstructural WM abnormalities, and atrophy of NMOSD patients to the Allen Human Brain atlas, which is a gene expression brain atlas. This allowed the identification of known and (potentially) unknown biological pathways associated with brain damage in NMOSD. It also suggested that lesions and WM microstructural abnormalities are specifically associated with the disease pathophysiology, while brain atrophy is likely more complex and at least in part due to secondary neurodegeneration.

5.1 Mapping white matter damage distribution in neuromyelitis optica spectrum disorders with a multimodal MRI approach

Cacciaguerra *et al.*, Multiple Sclerosis Journal 2021

This chapter describes the work published in Multiple Sclerosis Journal (PMID: 32672089, DOI: 10.1177/1352458520941493).

Mapping white matter damage distribution in neuromyelitis optica spectrum disorders with a multimodal MRI approach

Laura Cacciaguerra, Maria A Rocca , Loredana Storelli, Marta Radaelli and Massimo Filippi 

Abstract

Background: The pathogenetic mechanisms sustaining neuroinflammatory disorders may originate from the cerebrospinal fluid.

Objective: To evaluate white matter damage with diffusion tensor imaging and T1/T2-weighted ratio at progressive distances from the ventricular system in neuromyelitis optica spectrum disorders and multiple sclerosis.

Methods: Fractional anisotropy, mean, axial, and radial diffusivity and T1/T2-weighted ratio maps were obtained from patients with seropositive neuromyelitis optica spectrum disorders, multiple sclerosis, and healthy controls ($n=20$ each group). White matter damage was assessed as function of ventricular distance within progressive concentric bands.

Results: Compared to healthy controls, neuromyelitis optica spectrum disorders patients had similar fractional anisotropy, radial and axial diffusivity, increased mean diffusivity ($p=0.009-0.013$) and reduced T1/T2-weighted ratio ($p=0.024-0.037$) in all bands. In multiple sclerosis, gradient of percentage lesion volume and intra-lesional mean and axial diffusivity were higher in periventricular bands. Compared to healthy controls, multiple sclerosis patients had reduced fractional anisotropy ($p=0.001-0.043$) in periventricular bands, increased mean ($p<0.001$), radial ($p<0.001-0.004$), and axial diffusivity ($p=0.002-0.008$) and preserved T1/T2-weighted ratio in all bands.

Conclusion: White matter damage is higher at periventricular level in multiple sclerosis and diffuse in neuromyelitis optica spectrum disorders. Fractional anisotropy preservation, associated with increased mean diffusivity and reduced T1/T2-weighted ratio may reflect astrocyte damage.

Introduction

According to recent theories, the pathogenetic mechanisms sustaining neurological inflammatory diseases, with a particular focus on MS, may originate from CSF-mediated factors (Liu, Pardini et al., 2015c, Vidaurre, Haines et al., 2014). In support of this speculation, focal lesions in MS are preferentially located at the interface between CSF and brain parenchyma, involving the periventricular WM and the cortex (Thompson, Banwell et al., 2018). A gradient of subpial demyelination, starting from the outer surface of the cortex and progressively involving deeper cortical layers, has been observed with 7.0 T MRI (Mainero, Louapre et al., 2015), possibly preceding cortical atrophy (Granberg, Fan et al., 2017). The NAWM is characterized by a similar phenomenon, with damage being more severe in regions closer to the ventricular system and milder in the deep WM, following a so-called “gradient of microstructural damage” (Liu et al., 2015c).

This gradient has been detected from the initial phases of the disease and was confirmed using different quantitative MRI techniques exploring tissue water diffusivity and demyelination (Brown, Pardini et al., 2017, Pardini, Gualco et al., 2019).

Diffusion MRI provides an indirect characterization of tissue microstructural abnormalities by measuring water diffusion. The diffusion tensor (DT) model postulates an organization of brain tissue in bundles of parallel axons surrounded by myelin layers. Pathological studies have related specific alterations of diffusion indexes to microstructural modifications. FA reduction was associated to loss of tissue water-restricting barriers such axons (Tu, Williams et al., 2016). AD and RD increases have been interpreted as markers of axonal injury and myelin damage, respectively (Tu et al., 2016), whereas MD is considered a global measure of tissue density and of macromolecules integrity including myelin (Basser, Mattiello et al., 1994a, Tu et al., 2016).

T1/T2-weighted ratio (T1/T2-w) is proposed as a new index of myelin content. This measure derives from the observation that signal intensity is proportional to the myelin content in T1-weighted sequences, and inversely proportional to it in T2-weighted sequences. As a consequence, a ratio between these two signals should increase the myelin-derived hyperintensity (Glasser & Van Essen, 2011). Nonetheless, it is likely that other factors may also contribute to this measure. In line with this, two studies exploring the correlations between T1/T2-w and histopathological data in the GM provided different conclusions, since T1/T2-w correlated with myelin content in one study (Nakamura et al., 2017) and with dendritic density in the other (Righart et al., 2017). Interestingly, the measurement of this index in the NAWM was able to discriminate between patients with early MS and HC, with higher values in the latter group (Beer, Biberacher et al., 2016).

NMOSD is one of the main MS-mimics. Its pathogenetic mechanism differs from that of MS, resulting in an antibody-mediated astrocytopathy (Lennon et al., 2004). In around 80% of NMOSD patients, the pathogenic antibody is directed against the AQP4 water channel. Although higher IgG titers are found in the serum of these patients, anti-AQP4-IgG can be detected in the CSF (Wingerchuk et al., 2015).

In NMOSD, focal lesions are common at periventricular level, similarly to MS (Cacciaguerra et al., 2019b), and periependymal lesions following the ventricular profile

and the periaqueductal area are typical (Cacciaguerra et al., 2019b). NAWM involvement was also reported in NMOSD patients. However, at the state of the art, no data concerning the topographical distribution of such a damage in NMOSD are available.

In this study, we combined DTI and T1/T2-w measures to quantify WM damage and its correlation with clinical measures in NMOSD and MS patients, and to investigate possible differences in the pathogenesis of these two conditions by grading the extent of damage according to the distance from the CSF interface.

Materials and methods

Ethics committee approval. Approval was received from the local ethical standards committee on human experimentation; written informed consent was obtained from all subjects prior to study participation.

Subjects. In this cross-sectional study, we retrospectively evaluated MRI scans acquired from 20 AQP4-IgG positive NMOSD patients, 20 age- and disease duration-matched relapsing-remitting (RR) MS patients and 20 age-matched HC, referring to our hospital. To be included, all patients (NMOSD and MS) had to be clinically stable and steroids-free within the last three months. Other conditions such as drug/alcohol abuse, psychiatric comorbidities, history of head trauma and MRI contraindications were ruled out in all groups.

NMOSD patients were diagnosed according to 2015 International Consensus diagnostic criteria for NMOSD, and antibody testing was performed with cell-based assay (Wingerchuk et al., 2015). MS patients were diagnosed according to the most recent diagnostic criteria (Thompson et al., 2018).

Within 48 hours from the MRI acquisition, all patients underwent a clinical evaluation, inclusive of the EDSS assessment, (Kurtzke, 1983) and a neuropsychological screening with the SDMT. Z-scores were obtained from education-corrected results, according to normative data (Amato et al., 2006).

MRI acquisition. Using a 3.0 T scanner (Intera Philips Medical Systems), the following brain sequences were acquired: axial dual-echo turbo spin-echo (TSE) (repetition time [TR]/echo time [TE]=2599/16-80 ms, echo train length [ETL]=6, flip angle=90°,

matrix=256x256, field of view [FOV]=240x240 mm², 44 3-mm-thick slices), axial 3D T1-weighted fast field echo (FFE) (TR/TE=25/4.6 ms, flip angle=30°, matrix=256x256; FOV=230x230 mm², 220 0.8-mm-thick slices) and pulsed-gradient SE echo-planar (EP) diffusion weighted imaging (DWI) (TE/TR=58/8692 ms, matrix=112x88; FOV=231x231 mm², 2.3-mm-thick slices with SENSE=2, diffusion gradients applied in 35 non-collinear directions, b value =900 s/mm²).

MRI analysis. Brain lesions were segmented using a local thresholding segmentation technique (Jim 8.0 Xinapse Systems Ltd) on T2- and T1-weighted sequences and corresponding LV were calculated. After T1-hypointense lesion refilling, NBV, NGMV and NWMV volumes were assessed using the FSL SIENAx software (Smith et al., 2002).

WM analysis. T2-hyperintense lesion segmentations were binarized, therefore obtaining T2-hyperintense lesion masks. T2-weighted images were coregistered on DWI using a linear and nonlinear transformation, which was applied to T2-hyperintense lesion masks. To evaluate NAWM damage, the WM was automatically segmented on 3D T1-weighted FFE with the FSL segmentation tool and focal lesions were excluded (Zhang, Brady et al., 2001). A possible contamination effect of perilesional NAWM was ruled out by excluding a 2-mm border of NAWM concentric to each lesion (Brown et al., 2017, Liu et al., 2015c).

DTI measures: pre-processing of DWI included correction for off-resonance and eddy current induced distortions, as well as for movements using the Eddy tool within the FSL library (Andersson, Graham et al., 2017). Using linear regression, the diffusion tensor (DT) was estimated in each voxel on DWI and FA, MD, AD and RD maps of NAWM and T2-hyperintense lesion masks were derived (Basser et al., 1994a).

T1/T2-w: T1/T2-w was obtained with an in-house pipeline adapted from Ganzetti et al. (Ganzetti, Wenderoth et al., 2014) Native T1- and T2-weighted sequences underwent a first step consisting of intensity bias correction (unbiased images) and then were calibrated adjusting the intensity histograms using the lowest and highest intensity peaks derived from the ocular and temporal muscles masks on T1- and T2-weighted images

(calibrated images). T2-weighted sequences were coregistered on T1-weighted images and the T1/T2-w was finally calculated. The same transformation was applied to T2-hyperintense lesion masks. The percentage of lesioned band (PLB) was obtained by dividing the LV in each band for the volume of the band itself, multiplied by 100.

Gradient of damage assessment: microstructural values were assessed within 1-voxel concentric bands originating from CSF/WM interface and estimated as a function of the geodesic distance of the WM from the ventricular system. Infratentorial structures were excluded by establishing the superior border of the hippocampal formation (segmented with the FIRST FSL Toolbox)(Patenaude, Smith et al., 2011) as caudal limit of bands expansion. The choice of this limit also prevented the collision of those bands arising contemporary from the body and the temporal horns of the lateral ventricles, as previously described (Liu et al., 2015c). To avoid CSF contamination effects, the first band was excluded (Liu et al., 2015c).

Statistical analysis. Demographic and conventional MRI continuous variables were compared between-groups with two-sample-t-test or non-parametric Mann-Whitney U-test according to the satisfaction of the normality assumption and the number of comparisons. Pearson χ^2 test or Fisher's exact test were used to compare categorical variables.

Linear mixed-effect models, with DTI-derived and T1/T2-w measures as dependent variable and subject as grouping factor, were used to test the effect of group and band on microstructural damage. Models were adjusted for age-, sex- and V-scaling (derived from the SIENAx, as a measure of head size). This analysis, age-, sex-, disease duration- and T2 LV- adjusted, was repeated in the MS and NMOSD patients using lesion microstructural alterations and the PLB as the dependent variable. Between-group post hoc contrasts were Bonferroni-adjusted for multiple comparisons, when appropriate.

The gradient of NAWM damage was calculated comparing the DTI and T1/T2-w change in percentage units per voxel between patients and HC. The changes in percentage unit per voxels were obtained as a difference between pairs of bands divided by the number of intervals which were spanned (Liu et al., 2015c).

The gradient between bands 5 and 1, which are those nearer to the CSF, was defined as periventricular, whereas the gradient between bands 10 and 6, was defined as deep. Similarly, changes in percentage units per voxel of intra-lesional microstructural measures and of PLB were compared between periventricular and deep bands in patients. Correlations between clinical and MRI variables were tested using age- and sex-adjusted partial correlation coefficients (SPSS software, version 23.0).

Data availability. The dataset used and analyzed during the current study is available from the corresponding author on reasonable request.

Results

Demographic and clinical features. **Table 5.1.1** summarizes the main demographic and clinical characteristics of the study groups. HC, MS and NMOSD had similar age, but male/female ratio was significantly lower in NMOSD than MS patients (3/17 vs 10/10, $p=0.04$). MS and NMOSD patients had similar disease duration and disability.

Table 5.1.1. Main demographic, clinical and brain MRI features of HC, NMOSD and MS patients. Significant p values are shown in bold. Adapted from Cacciaguerra et al., MSJ 2021.

	NMOSD (n=20)	HC (n=20)	P NMOSD vs HC	MS (n=20)	P MS vs HC	P NMOSD vs MS
Mean age (SD) [years]	43.5 (11.8)	43.6 (9.6)	0.98*	43.1 (8.5)	0.87*	0.91*
Males/Females	3/17	8/12	0.06^^	10/10	0.75^	0.04^^
Median disease duration (IQR) [years]	5.3 (2.9-11.2)	-	-	7.6 (4.4-7.3)	-	0.25+
Median EDSS (IQR)	3.75 (1.5-6.0)	-	-	2.0 (1.5-3.0)	-	0.11+
Median SDMT (IQR) [z-scores]	-1.06 (-1.95 - 0.26)	-	-	-0.33 (-0.93 - 0.32)	-	0.09+
Median T2 LV (IQR) [ml]	0.16 (0.03-0.41)	0.00 (0.00-0.02)	0.002+	5.54 (2.96-8.38)	<0.001+	<0.001+
Median T1 LV (IQR) [ml]	0.10 (0.01-0.19)	0.00 (0.00-0.00)	0.002+	3.59 (2.15-6.61)	<0.001+	<0.001+
Mean NBV (SD) [ml]	1548 (59)	1581 (82)	0.16*	1510 (106)	0.02*	0.17*

Mean NWMV (SD) [ml]	842 (39)	851 (48)	0.53*	837 (44)	0.36*	0.72*
Mean NGMV (SD) [ml]	706 (39)	730 (43)	0.08*	672 (75)	0.006*	0.09*

*two-sample t test; χ^2 test; ^^ Fisher's exact test; + Mann-Whitney U-test.

Abbreviations: HC=healthy controls; NMOSD=neuromyelitis optica spectrum disorders; MS=multiple sclerosis; IQR=interquartile range; EDSS=Expanded Disability Status Scale; SDMT=Symbol Digit Modalities Test; LV=lesion volume; NBV=normalized brain volume; NWMV=normalized white matter volume; NGMV=normalized gray matter volume.

Conventional MRI measures. NMOSD patients had higher T2- and T1 LV than HC (p=0.002 for both) and lower T2- and T1 LV than MS patients (p<0.001 for both). NBV, NWMV and NGMV did not differ between NMOSD patients and HC or MS patients (**Table 5.1.1**). Compared to HC, MS patients had higher T2- and T1 LV (p<0.001 for both) and lower NBV (p=0.02) and NGMV (p=0.006, Table 6.1.1).

Global WM damage. T2-hyperintense WM lesions were detected in 9/20 NMOSD patients, who had lower PLB than MS patients (p<0.001). Compared to NMOSD, MS lesions had higher FA (p<0.001), MD (p=0.021), AD (p<0.001), T1/T2-w (p<0.001) and similar RD values (**Table 5.1.2**).

Table 5.1.2. Microstructural intra-lesional measures in NMOSD and MS patients at global level and in each concentric band (the lower the number, the nearer to the CSF). Measures are shown as mean value and 95% confidence interval (age-, sex-, T2 LV- and disease duration-adjusted). Significant p values are shown in bold and * is reported beside those surviving Bonferroni correction.

Mean Global measures	NMOSD (n=9)	MS (n=20)	p
Percentage of lesioned band	1.03 (0.01-2.05)	5.52 (4.67-6.38)	<0.001*
FA	0.23 (0.22-0.24)	0.25 (0.24-0.26)	<0.001*

MD		1.03 (1.02-1.04)	1.06 (1.04-1.06)	0.021
RD		0.82 (0.79-0.84)	0.82 (0.81-0.84)	0.72
AD		1.13 (1.12-1.24)	1.16 (1.14-1.18)	<0.001*
T1/T2-w		1.14 (1.12-1.16)	1.19 (1.17-1.20)	<0.001*
Measure	Band	NMOSD (n=9)	MS (n=20)	p MS vs HC
Percentage LV	1	1.57 (-2.69-5.83)	8.09 (4.52-11.66)	0.023
	2	1.49 (-2.84-5.82)	7.81 (4.18-11.43)	0.030
	3	1.28 (-2.86-5.42)	7.25 (3.78-10.71)	0.031
	4	1.13 (-2.70-4.98)	6.52 (3.29-9.74)	0.036
	5	1.08 (-2.47-4.63)	5.79 (2.82-8.77)	0.046
	6	0.92 (-2.19-4.04)	5.06 (2.45-7.67)	0.046
	7	0.80 (-1.92-3.52)	4.46 (2.19-6.74)	0.043
	8	0.72 (-1.65-3.09)	3.92 (1.94-5.91)	0.043
	9	0.71 (-1.34-2.28)	3.37 (1.65-5.10)	0.052
	10	0.59 (-1.22-2.14)	3.00 (1.45-4.49)	0.050
FA	1	0.25 (0.22-0.27)	0.25 (0.23-0.29)	0.14
	2	0.24 (0.22-0.27)	0.26 (0.23-0.28)	0.16
	3	0.23 (0.21-0.26)	0.27 (0.25-0.29)	0.040
	4	0.23 (0.21-0.25)	0.26 (0.23-0.28)	0.065
	5	0.22 (0.20-0.24)	0.25 (0.23-0.27)	0.086
	6	0.21 (0.19-0.23)	0.24 (0.23-0.27)	0.010
	7	0.21 (0.19-0.23)	0.24 (0.22-0.26)	0.014
	8	0.22 (0.19-0.24)	0.24 (0.22-0.26)	0.030
	9	0.25 (0.22-0.26)	0.24 (0.22-0.26)	0.71
	10	0.26 (0.24-0.29)	0.24 (0.22-0.26)	0.27
MD	1	1.04 (0.99-1.09)	1.09 (1.04-1.13)	0.21

	2	1.03 (0.98-1.08)	1.08 (1.03-1.12)	0.21
	3	1.03 (0.98-1.08)	1.06 (1.02-1.10)	0.37
	4	1.03 (0.98-1.09)	1.06 (1.02-1.09)	0.52
	5	1.04 (0.99-1.09)	1.06 (1.02-1.09)	0.77
	6	1.07 (1.02-1.10)	1.04 (1.00-1.08)	0.47
	7	1.03 (0.98-1.08)	1.04 (1.00-1.06)	0.86
	8	1.01 (0.96-1.06)	1.04 (1.00-1.08)	0.40
	9	0.98 (0.94-1.04)	1.04 (1.00-1.08)	0.12
	10	1.00 (0.95-1.04)	1.04 (1.00-1.08)	0.17
RD	1	0.82 (0.75-0.88)	0.82 (0.77-0.88)	0.80
	2	0.82 (0.75-0.88)	0.83 (0.78-0.88)	0.71
	3	0.82 (0.76-0.89)	0.82 (0.77-0.86)	0.81
	4	0.83 (0.77-0.89)	0.82 (0.77-0.86)	0.75
	5	0.84 (0.78-0.90)	0.82 (0.77-0.86)	0.55
	6	0.88 (0.82-0.94)	0.82 (0.77-0.86)	0.13
	7	0.78 (0.72-0.84)	0.82 (0.77-0.86)	0.56
	8	0.83 (0.77-0.89)	0.82 (0.77-0.88)	0.87
	9	0.77 (0.71-0.83)	0.82 (0.77-0.88)	0.28
	10	0.81 (0.75-0.86)	0.83 (0.78-0.88)	0.12
AD	1	1.21 (1.15-1.27)	1.31 (1.26-1.36)	0.017
	2	1.20 (1.13-1.25)	1.28 (1.23-1.33)	0.011
	3	1.17 (1.11-1.23)	1.26 (1.21-1.31)	0.002
	4	1.17 (1.11-1.24)	1.24 (1.19-1.29)	0.023
	5	1.17 (1.10-1.23)	1.22 (1.18-1.27)	0.095
	6	1.17 (1.11-1.23)	1.20 (1.15-1.25)	0.41
	7	1.04	1.19	0.062

		(0.98-1.10)	(1.14-1.24)	
	8	1.12 (1.06-1.18)	1.19 (1.14-1.24)	0.012
	9	1.13 (1.07-1.19)	1.19 (1.14-1.24)	0.050
	10	1.18 (1.12-1.24)	1.18 (1.14-1.23)	0.96
T1/T2-w	1	1.11 (1.05-1.18)	1.15 (1.10-1.20)	0.52
	2	1.11 (1.05-1.18)	1.16 (1.10-1.21)	0.38
	3	1.11 (1.05-1.17)	1.17 (1.12-1.22)	0.15
	4	1.12 (1.05-1.19)	1.18 (1.13-1.24)	0.13
	5	1.12 (1.05-1.19)	1.19 (1.14-1.24)	0.08
	6	1.13 (1.07-1.20)	1.20 (1.14-1.25)	0.14
	7	1.15 (1.08-1.22)	1.20 (1.15-1.25)	0.29
	8	1.17 (1.11-1.23)	1.21 (1.15-1.26)	0.13
	9	1.18 (1.11-1.24)	1.21 (1.16-1.26)	0.45
	10	1.18 (1.11-1.24)	1.21 (1.16-1.26)	0.40

Abbreviations: HC=healthy controls; NMOSD=neuromyelitis optica spectrum disorders; MS=multiple sclerosis; FA=fractional anisotropy; MD=mean diffusivity; RD=radial diffusivity; AD=axial diffusivity; T1/T2-w=T1/T2-weighted ratio.

Global NAWM FA was lower in MS patients compared to HC ($p=0.008$) and NMOSD ($p=0.004$), while MD, RD and AD were higher in MS compared to HC and NMOSD ($p<0.001-0.004$) and in NMOSD compared to HC ($p<0.001-0.004$). T1/T2-w was lower in NMOSD patients compared to MS and HC ($p<0.001$ for both) and in MS compared to HC ($p=0.004$) (**Table 5.1.3**).

Table 5.1.3. NAWM measures in HC, NMOSD and MS patients at global level and in each concentric band (the lower the number, the nearer to the CSF). Measures are shown as mean value and 95% confidence interval (age-, sex- and V-scaling-adjusted).

Significant p values are shown in bold and * is reported beside those surviving Bonferroni correction.

Mean measures		Global	HC (n=20)	NMOSD (n=20)	p NMOSD vs HC	MS (n=20)	p MS vs HC	p NMOSD vs MS
FA			0.27 (0.26-0.28)	0.27 (0.26-0.29)	0.74	0.25 (0.24-0.26)	0.008*	0.004*
MD			0.73 (0.70-0.75)	0.87 (0.85-0.89)	<0.001*	0.93 (0.91-0.96)	<0.001*	<0.001*
RD			0.75 (0.75-0.76)	0.77 (0.76-0.78)	0.004*	0.82 (0.81-0.83)	<0.001*	<0.001*
AD			1.10 (1.10-1.11)	1.12 (1.11-1.13)	0.002*	1.16 (1.15-1.16)	<0.001*	<0.001*
T1/T2-w			1.39 (1.38-1.41)	1.32 (1.31-1.34)	<0.001*	1.36 (1.35-1.38)	0.004*	<0.001*
Measure	Band		HC (n=20)	NMOSD (n=20)	p NMOSD vs HC	MS (n=20)	p MS vs HC	p NMOSD vs MS
FA	1		0.25 (0.24-0.25)	0.25 (0.25-0.26)	0.72	0.23 (0.22-0.23)	0.001*	0.001*
	2		0.25 (0.24-0.25)	0.25 (0.24-0.26)	0.68	0.23 (0.22-0.24)	0.004*	0.002*
	3		0.26 (0.25-0.26)	0.26 (0.25-0.27)	0.82	0.24 (0.23-0.24)	0.001*	0.001*
	4		0.26 (0.26-0.27)	0.26 (0.26-0.27)	0.94	0.25 (0.24-0.26)	0.009*	0.010*
	5		0.27 (0.26-0.28)	0.27 (0.27-0.28)	0.62	0.25 (0.24-0.26)	0.003*	0.001*
	6		0.27 (0.26-0.28)	0.28 (0.27-0.29)	0.49	0.26 (0.25-0.27)	0.021*	0.004*
	7		0.28 (0.27-0.29)	0.28 (0.27-0.29)	0.96	0.26 (0.25-0.27)	0.010*	0.011*
	8		0.28 (0.27-0.29)	0.28 (0.27-0.29)	0.56	0.26 (0.25-0.27)	0.043	0.013*
	9		0.28 (0.27-0.29)	0.28 (0.27-0.29)	0.98	0.27 (0.26-0.28)	0.052	0.058
	10		0.28 (0.27-0.29)	0.28 (0.27-0.29)	0.83	0.27 (0.26-0.28)	0.09	0.07
MD	1		0.79 (0.70-0.88)	0.96 (0.87-1.05)	0.010*	1.04 (0.95-1.13)	<0.001*	0.20
	2		0.77 (0.68-0.86)	0.93 (0.84-1.02)	0.011*	1.00 (0.92-1.09)	<0.001*	0.24
	3		0.75 (0.67-0.83)	0.90 (0.82-0.99)	0.010*	0.97 (0.89-1.05)	<0.001*	0.23
	4		0.74 (0.66-0.81)	0.88 (0.91-0.96)	0.009*	0.95 (0.87-1.02)	<0.001*	0.26
	5		0.73 (0.65-0.80)	0.86 (0.79-0.94)	0.013*	0.93 (0.85-1.00)	<0.001*	0.23
	6		0.71	0.85	0.009*	0.91	<0.001*	0.27

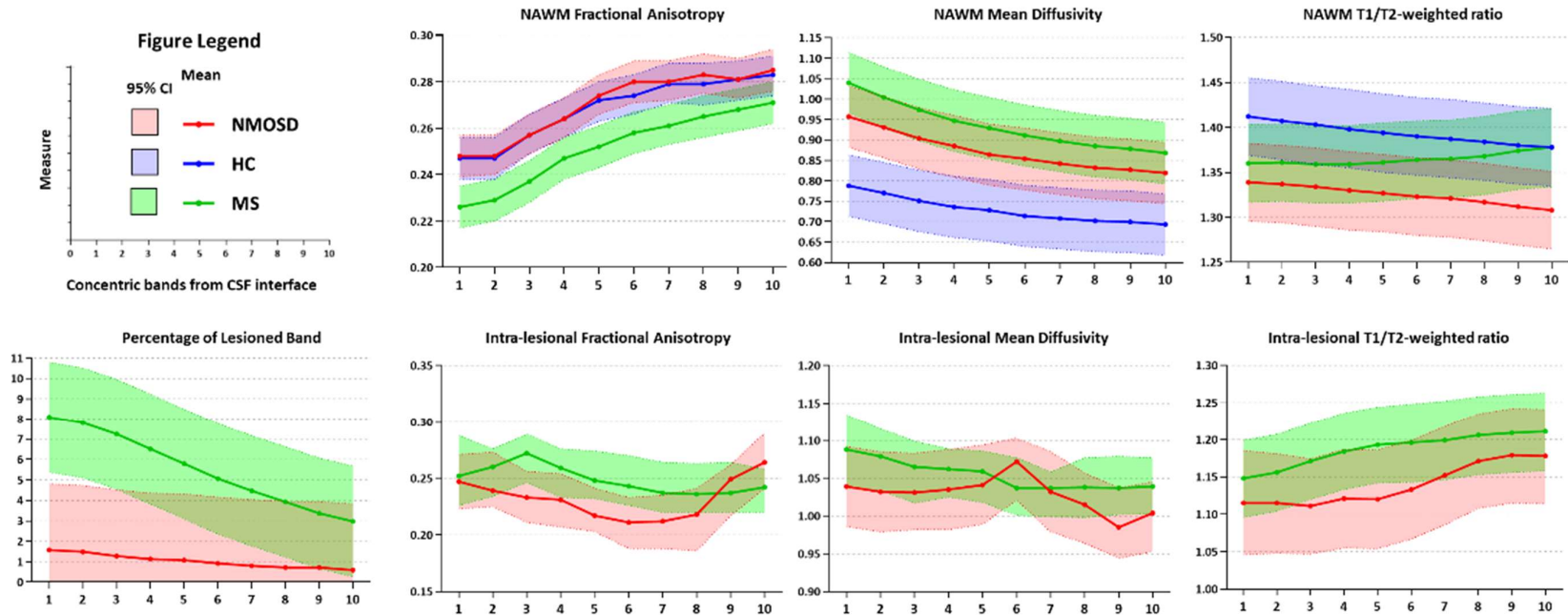
		(0.64-0.79)	(0.78-0.93)		(0.84-0.98)		
	7	0.71 (0.64-0.78)	0.84 (0.77-0.91)	0.010*	0.90 (0.83-0.97)	<0.001*	0.27
	8	0.70 (0.63-0.77)	0.83 (0.76-0.90)	0.011*	0.88 (0.81-0.95)	<0.001*	0.29
	9	0.70 (0.63-0.77)	0.83 (0.76-0.89)	0.011*	0.88 (0.81-0.95)	<0.001*	0.29
	10	0.69 (0.62-0.76)	0.82 (0.75-0.88)	0.010*	0.87 (0.80-0.93)	0.001*	0.31
RD	1	0.84 (0.81-0.87)	0.86 (0.83-0.89)	0.40	0.93 (0.90-0.96)	<0.001*	0.005*
	2	0.82 (0.79-0.84)	0.84 (0.81-0.87)	0.33	0.90 (0.87-0.93)	0.001*	0.016*
	3	0.79 (0.76-0.82)	0.81 (0.78-0.83)	0.43	0.87 (0.84-0.89)	0.001*	0.007*
	4	0.77 (0.74-0.80)	0.78 (0.76-0.81)	0.41	0.83 (0.81-0.86)	0.001*	0.014*
	5	0.75 (0.72-0.77)	0.77 (0.74-0.79)	0.32	0.82 (0.79-0.84)	0.001*	0.010*
	6	0.73 (0.71-0.76)	0.75 (0.73-0.78)	0.34	0.79 (0.77-0.82)	0.002*	0.022
	7	0.73 (0.70-0.75)	0.74 (0.71-0.77)	0.48	0.78 (0.76-0.81)	0.002*	0.014*
	8	0.71 (0.69-0.74)	0.73 (0.71-0.76)	0.28	0.77 (0.74-0.80)	0.002*	0.038
	9	0.71 (0.68-0.74)	0.73 (0.70-0.76)	0.25	0.77 (0.74-0.79)	0.002*	0.035
	10	0.70 (0.68-0.73)	0.72 (0.69-0.75)	0.32	0.75 (0.73-0.78)	0.004*	0.051
AD	1	1.19 (1.16-1.22)	1.21 (1.19-1.23)	0.38	1.26 (1.23-1.28)	0.003*	0.031
	2	1.16 (1.13-1.18)	1.17 (1.15-1.20)	0.38	1.22 (1.19-1.24)	0.006*	0.053
	3	1.13 (1.11-1.16)	1.15 (1.12-1.17)	0.34	1.19 (1.16-1.21)	0.004*	0.047
	4	1.12 (1.10-1.14)	1.14 (1.11-1.16)	0.39	1.17 (1.14-1.19)	0.004*	0.040
	5	1.10 (1.07-1.12)	1.12 (1.10-1.14)	0.27	1.15 (1.13-1.18)	0.002*	0.036
	6	1.09 (1.07-1.11)	1.10 (1.08-1.13)	0.41	1.14 (1.11-1.16)	0.005*	0.044
	7	1.08 (1.05-1.10)	1.09 (1.07-1.12)	0.36	1.12 (1.10-1.15)	0.008*	0.07
	8	1.07 (1.04-1.09)	1.08 (1.06-1.11)	0.30	1.11 (1.09-1.14)	0.006*	0.07
	9	1.06 (1.03-1.08)	1.08 (1.05-1.10)	0.17	1.10 (1.08-1.13)	0.003*	0.09
	10	1.05 (1.03-1.07)	1.07 (1.04-1.09)	0.19	1.09 (1.07-1.12)	0.002*	0.07
T1/T2-w	1	1.41 (1.37-1.45)	1.34 (1.30-1.38)	0.024	1.36 (1.32-1.40)	0.10	0.51
	2	1.41	1.34	0.031	1.36	0.15	0.45

		(1.36-1.45)	(1.29-1.38)		(1.32-1.40)		
	3	1.40 (1.36-1.45)	1.33 (1.29-1.38)	0.034	1.36 (1.32-1.40)	0.18	0.43
	4	1.40 (1.35-1.44)	1.33 (1.29-1.37)	0.032	1.36 (1.32-1.40)	0.21	0.35
	5	1.39 (1.35-1.44)	1.33 (1.28-1.37)	0.037	1.36 (1.32-1.40)	0.31	0.27
	6	1.39 (1.35-1.43)	1.32 (1.28-1.37)	0.035	1.36 (1.32-1.41)	0.40	0.19
	7	1.39 (1.34-1.43)	1.32 (1.28-1.36)	0.037	1.37 (1.32-1.41)	0.47	0.16
	8	1.38 (1.34-1.43)	1.32 (1.27-1.36)	0.034	1.37 (1.32-1.41)	0.61	0.10
	9	1.38 (1.34-1.42)	1.31 (1.27-1.35)	0.031	1.37 (1.33-1.42)	0.86	0.046
	10	1.38 (1.33-1.42)	1.31 (1.26-1.35)	0.026	1.38 (1.33-1.42)	0.99	0.027

Abbreviations: HC=healthy controls; NMOSD=neuromyelitis optica spectrum disorders; MS=multiple sclerosis; FA=fractional anisotropy; MD=mean diffusivity; RD=radial diffusivity; AD=axial diffusivity; T1/T2-w=T1/T2-weighted ratio.

WM damage in concentric bands. The results of WM analysis in concentric bands are shown in Tables 5.1.2 and 5.1.3 and Figure 5.1.1.

Figure 6.1.1. WM abnormalities in HC (blue line), MS (green line) and NMOSD (red line) patients. Numbers on the x axis represent the progressive NAWM concentric bands, with lower values corresponding to bands nearer the CSF and higher values corresponding to deeper bands. Shaded colors represent corresponding 95% confidence intervals. Figure is adapted from Cacciaguerra et al., Multiple Sclerosis Journal 2021. Author’s reuse as per Journal pre-approved permission (<https://us.sagepub.com/en-us/nam/pre-approved-permission-requests-journals>).



Abbreviations: NMOSD=neuromyelitis optica spectrum disorders; HC=healthy controls; MS=multiple sclerosis; CI=confidence interval; NAWM=normal appearing white matter.

Compared to NMOSD, MS patients had higher PLB in the first eight bands ($p=0.023-0.046$) and higher intra-lesional AD values in the first four bands ($p=0.002-0.023$) and in band 8 ($p=0.012$). Intra-lesional MD, RD and T1/T2-w values were similar between NMOSD and MS in each band.

In the NAWM, FA values were similar between NMOSD patients and HC. MS patients had reduced FA in the first eight bands nearer the CSF compared to HC ($p=0.001-0.043$) and NMOSD ($p=0.001-0.013$).

MD values were significantly higher along all concentric bands in both MS ($p<0.001$) and NMOSD patients ($p=0.009-0.013$) compared to HC. Compared to NMOSD, MS patients had similar MD values.

MS patients had higher RD and AD values in all concentric bands compared to HC ($p<0.001-0.004$ and $0.002-0.008$, respectively), higher RD in the first nine bands ($p=0.005-0.038$) and higher AD in the first six bands ($p=0.047-0.031$) compared to NMOSD. RD and AD values did not differ between NMOSD patients and HC.

T1/T2-w was reduced along all concentric bands in NMOSD patients compared to HC ($p=0.024-0.037$) and in NMOSD compared to MS patients in the last two bands ($p=0.046$ and 0.027). No differences of T1/T2-w values were found between MS patients and HC. MS lesions had different periventricular vs deep gradient of PLB ($p=0.040$), MD ($p=0.043$) and AD ($p=0.004$), and NMOSD lesions showed different gradients of FA ($p=0.023$) and RD ($p=0.008$, **Table 5.1.4**).

Table 5.1.4. Periventricular (bands 1-5) and deep (bands 6-10) microstructural gradients of intralesional damage in NMOSD and MS patients. All values are multiplied by 100. P values refer to non-parametric test for related groups and significant values are shown in bold.

Median Measures (IQR) [percentage units]	NMOSD (n=9)	p Periventricular vs Deep in NMOSD	MS (n=20)	p Periventricular vs Deep in MS
Periventricular PLB	-0.01 (-0.16-0.02)	0.73	-5.01 (-8.14- -2.33)	0.040
Deep PLB	-0.03 (-0.07-0.03)		-2.03 (-5.71- -0.03)	

Periventricular FA	-1.7 (-2.93-0.28)	0.023	-0.54 (-2.21- -0.26)	0.10
Deep FA	1.29 (0.01-2.08)		0.81 (-1.28-0.93)	
Periventricular MD	0.41 (-0.77-1.04)	0.071	-0.45 (-1.10-0.01)	0.043
Deep MD	-0.88 (-2.10-0.19)		0.15 (-0.82-0.60)	
Periventricular RD	0.50 (-0.02-2.07)	0.008	0.37 (-0.57-0.85)	0.63
Deep RD	-1.91 (-3.22-0.32)		0.35 (-1.07-1.52)	
Periventricular AD	-1.69 (-3.84-1.11)	0.43	-2.15 (-2.57- -1.05)	0.004
Deep AD	1.37 (-2.13-1.99)		-0.52 (-1.17-0.77)	
Periventricular T1/T2-w	0.53 (-1.41-1.07)	0.24	0.87 (0.40-1.37)	0.18
Deep T1/T2-w	1.17 (-0.19-1.83)		0.26 (-0.09-1.08)	

Abbreviations: NMOSD=neuromyelitis optica spectrum disorders; MS=multiple sclerosis; PLB=percentage of lesioned band; FA=fractional anisotropy; MD=mean diffusivity; RD=radial diffusivity; AD=axial diffusivity; T1/T2-w=T1/T2-weighted ratio.

In the NAWM, periventricular gradients of FA and MD were different between HC and MS patients ($p=0.04$ and $p=0.05$, respectively), whereas T1/T2-w gradients differed in both periventricular and deep concentric bands between HC and MS patients ($p<0.001$ for both) and between HC and NMOSD patients ($p=0.003$ in periventricular and $p=0.001$ in deep bands, **Table 5.1.5**).

Table 5.1.5. Periventricular (bands 1-5) and deep (bands 6-10) microstructural gradients of damage in the NAWM of HC, NMOSD and MS patients. All values are multiplied by 100. P values refer to non-parametric test for unrelated groups and significant values are shown in bold.

Median Measures (IQR) [percentage units]	HC (n=20)	NMOSD (n=20)	p NMOSD vs HC	MS (n=20)	p MS vs HC
---	------------------	---------------------	----------------------	------------------	-------------------

Periventricular FA	0.25 (0.05;0.75)	0.05 (0.05;0.75)	0.22	0.05 (0.02;0.25)	0.04
Deep FA	0.05 (0.00;0.25)	0.00 (0.00;0.25)	0.16	0.05 (0.00;0.25)	0.55
Periventricular MD	-0.15 (-2.25;0.25)	-1.75 (-2.25; -0.25)	0.84	-0.75 (-1.25; -1.00)	0.05
Deep MD	-0.05 (-0.75; -0.25)	-0.75 (-1.25; -0.05)	0.79	-0.25 (-2.75; -0.25)	0.08
Periventricular RD	-1.00 (-2.62; -2.25)	-2.25 (-2.62; -0.15)	0.47	-2.25 (-2.75; -0.25)	0.23
Deep RD	-0.20 (-0.75; -0.05)	-0.15 (-0.75; -0.01)	0.12	-0.75 (-1.25; -0.07)	0.48
Periventricular AD	-0.75 (-2.35; -0.03)	-1.00 (-2.12; -0.17)	0.15	-2.00 (-2.75; -0.25)	0.17
Deep AD	-0.10 (-0.75; -0.01)	-0.10 (-0.60; -0.01)	0.12	-0.75 (-0.75; -0.07)	0.46
Periventricular T1/T2-w	-0.25 (-0.62; -0.05)	-0.25 (-0.25; -1.25)	0.003	0.00 (-0.20;0.25)	<0.001
Deep T1/T2-w	-0.05 (-0.25; -0.05)	-0.25 (-0.25; -0.05)	0.001	0.05 (0.00;0.25)	<0.001

Abbreviations: HC=healthy controls; NMOSD=neuromyelitis optica spectrum disorders; MS=multiple sclerosis; FA=fractional anisotropy; MD=mean diffusivity; RD=radial diffusivity; AD=axial diffusivity; T1/T2-w=T1/T2-weighted ratio.

Correlations with clinical and lesion variables. In MS patients, significant correlations were found between clinical and lesion variables and periventricular and deep gradient of damage (**Table 5.1.6**). In NMOSD, correlations were observed only between SDMT z-scores and deep gradient of MD ($r=0.52$, $p=0.028$) and AD ($r=0.47$, $p=0.049$).

Table 5.1.6. Significant age- and sex-adjusted partial correlations between periventricular (bands 1-5) and deep (bands 6-10) microstructural gradients of intralésional and NAWM damage in MS patients.

Measure	Tissue	Periventricular gradient	r, p values	Deep gradient	r, p values
EDSS	Lesions	PLB	$r=0.51$, $p=0.039$	-	-

	NAWM	T1/T2-w	r=0.61, p=0.007	-	-
SDMT z-scores	Lesions	PLB	r=0.63, p=0.007	-	-
		MD	r=0.53, p=0.029	-	-
	NAWM	T1/T2-w	r=-0.56, p=0.015	-	-
Disease duration	Lesions	-	-	-	-
	NAWM	-	-	MD	r=-0.50, p=0.036
T2 LV	Lesions	PLB	r=-0.59, p=0.012	PLB	r=-0.94, p<0.001
				MD	r=-0.56, p=0.019
				RD	r=-0.55, p=0.021
				T1/T2-w	r=0.60, p=0.011
	NAWM	-	-	FA	r=0.95, p=0.014
				RD	r=-0.63, p=0.005
T1 LV	Lesions	PLB	r=-0.50, p=0.039	PLB	r=-0.90, p<0.001
				MD	r=-0.52, p=0.032
				RD	r=-0.51, p=0.036
				T1/T2-w	r=0.71, p=0.001
	NAWM	-	-	RD	r=-0.61, p=0.007

Abbreviations: NAWM=normal appearing white matter; MS=multiple sclerosis; EDSS=Expanded Disability Status Scale; SDMT= Symbol Digit Modalities Test; LV= lesion volume; PLB=percentage of lesioned band; FA=fractional anisotropy; MD=mean diffusivity; RD=radial diffusivity; AD=axial diffusivity; T1/T2-w=T1/T2-weighted ratio.

Discussion

A multiparametric approach was applied to evaluate microstructural alterations of the WM and the existence of a gradient of damage starting from the CSF-WM interface in NMOSD and MS patients.

In MS, NAWM was characterized by reduced FA, with increased MD, RD and AD values, while lesions had higher MD and AD. These alterations and PLB were more

severe in periventricular regions, thus confirming the previously shown distribution of WM abnormalities in this condition (Liu et al., 2015c, Pardini et al., 2019). On the other hand, NAWM in NMOSD patients showed no significant abnormalities of FA, intermediate values of MD between MS patients and HC and lower T1/T2-w than HC and MS patients. No evidence of NAWM gradient of damage emerged in this group. NMOSD lesions showed reduced T1/T2-w ratio and FA, which might be explained by extensive axonal loss and necrosis in long-lasting lesions (Wingerchuk et al., 2015). However, such results must be interpreted with caution, given the small sample-size, since they might suffer the effect of outliers.

The DTI-derived model has been largely applied to the study of WM damage in patients with MS (Cercignani & Gandini Wheeler-Kingshott, 2019), while, at the state of the art, the interpretation of T1/T2-w is more challenging.

In adult healthy subjects, T1/T2-w correlated with indices of myelination such as the myelin water fraction (MWF) in both GM and WM (Uddin, Figley et al., 2019). Nonetheless, T1/T2-w was unrelated to DTI-derived measures in the WM and shared only 11% variance with MWF, suggesting that other factors than myelin content (i.e., fiber orientation, tissue swelling, cellular density) are more likely to influence this measure. Interestingly, among all microstructural variables, FA was the one best correlating with MWF and shared the highest variance (53%) among different brain regions with this index, implying that a large proportion of this measure could be related to myelin (Uddin et al., 2019).

In our study, NMOSD patients had diffuse microstructural alterations of the NAWM. MD alteration and T1/T2-w reduction suggest the presence of demyelination, whereas the preservation of FA would be consistent with fiber integrity (Cercignani & Gandini Wheeler-Kingshott, 2019). According to previous considerations, it seems unlikely that myelin damage would not influence FA behavior (Uddin et al., 2019). Only a few studies have evaluated DTI measures in the NAWM of NMOSD patients, with discrepant findings, encompassing no NAWM abnormalities (Filippi et al., 1999) or limited and diffuse alterations (Pichiecchio et al., 2012). However, axonal integrity was also supported by MR spectroscopy (de Seze, Blanc et al., 2010).

Since NMOSD has been defined as an astrocytopathy (Lennon et al., 2004), the discrepancy between FA and MD findings could simply reflect the intrinsic limitations

of the DTI model, due to the possible increase of extracellular water in NMOSD. Evidence of increased blood-brain barrier (BBB) permeability in NMOSD patients under an acute attack is common, sometimes leading to PRES-like MRI presentations (Magana, Matiello et al., 2009). The BBB encompasses endothelial tight junctions, pericytes and astrocytes endfeet, which are rich of AQP4 water channel. This is the main regulator of water-exchanges in the CNS and is fundamental in CNS edematous conditions, respectively facilitating and eliminating cytotoxic and vasogenic edema (Saadoun & Papadopoulos, 2010). The reduction of AQP4 expression on otherwise healthy astrocytes by DNA modifications or RNA interference determines a consistent decrease of water diffusivity, measured with inter-compartmental exchange (Obata, Kershaw et al., 2018) and MRI apparent diffusion coefficient (Badaut, Ashwal et al., 2011). Moreover, several studies found an antibody-mediated internalization of the channel, although others did not confirm such finding (Rossi, Ratelade et al., 2012).

These results are apparently in contrast with our hypothesis of increased extracellular water in NMOSD. Nonetheless, AQP4 channels regulate water transcellular movement only, whereas astrocytes themselves control paracellular flows by providing paracrine signaling to maintain endothelial tight junction expression, limiting water and cellular entrance in the CNS (Keaney & Campbell, 2015). Pathological studies have provided evidence of extensive astrocytes loss driven by complement activation secondary to antibodies binding to AQP4 (Wingerchuk et al., 2015).

A hypothetical explanation for the increase of MD values despite normal FA, could be an increase of BBB permeability secondary to astrocytes damage, leading to higher extracellular water content in brain tissue. This effect could be further implemented by a reduced AQP4 expression or by its functional blockade, which would prevent tissue healing by water absorption.

Another interesting point is the significant T1/T2-w reduction in NMOSD patients. Although NMOSD is considered a demyelinating disorder, the presence of lower values than MS is unexpected. In vivo evidence of demyelination was found only at ultra-high field MRI (7.0 T) (Chou, Tanasescu et al., 2019). However, it is known that both T1 and T2 relaxation times heavily depend on water content and that changes in these measures modify tissue contrast and intensity (Bansal, Hao et al., 2013). Therefore, a theoretical

increase in tissue water could decrease T1 and increase T2 signal intensity, thus reducing the T1/T2-w.

In our work, measures of physical and cognitive disability of MS patients (EDSS and SDMT), correlated with the periventricular gradient of microstructural damage, while those variables associated to disease history (LV and disease duration) correlated with deep NAWM damage. A voxel-wise study disclosed an association between periventricular damage and cognitive and motor performance and ascribed that to the injury of periventricular long WM projections (Altermatt, Gaetano et al., 2018). On the other hand, since periventricular involvement occurs early in MS (Thompson et al., 2018), deep WM damage might be related to a more diffuse and late WM damage.

Interestingly, in NMOSD, NAWM alterations correlated with SDMT performance only. Cognitive deterioration is common in NMOSD and anti-AQP4-IgG has been shown to inhibit neuronal plasticity and long-term potentiation (Oertel et al., 2019). Although the structural substrates of cognitive impairment in NMOSD are still under investigation, diffuse and smoldering brain damage has been postulated (Oertel et al., 2019), and our findings further support this hypothesis.

To ameliorate and confirm our results, future studies should compensate for a few limitations by including larger samples of patients, favoring a longitudinal setting, and using more advanced models, able to discriminate between intra and extracellular water. To conclude, WM abnormalities are present in both MS and NMOSD, with different microstructural profiles and distribution. These findings support the serological origin of the pathogenic element in NMOSD and possibly provide a new perspective on the pathophysiology of this disorder, which could be helpful in the differential diagnosis with other neuroinflammatory disorders not affecting astrocytes.

5.2 MR T2-relaxation time as an indirect measure of brain water content and disease activity in NMOSD

Cacciaguerra *et al.*, *Journal of Neurology Neurosurgery and Psychiatry* 2022

This chapter describes the work published in *Journal of Neurology Neurosurgery and Psychiatry* (PMID: 35483915, DOI: 10.1136/jnnp-2022-328956).

Neuro-inflammation

Original research

MR T2-relaxation time as an indirect measure of brain water content and disease activity in NMOSD

Laura Cacciaguerra ^{1,2,3}, Elisabetta Pagani ¹, Marta Radaelli ^{1,2},
Sarlota Mesaros ⁴, Vittorio Martinelli ², Jovana Ivanovic ⁴,
Jelena Drulovic ⁴, Massimo Filippi ^{1,2,3,5,6}, Maria A Rocca ^{1,2,3}

ABSTRACT

Objective Since astrocytes at the blood–brain barrier are targeted by neuromyelitis optica spectrum disorder (NMOSD), this study aims to assess whether patients with NMOSD have a subclinical accumulation of brain water and if it differs according to disease activity.

Methods Seventy-seven aquaporin-4-positive patients with NMOSD and 105 healthy controls were enrolled at two European centres. Brain dual-echo turbo spin-echo MR images were evaluated and maps of T2 relaxation time (T2rt) in the normal-appearing white matter (NAWM), grey matter and basal ganglia were obtained. Patients with a clinical relapse within 1 month before or after MRI acquisition were defined 'active'. Differences between patients and controls were assessed using z-scores of T2rt obtained with age-adjusted and sex-adjusted linear models from each site. A stepwise binary logistic regression was run on clinical and MRI variables to identify independent predictors of disease activity.

Results Patients had increased T2rt in both white and grey matter structures (p range: 0.014 to <0.0001). Twenty patients with NMOSD were defined active. Despite similar clinical and MRI features, active patients had a significantly increased T2rt in the NAWM and grey matter compared with those clinically stable (p range: 0.010–0.002). The stepwise binary logistic regression selected the NAWM as independently associated with disease activity (beta=2.06, SE=0.58, Nagelkerke R²=0.46, p<0.001).

Conclusions In line with the research hypothesis, patients with NMOSD have increased brain T2rt. The magnitude of this alteration might be useful for identifying those patients with active disease.

Key messages

What is already known on this topic

⇒ Clinical observation and preclinical data suggest that neuromyelitis optica spectrum disorder (NMOSD) autoimmunity could alter the blood–brain barrier permeability. Still, radiological markers of disease activity in NMOSD are missing.

What this study adds

⇒ Using the T2-relaxation time as an indirect measure of water content, this study suggests that patients with NMOSD have an unbalance in water homeostasis, leading to subclinical brain water accumulation compared with controls. Also, the magnitude of this alteration is higher in clinically active compared with clinically stable patients.

How this study might affect research, practice and/or policy

⇒ This is the first study supporting the potential role of quantitative imaging in NMOSD, suggesting an easily obtainable measure likely dependent on disease pathophysiology and inflammatory activity.

Introduction

NMOSD is an autoimmune disease of the CNS (Wingerchuk et al., 2015). It is associated with pathogenetic autoantibodies targeting the AQP4 on astrocytes, leading to complement cascade activation and secondary astrocytes damage or loss (Wingerchuk et al., 2015).

In addition, recent pathology data pointed out that NMOSD patients suffer a sort of global astrocytopathy affecting both lesioned and non-lesioned tissue (Guo, Lennon et al., 2021). Since the AQP4 channel is the primary regulator of water homeostasis in the CNS (Saadoun & Papadopoulos, 2010), and astrocytes are part of the BBB (Keaney & Campbell, 2015), NMOSD-specific autoimmunity could theoretically alter the physiological BBB impermeability and brain water content.

Aligning with this hypothesis, several radiological signs suggest an increased BBB permeability during NMOSD attacks. These include the “cloud-like” enhancement (Kim et al., 2015), the posterior reversible encephalopathy syndrome (Kim et al., 2015), and the presence of a high intra-lesional T2-hyperintense signal in the spinal cord (“bright-spotty” lesions) (Hyun, Kim et al., 2015). Interestingly, although a hypothesis also attributes bright spotty lesions to tissue disruption, these lesions seem to disappear after the acute phase of the disease, suggesting that they might represent a transient phenomenon accompanying the acute attack rather than permanent tissue loss (Hyun et al., 2015).

In experimental models, sera from NMOSD patients had detrimental effects on BBB integrity (Shimizu, Sano et al., 2012) and histology revealed intramyelic edema, indicating water homeostasis unbalance, in the tissue nearby nondestructive lesions of AQP4-seropositive NMOSD patients (Hinson, Romero et al., 2012). In line with these results, a phase-I trial administered the monoclonal antibody bevacizumab as add-on therapy to high-dose steroids in a small-cohort of NMOSD patients under acute relapse. Although treatment efficacy was not the primary outcome, results were considered encouraging since all patients had a clinical improvement and did not require escalation to plasma exchange.

The hypothesis was that, since this anti-vascular endothelial growth factor restores BBB integrity in brain tumors, it could also reduce relapse-associated CNS damage in NMOSD by reestablishing BBB physiological impermeability (Mealy, Shin et al., 2015).

A recent study found increased MD and decreased T1/T2-w, but no FA modifications, in the periventricular NAWM of AQP4+NMOSD patients (Cacciaguerra, Rocca et al., 2021a). Since the water content influences MD, T1-, and T2-relaxation times, the interpretation was that NMOSD patients might have a chronic accumulation of water secondary to astrocyte damage.

Using conventional multi-echo MR sequences, it is possible to calculate the T2-relaxation time (T2rt), which measures the constant of magnetization decay on the transverse plane. T2rt reflects the movement of water protons in the tissue and increases in the presence of higher water content (i.e., edema) (Bonnier, Roche et al., 2014). MRI is an important tool for the diagnosis and comprehension of the pathophysiology of NMOSD (Wingerchuk et al., 2015). However, it remains unclear whether brain imaging is clinically relevant for disease monitoring, since asymptomatic lesions occur in 3.4% of patients only (Lee et al., 2020), and radiological correlates of NMOSD pathophysiology are still missing.

In contrast, the serum GFAP, a biomarker of astrocytes damage, was recently demonstrated useful for the monitoring of inflammatory activity, relapse risk, and treatment effect in NMOSD patients enrolled in the NMO-mentum trial (Aktas et al., 2021).

Following these premises, we hypothesize that NMOSD patients could be characterized by a subclinical increase in brain water content. Also, with the limitations of a cross-sectional setting, we tried to assess whether the magnitude of this phenomenon correlates with disease activity. To test this hypothesis, we performed an indirect estimation of brain water content in NMOSD patients compared to HC by measuring the T2rt and assessed whether this measure differed in clinically active and stable patients.

Materials and methods

Standard protocol approvals, registrations, and patient consents. Ethical approval was received from the local ethical standards committee of each participating center (Protocol ID: “Common Dataset” at IRCCS San Raffaele Scientific Institute, Milan, and Project 175031 at University of Belgrade, Belgrade), and written informed consent was obtained from all participants at the time of data acquisition according to the declaration of Helsinki. Patients agreed to undergo a single experimental MRI scan and a neurological examination without any clinical purpose. For patients’ safety, the experimental protocol did not include any contrast-agent administration.

Subjects. This study included 77 AQP4+NMOSD patients (2015 International Panel Consensus Diagnostic criteria) (Wingerchuk et al., 2015) and 105 HC. Subjects were recruited in two European centers: Milan (93 participants: 34 NMOSD and 59 HC) and Belgrade (89 participants: 43 NMOSD and 46 HC) from April 2007 to January 2017. AQP4-IgG serostatus was tested with a cell-based assay (Wingerchuk et al., 2015). For all participants, exclusion criteria were alcohol or drug abuse, history of head trauma or psychiatric comorbidities, and contraindications to MRI.

Clinical evaluation. Within 48 hours from the MRI acquisition, all NMOSD patients underwent a clinical evaluation, including rating of the EDSS and collection of anamnestic data (i.e., disease duration, number and type of previous relapses, annualized relapse-rate, date of the last clinical relapse).

Since enrolled patients regularly referred to our centers for follow-up visits and treatments, we retrospectively collected the date of the first relapse occurring after the MRI scan acquisition by looking through patients' medical records. Acute-phase treatment administration (i.e., intravenous steroids, plasma exchange) was collected as well.

Subjects having a relapse within one month before or after the MRI acquisition were defined "active," while the remaining were considered "stable."

MRI acquisition. All MRI scans were acquired over a ten-year period (from April 2007 to January 2017).

Using a 3.0 T (Intera Philips Medical Systems, Milan) and a 1.5 T (Achieva Philips Medical System, Belgrade) scanner, the following brain sequences were collected from all subjects in a single session: (1) axial dual-echo turbo spin-echo (TSE) (Milan: repetition time [TR]/echo time [TE]=2599/16-80 ms, echo train length [ETL]=6, flip angle [FA]=90°, matrix=256x256, field of view [FOV]=240x240 mm², 44 3-mm-thick slices; Belgrade: TR/TE=3141/20-100 ms, ETL=6, FA=90°, matrix=256x256, FOV=240x240 mm², 44 3-mm-thick slices), and (2) axial 3D T1-weighted fast gradient-echo scans (Milan fast field echo (FFE): TR/TE=25/4.6 ms, FA=30°, matrix=256x256; FOV=230x230 mm², 220 0.8-mm-thick slices; Belgrade turbo field echo (TFE):

TR/TE=7.2/3.2 ms; inversion time [TI]=1000 ms; FA=8°, matrix=256x256, FOV=256x256 mm², 180 1-mm-thick slices).

Conventional MRI analysis. Brain lesions were segmented using a local thresholding segmentation technique (Jim 8.0 Xinapse System Ltd) on T2- and T1-weighted sequences, and corresponding lesion volumes were calculated. After T1-hypointense lesion refilling, head-size NBV, NWMV, NGMV and basal ganglia (thalamus, caudate nucleus, putamen, and pallidum) were segmented and measured with the FSL SIENAX software and FMRIB's Integrated Registration and Segmentation Tool (FIRST) pipeline (FMRIB, Oxford, UK) (Patenaude et al., 2011, Smith et al., 2002). For basal ganglia, the head-size normalized volumes refer to the bilateral volume of the nuclei. The GM and WM were also automatically segmented on 3D T1-weighted images with the FSL segmentation tool (Zhang et al., 2001).

Analysis of the T2rt. The T2rt was calculated from brain dual-echo turbo spin-echo images using Image Least-Square Fitter tool in Jim8 (Xinapse System Ltd) and assuming a monoexponential decay through the function:

$$S=S_0*\exp(-TE/T2rt)$$

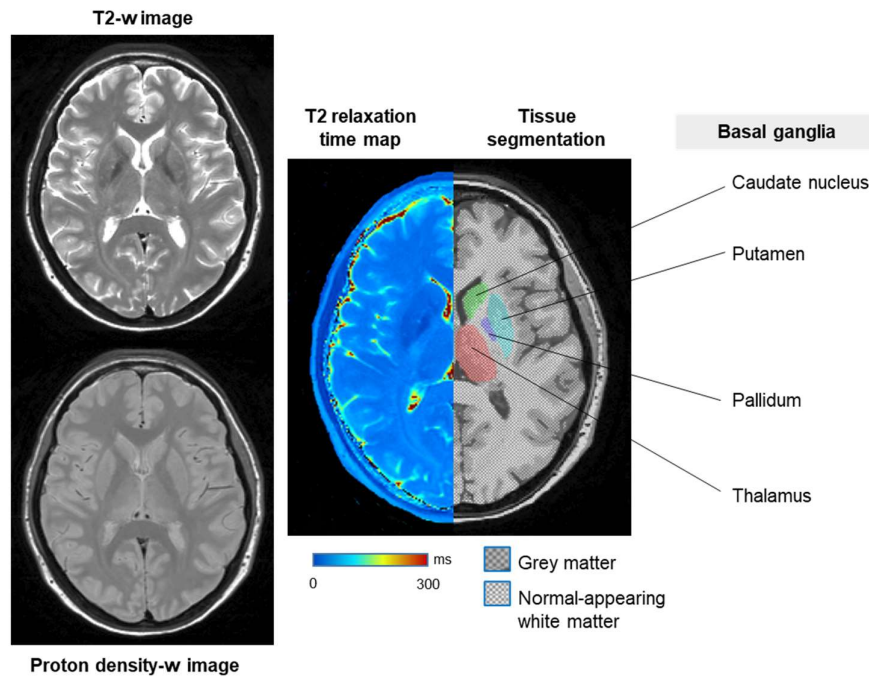
that relates the measured transverse magnetization S with the unknown of interest, the T2rt. S₀ is the second unknown of the problem, that depends on proton density, receive coil sensitivity and longitudinal relaxation.

Binary masks of the WM, GM and basal ganglia on 3D T1-weighted images were then registered on the T2rt maps using a linear rigid transformation. We considered the mean bilateral T2rt value in the thalamus, caudate nucleus, putamen, and pallidum for basal ganglia.

Focal T2-hyperintense lesions were excluded to retain only values corresponding to the normal-appearing tissue. **Figure 5.2.1** shows an example of T2rt map and tissue segmentation obtained from a HC.

Figure 5.2.1. T2-relaxation time map and tissue segmentation. Example of T2rt map and tissue segmentation in a healthy control. T2rt was obtained from proton-density and T2-weighted images, the color bar represents ms of T2rt. Modified from Cacciaguerra et

al., Journal of Neurology, Neurosurgery and Psychiatry 2022. Author's reuse as per Journal pre-approved permission (<https://www.bmj.com/company/products-services/rights-and-licensing/author-self-archiving-and-permissions/>).



Abbreviations: T2-w=T2-weighted; ms=millisecond.

Statistical analysis. Between-group comparisons of continuous demographic variables were performed with parametric or non-parametric tests according to normality assumption. We compared MRI volumes with age-, sex- and site-adjusted linear models. Categorical variables were compared using Pearson χ^2 or Fisher's exact test.

Although the T2rt is not heavily influenced by the scanner field strength (i.e., is similar at 1.5 and 3.0T) (Aboul-Enein, Krssak et al., 2010) and the sequence parameters are comparable, to mitigate possible inter-scanner differences due to B1 inhomogeneities (Majumdar, Orphanoudakis et al., 1986) and slice profile imperfections (Crawley & Henkelman, 1987), we computed T2rt z-scores in NMOSD patients. First, we calculated predicted residuals of T2rt by running age- and sex-adjusted linear models separately to

site of enrollment. Then, we obtained T2rt z-scores by subtracting the mean residual value of HCs in each center and subsequently dividing the results by the HC error terms (standard deviation in each center). We also reported mean (95% confidence interval) of T2rt estimated from age-, sex- and site-adjusted linear models to improve the interpretability of results. In patients, we estimated the mean z-scores of T2rt with one-sample t-tests.

The comparisons of T2rt between active and stable patients were assessed using linear models. To rule out the possible nuisance effect of steroids on water balance, models were adjusted according to steroid administration (dose of steroids). Between-group comparisons of patients having vs. those not having received steroid treatment, and bivariate Pearson's correlations between T2rt and steroid dose are reported as Supplementary material.

Given the small number of patients undergoing plasma-exchange (see below), the effect of this treatment was not included. Steroid-adjusted univariate binary logistic regressions were run to identify associations between the z-score of T2rt (in the GM, NAWM, and basal ganglia) and disease activity (active vs. stable patients). A stepwise binary logistic regression was run on clinical (EDSS, disease duration, annualized relapse rate, number of previous optic neuritis and number of previous myelitis) and MRI variables (T2 lesion volume, NBV, NGMV, NWMV, z-score of T2rt in the GM, NAWM and basal ganglia), to identify independent predictors of disease activity. The regression was then repeated by including steroid treatment into the model.

For stepwise variable selection we used a p value=0.10 for entry and =0.05 to remain in the multivariate model. Demographic and clinical variables (i.e., age, sex, and center) were not included into the final model as T2 relaxation-time z-scores values were obtained.

As exploratory analysis, we also compared T2rt z-scores in active patients relapsing before or after the MRI acquisition by running an independent samples median test. Details are provided as **Supplementary material**.

To improve readability, in the main text we will refer to “T2rt” instead of specifying “T2rt z-scores”.

Results

Demographic and clinical features. Motion artifacts, preventing an optimal brain structure segmentation, led to excluding nine participants (five NMOSD and four HC). Table 5.2.1 summarizes the main demographic and clinical features of NMOSD patients and HC.

Table 5.2.1. Demographic, clinical and MRI features of the study population. Data are reported according to the normality assumption.

	HC (n=101)	NMSOD (n=72)	p
Age (SD) [years]	42.6 (13)	43.9 (13)	0.52 ^a
Sex (F/M)	72/29	60/12	0.07 ^b
Disease duration (IQR) [years]	-	4.3 (1.4-10.2)	-
EDSS	-	4.0 (2.5-7.0)	-
# Myelitis (IQR)	-	2 (1-3)	-
# ON (IQR)	-	1 (0-3)	-
Presence of OCBs (%)	-	17 (27.9)	-
Highly effective treatment (%) ¹	-	20 (27.8%)	-
T2 LV (IQR) [ml]	0.11 (0.0-0.3)	0.25 (0.1-1.7)	0.18 ^c
NBV (95% CI) [ml]	1540 (1526-1553)	1490 (1474-1507)	<0.001 ^d
NGMV (95% CI) [ml]	753 (743-762)	715 (704-726)	<0.001 ^d
NWMV (95% CI) [ml]	784 (776-793)	773 (763-784)	0.12 ^d
N-Thalamus (95% CI) [ml]	20.9 (20.4-21.4)	19.9 (19.6-20.3)	0.006 ^d
N-Caudate (95% CI) [ml]	9.1 (8.8-9.5)	9.1 (8.9-9.3)	0.97 ^d
N-Putamen (95% CI) [ml]	12.8 (12.4-13.2)	12.3 (12.0-12.5)	0.02 ^d
N-Pallidum (95% CI) [ml]	4.5 (4.3-4.6)	4.5 (4.4-4.6)	0.74 ^d

¹Rituximab (n=17), tocilizumab (n=1), cyclophosphamide (n=2).

^aTwo-sample t-test; ^bPearson Chi-square test; ^cMann-Whitney U-test; ^dAge-, sex-, and site-adjusted general linear models.

Abbreviations: HC=healthy controls; NMOSD=neuromyelitis optica spectrum disorder; F/M=female to male ratio; SD=standard deviation; IQR=interquartile range; LV=lesion volume; NBV=normalized brain volume; NGMV=normalized grey matter volume; NWMV=normalized white matter volume; N-=normalized; CI=confidence interval.

NMOSD patients and HC were comparable in age (p=0.52) and sex distribution (p=0.07). For patients, the median (interquartile range [IQR]) EDSS and disease duration were 4.0

(2.5-7.0) and 4.3 (1.4-10.2) years, respectively. The median number of myelitis and optic neuritis were two (1-3) and one (0-3).

Conventional MRI analysis. **Table 5.2.1** reports the results of conventional MRI analysis. Compared to HC, NMOSD patients had significant atrophy in the NBV ($p<0.001$), NGMV ($p<0.001$), thalamus ($p=0.006$) and putamen ($p=0.02$).

Analysis of the T2rt.

NMOSD vs. HC. Compared to HC, NMOSD patients had increased T2rt in the NAWM ($p<0.0001$), GM ($p<0.0001$), thalamus ($p=0.001$), putamen ($p=0.001$) and caudate nuclei ($p=0.014$), whereas no significant between-group differences were found in the pallidum (**Table 5.2.2**).

Table 5.2.2. T2rt values of NMOSD patients and HC. T2rt values are reported as mean (95% confidence interval[ms]) and refer to age-, sex- and site-adjusted linear models. We also reported the mean estimated z-scores for the NMOSD group, obtained from age- and sex-adjusted linear models estimated in the HC cohort from each site. P values refer to the one-sample t-test for the nullity (i.e., HC expected value) of the mean estimated z-score.

	HC (n=101)	NMSOD (n=72)	z-score	p
Normal-appearing white matter	84.7 (83.9-85.6)	88.5 (87.5-89.5)	0.89 (0.65; 1.12)	<0.0001
Grey matter	97.9 (96.8-98.9)	102.4 (101.2-103.6)	0.90 (0.61; 1.18)	<0.0001
Thalamus	89.5 (88.2-90.9)	93.7 (92.3-95.3)	0.75 (0.49; 1.00)	0.001
Caudate nucleus	82.2 (81.3-83.0)	84.2 (83.2-85.2)	0.48 (0.23, 0.73)	0.014
Putamen	74.0 (73.3-74.7)	76.4 (75.6-77.2)	0.62 (0.39; 0.85)	0.001
Pallidum	66.6 (65.9-67.3)	66.8 (66.0-67.6)	0.06 (-0.17; 0.30)	0.93

Abbreviations: HC=healthy controls; NMOSD=neuromyelitis optica spectrum disorders.

Active vs. stable NMOSD. Twenty NMOSD patients (27.8%) were active. Relapses were myelitis (14/20, 70%), optic neuritis (5/20, 25%) or hemispheric (1/20, 5%). Fourteen/20 active patients (70%) had a recent relapse (i.e., within a month before the MRI), while six/20 patients (30%) had an incipient relapse (i.e., within a month after the MRI). As expected, none of the patient with incipient relapse received any acute-treatment at the time of the MRI acquisition, while patients with recent relapse were treated with intravenous steroids (10/14, 71.4%), and/or plasma-exchange (6/14, 42.8%). The analysis of the T2rt in patients having or not having received acute steroid treatment, and the estimated effect of steroids on the T2rt are available as **Supplementary material**.

Active and stable patients had similar demographic, clinical and conventional MRI features (**Table 5.2.3**).

Table 5.2.3. Demographic, clinical and MRI features of active and stable NMOSD patients. Data are reported as median (IQR) and p values refer to Mann-Whitney U-test, if not differently specified.

	Active (n=20)	Stable (n=52)	p
Age [years]	42.8 (31-56)	45.0 (32-55)	0.92
Sex (F/M)	17/3	43/9	0.56 ^a
Disease duration [years]	5.4 (1-11)	4.1 (2-10)	0.94
EDSS	6.0 (3.0-8.0)	4.0 (2.0-6.5)	0.12
# Myelitis	2 (1-5)	2 (1-3)	0.77
# ON	1 (0-3)	1 (0-2)	0.90
Presence of OCBs (%)	7/17 (41.2)	10/44 (22.7)	0.15 ^a
T2 LV [ml]	0.35 (0.1-7.1)	0.25 (0.1-1.4)	0.34
NBV (95% CI) [ml]	1461 (1431-1491)	1480 (1462-1499)	0.28 ^b
NGMV (95% CI) [ml]	717 (694-740)	725 (711-740)	0.53 ^b
NWMV (95% CI) [ml]	744 (724-763)	751 (739-764)	0.51 ^b
N- Thalamus (95% CI) [ml]	19.7 (19.0-20.4)	19.9 (19.4-20.3)	0.79 ^b
N-Caudate nucleus (95% CI) [ml]	8.8 (8.4-9.3)	9.2 (9.0-9.5)	0.11 ^b
N-Putamen (95% CI) [ml]	12.1 (11.6-12.6)	12.5 (12.1-12.8)	0.23 ^b
N-Pallidum (95% CI) [ml]	4.5 (4.3-4.8)	4.5 (4.3-4.7)	0.83 ^b

^aPearson Chi-square test; ^bAge-, sex-, and site-adjusted general linear models.

Abbreviations: F=female; M=male; EDSS=expanded disability status scale; ON=optic neuritis; OCBs=oligoclonal bands; LV=lesion volume; NBV=normalized brain volume;

NGMV=normalized grey matter volume; NWMV=normalized white matter volume; N=normalized.

T2rt in the NAWM and GM were significantly increased in active compared to stable patients (z-score 1.77 vs. 0.70, p=0.002; and z-score 1.69 vs. 0.57, p=0.010), while values were similar in the basal ganglia (**Table 5.2.4**).

Table 5.2.4. T2rt in active and stable NMOSD patients. Data are reported as mean (95% confidence interval) z-scores and refer to steroid-adjusted linear models.

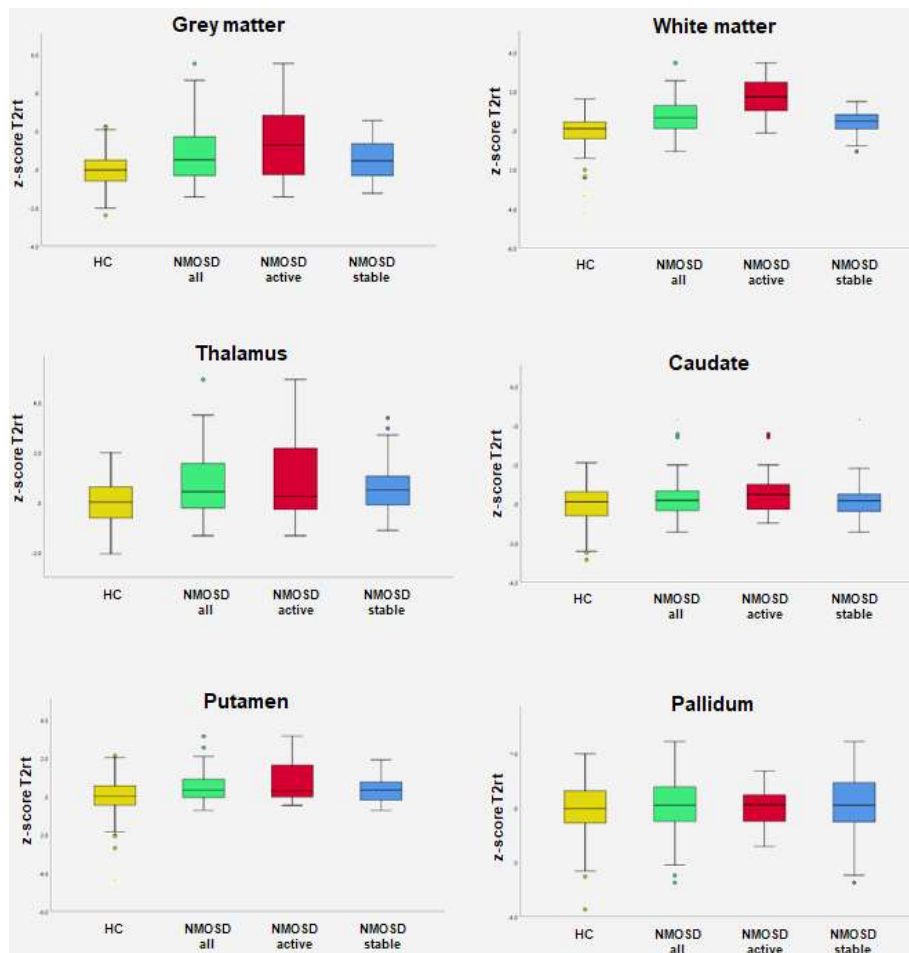
	Active (n=20)	Stable (n=52)	p
Normal-appearing white matter	1.77 (1.22; 2.33)	0.70 (0.41; 0.98)	0.002
Grey matter	1.69 (1.00; 2.38)	0.57 (0.24; 0.96)	0.010
Thalamus	1.18 (0.51; 1.85)	0.64 (0.24; 1.03)	0.18
Caudate nucleus	0.66 (0.05; 1.26)	0.46 (0.11; 0.81)	0.60
Putamen	1.03 (0.54; 1.52)	0.55 (0.27; 0.84)	0.12
Pallidum	-0.18 (-0.54; 0.50)	0.07 (-0.23; 0.37)	0.78

Abbreviations: HC=healthy controls; NMOSD=neuromyelitis optica spectrum disorders.

Barcharts of the steroid-adjusted estimated marginal means of T2rt in the NMOSD cohort (all patients), active NMOSD, and stable NMOSD are shown in **Figure 5.2.2**. Results in HC are also reported as reference.

Figure 5.2.2. Barcharts of T2rt in NMOSD and HC. Barcharts of the estimated marginal means of the T2rt z-score in NMOSD patients (all, active, and stable) and HC in steroid-adjusted linear models. Error bars represent 95% confidence intervals. Modified from Cacciaguerra et al., Journal of Neurology, Neurosurgery and Psychiatry 2022. Author's reuse as per Journal pre-approved permission

(<https://www.bmj.com/company/products-services/rights-and-licensing/author-self-archiving-and-permissions/>).



Abbreviations: NMO SD=neuromyelitis optica spectrum disorders; HC=healthy controls; T2rt=T2 relaxation time.

No significant differences were found between active patients with incipient and recent relapses, excepted for a higher T2rt in the GM of patients with incipient relapse (3.30 vs 0.32, $p=0.001$, see the Supplementary material for further details).

Associations between T2rt and disease activity. Significant univariate associations were found with the T2rt in the NAWM ($p=0.003$) and GM ($p=0.005$). A trend was observed in the thalamus ($p=0.05$, **Table 5.2.5**).

Table 5.2.5. Univariate logistic regressions between the T2rt (z-score) and disease activity in NMOSD patients. All models are adjusted according to steroid-treatment.

	Beta	Standard error	Wald Chi-Squared test	p
Normal-appearing white matter	1.86	0.62	9.08	0.003
Grey matter	1.17	0.42	7.93	0.005
Thalamus	0.53	0.27	4.01	0.05
Caudate nucleus	0.24	0.31	0.63	0.18
Putamen	0.42	0.35	1.44	0.23
Pallidum	-0.27	0.35	0.71	0.40

Stepwise binary logistic regression selected the NAWM T2rt (beta=2.06, standard error=0.58, Wald Chi-Squared Test=12.7, $p<0.001$) as independently associated with disease activity status (Nagelkerke R-squared=0.46). This was confirmed when steroid treatment was included into the model (beta=2.58, standard error=0.90, Wald Chi-Squared Test=8.27, $p=0.004$, Nagelkerke R-squared=0.83).

Discussion

This work tested the hypothesis that the pathogenetic mechanisms of NMOSD can alter BBB permeability, with a consequent increase of brain water content. Also, we hypothesized that the magnitude of this effect might be higher in chronological proximity to the disease flares. For these purposes, we indirectly evaluated brain water content using the T2rt, a quantitative metric easily obtainable from conventional MR sequences (i.e., dual-echo turbo spin-echo).

Despite similar demographic features with HC, NMOSD patients had a widespread increase of T2rt in the NAWM, GM and basal ganglia, except for the pallidum. T2rt of the NAWM and GM were higher in active than stable patients, the first resulting as the only significant independent predictor of disease activity net of other clinical and radiological variables.

Although the best strategy to measure water content is by estimating the quantitative proton density or exploiting the correlation with the longitudinal T1-relaxation time (Nakamura, Brown et al., 2014), the quantification of T2rt can also serve the aim in case of unchanged macromolecular concentration (i.e., myelin content), with the advantage of being derivable from a clinically feasible dual-echo sequence (Nakamura et al., 2014). The presence of occult brain damage is controversial in NMOSD patients. Most studies using diffusion-weighted imaging, magnetization transfer imaging or proton MR spectroscopy, documented no demyelination or selective alterations of the visual pathway or corticospinal tract (Solomon et al., 2021). This was also pathologically proven in the cortex of 19 NMOSD patients, where no evidence of cortical demyelination was detected (Popescu, Parisi et al., 2010). Therefore, if present, the amount of subclinical demyelination in NMOSD brain is likely limited, and the increase of T2rt is not primarily driven by myelin loss. This aligns with the results of two independent studies finding a diffuse increase of the mean brain water diffusivity in NMOSD patients (Cacciaguerra et al., 2021a, Liu et al., 2012b), and no concomitant reduction of the FA, which is a well-known measure of fiber integrity (Tu et al., 2016), but is also highly correlated with myelin content (Uddin et al., 2019). Variations (i.e., decrease) of T2rt have also been related to modifications of iron content (Bonnier et al., 2014). This could explain why the increase in T2rt did not affect the pallidum, which is the deep GM nucleus with the highest iron concentration (Darnai, Nagy et al., 2017).

When exploring clinical associations, T2rt of the NAWM and GM were higher in active than stable patients and associated with disease activity.

Both the WM and GM can be damaged by AQP4-autoimmunity, since the periependymal WM is considered a site with high AQP4-expression (Pittock, Weinschenker et al., 2006), and pathology data revealed an AQP4-dependent damage in the cortical GM (Saji et al., 2013). Experimental studies suggested that AQP4 expression in the WM is especially relevant for brain water balance, as it is involved in the development of post-stroke edema (Stokum, Mehta et al., 2015). Similarly, the spreading of vasogenic edema (i.e., due to increased BBB permeability, such as in cerebral neoplasms) occurs preferentially in the WM (Reulen, 1976). On the other side, the GM is characterized by higher vascular volume (Lierse & Horstmann, 1965) and by higher permeability of the BBB under physiological condition (Varatharaj, Liljeroth et al., 2019).

Astrocytes are the main component of the BBB and are injured by the pathophysiological mechanism of NMOSD also in non-lesioned tissue (Guo et al., 2021).

In-vivo, ongoing astrocytes damage in NMOSD patients can be detected by measuring GFAP in serum and CSF, where levels exceeded those of HC and other neurological disorders, including MS (Takano, Misu et al., 2010, Watanabe, Nakamura et al., 2019). Moreover, the longitudinal assessment of this biomarker in NMOSD patients revealed a time-varying behavior depending on disease activity, since GFAP levels progressively increased during the week preceding the acute attack and peaked at the time of relapse (Aktas et al., 2021).

Conventional MRI is a sensitive tool for detecting asymptomatic disease activity in MS (Sormani & Bruzzi, 2013), but not in NMOSD (Lee et al., 2020, Matthews et al., 2015). Quantitative MRI techniques contributed identifying microstructural abnormalities in the NAWM of MS patients before the appearance of a focal lesion (Filippi, Rocca et al., 1998, Rocca, Cercignani et al., 2000), encompassing a progressive focal decrease of magnetization transfer ratio (Filippi et al., 1998) and an increase of mean diffusivity (Rocca et al., 2000) over the weeks preceding a gadolinium-enhancing lesion formation. In contrast, microstructural indexes of axonal and myelin damage were not good candidates in NMOSD, since their longitudinal assessment was similar in patients and HC (Matthews et al., 2015).

As a consequence, acknowledging significant limitations, it is tempting to speculate that the T2rt could increase also in case of incipient relapse, mimicking GFAP dynamic.

Moreover, increased T2rt in the NAWM and GM was observed even in case of remote attacks, involving the spinal cord and the optic nerve.

Among the technical limitations, we must disclose that using only two echoes to estimate the T2rt implies a higher susceptibility to noise. In addition, we could not compensate for the imperfection of flip angles of refocusing pulses and of slice profiles in the multi-slice acquisition that are known to bias the estimate; however, in the case of mono-exponential decay, these issues have a minor impact than when using a multi-exponential fitting. Furthermore, the use of T2rt was aimed at separating two groups of patients based on a water content supposed to be uniformly and greatly increased within the tissue and not on a small, localized change of any microstructural tissue characteristic. The former is likely to be measured precisely enough with the proposed method.

Also, although T2 relaxometry is influenced by water content, it does not provide a direct measurement of BBB integrity, which could be better investigated with perfusion MR techniques. Permeability is usually investigated using dynamic contrast enhancement (DCE-MRI), but in this particular condition and considering the main question of the study, it would detect the strongest enlargements of the barrier, that allow gadolinium molecules to pass, such as in acute MS lesions. It would be more appropriate the application of the arterial spin labeling (ASL), that measures the influx of water from the capillary bed into the tissue as a measure of perfusion. In case of damage of BBB, it would also be influenced by barrier permeability. In this case, the issue would be the separation of the two effects, and one possibility would be relying on the use of multiple echo-time ASL (Ohene, Harrison et al., 2019).

Finally, our cohort of active NMOSD included patients having a recent relapse, who mostly underwent an acute treatment with steroids or plasma exchange. Although this was at least in part considered in the statistical analysis, we cannot exclude a nuisance effect of these therapies on water homeostasis and T2rt, with potentially different mechanisms. For instance, steroid administration reduces the amount of brain edema in the WM (Reulen, 1976), and exerts an indirect effect on astrocytes intracellular water content and swelling by acting on intracellular sodium (Hartmann, 1966, Reulen, 1976). Despite all these limitations, this work supports the application of quantitative MRI in NMOSD. The T2rt might be sensitive to the inflammatory activity in NMOSD, but the timing of its changes is yet to be determined.

Future longitudinal studies are needed to confirm these results and to explore correlations with markers of astrocytes damage (i.e., GFAP), to prove a dependency between the pathogenic mechanism of NMOSD and this MRI measure.

Supplementary material

Effect of acute steroid treatment on the T2 relaxation time in NMOSD patients.

In the cohort of “active” patients, 10/20 (50%) already underwent high-dose steroid treatment. Values of the T2rt were similar between treated and untreated patients (p values 0.07-0.88), although a trend towards higher values was observed in untreated patients, especially in the GM (**Supplementary Table 5.2.1**).

Supplementary Table 5.2.1. Between-group comparison of active patients having vs. not having received high-dose steroids. Data are presented as median (interquartile range) of T2rt z-scores, and p values refer to the Mann-Whitney U-test.

	Steroids - No (n=10)	Steroids – Yes (n=10)	p
Dose (g)	-	5.5 (4-8)	-
Normal-appearing white matter	1.73 (0.00-2.52)	1.35 (0.05; 1.76)	0.45
Grey matter	2.59 (-0.22; 3.71)	0.69 (-0.55; 1.48)	0.07
Thalamus	0.81 (-0.32; 3.26)	0.25 (-0.33; 1.76)	0.54
Caudate nucleus	0.13 (-0.46; 1.31)	0.53 (-0.15; 1.02)	0.60
Putamen	1.10 (-0.42; 1.98)	0.26 (-0.57; 1.96)	0.88
Pallidum	-0.07 (-1.24; 0.41)	0.16 (-0.34; 0.67)	0.41

Steroid dose was negatively correlated with the T2rt in the GM (**Supplementary Table 5.2.2** and **Supplementary Figure 5.2.1**).

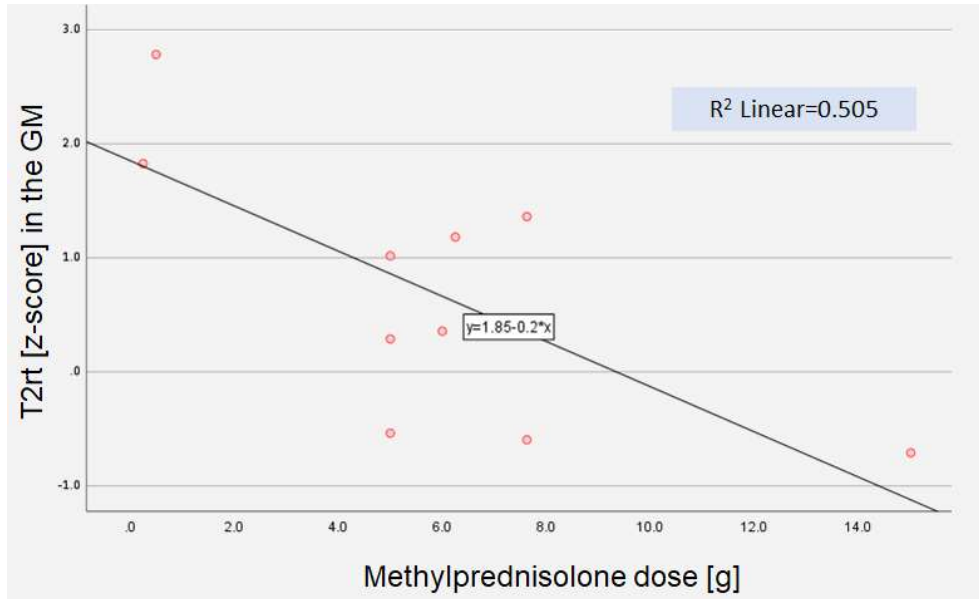
Supplementary Table 5.2.2. Bivariate Pearson’s correlations between T2rt z-scores and steroid dose in treated patients (n=10).

	NAWM	Grey matter	Thalamus	Caudate nucleus	Putamen	Pallidum
r values	-0.34	-0.71*	-0.20	-0.28	-0.28	-0.45
p values	0.33	0.021	0.57	0.43	0.44	0.19

Abbreviations: NAWM=normal-appearing white matter.

Supplementary Figure 5.2.1. Scatterplot of the bivariate correlation between the T2rt z-score in the grey matter and steroid dose in treated patients (n=10). Modified from

Cacciaguerra et al., Journal of Neurology Neurosurgery and Psychiatry 2022. Author's reuse as per Journal pre-approved permission (<https://www.bmj.com/company/products-services/rights-and-licensing/author-self-archiving-and-permissions/>).



Abbreviations: T2rt=T2 relaxation time; GM=grey matter.

Between-group comparison of NMOSD patients relapsing before or after the MRI acquisition.

NMOSD patients having a clinical relapse before or after the MRI acquisition had similar T2rt in all brain structures, except for the GM, where the T2rt was higher in patients with incipient rather than recent relapse. Details are reported in the **Supplementary Table 5.2.3**.

Supplementary Table 5.2.3. Between-group comparison of patients relapsing before and after the MRI acquisition. Data refer to the T2rt z-scores.

	Active patients		
	Relapse before MRI (n=14)	Relapse after MRI (n=6)	Independent samples median test

Normal-appearing white matter	1.03 (-0.03; 1.76)	2.18 (1.21; 2.52)	0.63
Grey matter	0.32 (-0.55; 1.48)	3.30 (2.73; 4.88)	0.001
Thalamus	-0.05 (-0.50; 1.76)	2.07 (-0.18; 3.86)	0.63
Caudate nucleus	0.32 (-0.26; 0.67)	1.00 (-0.73; 2.35)	0.63
Putamen	0.13 (-0.04; 1.62)	1.69 (0.49; 2.21)	0.46
Pallidum	0.12 (-0.34; 0.56)	-0.15 (-1.24; 0.60)	0.28

Abbreviations: MRI=magnetic resonance imaging.



5.3. Magnetic Resonance Imaging Evaluation of Perivascular Space Abnormalities in Neuromyelitis Optica

Cacciaguerra *et al.*, *Annals of Neurology* 2022

This chapter describes the work published in *Annals of Neurology* (PMID: 35596582, DOI: 10.1002/ana.26419), which is an open access article under the terms of the Creative Commons Attribution-NonCommercial-NoDerivs License, which permits use and distribution in any medium, provided the original work is properly cited, the use is non-commercial and no modifications or adaptations are made.

RESEARCH ARTICLE

Magnetic Resonance Imaging Evaluation of Perivascular Space Abnormalities in Neuromyelitis Optica

Laura Cacciaguerra, MD,^{1,2,3} Antonio Carotenuto, MD,¹ Elisabetta Pagani, MSc,¹
Damiano Mistri, MSc,¹ Marta Radaelli, MD, PhD,² Vittorio Martinelli, MD,²
Massimo Filippi, MD ^{1,2,4,5,3} and Maria A. Rocca, MD ^{1,2,3}

Objective: Astrocytes outline the perivascular space (PVS) and regulate fluid exchange through the aquaporin-4 water channel. As neuromyelitis optica is an autoimmune astrocytopathy targeting aquaporin-4, we hypothesized that it could be associated with PVS abnormalities.

Methods: A total of 34 patients, and 46 age- and sex-matched healthy controls from two independent cohorts (exploratory and validation dataset) underwent a standardized 3.0-T magnetic resonance imaging protocol including conventional and diffusion tensor imaging. Susceptibility-weighted imaging was also acquired in the exploratory dataset. We evaluated macroscopic and microstructural abnormalities of PVS in terms of enlargement and water diffusivity (DTI-ALPS index). In the exploration dataset, a susceptibility-weighted sequence was used to draw the regions of interest for the DTI-ALPS index calculation in areas having veins perpendicular to lateral ventricles. Between-group comparisons, correlations, and regression models were run to assess associations between PVS abnormalities, and clinical and magnetic resonance imaging variables.

Results: Patients had a higher frequency of severe PVS enlargement in the centrum semiovale (29.4% vs 8.7%), which correlated with brain atrophy, deep grey matter atrophy, and poorer cognitive performance (*r*-values range: -0.44, -0.36; *p* values: 0.01-0.046).

In both datasets, patients had reduced DTI-ALPS index compared with controls (*p* values 0.004-0.038). Lower DTI-ALPS index, deep grey matter volume, and cortical volume could discriminate between patients and controls ($R^2 = 0.62$), whereas lower DTI-ALPS index, higher number of myelitis, and higher T2-lesion volume were associated with worse disability ($R^2 = 0.55$).

Interpretation: Patients with neuromyelitis optica spectrum disorder are characterized by abnormal enlargement and impaired water diffusion along the PVS, whose clinical implications suggest a direct correlation with disease pathogenesis and severity.

ANN NEUROL 2022;92:173-183

Introduction

In the CNS astrocytes are at the interface between the vascular tree and the brain parenchyma. Their endfeet envelope the abluminal surface of blood vessels as part of the BBB, and delimit the perivascular space (Wuerfel, Haertle et al., 2008).

NMOSD is an autoimmune astrocytopathy caused by autoantibodies targeting the AQP4 water channel (Lucchinetti, Guo et al., 2014, Wingerchuk et al., 2015), a protein which guarantees brain water homeostasis through fluids influx and efflux (Saadoun & Papadopoulos, 2010).

Since AQP4 is highly expressed on the astrocytes' membrane abutting the perivascular space, this site is likely injured in NMOSD, as also suggested by pathology studies depicting a vasulocentric pattern of antibody deposition and complement activation (Roemer, Parisi et al., 2007).

Enlarged perivascular spaces, also referred as Virchow-Robin spaces, are visualized by using conventional T2- or T1-weighted MRI sequences, as fluid-filled structures paralleling perforating vessels in the basal ganglia and centrum semiovale (Wardlaw, Benveniste et al., 2020).

Since perivascular spaces have a three-dimensional tubular geometry, it was hypothesized that the diffusion of water molecules in this space is anisotropic (i.e., preferentially parallels the main vessel direction) (Sepehrband, Cabeen et al., 2019). This was confirmed with 7.0 T MRI using multi-shell diffusion imaging, an advanced technique able to separate the anisotropic movement of water molecules within white matter tracts, from the less constrained diffusion in the non-parenchymal compartment, including the perivascular space (Sepehrband et al., 2019).

However, the diffusion along perivascular spaces can also be measured at lower field strengths exploiting the DTI, in association with susceptibility-weighted imaging for vessel visualization. Accordingly, the diffusion along perivascular spaces (DTI-ALPS index) can be calculated as the ratio of (i) water diffusivity parallel to vessels and (ii) the set of diffusivities perpendicular to white matter tracts (Taoka, Masutani et al., 2017). Therefore, this technique can be considered as a stratagem to solve the problem in a known and simpler anatomical configuration when multishell diffusion weighted data are not available.

Both perivascular space enlargement and decreased water diffusion along the perivascular spaces have been found in a number of neurological conditions, including cerebrovascular diseases (Gouveia-Freitas & Bastos-Leite, 2021, Wardlaw et al., 2020), neurodegenerative (Chen, Chen et al., 2021, Taoka et al., 2017) and inflammatory disorders (Carotenuto, Cacciaguerra et al., 2021, Wardlaw et al., 2020).

Although the mechanism is not fully understood, these observations have raised the hypothesis that perivascular space abnormalities could be a common feature of several neurological diseases (Gouveia-Freitas & Bastos-Leite, 2021).

NMOSD autoimmunity involves an antigen highly expressed in the perivascular space (i.e., AQP4), and leads to damage of its anatomical borders (i.e., astrocytes) (Lucchinetti et al., 2014). Therefore, we explored macroscopic and microstructural perivascular space abnormalities in NMOSD by quantifying perivascular space enlargement and by measuring the DTI-ALPS index, respectively. Then, we assessed associations between these measures, clinical, and MRI outcomes.

Materials and methods

Ethics committee approval. Ethical approval was received from the local ethical standards committee and written informed consent was obtained from all participants at the time of data acquisition. Specifically, patients agreed to undergo a research MRI scan, a neurological and a neuropsychological examination without any clinical purpose.

Subjects. We computed DTI-ALPS index in two independent cohorts (exploratory-dataset and validation-dataset) of age- and sex-matched right-handed NMOSD patients and HC acquired using two different MRI scanners and standardized acquisition protocols.

The exploratory-dataset included 14 NMOSD patients and 16 HC acquired between February 2007 and December 2011; while the validation-dataset included 20 NMOSD patients and 30 HCs acquired between April 2019 and June 2021.

NMOSD diagnosis was achieved according to the 2015 International Panel Consensus Diagnostic criteria (Wingerchuk et al., 2015). For all participants, exclusion criteria were any contraindication to MRI, history of head trauma, psychiatric comorbidities, alcohol

or drug abuse. Patients were evaluated during the remission phase of the disease (i.e., at least four weeks apart from clinical relapse and intravenous steroids administration).

Clinical evaluation. Within 48 hours from the MRI acquisition, patients underwent a clinical examination with rating of the EDSS (Kurtzke, 1983) and collection of disease history (i.e., disease duration, number and type of previous relapses). Twenty-eight/34 patients (82.4%) also accepted to undergo a neuropsychological assessment including the BRB-N. Since former studies indicated that IPS/attention domain is the most frequently impaired in NMOSD (Cacciaguerra et al., 2021c, Meng, Xu et al., 2017), we analyzed the performance at the SDMT and PASAT-3 (i.e., at 3'') as cognitive screening. Results were converted in z-scores based on Italian normative data after subtracting the effects of relevant variables (i.e., education, gender) as described elsewhere (Amato et al., 2006). The presence of at least one abnormal test (i.e., corrected score < 1.5 standard deviations compared to the reference population) defined the presence of impairment in the domain (Sumowski, Benedict et al., 2018).

MRI acquisition. All participants underwent a single brain MRI session using two 3.0 T scanners (Ingenia CX and Intera Philips Medical Systems). To minimize possible inter-subject variability secondary to sleeping status, all participants were acquired between one p.m. and eight p.m., according to the following protocols:

1. Exploratory-dataset: (1) sagittal 3D fluid attenuated inversion recovery (FLAIR), field of view (FOV)=256×256 mm, pixel size=1×1 mm, 192 slices, 1 mm-thick, matrix=256×256, repetition time (TR)=4800 ms, echo time (TE)=270 ms, inversion time (TI)=1650 ms, echo train length (ETL)=167; (2) sagittal 3D T2-weighted sequence, FOV=256×256 mm², pixel size=1×1 mm, 192 slices, 1 mm-thick, matrix=256x256, TR=2500 ms, TE=330 ms, ETL=117; (3) sagittal 3D T1-weighted magnetization-prepared rapid gradient-echo, FOV=256×256, pixel size=1×1 mm, 204 slices, 1 mm-thick, matrix=256×256, TR=7 ms, TE=3.2 ms, TI=1000 ms, flip angle=8°; (4) axial pulsed-gradient spin echo single shot diffusion-weighted echo planar imaging; 3 shells at b-value=700/1000/2855 s/mm² along 6/30/60 non-collinear directions and 10 b=0 volumes were acquired, FOV=240×233 mm, pixel size=2.14×2.69 mm, 56 slices, 2.3 mm-thick, matrix=112×85, TR=5900 ms, TE=78 ms and three additional b=0 volumes

with reversed polarity of gradients for distortion correction; (5) 3D susceptibility weighted image (SWI), FOV=230x230, pixel size=0.60x0.60 mm, 135 slices, 2 mm-thick, matrix=384x382, TR=39 ms, TE=5.5:6:35.5 ms, flip angle=17; both magnitude and phase images for each echo were saved.

2. Validation-dataset: (1) axial dual-echo turbo spin-echo (TSE), FOV=240x240 mm², 44 slices, 3 mm-thick, matrix=256x256, pixel size=0.94x0.94 mm, TR=2599 ms, TE=16-80 ms, ETL=6, flip angle=90°; (2) axial 3D T1-weighted fast gradient-echo (fast field echo), FOV=230x230 mm, 220 slices, 0.8 mm-thick, matrix=256x256, pixel size=0.89x0.89 mm, TR=25 ms, TE=4.6 ms, flip angle=30°; (3) axial pulsed-gradient spin echo diffusion-weighted echo-planar imaging, single shell at b-value=900s/mm² along 35 non-collinear directions, FOV=240x231 mm, pixel size=2.14x2.62 mm, 56 slices, 2.3 mm-thick, matrix=112x88, SENSE=2, TR=8692 ms, TE=58 ms.

Conventional MRI analysis. In the exploratory-dataset, focal WM lesions were segmented using a fully automated approach based on two 3D patch-wise convolutional neural networks with 3D FLAIR and 3D T1-weighted MR images as inputs.(Valverde, Cabezas et al., 2017) In the validation-dataset, a local thresholding segmentation technique was adopted to segment T2-hyperintense lesions on T2-weighted sequences (Jim 8.0 Xinapse System Ltd). Corresponding lesion masks and volumes were then computed.

After lesion refilling (Battaglini et al., 2012), we measured head-size normalized NBV using SIENAx (Smith et al., 2002) and deep grey matter (NDGM) with FMRIB's Integrated Registration and Segmentation Tool (FIRST) software (Patenaude et al., 2011). NDGM volume was obtained by summing up volumes of bilateral thalamus, caudate, putamen, pallidum, amygdala and accumbens. We also obtained cortical volumes (normalized for head size) using Freesurfer 6.0. (<https://surfer.nmr.mgh.harvard.edu>).

Evaluation of enlarged perivascular spaces. According to the Potter's score, the presence of perivascular space enlargement was assessed visually on axial T2-weighted images in the basal ganglia and WM of the centrum semiovale using a 0 to 4 semi-quantitative scoring system. Briefly, a score equal to 0 corresponds to the absence of

enlarged perivascular spaces, 1 to 1-10, 2 to 11-30, 3 to 21-40, 4 to more than 40 enlarged perivascular spaces per region (Potter, Chappell et al., 2015).

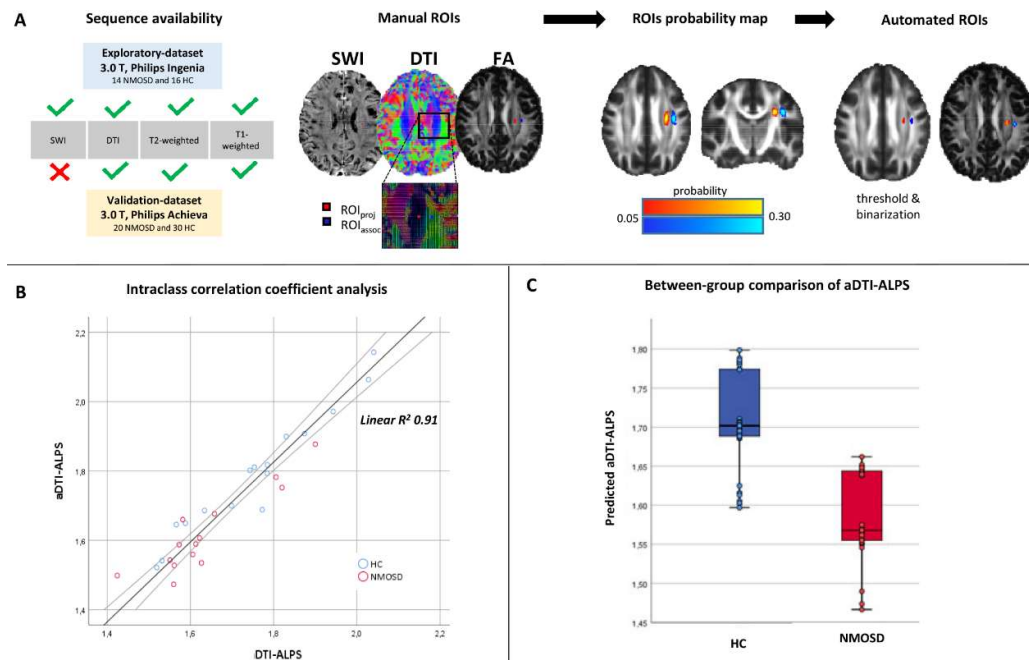
Pre-processing of diffusion-weighted imaging. Pre-processing of diffusion-weighted images included correction for off-resonance (exploratory-dataset) and eddy current-induced distortions- and movements using the Eddy tool in the FSL library (Andersson et al., 2017). The diffusion tensor was estimated by linear regression on diffusion-weighted imaging data at $b=700/1000$ s/mm² (exploratory-dataset) or $b=900$ s/mm² (validation-dataset). Then, maps of FA and MD were derived from the diffusion tensor (Basser, Mattiello et al., 1994b).

Processing of SWI. The multi-echo SWIs were used as inputs to obtain maps of local B0 field changes (where venous vessels are visible) using the software available at <https://github.com/sunhongfu/QSM>. First, phase images were unwrapped using the best path method to eliminate any discontinuity due to the limited range of phase values (Abdul-Rahman, Gdeisat et al., 2007). Then, the unwrapped phase images were fitted to the TE using a magnitude-weighted least-square regression. Small veins were made visible by removing the global spatial changes of the main magnetic field using regularization enabled sophisticated harmonic artifact reduction for phase data (Sun & Wilman, 2014).

Quantification of DTI-ALPS index. As SWI sequence was available in the exploratory-dataset only, we overcame the lack of SWI images in the validation dataset by setting an automated system of ROIs positioning on diffusion-weighted images based on the region of interests (ROIs) probability maps identified in this dataset, as summarized in **Figure 5.3.1**, panel A.

Figure 5.3.1. DTI-ALPS index measurement in the two datasets. Panel A: Susceptibility-weighted images (SWI) were available in the exploratory-dataset only. In this dataset, after choosing three contiguous slices with veins perpendicular to ventricles on SWI, we manually placed one ROI on projection fibers (ROI_{proj} in red) and a second ROI on associative fibers (ROI_{assoc}, in blue) on color-coded principal diffusion direction map. Then, we obtained ROIs probability maps in a standard space, which were 0.25 thresholded and binarized into two automated ROIs (aROI). Finally, aROI_{proj} and aROI_{assoc} were moved back to the single-subject diffusion imaging space. **Panel B:** An

absolute agreement intraclass correlation analysis was run to validate the use of aROIs on the validation-dataset. The graphic shows the scatterplot of the linear correlation between manual and automated DTI-ALPS index. **Panel C:** Scatterbox of age-, sex-, and scanner-adjusted predicted values of aDTI-ALPS index in HC (blue box) and NMOSD patients (red box). Reused with permission (license: 5431681039784).



Abbreviations: DTI=diffusion-tensor imaging; (a)DTI=(automated) diffusion along perivascular space; FA=fractional anisotropy; HC=healthy controls; NMOSD=neuromyelitis optica spectrum disorders; ROI_{assoc}=regions of interest in associative fibers; ROI_{proj}=regions of interest in projective fibers; SWI=susceptibility-weighted images.

Exploratory-dataset:

1. *Manual positioning of ROIs (single-subject space):* for each subject, we performed a rigid registration onto the SWI space of the FA map, 3D FLAIR images, T2 lesion masks and the principal diffusion direction field (first eigenvector) using the magnitude of the first echo of the SWI sequence as reference image through FLIRT (FMRIB's Linear Image Registration Tool)

(Alexander, Pierpaoli et al., 2001). Using SWI-derived venous images, we identified three contiguous axial slices having veins running perpendicular to lateral ventricles. Then, using the color-coded principal diffusion direction map, we manually drew two 3x3x3 mm cubic ROIs (Carotenuto et al., 2021, Taoka, Ito et al., 2021) over these slices in the left (i.e., dominant) hemisphere. The first ROI (ROI_{proj}) was positioned in projection fibers, the second ROI (ROI_{assoc}) was placed in the area of associative fibers (Carotenuto et al., 2021). We included only right-handed participants to ensure an adequate thickness of the left hemisphere's associative fibers, to minimize the possibility of losing the condition of perpendicularity between the fiber axis and the perivenous space, as previously described (Taoka et al., 2017). T2 lesion mask was used to avoid ROIs placement over visibly damaged tissue.

ROIs were then moved to the native diffusion imaging space by applying the inverse diffusion-to-SWI linear transformation. Diffusivity values along the x-, y, and z-axes were then extracted for each ROI and DTI-ALPS index was calculated as the ratio of diffusivities perpendicular to fiber bundles and parallel to veins (Dx_{proj} and Dx_{assoc}) over diffusivities perpendicular to fiber bundles and veins (Dy_{proj} and Dz_{assoc}) (Taoka et al., 2017). This was obtained by exploiting the frame of reference built with the diffusion tensor eigenvectors and the associated eigenvalues (Carotenuto et al., 2021). We also verified that secondary and tertiary eigenvectors were not affected by sorting bias (Ringstad, Vatnehol et al., 2017). DTI-ALPS index was calculated using the following formula:

$$DTI - ALPS\ index = \frac{mean(Dx\ proj, Dx\ assoc)}{mean(Dy\ proj, Dz\ assoc)}$$

For descriptive purposes, we also measured the mean FA and MD within the two ROIs.

2. *Automated positioning of ROIs (standard space)*: from the single-subject diffusion imaging space, all ROIs were then registered in a standard space by applying the nonlinear FA-to standard space transformation obtained from the second step of the Tract-Based Spatial Statistics (TBSS) (Smith, Jenkinson et al., 2006). Mean ROIs probability maps were produced separately for each ROI (ROI_{proj} and ROI_{assoc}). A threshold of 0.25 was applied to retain only voxels

occupied by the ROI_{proj} and ROI_{ass} in at least 25% of subjects, and the map obtained was binarized into two automated ROIs (aROI_{proj} and aROI_{assoc}). Finally, aROI_{proj} and aROI_{assoc} were registered to the subject diffusion imaging space by applying the inverse FA-to standard space transformation. Diffusivity values along the x-, y-, and z-axes were then extracted for each aROI, as previously described, to calculate the automated DTI-ALPS (aDTI-ALPS) index with the same formula. A linear correlation and the absolute agreement of the intraclass correlation coefficient (ICC) were used to assess the agreement between the DTI-ALPS index and the aDTI-ALPS index.

Validation-dataset:

Using TBSS, FA images of subjects were registered onto the customized FA atlas previously obtained with TBSS for the exploratory-dataset, where diffusivity values within the aROI_{proj} and aROI_{ass} were extracted. Then, aROI_{proj} and aROI_{ass} were transformed back to single-subject space. Before calculation of the aDTI-ALPS index, we visually checked that aROIs did not overlap with WM lesions.

Statistical analysis. After exploring the normal distribution of continuous variables with the Kolmogorov-Smirnov test, demographic, clinical and conventional MRI variables were compared between groups using two-sample t-test or Mann-Whitney U-test as appropriate. T2 WM LV were log-transformed to normalize their distribution. We grouped the perivascular space scores in three categories: mild or no enlargement (scores 0-1), moderate enlargement (score 2) and frequent or severe enlargement (scores 3-4). The distribution of categorical variables was assessed with Pearson χ^2 or Fisher's exact test.

Between-group comparisons of aDTI-ALPS index in exploratory- and validation-dataset were performed separately with non-parametric Mann-Whitney U-test. Age-, sex- and scanner-adjusted general linear models were used to explore between-group differences of the aDTI-ALPS index using the pooled data from the two datasets.

Correlations between the aDTI-ALPS index, perivascular space scores, demographic, clinical, neuropsychological, and MRI variables were assessed in the pooled cohort of NMOSD patients, using age-, sex-, and scanner-adjustment when appropriate.

Finally, stepwise age-, sex-, and scanner-adjusted multiple regression models were run to assess predictors of NMOSD diagnosis or impairment in information processing speed/attention domain (binary logistic regression) and clinical disability (linear logistic regression). In the stepwise variable selection, a p value=0.10 was retained for entry in the multivariate model. Dependent variables were: aDTI-ALPS index, perivascular space scores in the basal ganglia and centrum semiovale, logT2LV, NBV, NDGM, and the mean normalized cortical volume. All statistical analyses were performed with SPSS software (version 26.0; IBM, Armonk, NY). A p value < 0.05 was considered statistically significant.

Results

Demographic, clinical and conventional MRI measures. **Tables 5.3.1** and **5.3.2** summarize the main demographic, clinical and MRI features of the study subjects.

Table 5.3.1. Demographic and clinical variables in the two datasets. Data are presented as median (IQR). Unless otherwise specified, p values refer to non parametric Mann-Whitney U-test (quantitative variables) or Fisher’s exact test (qualitative variables).

	Exploratory-dataset			Validation-dataset			NMOSD *	HC *
	NMOSD (n=14)	HC (n=16)	p	NMOSD (n=20)	HC (n=30)	p	p	p
Demographic and clinical features								
Mean age (SD) [years]^a	48.5 (10.2)	48.4 (10.9)	0.98	46.9 (14.2)	44.1 (13.6)	0.90	0.73	0.29
F/M	14/0	13/3	0.23	17/3	22/8	0.49	0.25	0.72
Disease Duration	4.5 (1; 10)	-	-	8.2 (3;17)	-	-	0.19	-
EDSS	3.5 (1.5; 6.5)	-	-	4.0 (1.75; 6.75)	-	-	0.69	-
n Myelitis	2.0 (0.75; 3.5)	-	-	2.0 (1.0; 4.5)	-	-	0.69	-

n Optic neuritis	0.5 (0; 5.5)	-	-	2.0 (0.25; 4.0)	-	-	0.48	-
Autoimmune connective tissue disorders (%)	2 (14%)	-	-	0 (0%)	-	-	0.16	-
Anti-phospholipids antibodies (%)	1 (7%)	-	-	1 (5%)	-	-		-
Impairment in IPS/attention (%)	2 (18%) ¹	-	-	10 (59%) ²	-	-	0.05	-
SDMT	-0.48 (-1.0; 0.7)	-	-	-1.12 (-2.5; -0.8)	-	-	0.049	-
PASAT-3	-0.76 (-1.1; 0.3)	-	-	-1.42 (-2.4; 0.0)	-	-	0.11	-
Treatment (%)^b	14 (100%)	-	-	14 (70%)	-	-	0.03	-
Immunosuppressants (%)	3 (21%)	-	-	6 (30%)	-	-	0.70	-
Oral steroids (%)	0 (0%)	-	-	3 (15%)	-	-	0.25	-
Monoclonal antibodies (%)^b	11 (79%)	-	-	7 (35%)	-	-	0.01	

^aTwo-sample t-test; ^bPearson χ^2 . *Exploratory vs. validation-dataset.

¹n=11; ²n=17.

Abbreviations: HC=healthy controls; EDSS=expanded disability status scale; F/M=female/male ratio; NMOSD=neuromyelitis optica spectrum disorders; SD=standard deviation; IPS=information processing speed; SDMT= symbol digit modalities test z-score; PASAT-3= Paced Auditory Serial Addition Test 3” z-score.

Table 5.3.2. Between-group comparison of MRI variables and Virchow-Robin space enlargement score distribution. Data are presented as median (IQR) and p values refer to non parametric Mann-Whitney U-test, unless otherwise specified.

	Exploratory-dataset			Validation-dataset		
	NMOSD (n=14)	HC (n=16)	p	NMOSD (n=20)	HC (n=30)	p
Conventional MRI variables [ml]						
T2 LV	7.1 (5.9-7.8)	-	-	5.9 (5.1-7.1)	-	-
NBV	1541 (1527-1591)	1565 (1555-1583)	0.32	1545 (1509-1574)	1578 (1531- 1635)	0.08
NDGMV	56 (52-58)	57 (56-59)	0.10	49 (47-51)	53 (48-55)	0.003
N-Cortical volume	566 (330-566)	590 (475-750)	0.019	404 (332-498)	524 (399-633)	0.023
Perivascular space enlargement						
		NMOSD (all, n=34)	HC (all, n=46)	p		
Basal ganglia		2 (1-2)	1 (1-2)	0.17		
n (%) ^a	Mild ¹	16 (47.1)	26 (56.5)	0.26		
	Moderate ²	13 (38.2)	18 (39.1)			
	Severe ³	5 (14.7)	2 (4.3)			
Centrum semiovale		1 (1-3)	1 (0-2)	0.034		
n (%) ^a	Mild ¹	19 (55.9)	29 (63.0)	0.04		
	Moderate ²	5 (14.7)	13 (28.3)			
	Severe ³	10 (29.4)	4 (8.7)			

^aP values refer to Fisher's exact test.

¹PVS score: 0-1; ²PVS score=2; ³PVS score=3-4.

Abbreviations: HC=healthy controls; N-=normalized; NBV=normalized brain volume; NDGMV=normalized deep grey matter volume; NMOSD=neuromyelitis optica spectrum disorders; PVS=perivascular spaces; T2 LV= natural logarithm of T2 lesion volume.

NMOSD patients of the two datasets did not differ in terms of disease duration, EDSS, number of previous optic neuritis, and number of previous myelitis (p values range: 0.19-0.69). All NMOSD patients in the exploratory-dataset and 70% patients in the validation-dataset were under chronic immunosuppressive treatment at the time of the MRI acquisition. This included non-biologic immunosuppressants (i.e., azathioprine, n=7, micophenolate mophetil, n=1, cyclophosphamid, n=1), oral steroids (n=3, always administered in add-on), and monoclonal antibodies (rituximab, n=16, tocilizumab, n=2). In line with the different historical moment, the frequency of monoclonal antibody administration was higher in the exploratory-dataset.

Autoimmune connective tissue disorders were detected in two patients (6%), and included one case of Sjogren Syndrome and one undifferentiated connectivitis; anti-phospholipid antibodies were positive in two patients (6%).

The between-group comparison of NMOSD patients and HCs revealed significant cortical atrophy in both datasets (p values range: 0.019-0.023), whereas we detected a significant deep GM atrophy only in the validation-dataset (p=0.003).

Perivascular space scoring. The scoring of MRI-visible perivascular spaces was similar between NMOSD and HCs in the basal ganglia (p values range: 0.17-0.26). In the centrum semiovale, NMOSD patients had higher frequency of severe perivascular space enlargement compared to HCs (29.4 vs. 8.7%, p=0.040). Details are provided in **Table 5.3.2.**

DTI-ALPS index. The between-group comparison of aDTI-ALPS index is reported in **Table 5.3.3.**

Table 5.3.3. Between-group comparison of aDTI-ALPS index. Data are presented as median (IQR) and p values refer to non parametric Mann-Whitney U-test, unless otherwise specified.

	Exploratory-dataset			Validation-dataset		
	NMOSD (n=14)	HC (n=16)	p	NMOSD (n=20)	HC (n=30)	p
aDTI-ALPS index	1.59 (1.53-1.69)	1.79 (1.66-1.90)	0.004	1.57 (1.48-1.64)	1.63 (1.54-1.79)	0.038
Mean FA _{ROI}	0.49 (0.48-0.52)	0.51 (0.65-0.68)	0.61	0.50 (0.48-0.53)	0.50 (0.49-0.52)	0.94
Mean MD _{ROI} ¹	0.68 (0.66-0.69)	0.66 (0.65-0.68)	0.22	0.70 (0.69-0.72)	0.71 (0.70-0.73)	0.47
Pooled analysis ^a						
	NMOSD (all, n=34)		HC (all, n=46)	p		
aDTI-ALPS index	1.58 (1.53-1.63)		1.71 (1.67-1.76)	<0.001		
Mean FA _{ROI}	0.50 (0.49-0.51)		0.51 (0.50-0.51)	0.45		
Mean MD _{ROI} ¹	0.70 (0.69-0.71)		0.70 (0.69-0.70)	0.64		

^aAge-, sex-, and scanner-adjusted general linear models; estimated mean (95% confidence interval).

¹MD values are multiplied by 1000.

Abbreviations: aDTI-ALPS=automated diffusion along perivascular spaces index; FA_{ROI}=mean fractional anisotropy within the two ROIs (ROI_{proj} and ROI_{assoc}); HC=healthy controls; MD_{ROI}=mean mean diffusivity within the two ROIs (ROI_{proj} and ROI_{assoc}); NMOSD=neuromyelitis optica spectrum disorders.

1. Manual vs. aDTI-ALPS index (exploratory-dataset). Manual DTI-ALPS and aDTI-ALPS index showed an ICC of 0.97 (95% confidence interval: 0.94-0.99, $p < 0.0001$, linear $R^2 = 0.91$; **Figure 5.3.1**, panel B).
2. Between-group comparisons of aDTI-ALPS index (exploratory-dataset). NMOSD patients had a significant reduction of the aDTI-ALPS index compared to HCs ($p = 0.004$), while no differences were detected for FA and MD values (p values range: 0.22-0.61).
3. Between-group comparisons of aDTI-ALPS index (validation-dataset). Compared to HCs, NMOSD patients showed a significant reduction of aDTI-ALPS ($p = 0.038$), with similar FA and MD values (p values range: 0.47-0.94).

Between-group comparison of aDTI-ALPS index (pooled analysis). The pooled analysis confirmed the reduction of aDTI-ALPS in NMOSD patients ($p < 0.001$) (**Figure 5.3.1**, panel C).

Analysis of correlations. In NMOSD patients, lower aDTI-ALPS correlated with higher EDSS ($r = -0.46$, $p = 0.009$) and higher MD within the ROIs ($r = -0.48$, $p = 0.006$). No further significant correlations were observed between aDTI-ALPS index and the other clinical and MRI variables, including disease duration.

Perivascular space scores in the basal ganglia and centrum semiovale were highly correlated ($r = 0.70$, $p < 0.0001$). Higher perivascular space score in the basal ganglia correlated with lower NDGM volume ($r = -0.44$, $p = 0.013$), while higher perivascular space score in the centrum semiovale correlated with lower NBV ($r = -0.38$, $p = 0.036$), NDGM volume ($r = -0.36$, $p = 0.046$), and z-scores of PASAT-3 ($r = -0.42$, $p = 0.03$).

No correlations were found between aDTI-ALPS index and perivascular space scores.

Regression models. The results of age-, sex-, and scanner-adjusted logistic and linear regression models are shown in **Table 5.3.4**.

Independent predictors of NMOSD diagnosis were lower aDTI-ALPS index, NDGM volume, and normalized cortical volume (adjusted $R^2 = 0.62$).

Higher EDSS was associated with a higher number of myelitis, lower aDTI-ALPS index, and higher T2 LV (adjusted $R^2 = 0.55$).

No independent predictors of impairment in the information processing speed/attention domain were detected.

Table 5.3.4. Regression models, p values refer to age-, sex-, and scanner-adjusted binomial logistic regression (NMOSD diagnosis) or linear regression models (EDSS). Only statistically significant independent variables are reported.

Dependent variable	Significant IVs	Beta	Wald Chi square	p	Nagelkerke R²
NMOSD Diagnosis	aDTI-ALPS index	-10.16	9.75	0.002	0.62
	NDGMV	-3.78*10 ⁻³	10.04	<0.001	
	N-cortical volume	-1.35*10 ⁻¹¹	12.18	<0.001	
Dependent variable	Significant IVs	Standardized beta	p	Adjusted R²	
EDSS	Number of myelitis	0.47	0.003	0.55	
	aDTI-ALPS index	-0.33	0.033		
	logT2LV	0.38	0.035		

Abbreviations: aDTI-ALPS= automated diffusion along perivascular spaces index; EDSS=expanded disability status scale; logT2LV= natural logarithm of T2 lesion volume; IVs=independent variables; NDGMV=normalized deep grey matter volume; N-cortical=normalized cortical; NMOSD=neuromyelitis optica spectrum disorders.

Discussion

In this work we evaluated perivascular space abnormalities in patients with NMOSD, since disease pathogenesis involves the AQP4 water channel (i.e., located in the perivascular space) and leads to damage of the astrocytes (i.e., perivascular space boundaries).

For this purpose, we rated perivascular space enlargement with a well-established semiquantitative score (the Potter's score, the higher, the worse) (Potter et al., 2015) and measured water diffusion along perivascular spaces with the DTI-ALPS index in two independent cohorts of NMOSD patients and HCs.

Perivascular space enlargement in the centrum semiovale was more severe in NMOSD: about 30% of patients compared to less than 10% of age- and sex-matched HC showed more than 20 MRI-visible Virchow-Robin spaces. Although many conditions have been associated with perivascular space enlargement in the basal ganglia (i.e., aging, cardiovascular risk factors, and dementia) (Jessen, Munk et al., 2015), perivascular space enlargement in the centrum semiovale is less associated with aging and is rarely seen in neurodegenerative or cerebrovascular disorders.

In contrast, prior investigations found an association between perivascular space enlargement in the centrum semiovale and inflammatory diseases, such as systemic lupus erythematosus (Wiseman, Bastin et al., 2016), multiple sclerosis (Troili, Cipollini et al., 2020), and four aggressive cases of pediatric neuromyelitis optica (Zhang, Zhou et al., 2021), suggesting that perivascular spaces might represent a route to CNS infiltration and circulation by leukocytes, therefore increasing in size during inflammation (Wuerfel et al., 2008).

When we considered microstructural water movement along perivascular spaces, we found a reduced aDTI-ALPS index in both datasets of NMOSD patients.

To note, since subjects in the validation-dataset were acquired almost ten years before those in the exploratory-dataset, we first compensated for the lack of the SWI sequence in the first group by setting up an automated system of ROIs positioning based on the manual ROIs probability map in the exploratory-dataset. The obtained aDTI-ALPS index showed an almost perfect correspondence with the manual DTI-ALPS index (ICC=0.97), thus allowing its use in the validation-dataset.

Then, we took advantage of having two separate datasets to carry out two independent analyses of the aDTI-ALP index (i.e., exploratory analysis and validation analysis), which was consistently reduced in NMOSD patients compared to HC.

When we explored the clinical correlates, lower aDTI-ALPS index, together with deep GM and cortical atrophy, were independently associated with NMOSD diagnosis, in line with prior studies showing GM atrophy (Hyun, Park et al., 2017, Tian, Xiu et al., 2020) and a peculiar pattern of cortical AQP4 neuronal loss and nonlytic reaction of AQP4-negative astrocytes in NMOSD (Saji et al., 2013).

However, no correlations between aDTI-ALPS index and Potter's score or MRI measures were found. In contrast, higher perivascular space enlargement correlated with brain and deep GM atrophy.

Beyond the technical limitations of the aDTI-ALPS index, changes in microstructural diffusivity might be more sensitive to early perivascular space abnormalities associated with NMOSD, while macroscopic evidence of perivascular space enlargement could suggest an overt process associated with subsequent mechanisms of neurodegeneration, as also supported by the correlation between higher Potter's score and poorer cognitive performance at PASAT-3.

Recent lines of research indicate that perivascular spaces might be involved in fluid and waste drainage as a part of a clearance system called "glymphatic". According to this hypothesis, brain clearance is promoted by the convective influx of the CSF fluid, which enters in the brain parenchyma along the periarteriolar space, reaches the interstitium through an astrocytes-dependent process, and is finally collected back in the perivenous space to drain out in the meningeal lymphatic vessels (Iliff, Wang et al., 2012, Jessen et al., 2015). In this system, the AQP4 water channel is believed the leading promoter of CSF fluid flux through the glymphatic pathway (Iliff & Nedergaard, 2013), as suggested by the 65% reduction of CSF fluid flow through the parenchyma in experimental models lacking AQP4 (Jessen et al., 2015).

Since the DTI-ALPS index was proposed as a non-invasive proxy for glymphatic functioning (Taoka et al., 2017), and considering the central role of AQP4, it is tempting to speculate that the perivascular space abnormalities detected in NMOSD might be due to impaired glymphatic functioning.

Indeed, reduced DTI-ALPS index was detected in different neurological disorders such as Alzheimer's disease (Taoka et al., 2017), Parkinson's disease (Chen et al., 2021), idiopathic normal pressure hydrocephalus (Yokota, Vijayasarathi et al., 2019), and, more recently, multiple sclerosis (Carotenuto et al., 2021).

The accumulation of protein aggregates and a reduced density of AQP4 water channels (Hasan-Olive, Enger et al., 2019) have been proposed as mechanisms of "glymphatic impairment" in neurodegenerative conditions, since the former would prevent the normal perivascular outflow, while the latter would impair fluids drainage in the interstitium.

So far, reduced glymphatic functioning in neuroinflammatory conditions was detected only in MS using DTI-ALPS index or PET imaging (Carotenuto et al., 2021, Schubert, Veronese et al., 2019). In this disease, both ongoing inflammation and neurodegeneration might contribute to this finding, since reduced glymphatic functioning correlated with white (Carotenuto et al., 2021, Schubert et al., 2019) and GM lesion volume (Carotenuto et al., 2021), but also greater abnormalities were observed in patients with progressive disease course and worse cortical and deep GM atrophy (Carotenuto et al., 2021).

Similarly to NMOSD, loss of astrocytes endfeet (Prineas & Lee, 2019) and astrocyte-oligodendrocyte connexins (Masaki, Suzuki et al., 2013) have been observed in acute demyelinating lesions in MS. However, in contrast with NMOSD, where AQP4 immunoreactivity is lost at any stage of demyelination, AQP4 loss in MS is observed in inactive lesions, while its expression is increased at the border of active lesions, and in remyelinating ones (Roemer et al., 2007).

In MS, DTI-ALPS index reduction correlated with EDSS, disease duration and measures of brain atrophy (Carotenuto et al., 2021). This was partially in contrast with our findings in NMOSD, where this index was associated with clinical disability, but unrelated to disease duration nor brain atrophy.

This evidence might support an early impairment of glymphatic functioning in NMOSD, possibly associated with the disease pathophysiology. In fact, the magnitude of the pathogenic mechanism is likely to influence the severity of the clinical manifestations, regardless disease duration.

In contrast, the reduction of glymphatic functioning in MS could be secondary to inflammatory damage (i.e., leukocytes infiltrates and astrocytes damage in active demyelinating lesions) and might fuel a vicious circle by prolonging the contact between brain tissue and detrimental factors (i.e., CSF, inflammatory cytokines, and reactive oxygen species), therefore triggering subsequent parenchymal damage and neurodegeneration.

However, the existence and functioning of the glymphatic system is still controversial, and its possible biological correlate deserves to be further investigated.

In NMOSD, another possibility is that the damage at perivascular site, together with hyalinization around vessels (Roemer et al., 2007), and gap junction enlargement (Richard, Ruiz et al., 2020) might be responsible for the reduction of DTI-ALPS index

by altering perivascular space anatomy. Although we cannot exclude this possibility, we believe that this effect should be at least tempered on our data, since this index was not measured at small-caliber vessels level (i.e., the capillary bed) and the visual check of aROI positioning avoided its measurement in correspondence of visible vascular or inflammatory focal abnormalities.

Moving to limitations, the rarity of the disease and the need of advanced sequences limited our sample size. However, the concordant results obtained in two different datasets encourage the future application of this method in a multicentric setting.

Second, this study has a cross-sectional design: if the perivascular abnormalities are secondary to the antibody-dependent pathogenetic mechanism of the disease, a longitudinal setting would better underpin changes associated with disease activity.

Third, there are intrinsic limitations of the technique itself. Since the DTI-ALPS index is based on only two, small-sized, ROIs in the left hemispheric WM, we cannot exclude the existence of a sampling bias.

Finally, in patients with NMOSD, concomitant vascular or autoimmune comorbidities, including connective tissue disorders and anti-phospholipids syndrome might further contribute to the perivascular damage through an AQP4- and astrocytes-independent mechanism.

However, to the best of our knowledge, this is the first work systematically evaluating macroscopic and microstructural perivascular space abnormalities in NMOSD. By depicting an association between reduced water diffusion along the perivascular spaces and both the presence of the disease and the severity of clinical disability, it also suggested a potential role of aDTI-ALPS index in the identification of NMOSD patients and in their monitoring. Future studies are warranted to better clarify the pathophysiological correlates of this finding and its clinical value.

5.4. Spatial association between gene expression and brain damage in Neuromyelitis Optica Spectrum Disorders

Cacciaguerra et al., unpublished data.

Abstract

Objectives. Antibodies in autoimmune disorders of the central nervous system (CNS) target antigens with different expression across CNS regions. A former study suggested that typical brain lesions in aquaporin-4 positive Neuromyelitis Optica Spectrum Disorders (AQP4+NMOSD) occur at areas with high AQP4 expression. However, this represents a partial view of both brain damage and NMOSD pathogenesis, since the former also includes atrophy and microstructural abnormalities, and the latter involves other elements of the immune system such as complement and granulocytes. In this study we sought to investigate the spatial association between brain damage and gene expression in NMOSD.

Materials and methods. 3.0 and 1.5 T brain magnetic resonance imaging (MRI) scans were acquired from 80 AQP4+NMOSD and 94 controls at two European centers. In patients, brain damage was assessed through (i) T2-hyperintense lesion probability map, (ii) white (WM) and grey matter (GM) atrophy at voxel-based morphometry on 3D T1-weighted sequences, (iii) WM microstructural abnormalities at tract-based spatial statistics on diffusion-tensor imaging. The spatial association between imaging maps and gene expression was obtained with the MENGA platform, according to the Allen Human Brain Atlas, using a list of 266 candidates genes. We performed a functional-enrichment analysis to investigate the overrepresented biological processes involving the genes significantly associated with the different types of brain damage.

Results. T2-hyperintense lesions were mainly located in the periventricular WM; GM atrophy was observed in the visual, prefrontal cortex, and insula, WM atrophy selectively involved the optic tracts; patients also had a widespread increase of WM mean diffusivity and no fractional anisotropy abnormalities. Among significant genes, the expression of AQP4 and C5 associated with all types of brain damage, IL6 family signal transducer associated with brain atrophy only.

Activation of C3/C5 and the regulation and uptake of insulin-like growth factor were associated with all types of damage. A number of pathways, sometimes not specific for NMOSD pathogenesis, emerged for brain atrophy.

Conclusions. A joint application of MRI quantitative measures and available gene expression atlases may pave the way to a novel type of imaging analysis, able to underpin ongoing pathophysiological processes in antibody-mediated autoimmune disorders.

Introduction

Antibody-associated autoimmune conditions affecting the CNS can target surface or intracellular antigens. While intracellular autoimmunity usually represents the epiphenomenon of cytotoxic CD8⁺ T cell activation (e.g., in case of paraneoplastic autoimmune syndromes), antibodies binding membrane proteins likely embody the pathogenetic element of pure autoimmune diseases with specific clinical manifestations (Balint, Vincent et al., 2018, McKeon & Pittock, 2011). This is the case of AQP4+NMOSD, an antibody-mediated autoimmune disease targeting the AQP4 water channel, which is particularly expressed on astrocytes endfeet (Lennon, Kryzer et al., 2005, Wingerchuk et al., 2015).

Pre-clinical studies demonstrated that AQP4 expression in tissues defines the susceptibility to damage of different CNS regions in AQP4+NMOSD, since the expression of the AQP4 messenger RNA and proteins are significantly higher in the optic nerve and spinal cord (Matiello, Schaefer-Klein et al., 2013). Similarly, MRI demonstrated that brain lesions in patients with NMOSD and are typically located at areas with high AQP4 expression, such as the periependymal lying and the area postrema (Pittock et al., 2006).

However, this might only partially underpin the variety of AQP4+NMOSD brain damage and pathogenesis. In fact, quantitative imaging also documented brain atrophy, especially in the GM (Pichiecchio et al., 2012), and microstructural abnormalities of the NAWM, mainly in terms of increased MD (Cacciaguerra et al., 2021a, Liu et al., 2012b). Likewise, it is already established that the binding between the antibody and AQP4 elicits the activation of the complement cascade, with the assembly of the final complex, consequent astrocytes damage, local recruitment of granulocytes (especially eosinophils and neutrophils) and secondary demyelination and damage of the standby tissue (Lucchinetti et al., 2002).

Recent efforts allowed the characterization of transcriptomic profiles of the human brain, leading to the definition of atlases enclosing both quantitative genes expression and their spatial location, such as the Allen Human Brain Atlas (AHBA) (Hawrylycz, Lein et al., 2012). This information can be translated to the standard reference space for MRI, the Montreal National Institute (MNI), through novel computational tools such as the MENGA platform (Rizzo, Veronese et al., 2016).

In this study we tried to establish whether the joint application of human brain gene expression atlases and quantitative MRI can provide an explanation to damage distribution in NMOSD by underpinning the link with key elements of disease pathogenesis.

We investigated the spatial association between brain damage and gene expression in NMOSD through a multimodal quantitative assessment of brain damage, including lesion distribution, WM and GM atrophy, and WM microstructural abnormalities.

In the interpretation of results, we specifically focused on immune-system elements targeted by the FDA-approved treatments for AQP4+NMOSD, namely complement (eculizumab), B cells (inebilizumab), and interleukin-6 pathway (satralizumab).

Materials and methods

Ethics committee approval. Approval was received from the local ethical standards committee of each participating center, and written informed consent was obtained from all participants at the time of data acquisition.

Subjects. Brain MRI scans were acquired from 80 AQP4+NMOSD patients diagnosed according to 2015 International Panel Consensus Diagnostic criteria (Wingerchuk et al., 2015), and 94 HC. AQP4-IgG serostatus was tested using a cell-based assay (Wingerchuk et al., 2015). Participants were recruited at two European centers: Milan (92 subjects: 40 AQP4+NMOSD and 52 HC), and Belgrade (82 subjects: 40 AQP4+NMOSD and 42 HC). Exclusion criteria were alcohol or drug abuse, history of head trauma, psychiatric comorbidities, and contraindications to MRI. On the same day of the MRI, patients also underwent a neurological examination including the assessment of the EDSS (Kurtzke, 1983) and history collection.

MRI acquisition protocol. Using two 3.0 T scanners (in Milan, Ingenia CX and Inera Philips Medical Systems) and a 1.5 T scanner (in Belgrade, Achieva Philips Medical System) scanner, the following brain sequences were collected from all subjects in a single session:

- (i) T2-weighted images: axial dual-echo turbo spin-echo (TSE) (Intera scanner in Milan and Belgrade) or sagittal 3D fluid attenuated inversion recovery (FLAIR) (Ingenia CX scanner in Milan);
- (ii) 3D T1-weighted images: axial 3D T1-weighted fast gradient-echo (Intera scanner in Milan), axial 3D T1-weighted turbo field echo (Belgrade) and sagittal 3D T1-weighted magnetization-prepared rapid gradient-echo (Ingenia scanner in Milan);
- (iii) Diffusion-weighted images (DWI): axial pulsed-gradient spin echo diffusion-weighted echo-planar imaging (single shell, Intera scanner in Milan and Belgrade), axial pulsed-gradient spin echo single shot diffusion-weighted echo planar imaging (3 shells, Ingenia scanner in Milan).

Details of the MRI protocols are available as **Supplementary Table 5.4.1**.

MR images analysis.

Conventional MRI analysis. Focal WM lesions were segmented on T2-weighted images using a fully-automated approach based on two 3D patch-wise convolutional neural networks (Valverde et al., 2017) (Milan, Ingenia scanner) or using a local thresholding segmentation technique (Jim 8.0 Xinapse System Ltd; Milan, Intera scanner and Belgrade) to obtain lesion masks and volumes. Head-size normalized NBV, NGMV, and NWMV, were measured after lesion refilling (Battaglini et al., 2012) using the FSL SIENAx software (Smith et al., 2002).

Lesion probability map in AQP4+NMOSD patients. By exploiting the transformation matrix of the VBM (please, refer to the “Voxel-based morphometry” section for further details), we coregistered the single-subject T2-lesion masks to the standard space, obtaining a lesion probability map (i.e., 0-100% probability of a voxel of being involved by a lesion). Since only patients with brain lesions were included, and the lesion volume in the disorder is usually moderate, the lesion mask of the right hemisphere was mirrored on the left hemisphere to strength our statistical power (i.e., if corresponding voxels on the two hemispheres were involved by a lesion, the probability of having a lesion in that voxel was calculated as the sum of both probabilities).

Voxel-based morphometry. VBM analysis was used to identify regions of significant GM and WM atrophy in AQP4+NMOSD patients compared to HC. The opposite contrast was also performed as negative control.

3D T1-weighted images were segmented using the Segmentation tool available in SPM12 (i.e. GM, WM and CSF), and normalized through the Diffeomorphic Anatomical Registration using Exponentiated Lie Algebra (DARTEL) registration method (Ashburner, 2007). GM and WM maps were modulated and smoothed (3D 8-mm Gaussian kernel). Between-group comparisons were run with a two-factor (i.e., NMOSD and HC groups) and three-level (i.e., scanners) ANOVA, with age, sex, and the SIENAX-derived V-scaling as covariates.

Tract-based spatial statistics (TBSS). Differences in the microstructural composition of the whole-brain WM between NMOSD and HC were analyzed with the TBSS (<http://www.fmrib.ox.ac.uk/fsl/tbss/index.html>) (Smith et al., 2006). The pre-processing of images included the Eddy tool in the FSL library for off-resonance (Milan, Ingenia CX scanner) and eddy current-induced distortions-correction (all scanners) (Andersson et al., 2017). The diffusion tensor was estimated by linear regression on diffusion-weighted imaging data at $b=700/1000$ s/mm² (Milan, Ingenia CX scanner), $b=900$ s/mm² (Milan, Intera scanner), or $b=1000$ (Belgrade). Then, maps of FA and MD were derived (Basser et al., 1994b).

Individual FA images were nonlinearly registered to the FMRIB58_FA atlas within the FSL tool, and averaged to obtain a customized FA-atlas, which was thinned to obtain a WM tract “skeleton” with FA values thresholded at 0.2 to retain voxels within the WM only. Then, single-subject normalized FA maps were warped onto the FA skeleton by searching perpendicularity to the maximum FA values in the skeleton (Smith et al., 2006). Between-group comparisons were run with a two-factor (i.e., NMOSD and HC) and three level (i.e., scanners) ANOVA, with the demeaned age and sex as covariates.

The TBSS “randomize” option with 2000 computations was used to identify FA voxels significantly different between patients and controls, using the threshold-free cluster enhancement (TFCE) option.

Statistical analysis.

Spatial associations between image-derived maps and genetics. Brain-wide gene expression profiles were obtained from the AHBA transcriptome, comprising gene expression data for more than 20000 genes taken from about 3700 spatially distinct tissue samples from six neurotypical adult brains (aged 24–57 years) (Hawrylycz et al., 2012, Shen, Overly et al., 2012). We pre-selected disease-specific genes of interest using the Open Target Platform and the search term: Neuromyelitis optica (<https://platform.opentargets.org/disease/>)(Ochoa, Hercules et al., 2021) which were also included in the Allen Human Brain database and MENGA platform, obtaining a list of 266 candidate genes, which are available as **Supplementary Table 5.4.2**.

To investigate the spatial association between the imaging maps obtained from the previous MRI analyses (T-maps from VBM GM atrophy, lesion probability map, and TBSS map) and the candidate gene expression, we used the MENGA platform (Rizzo et al., 2016) following published guidelines (Arnatkeviciute, Fulcher et al., 2019).

The pre-processing of genomic data consisted in (i) representative probe selection to index expression for a gene, and (ii) normalization of expression measure to account for inter-individual differences (<https://github.com/BMHLab/AHBAprocessing>) (Arnatkeviciute et al., 2019). These pre-processing steps on gene expression data are better described in the **Supplementary Material**.

Then, image maps in the MNI ICBM152 space were resampled into the AHBA coordinates, separately for each donor, to obtain image-to-sample spatial correspondence according to MNI coordinates of each sample provided by the AHBA. Image data are normalized to z-scores and each image sample is estimated as the average of the voxels within a 3D window of a specified size (here set to 5 mm) centered on the MNI coordinates of the genomic sample. Since only two of the six donors were sampled across the whole brain, we restricted our analyses the left hemisphere only, to increase the robustness of the results. Spatial association between imaging and genomic data have been therefore assessed with MENGA platform using a weighted multiple regression, with the directionality of the imaging-genomic data correlation also provided.

A measure of cross-correlation reliability is estimated with the chance likelihood, according to (Rizzo et al., 2016):

$$\text{chance likelihood} = \frac{\text{number of instances } (R^2 > R_{or}^2)}{\text{number of bootstraps}}$$

where R_{or}^2 is the value of the coefficient obtained from the real data, and R^2 is that obtained using the bootstrapped genomic data. It returns the probability that genomic data are unrelated to the image values.

Thus, smaller values of chance likelihood denoted a higher reliability of the obtained results. In this work, we set a cut-off <0.05 likelihood to assess significant spatial associations between brain damage and gene expression.

Enrichment analysis. To better understand genetic functionalities, we performed a functional-enrichment according to the Reactome pathway database (Gillespie, Jassal et al., 2022) using the g:Profiler platform (Raudvere, Kolberg et al., 2019). Briefly, the list of the genes significantly associated with the different types of structural damage (i.e., lesion probability map, grey and white matter atrophy, and microstructural abnormalities) was used as input for the g:Profiler platform, which investigated overrepresented biological processes through over-representation analysis (threshold: 5-2500 genes per enriched pathway). Only significant results at Bonferroni-corrected threshold were retained. Then, Cytoscape was used to visualize the interactions between the enriched pathways (Shannon, Markiel et al., 2003).

Results

Demographic, clinical, and conventional MRI features of the study population. AQP4-IgG+NMOSD patients and HC had similar age, but female sex was more common in patients. The proportion of participants acquired on each scanner was balanced between patients and controls. The median disease duration and EDSS score in patients were 3.5 years and 4.0, respectively. Compared to HC, AQP4-IgG+NMOSD patients had brain and GM atrophy, but similar WM volumes. Details are reported in **Table 5.4.1**.

Table 5.4.1. Demographic, clinical, and conventional MRI features of the study population. Data are presented as mean (standard deviation) or median (interquartile range), according to the normality assumption. If not otherwise specified, p values refer to Mann-Whitney U-test (quantitative variables) or Pearson's Chi square test (qualitative variables).

	AQP4-IgG+NMOSD (n=80)	HC (n=94)	p value
Demographic features			
Age (SD) ^a [years]	45.2 (13.8)	45.3 (13.3)	0.95
Sex (F/M)	68/12	66/28	0.02
Scanner 1/2/3*	31/9/40	36/16/42	
Disease duration (IQR) [years]	3.5 (0-34)	-	-
EDSS (IQR)	4.0 (1-9)	-	-
Conventional MRI measures			
T2-hyperintense lesion volume (IQR) [ml]	0.25 (0.06-1.25)	-	-
Normalized brain volume (SD) [ml]	1468 (189)	1537 (96)	<0.001
Normalized grey matter volume (SD) [ml]	729 (108)	776 (74)	<0.001
Normalized white matter volume (SD) [ml]	737 (116)	759 (85)	0.34

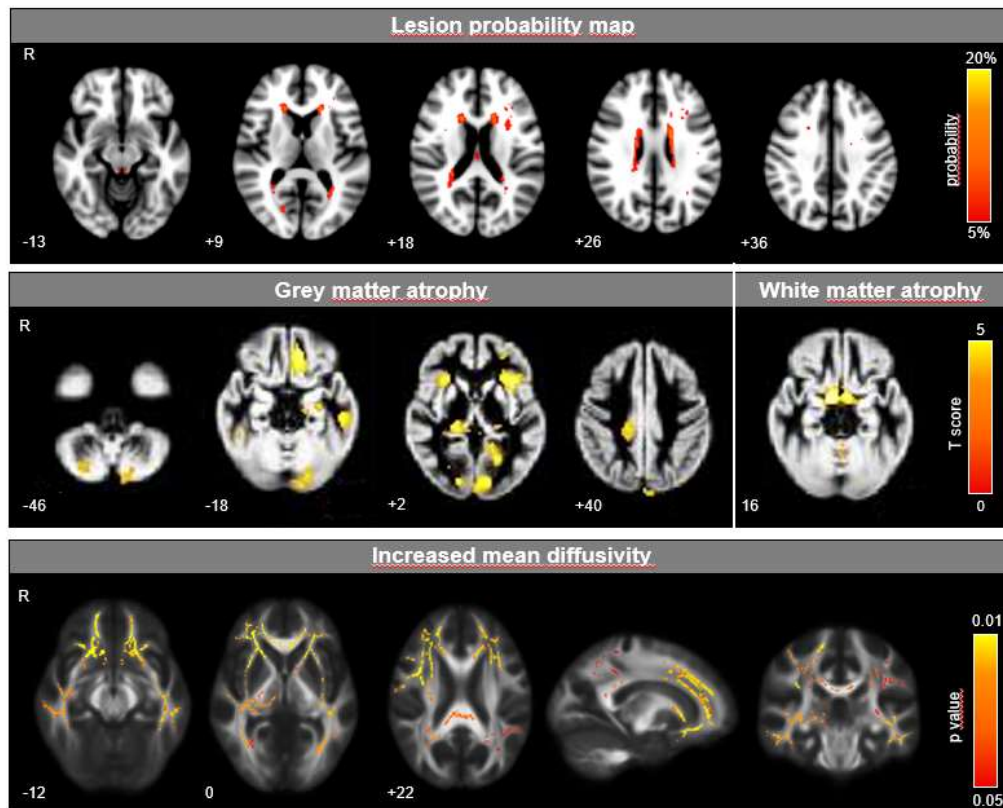
^aIndependent sample t-test.

*Scanner 1 is Milan, Intera; scanner 2 is Milan, Ingenia; scanner 3 is Belgrade.

Abbreviations: AQP4-IgG+NMOSD=aquaporin-4-IgG-seropositive neuromyelitis optica spectrum disorders; HC=healthy controls; SD=standard deviation; F=females; M=males; IQR=interquartile range; EDSS=expanded disability status scale.

Lesion probability map. T2-hyperintense lesions were detected in 59/80 patients (73.7%). Lesions were mainly located in the periventricular white matter. Additional locations were the subcortical white matter, the corpus callosum, and the periaqueductal grey (**Figure 5.4.1**).

Figure 5.4.1. Brain damage distribution in AQP4+NMOSD patients in terms of lesion location, grey and white matter atrophy, and microstructural abnormalities.



Abbreviations: R=right.

Grey and white matter atrophy – Voxel-based morphometry. Compared to HC, AQP4-IgG+NMOSD patients had significant GM atrophy in the visual cortex (left lingual gyrus, left calcarine fissure), in the bilateral insula, and in the left prefrontal cortex (orbitofrontal and rectus gyri) (**Figure 5.4.1**). WM atrophy selectively involved the optic tracts bilaterally (**Figure 5.4.1**). Details are reported in **Table 5.4.2**. No voxels of significant atrophy were found in HC compared to AQP4-IgG+NMOSD patients.

Table 5.4.2. Clusters of significant atrophy in AQP4-IgG+NMOSD patients compared to HC. Only results having a family-wise-corrected p value below a relaxed threshold of 0.10 are reported. Brain regions were identified according to the Automated Anatomical Labeling or attributed by visual inspection in case of nasty regions.

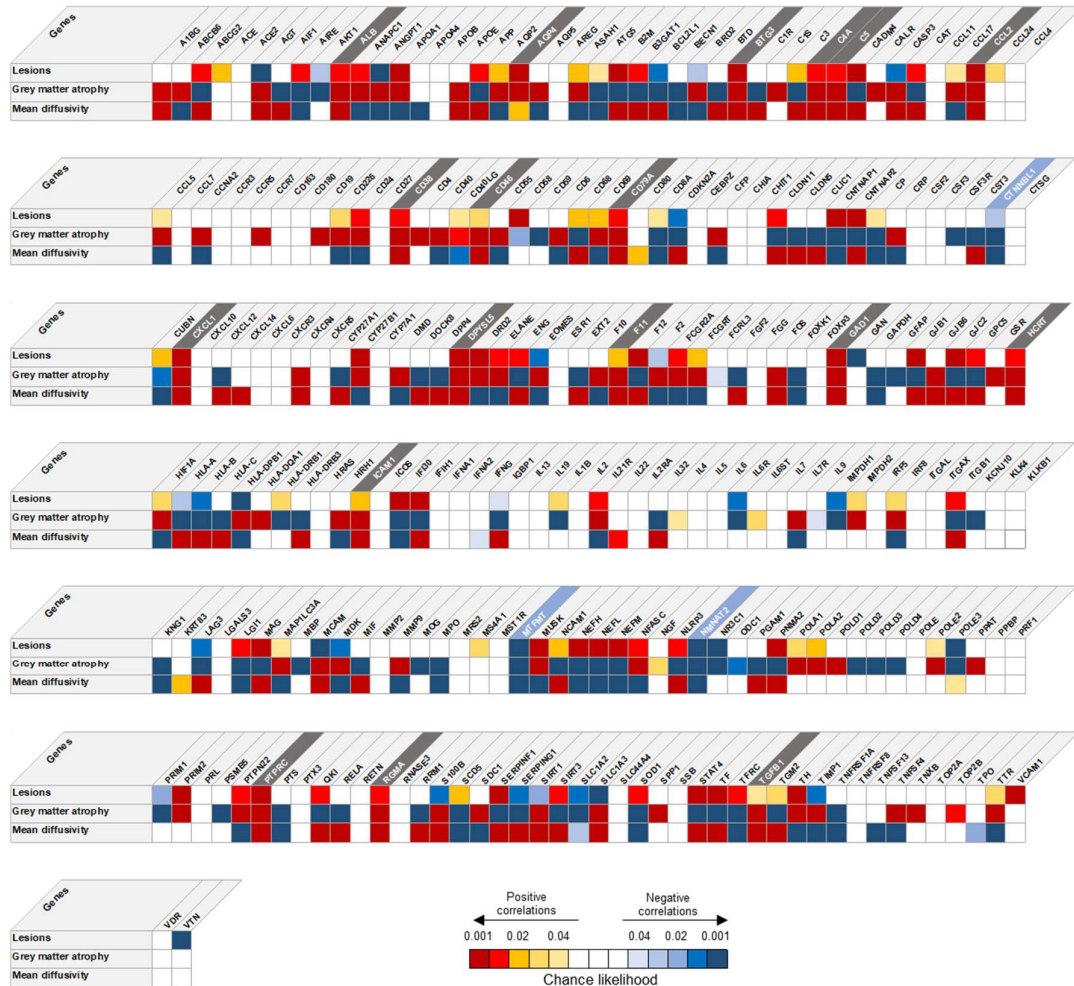
Cluster extent	pFWE	T score	Montreal Neurological Institute coordinates x, y, z			Brain region
Grey matter atrophy						
4028	<0.0001	5.13	-16	-84	-12	Left lingual gyrus
		4.84	-15	-87	-4	Left lingual gyrus
		4.68	-8	-87	4	Left calcarine scissure
1473	0.015	4.90	33	18	10	Right insula
		4.14	32	21	-4	Right insula
		3.61	40	8	-14	Right insula
1849	0.006	4.80	-34	21	4	Left insula
		3.53	-27	33	-3	Left frontal inferior orbital gyrus
984	0.062	4.24	21	-28	0	Right thalamus
		3.90	20	-21	12	Right thalamus
		3.51	6	-33	3	Right thalamus
953	0.068	4.79	-9	34	-20	Left rectus gyrus
		3.59	-16	22	-12	Left rectus gyrus
871	0.088	3.81	-21	-15	-24	Left parahippocampal gyrus
		3.77	-21	-27	-2	Left thalamus, geniculate body
		3.65	-32	-22	-9	Left hippocampus
White matter atrophy						
952	0.044	5.47	9	0	-16	Right optic tract
		4.77	-6	3	-16	Left optic tract
		3.64	-9	12	-24	Left optic tract

Abbreviations: pFWE=family-wise error corrected p value

White matter microstructural abnormalities – Tract-based morphometry. Compared to HC, AQP4-IgG+NMOSD had increased MD in the callosal WM projecting tracts (bilateral forceps minor and major), in the bilateral external capsule (cortico-cortical associative fibers), posterior thalamic radiation (associative tracts to visual areas), superior longitudinal fasciculus (fronto-parieto-temporo-occipital associative tract), inferior longitudinal fasciculus (occipito-temporal associative tract), and right posterior limb of the internal capsule (corticospinal tract and medial lemniscus) (**Figure 5.4.1**). No significant differences in terms of FA were observed between patients and controls.

Spatial association between gene expression and brain damage in AQP4+NMOSD patients. Since WM tracts are not sampled in the AHBA, the association between atrophy and gene expression was run considering only the GM. Significant associations are reported in **Figure 5.4.2**.

Figure 5.4.2. Spatial association between gene expression and brain damage in AQP4+NMOSD patients. Genes positively associated with all types of damage are highlighted in grey, while those negatively associated with all types of damage are highlighted in light blue.

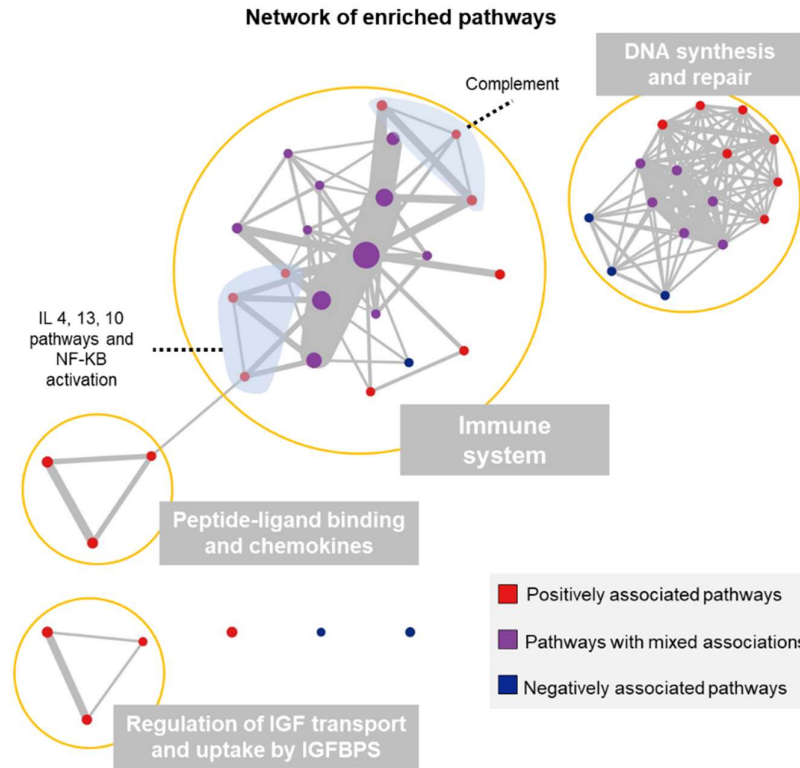


The expression of AQP4 was significantly associated with all the types of damage, namely lesions, GM atrophy and increased MD. When we focused on targets of the FDA-approved AQP4+NMOSD treatments, such as eculizumab (complement inhibitor), satralizumab (IL6 receptor inhibitor) and inebilizumab (CD19 inhibitor on B cells) we found that, likewise AQP4, a higher expression of complement factors (i.e., C5 and C4a) was associated with all types of brain damage. In contrast, IL6 pathway showed mixed association with brain damage, since the expression of IL6 showed no significant

association, the IL6 receptor resulted negatively associated with the presence of brain lesions and atrophy, and that of IL6 signal transducer was positively correlated with the presence of brain atrophy. The B cell marker CD19 was associated with atrophy development only.

Gene enrichment analysis. A total of 46 biological processes resulted enriched, of whom the association with damage was purely positive in 23, purely negative in six, and mixed positive/negative in 17. The enriched biological processes and were distributed among four main clusters as shown in **Figure 5.4.3**.

Figure 5.4.3. Network of enriched biological processes. Nodes size represents the size of the pathway, while edges width represents the number of genes shared by the connected pathways (i.e., nodes).



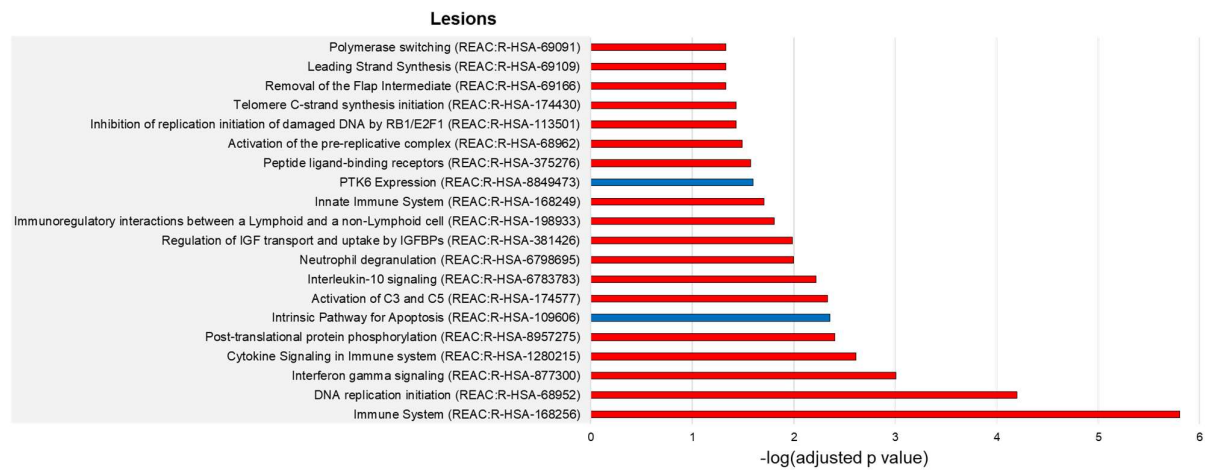
Abbreviations: IGF=insulin-like growth factor; IGFBPS= insulin-like growth factor-binding protein; IL=interleukin; NF-KB=nuclear factor kappa-light-chain-enhancer of activated B cells.

Complement activation, and the regulation of insulin-like growth factor (IGF) and uptake by insulin-like growth factor binding proteins (IGFBPs) were positively associated with all types of brain damage (**Figure 5.4.4**). Broader processes were also significantly associated, including DNA replication initiation the response to peptide-ligand binding receptors.

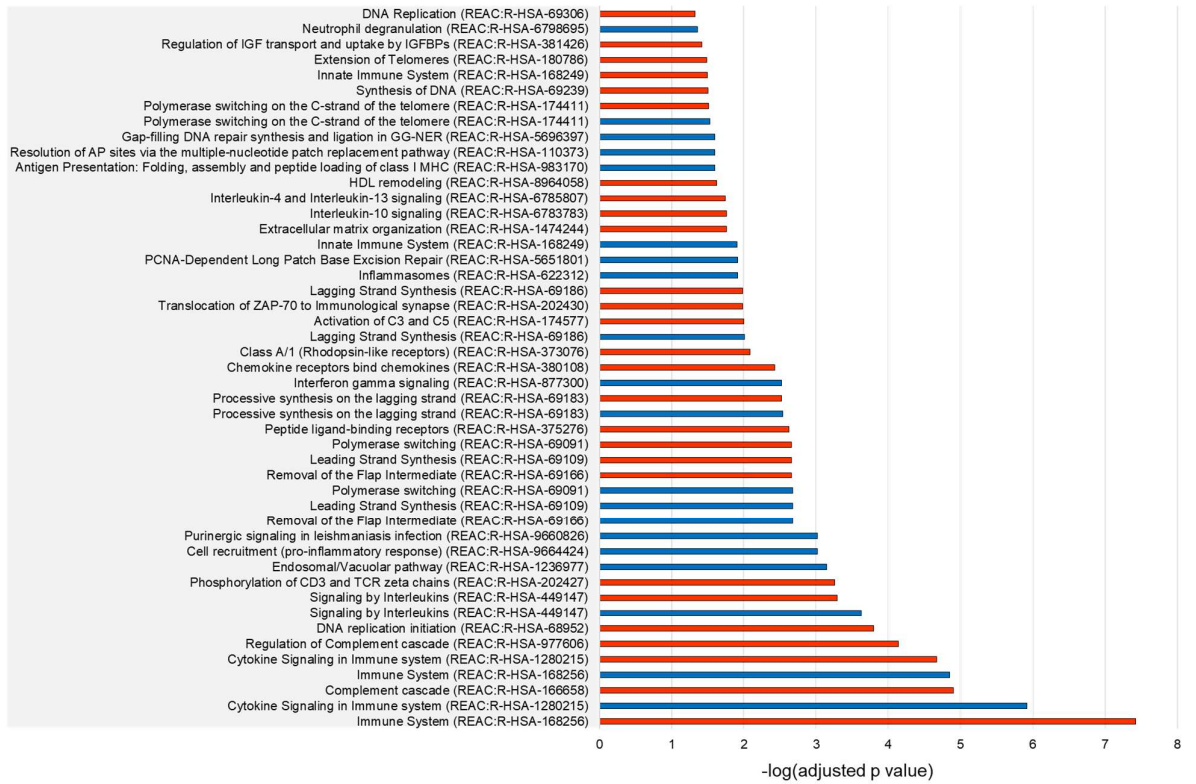
Furthermore, neutrophil degranulation and the interferon gamma pathway were positively associated with lesions and increased MD, IL10 signaling with lesions and GM atrophy, IL4 and -13 signaling with GM atrophy, and TRAF6 (TNF Receptor Associated Factor 6)-NF-KB (nuclear factor kappa-light-chain-enhancer of activated B cells) activation with increased MD.

Overall, the enrichment analysis disclosed a limited number of enriched biological processes spatially associated with the presence of brain lesions and increased MD. In contrast, such an analysis identified a high number of biological processes both positively and negatively associated with GM atrophy (**Figure 5.4.4**).

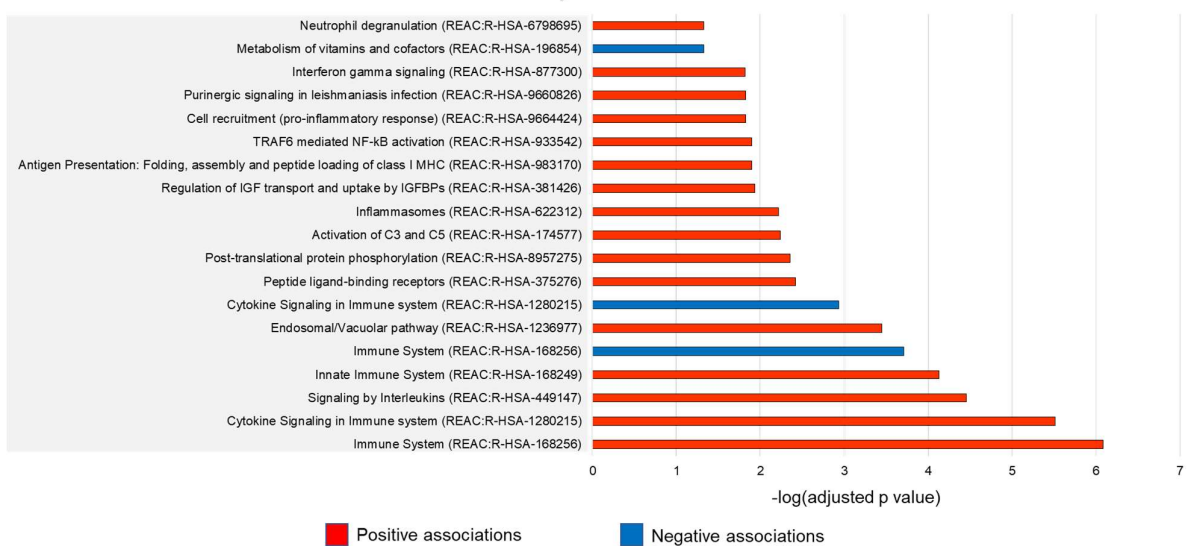
Figure 5.4.4. Enrichment analysis of biological processes associated with brain damage in AQP4+NMOSD. Positive associations are red, while blue indicates negative associations.



Grey matter atrophy



Increased mean diffusivity



Discussion

In this study we used a joint methodology merging quantitative measures of brain damage and the a-priori mapping of gene expression in the human brain, to study its potential for the assessment and understanding of in-vivo correlates of AQP4+NMOSD pathophysiology.

Our results confirmed the key role of AQP4 expression for the development of brain lesions, atrophy, and microstructural abnormalities, but we were also able to identify other relevant biological pathways, namely the activation of C3 and C5 and the regulation of IGF and uptake by IGFbps, which were positively associated with all types of brain damage. IL4, -13, and -10 signaling, neutrophil degranulation, interferon-gamma signaling, and NF-KB activation also contributed to specific types of brain injury.

In prior studies, the activation of the complement cascade and the recruitment of neutrophils and eosinophils at the site of damage were already identified as key steps of AQP4+NMOSD pathophysiology, as demonstrated by complement deposition and extensive granulocytes infiltrates observed in pathological tissue of patients (Lucchinetti et al., 2002). Therefore, the spatial association with eosinophils chemoattractants and neutrophil-related biological pathways such as such as IL4/-13 or interferon-gamma signaling is not surprising. NF-KB activation through TRAF6 was also described as a potential mechanism bridging inflammation and autoimmunity by promoting the survival of dendritic cells and the production of pro-inflammatory cytokines (Thomas, 2005).

Treatments inhibiting the complement cascade, such as eculizumab and ravulizumab, were demonstrated highly effective in AQP4+NMOSD and almost invariably prevented relapses (Pittock, Barnett et al., 2022, Pittock et al., 2019). Although a head-to-head comparison was never done and studies slightly differ for inclusion criteria and pre-enrollment disease activity, a recent metanalysis suggested that complement inhibition may be overall more effective than B cells depletion or the inhibition of the IL6 pathway in AQP4+NMOSD (Wingerchuk, Zhang et al., 2022). In our data, higher CD19 expression was only associated with brain atrophy, and so was IL6 signal transducer, while other elements within the IL6 pathway were protective or lacked association.

However, we do not believe that our results argue against the relevance of these pathways in AQP4+NMOSD pathophysiology, but rather highlight that, while the complement system exerts a local role, hence being directly correlated with the presence of local brain

damage, B cells and IL6 act remotely from the periphery (e.g., by enhancing the antibody-production, favoring a pro-inflammatory environment, and increasing the blood-brain barrier permeability) (Fujihara, Bennett et al., 2020, Levy & Mealy, 2021) or in a dynamic way. In our cohort the MRI scans were acquired during disease remission. Recent studies demonstrated that about 5% of brain lesions completely resolve and almost invariably reduce in size after the acute attack in AQP4+NMOSD (Sechi, Krecke et al., 2021c), so, we might have missed associations if only present during the acute phase of the disease. We also found a significant spatial association between IL10 signaling, lesions and grey matter atrophy, but literature is controversial. Both reduced and increased levels of IL10 have been described in AQP4+NMOSD patients (Kong, Kim et al., 2017, Uzawa, Mori et al., 2014). Despite the classical interpretation of IL10 as an anti-inflammatory molecule, the recent SARS-CoV-2 pandemic has questioned this hypothesis given that high IL10 levels were found associated with a more severe disease course (Lu, Zhang et al., 2021).

We also found an association between brain damage and the regulation of IGF transport and uptake by IGPBPs. The role of this process was not previously investigated in AQP4+NMOSD, but experimental data highlighted that the IGF dysregulation (i.e., reduction) fuels autoimmunity through T reg unbalance (Bilbao, Luciani et al., 2014) and favors tissue damage through glutamate-induced exotoxicity (Prabhu, Khan et al., 2019) and hampered remyelination (Mason, Xuan et al., 2003). Astrocytes produce IGF in response to brain injury (Garcia-Estrada, Garcia-Segura et al., 1992), so this protective mechanism might be deficient in AQP4+NMOSD, but future studies are warranted to confirm this result.

In general, the biological processes colocalizing with brain lesions and microstructural abnormalities were specific of AQP4+NMOSD pathogenesis, suggesting that lesions and WM damage are specific MRI manifestations of the disease. In contrast, brain atrophy was associated with many pathways, not always directly involved in the pathophysiology of the disease, and sometimes with unexpected directions (i.e., negative association with neutrophils degranulation and interferon-gamma signaling). In our patients, brain atrophy mainly involved WM and GM structures within the visual pathways, such as the optic tracts, the geniculate body of the thalamus and the occipital cortex. This suggests that atrophy is largely associated to both the direct injury of the anterior visual pathway

typically observed in the disease, and to mechanisms of secondary neurodegeneration occurring in posterior regions. Similar results were already obtained by others (Pichiecchio et al., 2012) and support the lack of primary neurodegeneration in this disease. Therefore, it is likely that more complex mechanisms contributing to neurodegeneration cannot be successfully underpinned with this imaging analysis.

Moving to the main limitations of the study, we acknowledge the cross-sectional design, and the abovementioned nuisance effect of lesion resolution. Unfortunately, biological samples of patients were unavailable at our facility, hence a biological confirmation of this approach is missing. However, we believe that this might be the starting point for future studies specifically designed to prove the biological associations between quantitative MRI data, gene expression atlases, and the pathophysiology of antibody-mediated autoimmune disorders affecting the CNS. Potential approaches may include patients' genotyping, the measurement of serum or CSF cytokines involved in the main enriched biological processes (i.e., IL4, IL13, IL10, IL6 in this study), biomarkers of neuronal loss (i.e., neurofilament light chain) or more sophisticated methodologies such as the assessment of damage on patients' brain organoids.

Supplementary materials

Supplementary Table 5.4.1. Detailed description of the standardized MRI protocol at each participating center and scanner.

	Scanner	Field strength [T]	Sequence	TR/TE [ms]	TI [ms]	FOV	Matrix	Thickness [mm]
T2-w	Milan, Intera	3.0	Axial dual-echo TSE	2599/16-80	-	240x240	256x256	3
	Milan, Ingenia	3.0	Sagittal 3D FLAIR	4800/270	1650	256x256	256x256	1
	Belgrade	1.5	Axial dual-echo TSE	3141/20-100	-	240x240	256x256	3
T1-w	Milan, Intera	3.0	Axial 3D FFE	25/4.6	-	230x230	256x256	0.8
	Milan, Ingenia	3.0	Sagittal 3D MPRAGE	7/3.2	1000	256x256	256x256	1
	Belgrade	1.5	Axial 3D TFE	7.2/3.2	1000	256x256	256x256	1
b-value								
DWI	Milan, Intera	3.0	Axial pulsed-gradient spin echo diffusion-weighted echo-planar imaging	8692/58	900	240x231	112x88	2.3
	Milan, Ingenia	3.0	Axial pulsed-gradient spin echo single shot diffusion-weighted echo planar imaging	5900/78	700/1000/2855	240x233	112x85	2.3
	Belgrade	1.5	Axial pulsed-gradient spin echo diffusion-weighted echo-planar imaging	6717/86	1000		112x110	2.6

Abbreviations: 3D=three-dimensional; DWI=diffusion-weighted images; ETL=echo train length; FA=flip angle; FFE=fast field echo; FLAIR=fluid attenuated inversion recovery; FOV=field of view; mm=millimeters; MPRAGE= magnetization prepared rapid gradient echo; ms=milliseconds; SENSE=sensitivity encoding; T=tesla; T1-w=T1-weighted sequences; T2-w=T2-weighted sequences; TE=echo time; TFE=turbo field echo; TI=inversion time; TR=relaxation time; TSE=turbo spin-echo.

Supplementary Table 5.4.2. List of candidate genes analyzed in the study with the overall association score (i.e., degree of association with AQP4+NMOSD according to the Open Target Platform).

Ranking	Symbol	Overall association score	Target Name
1	IL6R	0.53257	Interleukin 6 receptor
2	IL6ST	0.52442	Interleukin 6 cytokine family signal transducer
3	TOP2A	0.47019	DNA topoisomerase II alpha
4	IMPDH1	0.43426	Inosine monophosphate dehydrogenase 1
5	IMPDH2	0.43426	Inosine monophosphate dehydrogenase 2
6	MS4A1	0.40109	Membrane spanning 4-domains A1
7	NR3C1	0.40043	Nuclear receptor subfamily 3 group C member 1
8	CD19	0.39164	CD19 molecule
9	C5	0.36215	Complement C5
10	PPAT	0.28540	Phosphoribosyl pyrophosphate amidotransferase
11	HLA-DQA1	0.13565	Major histocompatibility complex, class II, DQ alpha 1
12	AQP4	0.11965	Aquaporin 4
13	HLA-DRB1	0.09750	Major histocompatibility complex, class II, DR beta 1
14	IFNA1	0.08614	Interferon alpha 1
15	CSF3R	0.08316	Colony stimulating factor 3 receptor
16	MOG	0.08278	Myelin oligodendrocyte glycoprotein
17	POLA1	0.08223	DNA polymerase alpha 1, catalytic subunit
18	POLA2	0.08223	DNA polymerase alpha 2, accessory subunit
19	POLD1	0.08223	DNA polymerase delta 1, catalytic subunit
20	POLD2	0.08223	DNA polymerase delta 2, accessory subunit
21	POLD3	0.08223	DNA polymerase delta 3, accessory subunit
22	POLD4	0.08223	DNA polymerase delta 4, accessory subunit
23	POLE	0.08223	DNA polymerase epsilon, catalytic subunit
24	POLE2	0.08223	DNA polymerase epsilon 2, accessory subunit
25	POLE3	0.08223	DNA polymerase epsilon 3, accessory subunit
26	PRIM1	0.08223	DNA primase subunit 1
27	PRIM2	0.08223	DNA primase subunit 2
28	IL1B	0.08036	Interleukin 1 beta
29	SPP1	0.07957	Secreted phosphoprotein 1
30	CD38	0.07502	CD38 molecule
31	APOA1	0.07484	Apolipoprotein A1
32	CD59	0.07430	CD59 molecule (CD59 blood group)
33	GSR	0.07392	Glutathione-disulfide reductase
34	PSMB5	0.07392	Proteasome 20S subunit beta 5
35	TOP2B	0.07392	DNA topoisomerase II beta
36	CCR7	0.05802	C-C motif chemokine receptor 7

37	IL6	0.05575	Interleukin 6
38	TNXB	0.05066	Tenascin XB
39	C1S	0.04607	Complement c1s
40	KCNJ10	0.04540	Potassium inwardly rectifying channel subfamily J member 10
41	CD58	0.04396	CD58 molecule
42	GFAP	0.04074	Glial fibrillary acidic protein
43	FCRL3	0.04071	Fc receptor like 3
44	CXCL10	0.04054	C-X-C motif chemokine ligand 10
45	IL7	0.03909	Interleukin 7
46	F11	0.03696	Coagulation factor XI
47	F12	0.03696	Coagulation factor XII
48	HRH1	0.03696	Histamine receptor H1
49	KLKB1	0.03696	Kallikrein B1
50	MBP	0.03688	Myelin basic protein
51	RRM1	0.03326	Ribonucleotide reductase catalytic subunit M1
52	AIRE	0.03253	Autoimmune regulator
53	ICOS	0.03104	Inducible T cell costimulator
54	NMNAT2	0.03088	Nicotinamide nucleotide adenylyltransferase 2
55	CLIC1	0.03085	Chloride intracellular channel 1
56	GJB1	0.02938	Gap junction protein beta 1
57	CSF3	0.02801	Colony stimulating factor 3
58	IL7R	0.02716	Interleukin 7 receptor
59	RETN	0.02716	Resistin
60	CD40LG	0.02632	CD40 ligand
61	SDC1	0.02605	Syndecan 1
62	IL4	0.02520	Interleukin 4
63	MMP9	0.02493	Matrix metalloproteinase 9
64	SLC44A4	0.02455	Solute carrier family 44 member 4
65	DPYSL5	0.02370	Dihydropyrimidinase like 5
66	ALB	0.02294	Albumin
67	TGM2	0.02217	Transglutaminase 2
68	GJC2	0.02215	Gap junction protein gamma 2
69	CXCR3	0.02204	C-X-C motif chemokine receptor 3
70	S100B	0.02191	S100 calcium binding protein B
71	HLA-DPB1	0.02147	Major histocompatibility complex, class II, DP beta 1
72	CD55	0.02096	CD55 molecule (Cromer blood group)
73	IFIH1	0.02070	Interferon induced with helicase C domain 1
74	GAN	0.01982	Gigaxonin
75	CD8A	0.01892	CD8a molecule
76	TH	0.01891	Tyrosine hydroxylase
77	SLC1A2	0.01870	Solute carrier family 1 member 2
78	TIMP1	0.01848	TIMP metalloproteinase inhibitor 1
79	IFI30	0.01846	IFI30 lysosomal thiol reductase
80	CRP	0.01762	C-reactive protein

81	IRF5	0.01682	Interferon regulatory factor 5
82	CD4	0.01628	CD4 molecule
83	AKT1	0.01626	AKT serine/threonine kinase 1
84	ANGPT1	0.01626	Angiopoietin 1
85	QKI	0.01626	QKI, KH domain containing RNA binding
86	CD226	0.01608	CD226 molecule
87	RELA	0.01571	RELA proto-oncogene, NF-kb subunit
88	C4A	0.01524	Complement C4A (Rodgers blood group)
89	NEFL	0.01515	Neurofilament light chain
90	BECN1	0.01478	Beclin 1
91	CCL7	0.01478	C-C motif chemokine ligand 7
92	MIF	0.01404	Macrophage migration inhibitory factor
93	IL22	0.01384	Interleukin 22
94	CCL4	0.01330	C-C motif chemokine ligand 4
95	IL32	0.01277	Interleukin 32
96	NGF	0.01263	Nerve growth factor
97	IL2RA	0.01238	Interleukin 2 receptor subunit alpha
98	AQP5	0.01222	Aquaporin 5
99	CYP27B1	0.01222	Cytochrome P450 family 27 subfamily B member 1
100	NEFH	0.01218	Neurofilament heavy chain
101	CYP7A1	0.01202	Cytochrome P450 family 7 subfamily A member 1
102	MMP2	0.01186	Matrix metalloproteinase 2
103	APOE	0.01183	Apolipoprotein E
104	ICAM1	0.01177	Intercellular adhesion molecule 1
105	HLA-DRB3	0.01146	Major histocompatibility complex, class II, DR beta 3
106	CSF2	0.01134	Colony stimulating factor 2
107	IFNG	0.01133	Interferon gamma
108	ABCG2	0.01109	ATP binding cassette subfamily G member 2 (Junior blood group)
109	CXCL1	0.01109	C-X-C motif chemokine ligand 1
110	PPBP	0.01109	Pro-platelet basic protein
111	VCAM1	0.01056	Vascular cell adhesion molecule 1
112	APOA4	0.01035	Apolipoprotein A4
113	CXCL6	0.01035	C-X-C motif chemokine ligand 6
114	ESR1	0.01035	Estrogen receptor 1
115	MAP1LC3A	0.01035	Microtubule associated protein 1 light chain 3 alpha
116	IGBP1	0.01031	Immunoglobulin binding protein 1
117	APOB	0.00961	Apolipoprotein B
118	A1BG	0.00924	Alpha-1-B glycoprotein
119	TGFB1	0.00902	Transforming growth factor beta 1
120	SOD1	0.00887	Superoxide dismutase 1
121	TPO	0.00887	Thyroid peroxidase
122	PTPN22	0.00861	Protein tyrosine phosphatase non-receptor type 22
123	GJB6	0.00856	Gap junction protein beta 6

124	CALR	0.00848	Calreticulin
125	IL2	0.00847	Interleukin 2
126	AIF1	0.00832	Allograft inflammatory factor 1
127	CASP3	0.00832	Caspase 3
128	PRF1	0.00832	Perforin 1
129	CXCL12	0.00828	C-X-C motif chemokine ligand 12
130	CXCL14	0.00819	C-X-C motif chemokine ligand 14
131	AGT	0.00813	Angiotensinogen
132	CAT	0.00813	Catalase
133	C3	0.00796	Complement C3
134	CD79A	0.00795	CD79a molecule
135	BTD	0.00739	Biotinidase
136	DOCK8	0.00739	Dedicator of cytokinesis 8
137	DPP4	0.00739	Dipeptidyl peptidase 4
138	FGG	0.00739	Fibrinogen gamma chain
139	LAG3	0.00739	Lymphocyte activating 3
140	SERPINF1	0.00739	Serpin family F member 1
141	TNFRSF8	0.00739	TNF receptor superfamily member 8
142	SSB	0.00739	Small RNA binding exonuclease protection factor La
143	ITGAL	0.00665	Integrin subunit alpha L
144	BTG3	0.00615	BTG anti-proliferation factor 3
145	TNFSF13	0.00607	TNF superfamily member 13
146	CCL11	0.00591	C-C motif chemokine ligand 11
147	CCL17	0.00591	C-C motif chemokine ligand 17
148	CCR5	0.00591	C-C motif chemokine receptor 5
149	IL9	0.00591	Interleukin 9
150	CD163	0.00561	CD163 molecule
151	BCL2L1	0.00554	BCL2 like 1
152	F2	0.00524	Coagulation factor II, thrombin
153	AREG	0.00517	Amphiregulin
154	CCNA2	0.00517	Cyclin A2
155	SIRT1	0.00517	Sirtuin 1
156	LGI1	0.00499	Leucine rich glioma inactivated 1
157	PRL	0.00480	Prolactin
158	TNFRSF1A	0.00480	TNF receptor superfamily member 1A
159	HLA-C	0.00478	Major histocompatibility complex, class I, C
160	PTPRC	0.00462	Protein tyrosine phosphatase receptor type C
161	BRD2	0.00460	Bromodomain containing 2
162	NFASC	0.00451	Neurofascin
163	CD24	0.00443	CD24 molecule
164	CD6	0.00443	CD6 molecule
165	CHIA	0.00443	Chitinase acidic
166	CST3	0.00443	Cystatin C
167	GAPDH	0.00443	Glyceraldehyde-3-phosphate dehydrogenase

168	IRF8	0.00443	Interferon regulatory factor 8
169	PGAM1	0.00443	Phosphoglycerate mutase 1
170	PTS	0.00443	6-pyruvoyltetrahydropterin synthase
171	SCD5	0.00443	Stearoyl-coa desaturase 5
172	VDR	0.00443	Vitamin D receptor
173	CD27	0.00432	CD27 molecule
174	MAG	0.00425	Myelin associated glycoprotein
175	ATG5	0.00407	Autophagy related 5
176	CCL2	0.00386	C-C motif chemokine ligand 2
177	ACE	0.00370	Angiotensin I converting enzyme
178	ACE2	0.00370	Angiotensin converting enzyme 2
179	ANAPC1	0.00370	Anaphase promoting complex subunit 1
180	ASAH1	0.00370	N-acylsphingosine amidohydrolase 1
181	B2M	0.00370	Beta-2-microglobulin
182	C1R	0.00370	Complement c1r
183	CD40	0.00370	CD40 molecule
184	CD80	0.00370	CD80 molecule
185	CLDN11	0.00370	Claudin 11
186	CTNNB1	0.00370	Catenin beta like 1
187	CXCR4	0.00370	C-X-C motif chemokine receptor 4
188	CXCR5	0.00370	C-X-C motif chemokine receptor 5
189	DMD	0.00370	Dystrophin
190	ENG	0.00370	Endoglin
191	EOMES	0.00370	Eomesodermin
192	EXT2	0.00370	Exostosin glycosyltransferase 2
193	FOS	0.00370	Fos proto-oncogene, AP-1 transcription factor subunit
194	FOXP1	0.00370	Forkhead box K1
195	GPC5	0.00370	Glypican 5
196	HIF1A	0.00370	Hypoxia inducible factor 1 subunit alpha
197	HRAS	0.00370	Hras proto-oncogene, gtpase
198	IFNA2	0.00370	Interferon alpha 2
199	KRT83	0.00370	Keratin 83
200	MDK	0.00370	Midkine
201	MST1R	0.00370	Macrophage stimulating 1 receptor
202	MTFMT	0.00370	Mitochondrial methionyl-trna formyltransferase
203	NEFM	0.00370	Neurofilament medium chain
204	SIRT3	0.00370	Sirtuin 3
205	TFRC	0.00370	Transferrin receptor
206	TTR	0.00370	Transthyretin
207	ELANE	0.00368	Elastase, neutrophil expressed
208	IL5	0.00351	Interleukin 5
209	VTN	0.00351	Vitronectin
210	TF	0.00333	Transferrin
211	PTX3	0.00316	Pentraxin 3

212	NLRP3	0.00311	NLR family pyrin domain containing 3
213	CCL5	0.00296	C-C motif chemokine ligand 5
214	CD180	0.00296	CD180 molecule
215	CUBN	0.00296	Cubilin
216	CYP27A1	0.00296	Cytochrome P450 family 27 subfamily A member 1
217	FOXP3	0.00296	Forkhead box P3
218	ITGB1	0.00296	Integrin subunit beta 1
219	KLK4	0.00296	Kallikrein related peptidase 4
220	KNG1	0.00296	Kininogen 1
221	SLC1A3	0.00296	Solute carrier family 1 member 3
222	RGMA	0.00294	Repulsive guidance molecule BMP co-receptor a
223	ABCB6	0.00259	ATP binding cassette subfamily B member 6 (Langereis blood group)
224	CD46	0.00259	CD46 molecule
225	CHIT1	0.00259	Chitinase 1
226	IL13	0.00259	Interleukin 13
227	CD68	0.00222	CD68 molecule
228	CD69	0.00222	CD69 molecule
229	CFP	0.00222	Complement factor properdin
230	CNTNAP2	0.00222	Contactin associated protein 2
231	CP	0.00222	Ceruloplasmin
232	F10	0.00222	Coagulation factor X
233	FCGRT	0.00222	Fc gamma receptor and transporter
234	LGALS3	0.00222	Galectin 3
235	MUSK	0.00222	Muscle associated receptor tyrosine kinase
236	NCAM1	0.00222	Neural cell adhesion molecule 1
237	ODC1	0.00222	Ornithine decarboxylase 1
238	PNMA2	0.00222	PNMA family member 2
239	RNASE3	0.00222	Ribonuclease A family member 3
240	SERPING1	0.00222	Serpin family G member 1
241	APP	0.00201	Amyloid beta precursor protein
242	AQP2	0.00185	Aquaporin 2
243	CCL24	0.00185	C-C motif chemokine ligand 24
244	HCRT	0.00185	Hypocretin neuropeptide precursor
245	HLA-B	0.00185	Major histocompatibility complex, class I, B
246	ITGAX	0.00185	Integrin subunit alpha X
247	B3GAT1	0.00148	Beta-1,3-glucuronyltransferase 1
248	CADM4	0.00148	Cell adhesion molecule 4
249	CCR3	0.00148	C-C motif chemokine receptor 3
250	CDKN2A	0.00148	Cyclin dependent kinase inhibitor 2A
251	CEBPZ	0.00148	CCAAT enhancer binding protein zeta
252	CLDN5	0.00148	Claudin 5
253	CNTNAP1	0.00148	Contactin associated protein 1
254	CTSG	0.00148	Cathepsin G
255	DRD2	0.00148	Dopamine receptor D2

256	FCGR2A	0.00148	Fc gamma receptor iia
257	FGF2	0.00148	Fibroblast growth factor 2
258	GAD1	0.00148	Glutamate decarboxylase 1
259	HLA-A	0.00148	Major histocompatibility complex, class I, A
260	IL19	0.00148	Interleukin 19
261	IL21R	0.00148	Interleukin 21 receptor
262	MCAM	0.00148	Melanoma cell adhesion molecule
263	MPO	0.00148	Myeloperoxidase
264	MRS2	0.00148	Magnesium transporter MRS2
265	STAT4	0.00148	Signal transducer and activator of transcription 4
266	TNFSF4	0.00148	TNF superfamily member 4

Pre-processing of gene expression data

Pre-processing steps on transcriptomic data from available atlases are needed in order to reduce variability and ensure consistent and reproducible results (Arnatkeviciute et al., 2019). The preprocessed Allen Human Brain database used in this study underwent the following steps:

- (i) Probe selection: One probe was collected as representative of the particular gene transcript for all donors. However, 71% of genes in the AHBA were measured with at least two probes. Thus, a unique association between the probe and the gene profile is needed. Probe selection was performed by evaluating the distribution of the expression values: the one with the most symmetric and least skewed profile was selected, in order to avoid the non-linearity effect on the microarray measures (Rizzo et al., 2016).
- (ii) Normalization of the expression measure: To address donor-specific effects and remove the inter-individual differences in expression measure, an appropriate approach is to normalize the gene expression data separately for each subject. In this case, each gene's expression values are normalized across brain regions for each donor separately to reflect its relative expression across regions of a given brain. Z-score normalization was used in this study:

$$Z_{score} = \frac{x_i - \bar{x}}{\sigma};$$

where \bar{x} and σ are the mean and standard deviation, respectively, and x_i is the expression value of a specific gene in a single sample.

6. SERONEGATIVE PATIENTS AND MOGAD

This section covers two main topics: seronegative NMOSD and MOGAD.

Initially we tried to focus on AQP4-seronegative NMOSD patients and AQP4-seronegative patients with NMOSD-like clinical manifestations such as idiopathic recurrent optic neuritis and recurrent myelitis. Our aim was to apply artificial intelligence on conventional MR images in order to get hints on the underlying pathophysiology. We started from the hypothesis that disorders sharing similar pathophysiological processes would have similar MRI features, even among those that can be identified by artificial intelligence algorithms but are undetectable by a human eye (e.g., tissue texture, signal intensity etc).

Despite some interesting inputs, such as ability of the automated algorithm to identify patients with anti-MOG-IgG as different from both AQP4+NMOSD and MS, I acknowledge that the choice of studying AQP4-seronegative patients with NMOSD diagnosis or NMOSD-like clinical manifestations is probably no more up to date. Autoimmune Neurology is now moving towards a pathophysiological rather than phenotypical classification of disorders, and this was demonstrated extremely successful in terms of treatment efficacy of tailored biologics (for example in AQP4+NMOSD patients). Future efforts should probably focus on the identification of novel biomarkers, antibodies, or more sensitive tests for the achievement of a pathophysiologically-based diagnoses of the patients so far considered “seronegative”.

During the final year of my PhD course, I had the chance to study more in depth MOGAD patients, that are now considered a separate disease entity from NMOSD, although diagnostic criteria have not been updated yet. This is discussed in the second part of the Chapter, where are reported the studies conducted at the Mayo Clinic. We investigated the MRI features of MOGAD patients with tumefactive demyelination compared to AQP4+NMOSD and MS, and the timing and predictors of lesion resolution, a specific radiological signature of MOGAD.

6.1. Application of deep-learning to the seronegative side of the NMO spectrum Cacciaguerra *et al.*, Journal of Neurology 2021

This chapter describes the work published in Journal of Neurology (PMID: 34328544, DOI: 10.1007/s00415-021-10727-y).

Journal of Neurology (2022) 269:1546–1556
<https://doi.org/10.1007/s00415-021-10727-y>

ORIGINAL COMMUNICATION



Application of deep-learning to the seronegative side of the NMO spectrum

Laura Cacciaguerra^{1,2} · Loredana Storelli¹ · Marta Radaelli³ · Sarlota Mesaros⁴ · Lucia Moiola³ · Jelena Drulovic⁴ · Massimo Filippi^{1,2,3,5,6} · Maria A. Rocca^{1,2,3} 

Received: 24 June 2021 / Revised: 19 July 2021 / Accepted: 24 July 2021 / Published online: 30 July 2021
© Springer-Verlag GmbH Germany, part of Springer Nature 2021

Abstract

Objectives To apply a deep-learning algorithm to brain MRIs of seronegative patients with neuromyelitis optica spectrum disorders (NMOSD) and NMOSD-like manifestations and assess whether their structural features are similar to aquaporin-4-seropositive NMOSD or multiple sclerosis (MS) patients.

Patients and methods We analyzed 228 T2- and T1-weighted brain MRIs acquired from aquaporin-4-seropositive NMOSD ($n = 85$), MS ($n = 95$), aquaporin-4-seronegative NMOSD [$n = 11$, three with anti-myelin oligodendrocyte glycoprotein antibodies (MOG)], and aquaporin-4-seronegative patients with NMOSD-like manifestations (idiopathic recurrent optic neuritis and myelitis, $n = 37$), who were recruited from February 2010 to December 2019. Seventy-three percent of aquaporin-4-seronegative patients with NMOSD-like manifestations also had a clinical follow-up (median duration of 4 years). The deep-learning neural network architecture was based on four 3D convolutional layers. It was trained and validated on MRI scans of aquaporin-4-seropositive NMOSD and MS patients and was then applied to aquaporin-4-seronegative NMOSD and NMOSD-like manifestations. Assignment of unclassified aquaporin-4-seronegative patients was compared with their clinical follow-up.

Results The final algorithm differentiated aquaporin-4-seropositive NMOSD and MS patients with an accuracy of 0.95. All aquaporin-4-seronegative NMOSD and 36/37 aquaporin-4-seronegative patients with NMOSD-like manifestations were classified as NMOSD. Anti-MOG patients had a similar probability of being NMOSD or MS. At clinical follow-up, one unclassified aquaporin-4-seronegative patient evolved to MS, three developed NMOSD, and the others did not change phenotype.

Conclusions Our findings support the inclusion of aquaporin-4-seronegative patients into NMOSD and suggest a possible expansion to aquaporin-4-seronegative unclassified patients with NMOSD-like manifestations. Anti-MOG patients are likely to have intermediate brain features between NMOSD and MS.

Introduction

NMOSD is an autoimmune, inflammatory disorder of the CNS (Wingerchuk *et al.*, 2015) whose classical manifestations include optic neuritis and transverse myelitis.

Up to 80% of NMOSD patients present a serum anti-AQP4 antibody, which is highly specific (Hamid, Elson *et al.*, 2017, Hyun *et al.*, 2016) and pathogenetic (Papadopoulos & Verkman, 2012, Ratelade & Verkman, 2012).

Consequently, current diagnostic criteria allow the achievement of NMOSD diagnosis in AQP4-seropositive patients with both limited and complete manifestations (i.e., recurrent optic neuritis and myelitis). In contrast, AQP4-seronegative patients with similar phenotypes (i.e., idiopathic recurrent optic neuritis [IRON] and idiopathic recurrent myelitis [IRM]) remain unclassified (Wingerchuk et al., 2015) and are usually considered as prodromal phases of MS.

The uncertain categorization of these patients prevents standardized management, and their treatment is based on physicians' personal experience (Waschbisch, Atiya et al., 2013).

AQP4-seronegative patients with a complete phenotypical expression (at least two core clinical features) and typical MRI are included in the NMOSD, but it is still controversial whether they should be considered separate entities.

In fact, despite a similar demographic profile, AQP4-seronegative patients usually experience a monophasic rather than relapsing-remitting course, suffer more disabling attacks, and have an overall better long-term prognosis (Jarius, Ruprecht et al., 2012). AQP4-seronegative patients with an antibody targeting MOG can be diagnosed as NMOSD if meeting the above-listed requirements, although current evidence suggests their belonging to the separate entity of MOGAD. Anti-MOG patients have a lower female to male ratio, a younger age of onset, better clinical recovery, and a tendency to steroid-dependence (Cobo-Calvo, Ruiz et al., 2018, Jarius, Ruprecht et al., 2016).

MRI is a fundamental paraclinical tool in the diagnostic work-up of inflammatory disorders of the CNS (Wingerchuk et al., 2015), and MRI-based algorithms were proposed to discriminate between NMOSD and MS, which represents its primary differential diagnosis (Cacciaguerra et al., 2019b, Matthews et al., 2013b).

Deep-learning (DL)-based imaging diagnostics is a form of artificial intelligence, which allows a classification of input images without any *a priori* human intervention (LeCun, Bengio et al., 2015).

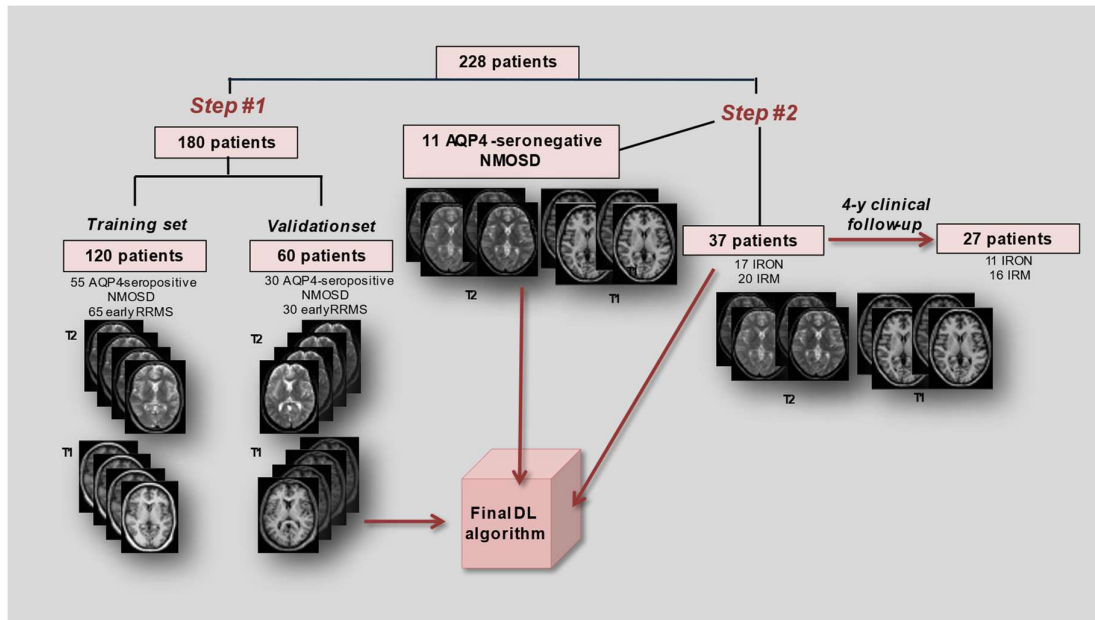
DL might benefit from other image features (undetectable by human eyes), such as the relationship between contiguous image voxels, image intensity histograms, texture, and atrophy, aside from lesion distribution (McBee, Awan et al., 2018), hence possibly providing a structurally based classification of diseases.

In this study, we applied DL to conventional brain MRI scans from NMOSD and MS patients. In the first step of the study, we trained and validated a DL algorithm to discriminate between AQP4+NMOSD and MS patients. Then, we ran the validated algorithm on a cohort of AQP4-seronegative NMOSD and a cohort of unclassified AQP4-seronegative patients with NMOSD-like manifestations to test whether DL classified these subjects as NMOSD or MS. Finally, we compared the DL classification of AQP4-seronegative patients with NMOSD-like manifestations with their clinical follow-up.

Patients and Methods

Patients. **Figure 6.6.1** provides a schematic representation of subjects and study design. Two hundreds-twenty-eight patients were recruited at two European Centers (Milan, Italy, n=124 and Belgrade, Serbia, n=104) from February 2010 to December 2019, except for AQP4-seronegative patients with NMOSD-like manifestations, who were acquired until April 2015. The study population included 85 AQP4+NMOSD patients, 95 early RR MS patients (Thompson et al., 2018), 11 AQP4-seronegative NMOSD patients (three/11 with anti-MOG-IgG), and 37 unclassified AQP4-seronegative patients with NMOSD-like manifestations (17 IRON and 20 IRM).

Figure 6.1.1. Schematic representation of the study design. The work was structured in two consecutive steps. Starting from a population of 228 patients, during the first step we trained and validated an in-house implemented DL algorithm to classify AQP4+NMOSD and MS patients according to their T2- and T1-weighted MRI images. In the second step, AQP4-seronegative NMOSD patients and AQP4-seronegative patients with limited NMOSD manifestations (IRON and IRM) were classified as NMOSD or MS by the validated DL algorithm. The classification of IRON and IRM was compared to their clinical follow-up. Modified from Cacciaguerra et al., *Journal of Neurology* 2021 (Cacciaguerra et al., 2022d), reused with permission (license: 5431700228343).



Abbreviations: DL=deep-learning; AQP4=aquaporin-4; NMOSD=neuromyelitis optica spectrum disorders; MS=multiple sclerosis; IRON=idiopathic recurrent optic neuritis; IRM=idiopathic recurrent transverse myelitis; T1=T1-weighted images; T2=T2-weighted images.

NMOSD diagnosis was achieved according to the most recent criteria (Wingerchuk et al., 2015).

To avoid the bias of higher lesion load and specific lesion distribution in MS, we enrolled subjects at the beginning of their neurologic history, such as patients at the time of MS diagnosis (according to the 2017 revision of McDonald criteria, n=56), and patients at the time of their first clinical neurological event (clinically isolated syndrome [CIS] patients, n=39). CIS patients did not fulfill MS diagnostic criteria at the time of MRI acquisition but evolved to MS during their clinical follow-up (Thompson et al., 2018).

For all patients, exclusion criteria were intravenous steroid administration within the last four weeks before MRI, previous history of other neurological or psychiatric comorbidities, head or spinal cord trauma, and substance abuse.

To be included, seronegative unclassified patients with NMOSD-like manifestations were tested negative for both anti-AQP4-IgG and anti-MOG-IgG with cell-based assay (Tobin, Weinshenker et al., 2014, Wingerchuk et al., 2015).

The IRON group included patients suffering at least two episodes of optic neuritis, defined as an acute visual loss associated with at least two out of pain during eye movement, color desaturation, afferent pupillary defects, abnormal visual evoked potentials, and centro-cecal field deficit (Waschbisch et al., 2013). IRM patients had at least two episodes of transverse myelitis, defined as an acute inflammatory spinal cord syndrome characterized by a nadir between four to 21 days from symptoms onset (Transverse Myelitis Consortium Working, 2002). For IRON and IRM patients, exclusion criteria were concomitant infections, metabolic or vascular disorders, genetic diseases, optic nerve or spinal cord compression, and other autoimmune or granulomatous diseases. By definition, IRON and IRM patients did not fulfill MS MRI criteria for dissemination in space (Thompson et al., 2018).

Clinical variables. Within 48 hours from MRI acquisition, all patients received a complete neurological evaluation, including the EDSS (Kurtzke, 1983) and ongoing treatments. Whenever possible, we collected the presence of oligoclonal bands in the CSF and the clinical evolution of IRON and IRM patients after a minimum follow-up of one year.

MRI acquisition protocol. All patients underwent a conventional brain MRI protocol including T2- and T1-weighted sequences with a 3.0 T (Intera, Philips Medical Systems, Best, the Netherlands, in Milan) and a 1.5 T scanner (Achieva, Philips Medical Systems, in Belgrade): axial dual-echo turbo spin-echo (TSE) (Milan: repetition time [TR]/echo time [TE]=2599/16-80 milliseconds [ms], echo train length [ETL]=6, flip angle [FA]=90°, matrix=256x256, field of view [FOV]=240x240 mm², 44 3-mm-thick slices; Belgrade: TR/TE=3141/20–100 ms, ETL=6, FA=90°, matrix =256x256, FOV =240x240 mm², 44 3-mm-thick slice), axial 3D T1-weighted gradient-echo scans (Milan: fast field echo (FFE), TR/TE=25/4.6 ms, FA=30°, matrix=256x256; FOV=230x230 mm², 220 0.8-mm-thick slices; Belgrade: turbo field echo: TR/TE =7.2/3.2 ms; inversion time [TI] = 1.000 ms; FA=8, matrix= 256x256, FOV=256x256 mm², 180 1-mm-thick slices).

MRI data preprocessing. Brain T2 and T1 LV were measured using a local thresholding segmentation technique (Jim version 8.0, Xinapse Systems Ltd).

From each patient, axial T1-weighted and T2-weighted images were registered on the MNI 152 atlas space (<https://fsl.fmrib.ox.ac.uk/fsl/fslwiki/Atlases>) applying an affine transformation (FLIRT, FSL toolbox, version 5.0.5) to obtain comparable anatomical locations among patients, without modifying their brain anatomy through the addition of a non-linear registration. Coregistered T1-weighted and T2-weighted images in the MNI space were the input to the DL algorithm.

AQP4+NMOSD and MS patients (n=180) were randomly 2:1 assigned to a training (n=120) and a validation set (n=60). AQP4-seronegative patients were used as a test set (n=48, including 11 AQP4-seronegative NMOSD, 20 IRM, and 17 IRON). To deal with MRI data heterogeneity, both the training and the validation sets were balanced between the two centers. The diversification of the training data may increase generalization by enabling the system to ignore variations due to the measurement process and even become applicable to multiple data acquisition procedures.

Once the training and validation were completed, the optimized convolutional neural network (CNN) architecture was applied to the unseen images of the test set. The output of the model was a probability value for each patient to belong to each disease class. A threshold (t) was applied to output values ($t \geq 0.5$) to classify patients.

Network architecture. We used an in-house implemented DL pipeline adapted from the ResNet architecture (Kaiming H., 2016) (Russakovsky* O., 2015). The network architecture consisted of a sequence of four 3D convolutional blocks for each MR image (T2- and T1-weighted) subsequently merged, followed by a fully connected layer. Each block was composed of a 3x3x3 convolutional layer, followed by a Rectified Linear Unit (ReLU) activation function (Hinton, 2010).

A max-pooling layer followed the activation function to reduce computational costs and overfitting (Gu, 2015). A dropout function was added to each block's final layer, randomly deactivating half of the outputs in a layer during the training phase, forcing it to learn the same information using different nodes (Nitish Srivastava, 2014). To obtain a good accuracy of neural network classification without exceeding the number of model parameters to fit, the previously described block was repeated just four times for each of the two MR image contrasts (T2-weighted and T1-weighted), and outputs were concatenated. A final fully connected layer (dense layer) was included to connect each

input to each output of the previous convolutional concatenated layer, which performed a classification according to the previously extracted features. It outputs a vector of disease probability representing each patient's probability of belonging independently to each classification label (S.H. Shabbeer Basha, 2019).

Implementation details and data augmentation. We performed both rotation (30 degrees in the axial plane) and left-right flipping on the training and validation sets. Image intensities were normalized across different MRI by subtracting each training and validation image by the mean intensity and dividing by the intensity standard deviation (Y. Lecun, 1998).

The four convolutional layers filtered the input images with 32, 28, 24, and 12 kernels of size 3x3x3 and with a stride of 13 pixels, respectively. The size of the fully-connected layer was 265, whereas the max-pooling window size was 2x2x2. The Adam optimization algorithm was selected with a loss rate of 0.001 (Diederik P. Kingma, 2015). To prevent overfitting, “early stopping” was added to the training, and the final network parameters were extracted from the epoch with the lowest error before interruption (Diederik P. Kingma, 2015, Yao Yuan, 2007).

Using Keras library with Theano backend, the DL architecture was implemented in Python language 2.7.14. A Dell PowerEdge T630 Linux was used for this study, including high-performance GPU NVIDIA Tesla K40, with 2880 CUDA cores and High-Frequency Intel Xeon E5–2623 v3 and 78 GB of memory overall.

DL metrics. Classification accuracy, mean absolute error (MAE), and mean squared error (MSE) between the labels and the predictions were estimated by the model during the training and the cross-validation phase.

On the test set, global accuracy of the DL algorithm (accuracy=true positive (TP) classification/ total number of patients) and false positive rate (FPR) between prediction and true classification ($FPR=FP/[FP+TP]$, where FP is the number of patients falsely classified as belonging to a class) were calculated for the DL classification of AQP4+NMOSD patients and AQP4-seronegative patients with NMOSD-like manifestations.

For the latter group, a follow-up evolution contrary to the classification (i.e., diagnosis of MS in a patient classified as NMOSD) was considered an algorithm failure. We computed a ROC curve to illustrate the performance of the DL method on the test set.

Statistical analysis. Between-group comparisons of independent continuous variables were performed with two-sample t-test/ANOVA or Mann-Whitney U-test/Kruskal-Wallis test according to the normality assumption and the number of groups. In case of paired samples, non-parametric Wilcoxon test was applied. Categorical variables were compared with Pearson χ^2 or Fisher exact test.

Results

Clinical, demographic, and conventional MRI variables. AQP4+NMOSD patients were older ($p < 0.001$) and more disabled ($p < 0.001$) than MS patients. The AQP4-seronegative cohort had a sex distribution similar to MS and CSF oligoclonal bands expression similar to AQP4+NMOSD patients. Age, disease duration, and EDSS of AQP4-negative patients were intermediate between MS and AQP4+NMOSD.

The proportion of patients with T2-hyperintense brain lesions was similar between AQP4+NMOSD patients and MS patients (95.3% vs 96.8%, $p = 0.48$), but higher than AQP4-seronegative patients (68.7%, $p < 0.001$ vs both). T2 LV was similar among all groups (Table 6.1.1). Table 6.1.2 reports details of clinical and MRI features of AQP4-seronegative patients.

Table 6.1.1. Main demographic, clinical, and MRI data of the studied populations. Significant p values are shown bold.

	AQP4-seropositive NMOSD (n=85)	MS (n=95)	p	All AQP4-seronegative patients (NMOSD plus unclassified) (n=48)	p vs AQP4-seropositive NMOSD	p vs MS
Female/Male	70/15	63/32	0.01^a	31/17	0.03^a	0.85 ^a
Mean age (SD) [years]	46.1 (12.9)	32.7 (10.1)	<0.001^b	39.2 (12.9)	0.004^b	0.001^b
Median disease duration (IQR) [years]	6.0 (2.0-11.0)	2.2 (0.25-3.0)	<0.001^c	3.0 (2.0-8.0)	0.02^c	0.001^c

Median EDSS (IQR)	4.5 (3.0-6.5)	1.5 (1.0-2.0)	<0.001^c	2.0 (1.5-4.0)	<0.001^c	<0.001^c
Median n° of myelitides (range)	2 (0-15)	0 (0-2)	<0.001^c	2 (0-9)	0.06 ^c	<0.001^c
Median n° of optic neuritides (range)	1 (0-16)	0 (0-1)	<0.001^c	1 (0-16)	0.92 ^c	<0.001^c
Patients with oligoclonal bands (%)	23/67 (34.3)	50/68 (73.5)	<0.001^a	25/42 (59.5)	0.54 ^{\$}	<0.001^a
Patients with visible T2-hyperintense lesions (%)	81/85 (95.3)	92/95 (96.8)	0.48 ^a	33/48 (68.7)	<0.001^a	<0.001^a
Mean T2 LV (SD) [ml]	2.9 (6.5)	4.0 (5.7)	0.25 ^b	2.4 (7.8)	0.66 ^b	0.17 ^b
Mean T1 LV (SD) [ml]	1.4 (3.7)	3.3 (4.5)	0.01^b	1.3 (4.7)	0.88 ^b	0.03^b
Treatments						
- None	16 (18.8)	39 (41.1)	<0.001^a	9 (18.7)	0.95 ^a	0.005^a
- First line	35 (41.2) ¹			21 (43.7) ³		
- Second line	34 (40.0) ²	40 (42.1)		18 (37.5) ⁴		
		16 (16.8)				

^aPearson χ^2 ; ^btwo-sample t test; ^cMann–Whitney U test.

¹Azathioprine (n=24), oral steroids (n=10), mycophenolate mophetil (n=1); ²rituximab (n=23), tocilizumab (n=3), other (cyclophosphamide, hematopoietic stem cell transplantation, intravenous immunoglobuline, n=8).

³Azathioprine (n=12), oral steroids (n=6), mycophenolate mophetil (n=3); ⁴rituximab (n=8), tocilizumab (n=1), other (cyclophosphamide, hematopoietic stem cell transplantation, intravenous immunoglobuline, n=9).

Abbreviations: AQP4=aquaporin-4; NMOSD=neuromyelitis optica spectrum disorders; RRMS=relapsing-remitting multiple sclerosis; SD=standard deviation; IQR=interquartile range; LV=lesion volume.

Table 6.1.2. Main demographic, clinical and MRI data of AQP4-seronegative patients. Significant p values are shown bold.

	AQP4-seronegative NMOSD (n=11)	IRON (n=17)	IRM (n=20)	p
Female/Male	8/3	11/6	12/8	0.77 ^a
Mean age (SD) [years]	34.9 (10.1)	39.12 (14.8)	41.6 (12.5)	0.44 ^b
Median disease duration (IQR) [years]	3.0 (3.0-8.0)	6.0 (2.0-8.0)	3.0 (2.0-5.7)	0.31 ^c
Median EDSS (IQR)	4.0 (1.5-4.0)	1.5 (1.0-3.0)	2.5 (1.5-5.5)	0.05^c
Median n° of myelitides (range)	2 (1-6)	-	3 (2-9)	-
Median n° of optic neuritides (range)	1 (0-10)*	3 (2-16)	-	-
N° patients with oligoclonal bands	2/10 (20.0)	4/16 (25.0)	11/16 (68.7)	0.01^a
N° patients with visible T2-hyperintense lesions (%)	5/11 (45.4)	12/17 (70.6)	16/20 (80.0)	0.14 ^a
N° patients fulfilling 2017 McDonald criteria for DIS (%)	2/11 (18.2)	0/17 (0.0)	0/20 (0.0)	0.05 ^a
N° patients with clinical follow-up	-	11/17 (64.7)	16/20 (80.0)	0.30 ^a
Median follow-up duration (IQR) [years]	-	3.0 (1.0-4.0)	5.0 (2.5-6.7)	0.09 ^c
Mean T2 LV (SD) [ml]	0.9 (1.7)	0.42 (0.7)	4.8 (11.9)	0.19 ^b
Mean T1 LV (SD) [ml]	0.47 (1.0)	0.18 (0.3)	2.7 (7.0)	0.22 ^b
Treatments				
- None	1/11 (9.1)	4/17 (23.5)	4/20 (20.0)	0.71 ^a
- First line	4/11 (36.4) ¹	8/17 (47.1) ³	9/20 (45.0) ⁵	
- Second line	6/11 (54.5) ²	5/17 (29.4) ⁴	7/20 (35.0) ⁶	

¹Azathioprine (n=1), oral steroids (n=3); ²rituximab (n=5), tocilizumab (n=1).

³Azathioprine (n=4), oral steroids (n=1), mycophenolate mophetil (n=3); ⁴rituximab (n=2), other (cyclophosphamide, hematopoietic stem cell transplantation, intravenous immunoglobuline, n=3).

⁵Azathioprine (n=7), oral steroids (n=2); ⁶rituximab (n=1), other (cyclophosphamide, hematopoietic stem cell transplantation, intravenous immunoglobuline, n=6).

^aChi-square/Fisher exact test; ^bANOVA; ^cKruskal-Wallis test.

*The patient without history of optic neuritis suffered an area postrema flare and a myelitis.

Abbreviations: AQP4=aquaporin-4; NMOSD=neuromyelitis optica spectrum disorders; IRON=idiopathic recurrent optic neuritis; IRM=idiopathic recurrent myelitis; DIS=dissemination in space; SD=standard deviation; IQR=interquartile range; LV=lesion volume.

DL classification of AQP4+NMOSD and MS patients. The training set included a total of 120 patients (55 AQP4+NMOSD and 65 MS), whereas the validation set included 60 patients (30 MS and 30 AQP4+NMOSD). Clinical, demographic, and conventional MRI features of the two sets were similar, and the distribution of patients between the two participating centers in the training and validation sets was balanced (**Table 6.1.3**).

In the training and validation set, the DL algorithm had a diagnostic accuracy of 0.97-0.95, an MAE of 0.17-0.21, and an MSE of 0.05-0.07, respectively.

Table 6.1.3. Main demographic, clinical, and MRI data of the training and validation sets. Significant p values are shown bold.

Demographic, clinical, and MRI data						
	Training set		Validation set		p Training vs Validation	
	AQP4-seropositive NMOSD (n=55)	MS (n=65)	AQP4-seropositive NMOSD (n=30)	MS (n=30)	AQP4-seropositive NMOSD	MS
Patients from Milan/Belgrade	25/30	36/29	14/16	15/15	0.91 ^a	0.66 ^a
Female/Male	47/8	39/26	23/7	24/6	0.31 ^a	0.06 ^a
Mean age (SD) [years]	47.7 (12.4)	32.6 (9.4)	43.2 (13.6)	32.7 (11.7)	0.14 ^b	0.96 ^b
Median disease duration (IQR) [years]	8.0 (2.0-12.0)	2.4 (0.3-3.0)	3.0 (1.7-9.5)	2.0 (0.2-2.7)	0.17 ^c	0.93 ^c
Median EDSS (IQR)	6.0 (3.5-7.5)	1.5 (1.0-2.0)	3.5 (2.0-5.5)	1.0 (1.0-2.0)	0.005^c	0.18 ^c
Mean T2 LV (SD) [ml]	2.5 (4.3)	4.5 (6.3)	3.7 (9.3)	2.9 (2.9)	0.42 ^b	0.15 ^b
Mean T1 LV (SD) [ml]	1.1 (2.0)	3.7 (5.0)	2.0 (5.7)	2.2 (2.7)	0.32 ^b	0.30 ^b

^aPearson χ^2 ; ^b2-sample t test; ^cMann–Whitney U test.

Abbreviations: AQP4=aquaporin-4; NMOSD=neuromyelitis optica spectrum disorders; MS=multiple sclerosis; SD=standard deviation; IQR=interquartile range; LV=lesion volume.

DL classification of AQP4-seronegative NMOSD patients. Eleven/48 (22.9%) patients of the AQP4-seronegative cohort had a diagnosis of AQP4-seronegative NMOSD. Three/11 (27.3%) AQP4-seronegative NMOSD had anti-MOG-IgG. All AQP4-seronegative NMOSD patients were classified as NMOSD. Their median classification probability of being NMOSD was higher than MS (0.74 vs 0.25, $p=0.003$).

DL classification of unclassified AQP4-seronegative patients with NMOSD-like manifestations and comparison with their clinical follow-up. In the AQP4-seronegative cohort, 20/48 patients (41.7%) were IRM, and 17 (35.4%) were IRON.

The DL algorithm classified all IRM and 16/17 (94.1%) IRON patients as NMOSD, with a median probability of NMOSD diagnosis equal to 0.99 (interquartile range [IQR]=0.97-1.00) and 0.99 (IQR=0.84-0.99) respectively.

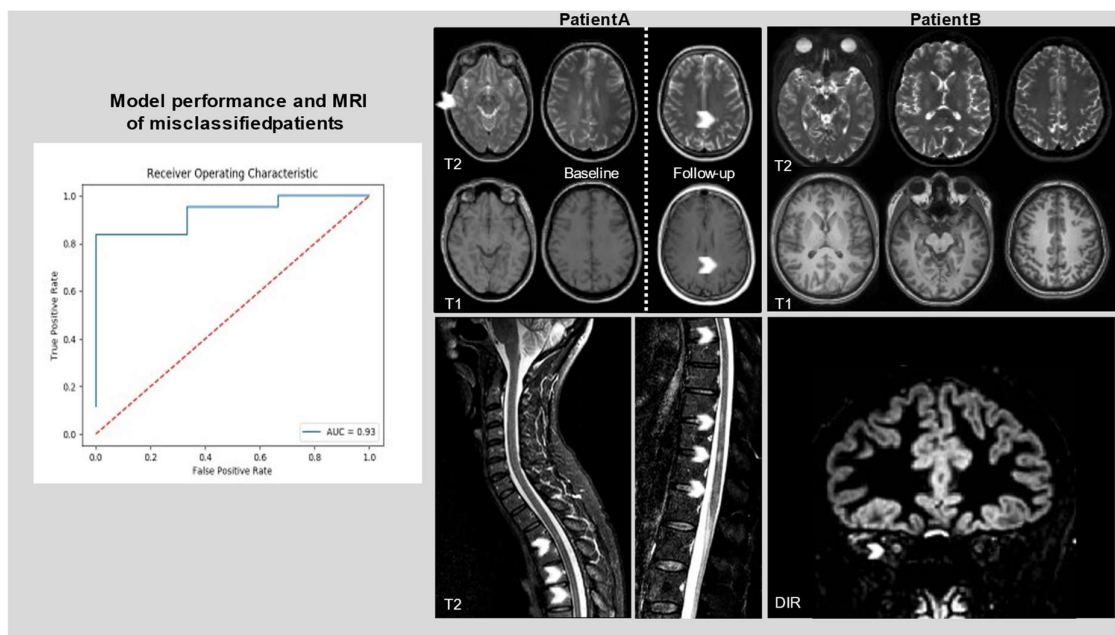
A clinical follow-up was available in 27/37 (73.0%) patients (16/20 IRM, median follow-up=5.0 years, IQR=2.5-6.7; 11/17 IRON, median follow-up=3.0 years, IQR=1.0-4.0). Treatments at follow-up included: cyclophosphamide (38.0%), intravenous immunoglobulins (3.4%), rituximab (13.8%), azathioprine (34.5%) and mycophenolate mofetil (10.3%).

Only one patient with IRM evolved to MS at follow-up; three patients developed NMOSD, and the remaining did not change phenotype (including the IRON patient classified as MS by the CNN). Therefore, the performance of the CNN had a global accuracy of 0.93 and FPR of 0.04. The ROC curve illustrating the model performance is reported in **Figure 6.1.2**.

Figure 6.1.2. Model performance and MRI images of the two AQP4-seronegative patients misclassified by the DL algorithm. ROC curve showing the model performance, corresponding to an AUC of 0.93. Patient A: Patient affected by IRM, developing MS at follow-up. Baseline MRI shows a paraventricular brain lesion (visible on T2-weighted sequences only) and multiple spinal cord lesions on short-tau inversion

recovery (STIR) sequence (located at T3, between T5 and T8 [longitudinally extensive myelitis], between T11 and T12, and involving the conus medullaris). At follow-up, a new gadolinium-enhancing juxtacortical lesion is visible.

Patient B: Patient affected by IRON. Brain MRI shows no visible hyperintense lesions, whereas a hyperintense right optic nerve lesion is visible on double inversion recovery (DIR) sequence. Modified from Cacciaguerra et al., Journal of Neurology 2021 (Cacciaguerra et al., 2022d), reused with permission (license: 5431700228343).



Abbreviations: DL=deep-learning; IRM=idiopathic recurrent myelitis; MS=multiple sclerosis, NMOSD=neuromyelitis optica spectrum disorders; T=thoracic spinal cord; IRON=idiopathic recurrent optic neuritis; ROC=receiver operating characteristics; AUC=area under the curve.

In the three patients developing NMOSD, the diagnosis was done after a median follow-up of 3.0 years (range=1.0-4.0) following a clinical relapse associated with anti-AQP4-IgG (n=2) and anti-MOG-IgG (n=1). The CNN algorithm classified these patients as NMOSD with a median probability of 1.0 (range=0.84-1.0) vs a probability of being MS of 0.09 (range=0.09-0.16).

The DL classification of AQP4-seronegative NMOSD patients and unclassified AQP4-seronegative patients with NMOSD-like manifestations are reported in **Table 6.1.4**.

Notably, although the DL classified the four subjects with anti-MOG-IgG as NMOSD, the median probability was similar to that of MS (0.61 vs 0.37, p=0.07).

Table 6.1.4. DL-estimated classification of AQP4-seronegative NMOSD patients and unclassified AQP4-seronegative patients with NMOSD-like manifestations. For unclassified AQP4-seronegative patients with NMOSD-like manifestation, data are restricted to those with clinical follow-up. All p values refer to non-parametric Wilcoxon test for paired samples. Significant p values are shown bold.

	DL Classification		
	Median NMOSD p (IQR)	Median MS p (IQR)	p
AQP4-seronegative NMOSD	n=11		
	0.74 (0.56-0.81)	0.25 (0.14-0.41)	0.003
AQP4-seronegative NMOSD (anti-MOG excluded)	n=8		
	0.78 (0.66-0.94)	0.24 (0.14-0.35)	0.01
AQP4-seronegative NMOSD with anti-MOG-IgG*	n=4		
	0.61 (0.51-0.72)	0.37 (0.24-0.41)	0.07
IRON	n=8		
	0.99 (0.87-1.00)	0.09 (0.07-0.23)	0.03
IRM	n=14		
	0.98 (0.90-1.00)	0.06 (0.04-0.01)	0.001

*Range instead of IQR.

Abbreviations: AQP4=aquaporin-4; NMOSD=neuromyelitis optica spectrum disorders; MS= multiple sclerosis; MOG= myelin oligodendrocyte glycoprotein; IRON=idiopathic recurrent optic neuritis; IRM=idiopathic recurrent myelitis; IQR=interquartile range.

Discussion of DL misclassified patients. The IRM patient developing MS was classified as NMOSD (p=1.00 vs 0.03). At MRI, the patient had a 13-year-old history of IRM (five episodes) and oligoclonal bands. Six years after an initial treatment with cyclophosphamide, followed by azathioprine, the patient developed a juxtacortical brain lesion (**Figure 6.1.2**).

The patient classified as MS ($p=0.92$ vs 0.09) was a patient with IRON (3 episodes, disease duration 2.0 years), no oligoclonal bands, and no visible brain lesions. The patient was treated with an anti-CD20 drug (rituximab).

MRI scans of the two misclassified patients are shown in **Figure 6.1.2**.

Discussion

In this work, we implemented a DL algorithm discriminating between AQP4+NMOSD and MS patients with high accuracy.

It was applied to a group of AQP4-seronegative NMOSD, who were all classified so, and to a group of unclassified AQP4-seronegative patients with NMOSD-like manifestations (IRON and IRM), who were all but one classified as NMOSD.

At clinical follow-up, unclassified AQP4-seronegative patients did not usually evolve to MS.

Several MRI-based criteria to differentiate between MS and NMOSD have been proposed, showing an overall sensitivity equal to 0.92 and a specificity of 0.91-0.96 (Cacciaguerra et al., 2019b, Jurynczyk et al., 2017c, Matthews et al., 2013b). Accordingly, clinicians must identify or rule-out several qualitative MRI-criteria which can discriminate between the two disorders. However, despite their excellent performance in highly specialized settings, such criteria require a subjective interpretation of MRI features, with consequent possible misdiagnosis, as observed with MS criteria (Solomon, Bourdette et al., 2016).

Other MRI measures, such as brain volumes and cortical thickness, were used in a machine learning approach to overcome this issue but with lower accuracy (0.74-0.80) (Eshaghi et al., 2016).

DL can independently identify image classification features and can potentially benefit from image characteristics undetectable by a human eye (McBee et al., 2018). However, the high number of images corresponding to a single scan, hence requiring a more complex computational algorithm, has limited its application on MRI exams.

Our classification algorithm achieved a diagnostic accuracy of at least 0.95 in both the training and the validation cohort, using images from two different centers with different MRI protocols and scanners (1.5 T and 3.0 T). Since 7/120 (5.8%) of our patients (equally distributed between the NMOSD and MS cohort) were lesion-free, differently from

previously published algorithms, the CNN model likely learned the classification also from other features than lesions, as a further potential advantage.

The application of our CNN algorithm to the AQP4-seronegative NMOSD cohort classified all these patients as NMOSD, supporting their current inclusion into the NMO spectrum.

Interestingly, with the small sample size limitation, anti-MOG patients showed similar probabilities of belonging to the MS or the NMOSD class, possibly mirroring their different pathological substrates.

In line with this, anti-MOG disease is likely a demyelinating disorder rather than an astrocytopathy.

Levels of myelin-basic protein are increased in the CSF of anti-MOG patients, while biomarkers of astrocyte damage (GFAP and S100 calcium-binding protein B [S100B]) are normal. Opposite findings, more in line with a mechanism of damage similar to AQP4+NMOSD, were unraveled in double-seronegative NMOSD (Alves Do Rego & Collongues, 2018, Wei, Chang et al., 2018).

Despite several epidemiologic discrepancies between AQP4+NMOSD and seronegative patients (Jarius et al., 2012), their primary clinical outcomes are independent of serostatus (Mealy, Kim et al., 2018), and MRI lesion distribution (Cacciaguerra et al., 2019b, Wang, Chen et al., 2018) or brain occult damage (Sun, Sun et al., 2017) are likely to be similar, possibly explaining the classification of our CNN algorithm.

Additionally, since all AQP4-seronegative NMOSD patients were classified as NMOSD (thus reaching a diagnostic accuracy of 1.0 in this group), a DL approach is potentially useful for clinical practice, as no biomarkers for seronegative NMOSD diagnosis are currently available (Wingerchuk et al., 2015).

The final part of our experiment tried to assess whether unclassified AQP4-seronegative patients with NMOSD-like manifestations limited to the optic nerve or spinal cord are more similar to AQP4+NMOSD or MS patients. Using updated assays (cell-based assay and fluorescence-activated cell-sorting assay), the retrospective evaluation of sera from patients suffering immune-mediated IRON and recurrent longitudinally extensive transverse myelitis allowed to detect AQP4-IgG or anti-MOG-IgG in a significant proportion (Alvarenga, Alvarenga et al., 2012, Jiao, Fryer et al., 2014, Petzold, Woodhall et al., 2019). From a clinical perspective, visual and motor outcomes of IRON and IRM

patients were consistently rated as similar to those of AQP4+NMOSD patients (Carnero Contentti, Hryb et al., 2017, Deschamps, Gueguen et al., 2018, Jiao et al., 2014).

However, other pieces of evidence point out possible disease heterogeneity. For instance, among IRON patients, only the subgroup of those with “chronic relapsing inflammatory optic neuropathy” (CRION), characterized by steroid-dependence or by early relapse during steroid tapering, showed increased seral levels of GFAP and S100B, in contrast to those with recurrent isolated optic neuritis (RION) (Petzold et al., 2019). Similarly, pathological data from a single patient suffering recurrent episodes of myelitis showed several features compatible with NMOSD, such as vessel wall hyalinization and necrosis, and atypical manifestations like a prominent T cell infiltrate and a diffuse rather than localized complement deposition (Takahashi-Fujigasaki, Takagi et al., 2009). However, this patient was also affected by hepatitis C, which could have biased pathological findings.

Our results suggest that the brain structure of unclassified AQP4-seronegative patients with NMOSD-like manifestations is similar to that of AQP4+NMOSD. Furthermore, these patients are likely to evolve to NMOSD or to maintain their clinical phenotype rather than evolving to MS.

Moving to limitations, the DL approach is biased by the “black-box” issue. In fact, the algorithm does not provide the features relevant for patients’ classification, preventing a comprehensive model interpretability. Since the identification of these key elements could provide both hints on pathophysiological processes and relevant information for clinical practice, there is a growing research area aimed to explain neural network decision (Castelvecchi, 2016). Therefore, it is likely that in the nearby future, studies will overcome this limitation.

Second, our algorithm did not include spinal cord imaging as input, which might further contribute to the classification of these patients. Finally, we cannot exclude that ongoing immunosuppressive treatment, or the relatively short duration are responsible for the low rate of AQP4-IgG and MOG-IgG at follow-up.

Conclusions

To the best of our knowledge, this is the first study applying a DL technique to solve the clinical challenge of unraveling the spectrum of NMO. This completely blinded approach

provided supportive evidence to the current NMOSD classification by correctly classifying AQP4-seronegative NMOSD patients, with a further advantage of being a promising tool for their diagnostic work-up.

Moreover, this method suggested starting points for further debates. Anti-MOG patients have intermediate brain features between NMOSD and MS, in line with the emerging concept of MOGAD. Also, the DL revealed, at least from an imaging perspective, a structural similarity between AQP4-seronegative patients with NMOSD-like manifestations and patients with AQP4+NMOSD, questioning whether we could expand the spectrum of NMO to these seronegative unclassified patients.

6.2. Tumefactive demyelination in MOG antibody-associated disease versus other demyelinating disorders

Cacciaguerra et al., unpublished data.

Abstract

Background and Objectives. Studies on tumefactive brain lesions in myelin-oligodendrocyte-glycoprotein-IgG-associated disease (MOGAD) are lacking. We sought to characterize the frequency, clinical, laboratory, and MRI features of these lesions in MOGAD and compare them to multiple sclerosis (MS) and aquaporin-4-IgG-positive-neuromyelitis-optica-spectrum-disorder (AQP4+NMOSD).

Methods. We retrospectively searched 194 MOGAD and 359 AQP4+NMOSD patients with clinical/MRI details available from the Mayo Clinic databases and included those with ≥ 1 tumefactive brain lesion (maximum transverse diameter ≥ 2 cm) on MRI. Tumefactive MS patients were identified using the Mayo Clinic medical-record-linkage-system. Binary multivariable stepwise logistic regression identified independent predictors of MOGAD diagnosis; Cox proportional regression models were used to assess the risk of relapsing disease and gait aid in tumefactive *vs.* non-tumefactive MOGAD patients.

Results. We included 108 patients with tumefactive demyelination (MOGAD=43; AQP4+NMOSD=16; MS=49). Tumefactive lesions were more frequent among MOGAD (43/194[22%]) than AQP4+NMOSD (16/359[5%]) ($p < 0.001$). Risk of relapse and need for gait aid were similar in tumefactive and non-tumefactive MOGAD. Clinical features more frequent in MOGAD than MS included headache (18/43[42%] *vs.* 10/49[20%]; $p = 0.03$) and somnolence (12/43[28%] *vs.* 2/49[4%]; $p = 0.003$), the latter also more frequent than AQP4+NMOSD (0/16[0%]; $p = 0.02$). The presence of: peripheral T2-hypointense rim, T1-hypointensity, diffusion restriction (particularly an arc pattern), ring enhancement, Balo'-like or cystic appearance favored MS over MOGAD ($p \leq 0.001$). MRI features were broadly similar in MOGAD and AQP4+NMOSD, except for more frequent diffusion restriction in AQP4+NMOSD (10/15[67%]) than MOGAD (11/42[26%], $p = 0.005$). CSF fluid analysis revealed less frequent positive oligoclonal bands in MOGAD (2/37[5%]) than MS (30/43[70%]) ($p < 0.001$) and higher median white cell count in MOGAD than MS (33 *vs.* 6 cells/ μ l, $p < 0.001$). At baseline, independent

predictors of MOGAD diagnosis were presence of somnolence/headache, absence of T2-hypointense rim, lack of T1-hypointensity, and no diffusion restriction (Nagelkerke R Squared=0.67). Tumefactive lesion resolution was more common in MOGAD than MS or AQP4+NMOSD and improved model performance.

Discussion. Tumefactive lesions are frequent in MOGAD but are not associated with a worse prognosis. The clinical, MRI, and CSF attributes of tumefactive MOGAD differ from tumefactive MS, and are more similar to tumefactive AQP4+NMOSD with the exception of lesion resolution, which favors MOGAD.

Introduction

MOGAD is a recently defined inflammatory demyelinating disease of the CNS, distinct from MS, and AQP4+NMOSD (Jarius, Paul et al., 2018, Reindl & Waters, 2019). Given the partial clinical overlap of these diseases with acute attacks involving the brain, optic nerve and spinal cord, efforts have focused on their radiological characterization using MRI.

Tumefactive brain lesions (≥ 2 cm maximum transverse diameter) (Hardy & Chataway, 2013) are a rare but well-recognized manifestation of inflammatory CNS disorders (Kim et al., 2015, Lucchinetti, Gavriloova et al., 2008, Shu, Long et al., 2019). They can be accompanied by severe clinical manifestations (with potential for intensive-care unit admission), and often represent a diagnostic challenge for neurologists, especially when encountered in isolation as initial manifestation of the disease (Sinha, Banwell et al., 2022, Vakharia, Kamal et al., 2018).

These lesions have been described in up to 2% of patients with MS (Fereidan-Esfahani, Decker et al., 2022), 3% of patients with AQP4+NMOSD (Cacciaguerra et al., 2019b), and during MOGAD attacks (Banks, Morris et al., 2020, Shu et al., 2019). However, the frequency of this manifestation in MOGAD is still unknown, since no studies have systematically evaluated tumefactive demyelination in this disease.

Previous studies identified MRI patterns accompanying tumefactive demyelination and tumefactive MS to distinguish them from alternative non-demyelinating etiologies (e.g., tumors) (Abou Zeid, Pirko et al., 2012, Lucchinetti et al., 2008). These patterns include a Balò-like appearance, a cystic core, a rim of T2-hypointensity, an arc of restricted diffusion, and a ring or open-ring of enhancement (Abou Zeid et al., 2012, Lucchinetti et al., 2008).

Data on tumefactive demyelination in MOGAD are scarce, but lesions might have different characteristics compared to what is observed in MS and AQP4+NMOSD (Jeong, Kim et al., 2015), assisting in the diagnosis and providing new insights into pathophysiology.

Therefore, in this study we sought to characterize the frequency of tumefactive lesions in MOGAD patients as well as the associated clinical, laboratory, MRI features and outcome, and compare them to MS and AQP4+NMOSD.

Materials and methods

Standard Protocol Approvals, Registrations, and Patient Consents. The study was approved by the Mayo Clinic institutional review board (IRB 08-006647). All patients at or above the age of 18 and the guardians of pediatric patients gave written consent to the passive use of their medical records for research purposes.

Identification of MOGAD patients. We searched our MOGAD databases from 1/1/1996 to 9/1/2020 (including both adults and pediatric patients) and identified 194 patients with clinical and MRI details available. Then, we included those who: 1) had at least one tumefactive T2-hyperintense lesion (maximum transverse diameter ≥ 2 cm) (Hardy & Chataway, 2013); 2) fulfilled current MOGAD criteria (Lopez-Chiriboga, Majed et al., 2018) and were negative for AQP4-IgG. The remaining non-tumefactive MOGAD patients were used as control group to assess the cumulative risk of relapsing disease and disability in MOGAD patients with tumefactive lesions.

Identification of the comparison groups. Patients with AQP4+NMOSD and MS were identified with two different methodologies. We searched our AQP4+NMOSD database (including both adults and pediatric patients) from 1/1/2000 to 8/31/2020 and found 359 patients with clinical and MRI data available. We included those who had at least one tumefactive T2-hyperintense lesion (maximum transverse diameter ≥ 2 cm), fulfilled 2015 diagnostic criteria for NMOSD with AQP4-IgG (Wingerchuk et al., 2015), and were negative for MOG-IgG.

For MS patients, we searched the Mayo Clinic electronic medical record for consecutive patients seen from 1/1/2018 to 12/31/2020 with an ICD10 diagnosis of MS (G35) and “tumefactive” term present in chart via natural language search, and this identified 42 patients and a further 7 patients were identified from a pediatric MS database. Patients had at least one T2-lesion of maximum transverse diameter ≥ 2 cm, fulfilled 2017 revised diagnostic criteria (Thompson et al., 2018) and were negative for both MOG-IgG and AQP4-IgG.

Antibody testing. The analyzed serum and CSF samples were fresh or stored. All MOGAD patients were seropositive for MOG-IgG₁ tested in the Mayo Clinic

Neuroimmunology Laboratory using a live cell-based assay expressing full-length native-conformation human MOG with a cut-off IgG-binding index of ≥ 2.5 , and end-titration of $\geq 1:20$ as previously described (Sechi, Buciuc et al., 2021b). When available, we also reported the end antibody titer, obtained with progressive dilutions of 1:20, 1:40, 1:100, 1:1000, 1:10000 (Sechi et al., 2021b). End-titers were stratified as low (1:20 or 1:40) or high ($\geq 1:100$). When available, MOG-IgG was tested in CSF by fluorescence-activated cell sorting (FACS) assay.

AQP4-IgG was tested with live or fixed cell-based assays as previously described (Redenbaugh, Montalvo et al., 2021, Waters et al., 2012).

Collection of demographic, clinical, and cerebrospinal fluid data. Two neurologists (L.C., E.P.F.) abstracted from medical records the following demographic and clinical data of patients: age, sex, disease duration, EDSS (Kurtzke, 1983) at nadir, neurological manifestations, presence of somnolence, vomiting or nausea, headache, and seizures. CSF data included the detection of oligoclonal bands at any time (including the tumefactive attack), while white blood cell count, protein, and glucose levels were only collected when within 30 days of the attack with the tumefactive lesion(s). We also collected information on if patients underwent brain biopsy and treatment at follow-up.

Long-term prognosis of MOGAD patients with tumefactive lesions. To assess the long-term prognosis of tumefactive MOGAD patients, the occurrence and timing of relapsing disease course, need of a gait aid (i.e., EDSS milestone of 6) and death among our MOGAD cohort with and without tumefactive lesions were also collected.

MRI analysis. In each brain MRI scan, we identified the largest tumefactive lesion as the “index lesion” on the FLAIR sequence or T2-weighted sequence. For each MRI scan we evaluated FLAIR and/or T2-weighted sequences, diffusion-weighted images, and pre- and post-contrast T1-weighted sequences at Mayo Clinic or outside facilities.

In patients with more than one attack associated with a tumefactive lesion, the first one was included in the cross-sectional analysis (i.e., differential diagnosis of tumefactive lesions).

Lesion location

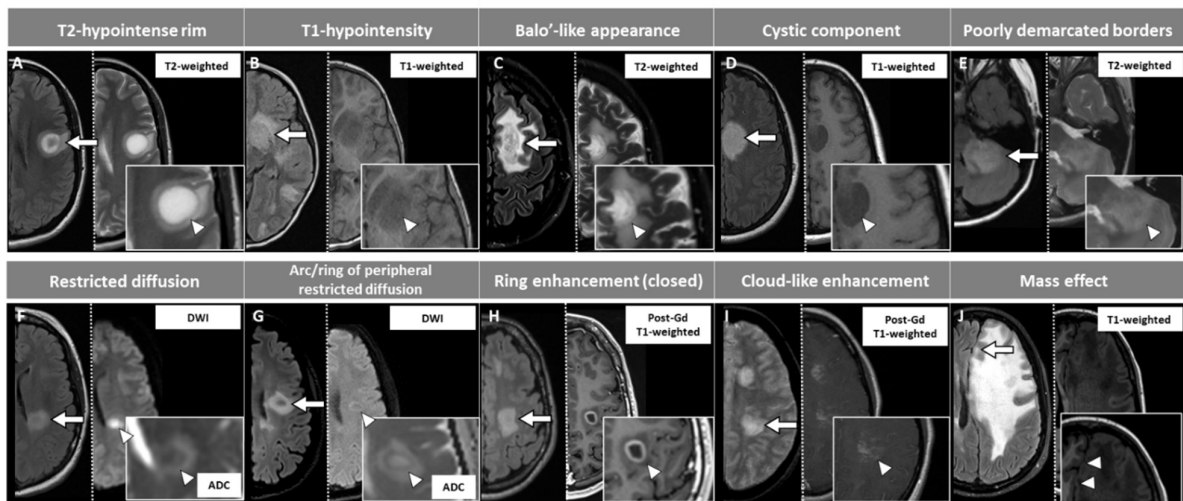
Lesions were classified according to their location into: periventricular (ovoid lesions with the maximum diameter perpendicular to the lateral ventricles and in direct contact with them (Filippi, Preziosa et al., 2019), or any-shaped periventricular lesions), involving other hemispheric white matter, deep grey matter, corticospinal tract, corpus callosum, or infratentorial region.

Index lesion characteristics

Index lesions were independently assessed by a neurologist (Laura Cacciaguerra) and a neuroradiologist, blinded to patients' diagnosis. When there was disagreement, a third blinded reviewer evaluated images in an anonymous fashion for consensus. The definition and pictorial explanation of features evaluated are reported in **Figure 6.2.1**, and included the presence of: (1) T2-hypointense rim on T2-weighted image (Llufriu, Pujol et al., 2010), (2) T1-hypointensity on T1-weighted image (Lucchinetti et al., 2008), (3) Balò-like appearance (Hardy, Tobin et al., 2016), (4) cystic component (Seewann, Enzinger et al., 2008), (5) poorly demarcated borders (i.e., fluffy appearance) (Jurynczyk et al., 2017a), (6) restricted diffusion within the lesion (Schaefer, Grant et al., 2000), (7) arc/ring of peripheral restricted diffusion (Abou Zeid et al., 2012), (8) enhancement on post-contrast T1-weighted images, (9) pattern of enhancement on post-contrast T1-weighted images including: ring (closed if complete, otherwise open) (Llufriu et al., 2010) and cloud-like (Ito, Mori et al., 2009), and (10) mass effect (i.e., if the lesion exerted a secondary effect on adjacent structures such as sulci, ventricles, or midline).

Figure 6.2.1. Pictorial overview of the MRI features evaluated in the study, with corresponding definitions. Lesions are shown by arrows and are displayed on axial T2-fluid-attenuated inversion recovery (T2-FLAIR, left half of each image) and on the most appropriate sequence for the evaluation of each specific feature, indicated by an arrowhead (right half of each image). Exceptions are images E and J, where the second sequence (T2-weighted image in E, and T1-weighted image in J) is reported for descriptive purposes only since the T2-FLAIR sequence is suitable for the visualization of those features. For image I, T2-FLAIR image was unavailable and therefore substituted

with T2-weighted sequence. Features were defined as follows: (A) T2-hypointense rim: rim-shaped relative T2-hypointensity compared to the T2-hyperintensity of the lesion center and surrounding edema; (B) T1-hypointensity: hypointensity on T1-weighted images compared to the normal-appearing white matter; (C) Baló-like appearance: presence of ≥ 2 concentric rings or a pattern of alternating bands of signal intensity on any MRI sequence; (D) Cystic component: T2- or T1-weighted signal of similar intensity to cerebrospinal fluid; (E) Poorly demarcated borders: “fluffy appearance” on T2-FLAIR or T2-weighted sequences; (F) Restricted diffusion: DWI hyperintensity with corresponding hypointensity on the ADC map; (G) Arc/ring of peripheral restricted diffusion: dark peripheral ADC arc or ring with brighter center; (H) Ring-enhancement (closed-ring shown in this figure): circular border of enhancement, closed if complete, otherwise open; (I) Cloud-like enhancement: multiple patchy enhancement with ill-defined margins; (J) Mass effect: lesion exerting a secondary effect on adjacent structures such as sulci, ventricles, or midline.



Abbreviations: ADC=apparent diffusion coefficient map; DWI=diffusion-weighted images; Gd=gadolinium; MRI=magnetic resonance imaging.

Index lesion size and number of T2-hyperintense and enhancing lesions

Additional MRI parameters were recorded or measured including: the maximum diameter (cm) of the index tumefactive lesion, the total number of T2-hyperintense lesions, the

total number of contrast-enhancing lesions, the presence of concomitant multiple tumefactive lesions and the total number of tumefactive lesions.

Lesion evolution and subsequent tumefactive attacks

When available, we analyzed the first follow-up MRI, at least three months from the tumefactive attack, and the last available follow-up MRI scan to assess for complete resolution of the index tumefactive lesion on T2- or T1-weighted images. In those with multiple tumefactive lesions, we compared the MRIs of initial and subsequent tumefactive lesions.

Statistical analysis. We used Kaplan-Meier survival curves with MOGAD patients censored according to their follow-up to represent the cumulative risk of relapses or EDSS of 6 over ten years of disease duration. Proportional Cox regression models with time to relapse as outcome, adjusted for age at onset (continuous variable) and sex (binary variable) were run to calculate adjusted hazard ratio (HR) and corresponding 95% confidence intervals (95%CI).

Between-group comparisons of continuous variables were assessed by using the Kruskal-Wallis test or the independent-sample t test, according to the normality assumption. For categorical variables, comparisons were performed with the Chi-squared tests or Fisher's exact test as appropriate. An exploratory between-group comparison of clinical and radiological features of MOGAD patients according to the age of onset was similarly performed.

A p value of <0.05 was considered significant. To identify clinical and MRI variables associated with MOGAD diagnosis, we first ran univariable binary logistic regression models, and then the significant variables (i.e., those significantly associated with MOGAD vs. the other demyelinating disorders) were included in a binary multivariable stepwise logistic regression (forward selection: likelihood ratio). If separation was encountered, we excluded or merged similar features as described below.

Data availability. Anonymized data used for this study are available upon reasonable request from the corresponding author.

Results

Frequency of tumefactive lesions in MOGAD. We included 43 patients with MOGAD. The frequency of at least one tumefactive brain lesion among the total MOGAD cohort was 22% (43 of 194) and even higher when only patients with inflammatory brain lesions were considered (43 of 88, 49%).

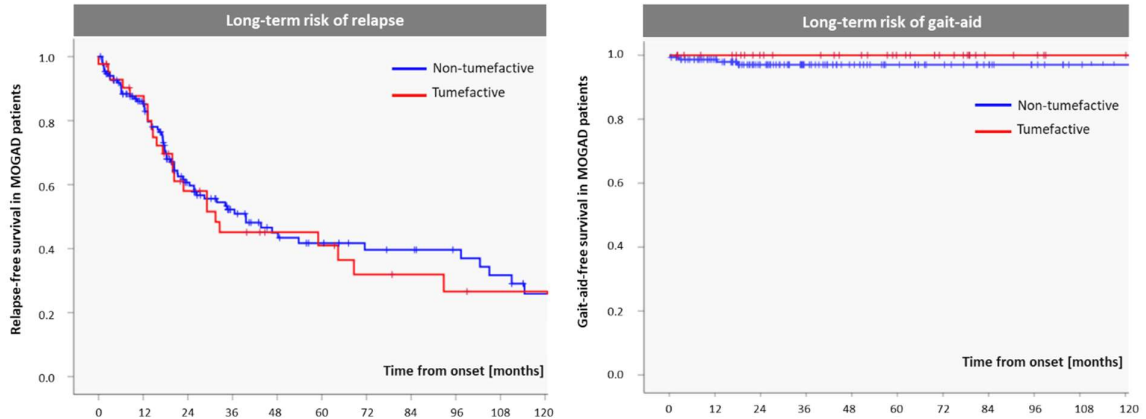
MOG-IgG serology. Antibody titers in serum were available in 31 MOGAD patients (72%). The median titer of MOG-IgG₁ was 1:100 (range 1:20 – 1:10,000), with 21 of 31 (68%) having high titers of $\geq 1:100$. MOG-IgG in CSF was positive in seven of nine (78%) tested.

Comparison of pediatric-onset and adult-onset MOGAD patients with tumefactive lesions (Supplementary Table 6.2.1 and 6.2.2). When MOGAD patients were divided according to the age at onset, seizures and sleepiness were more common in pediatric-onset patients. MRI analysis revealed multiple concomitant tumefactive lesions occurred more frequently and lesions were larger in children, but other attributes were similar (Supplementary Table 6.2.1 and 6.2.2).

Long-term prognosis of MOGAD patients with tumefactive lesions. The median (interquartile range) duration of the clinical follow-up was 63 months (25-97) in tumefactive MOGAD and 35 months (18-83) in non-tumefactive MOGAD patients ($p=0.046$). A gait aid was required in five of 151 non-tumefactive MOGAD (3%) and one of 43 tumefactive MOGAD patients (2%, $p>0.99$) at last follow-up after over 282 months of disease duration. Deaths were also similarly rare in the two groups, occurring in two non-tumefactive patients (1%) and one tumefactive MOGAD patient (2%) ($p=0.53$) at last follow-up. The presence of tumefactive lesions was not significantly associated with a higher risk of relapses (aHR [95% CI]= 0.91 [0.57-1.45], $p=0.69$), need for gait aid (aHR [95% CI]= 1.00 [0.11-8.98], $p>0.99$), or death (aHR [95% CI]= 0.17 [0.00-5.14], $p=0.31$). The Kaplan-Meier curves estimating the cumulative risk of relapses and disability over ten years of disease duration are shown in **Figure 6.2.2**.

Figure 6.2.2. Long-term outcomes of patients with tumefactive lesions. Kaplan-Meier curves of survival probability estimates of not developing relapse or reaching the EDSS

disability milestone of 6 in MOGAD patients up to 120 months from disease onset, according to the presence of tumefactive lesions.



Abbreviations: MOGAD=Myelin-oligodendrocyte-glycoprotein-IgG-associated disease.

Comparison of frequency, patient demographics, clinical, and cerebrospinal fluid characteristics between MOGAD, AQP4+NMOSD and MS (Table 6.2.1).

We compared 43 MOGAD patients with tumefactive lesions to 49 MS, and 16 AQP4+NMOSD patients. The frequency of tumefactive lesions in MOGAD (43 of 194, 22%, see above) was higher than that observed in patients with AQP4+NMOSD (16 of 359, 5%, $p < 0.001$) but our methodology did not allow comparison to frequency of tumefactive lesions in MS. MOGAD patients were younger and more frequently had somnolence and headache, while aphasia was more suggestive of MS. CSF oligoclonal bands were most frequent in MS while greater elevations in CSF white blood cell count were noted in MOGAD than MS. Brain biopsies were rarely undertaken and did not reveal alternative etiologies. The complete details of the comparison of the demographics, clinical, and CSF features of the study population between these groups are summarized in **Table 6.2.1**.

Table 6.2.1. Demographic, clinical and cerebrospinal fluid attributes of tumefactive demyelination across the three groups. Unless otherwise specified, quantitative variables are presented as median (interquartile range) and p values refer to two-way Kruskal

Wallis test, while categorical variables are reported as number (percentage) and p values refer to Pearson's Chi squared test.

	MOGAD (n=43)	MS (n=49)	MOGAD vs. MS p value	AQP4+NMOSD (n=16)	MOGAD vs. AQP4+NMOSD p value
Age [years]	21 (8-37)	36 (23-44)	0.003	40 (22-48)	0.02
Females	23 (54%)	31 (63%)	0.34	16 (100%)	<0.001^a
Pediatric-onset	21 (49%)	10 (20%)	0.004	4 (25%)	0.14 ^a
Disease duration prior to initial tumefactive lesion detection [days]	24 (11-195)	38 (11-640)	0.39	699 (15-2,272)	0.07
Tumefactive at onset	26 (61%)	26 (53%)	0.48	6 (38%)	0.12
Tumefactive attack severity					
EDSS at nadir	3.5 (2.0-4.0)	3.0 (2.5-4.5)	0.57	4.0 (3.5-7.5)	0.11
ICU admission	3 (7%)	2 (4%)	0.66 ^a	4 (25%)	0.08 ^a
Mechanical ventilation	2 (5%)	0 (0%)	0.22 ^a	1 (6%)	>0.99 ^a
Clinical features					
Asymptomatic	4 (9%)	6 (12%)	0.65	3 (19%)	0.28 ^a
Symptoms/signs referable to brainstem or cerebellum	12 (28%)	14 (29%)	0.94	3 (19%)	0.74 ^a
Hemiparesis/monoparesis/quadriparesis	5 (12%)	11 (22%)	0.17	3 (19%)	0.48 ^a
Aphasia	1 (2%)	10 (20%)	0.009^a	1 (6%)	0.47 ^a
Seizures	4 (9%)	6 (12%)	0.75 ^a	2 (13%)	0.66 ^a
Somnolence	12 (28%)	2 (4%)	0.003^a	0 (0%)	0.02^a
Vomiting or nausea	12 (28%)	6 (12%)	0.06	4 (25%)	>0.99 ^a
Headache	18 (42%)	10 (20%)	0.03	2 (13%)	0.06 ^a
Concomitant involvement of other CNS sites					
Optic neuritis	8 (19%)	3 (6%)	0.11 ^a	0 (0%)	0.09 ^a
Myelitis	16 (37%)	9 (18%)	0.04	5 (31%)	0.76
Cerebrospinal fluid findings					
Positive oligoclonal bands ^b	2 of 37 (5%)	30 of 43 (70%)	<0.001^a	1 of 10 (10%)	0.52 ^a
White blood cell count [cells/ μ l] ^c	33 (0-890)	6 (0-84)	<0.001	7 (0-188)	0.23
Elevated white blood cells ^d	32 of 40 (80%)	18 of 34 (53%)	0.01	6 of 9 (67%)	0.39
Protein [mg/dl] ^c	52 (13-126)	40 (17-160)	0.10	47 (26-251)	0.47
Glucose [mg/dl] ^c	56 (38-87)	59 (44-96)	0.16	57 (39-93)	0.66
Brain biopsy	4 (9%)	4 (8%)	>0.99 ^a	1 (6%)	>0.99 ^a

^aFisher's exact test

^bOligoclonal bands were tested at the time of the index clinical event in 21 of 37 patients with MOGAD (57%), 29 of 43 patients with MS (67%), and four of ten patients with AQP4+NMOSD (40%)

^cData reported as median (range)

^dWhite blood cell count >5 cells/ μ l

Abbreviations: MOGAD=Myelin-oligodendrocyte-glycoprotein-IgG-associated disease; MS=multiple sclerosis; MRI=magnetic resonance imaging; AQP4+NMOSD=aquaporin-4-IgG positive neuromyelitis optica spectrum disorders; CNS=central nervous system.

Comparison of number of brain lesions and number of tumefactive brain lesions (Table 6.2.2). MOGAD patients had a lower median number of brain T2-hyperintense and gadolinium-enhancing lesions compared to MS, but similar to AQP4+NMOSD. Comparison of lesion frequency, including how many had multiple tumefactive lesions are summarized in **Table 6.2.2**.

Before the development of tumefactive brain lesions, a negative MRI was observed in one MOGAD patient at eleven days from symptom onset and two MS patients, both at five days from onset. None of the AQP4+NMOSD patients had a negative MRI while symptomatic.

Table 6.2.2. Comparison of MRI features of tumefactive demyelination across the three groups. Unless otherwise specified, quantitative variables are presented as median (interquartile range) and p values refer to two-way Kruskal Wallis test, while categorical variables are reported as number (percentage) and p values refer to Pearson's Chi squared test.

	MOGAD (n=43)¹	MS (n=49)¹	MOGAD vs. MS p value	AQP4+NMOSD (n=16)¹	MOGAD vs. AQP4+NMOSD p value
Time from symptoms onset [days]	15 (7-21)	12 (5-29)	0.77	9 (3-15)	0.09
Total number of T2-hyperintense lesions	5 (3-14)	10 (5-27)	0.008	3.5 (2-10)	0.29

Total number of enhancing lesions	1 (0-2)	3 (1-6)	<0.001	1 (0-2)	0.78
Concomitant multiple tumefactive lesions	17 (40%)	20 (41%)	0.90	4 (25%)	0.37 ^a
Total number of concomitant tumefactive lesions	1 (1-2)	1 (1-2)	0.91	1 (1-2)	0.32
Diameters of the index lesion					
Longitudinal [cm]	2.8 (2.3-3.3)	3.0 (2.4-4.5)	0.22	3.5 (2.5-4.1)	0.13
Cross-sectional [cm]	1.7 (1.2-2.2)	2.3 (1.7-2.9)	<0.001	1.7 (1.3-2.2)	0.57
Location of the index lesion					
Infratentorial ^b	18 (42%)	5 (10%)	<0.001	5 (31%)	0.57 ^a
Deep grey matter	10 (23%)	0 (0%)	<0.001^a	3 (19%)	>0.99 ^a
Periventricular ^c	4 (9%)	23 (47%)	<0.001^a	4 (25%)	0.19 ^a
Corticospinal tract ^d	6 (14%)	0 (0%)	0.009^a	5 (31%)	0.15 ^a
Corpus callosum	2 (5%)	0 (0%)	0.22 ^a	3 (19%)	0.12 ^a
Hemispheric	8 (19%)	21 (43%)	0.012	1 (6%)	0.42 ^a
Other locations ^c	1 (2%)	0 (0%)	0.47 ^a	0 (0%)	>0.99 ^a
Index lesion characteristics					
Mass effect	12 (28%)	10 (20%)	0.40	6 (38%)	0.48
Balò-like	1 (2%)	13 (27%)	0.001^a	0 (0%)	>0.99 ^a
Cystic component	2 (5%)	20 (41%)	<0.001^a	1 (6%)	>0.99 ^a
Poorly demarcated borders	30 (70%)	11 (22%)	< 0.001	8 (50%)	0.16
T2-hypointense rim	1 (2%)	32 (65%)	<0.001^a	0 (0%)	>0.99 ^a
T1-hypointensity	21 (49%)	46 (94%)	< 0.001	12 (75%)	0.07
DWI restriction	11 of 42 (26%)	48 (98%)	< 0.001	10 of 15 (67%)	0.005
Arc peripheral DWI restriction	2 of 42 (5%)	38 (78%)	<0.001^a	1 of 15 (7%)	>0.99 ^a
Contrast enhancement	23 (54%)	43 of 47 (92%)	< 0.001	8 (50%)	0.81

Ring ^f	1 (2%)	18 of 47 (38%)	<0.001^a	1 (6%)	0.47 ^a
Cloud-like	3 (7%)	3 of 47 (6%)	>0.99 ^a	2 (13%)	0.61 ^a
Concomitant MRI features of other CNS sites					
Optic nerve					
Optic nerve enhancement	6 of 15 (40%)	2 of 9 (22%)	0.66 ^a	0 of 4 (0%)	0.26 ^a
Bilateral optic nerve enhancement	2 of 15 (13%)	0 of 9 (0%)	0.51 ^a	0 of 4 (0%)	>0.99 ^a
Optic nerve enhancement involving >50% of length	4 of 15 (27%)	1 of 9 (11%)	0.62 ^a	0 of 4 (0%)	0.53 ^a
Optic nerve sheath enhancement	3 of 15 (20%)	0 of 9 (0%)	0.27 ^a	0 of 4 (0%)	>0.99 ^a
Spinal cord					
Presence of T2-hyperintense spinal cord lesion	16 of 27 (59%)	21 of 39 (54%)	0.66	8 of 10 (80%)	0.24
Presence of T2-hyperintense spinal cord lesion in the conus	11 of 27 (41%)	3 of 33 (9%)	0.006^a	1 of 9 (11%)	0.22 ^a
Central lesions	9 of 16 (56%)	2 of 21 (10%)	0.003^a	3 of 8 (38%)	0.67 ^a
Peripheral lesions	0 of 16 (0%)	14 of 21 (67%)	<0.001^a	0 of 8 (0%)	-
Mixed centro-peripheral lesions	7 of 16 (44%)	5 of 21 (24%)	0.20	5 of 8 (63%)	0.39
Longitudinally-extensive T2-hyperintense spinal cord lesion	13 of 27 (48%)	3 of 39 (8%)	<0.001^a	8 of 10 (80%)	0.08
Spinal cord enhancement	12 of 27 (44%)	11 of 39 (28%)	0.17	6 of 10 (60%)	0.40
Follow-up evolution of the index lesion					
Time from baseline to first follow-up MRI scan [days]	195 (141-518)	189 (130-266)	0.25	369 (237-2,135)	0.02

Complete resolution on T2-images at first follow-up MRI scan	19 of 35 (54%)	0 of 42 (0%)	<0.001 ^a	0 of 14 (0%)	<0.001 ^a
Complete resolution on T1-images at first follow-up MRI scan	24 of 35 (69%)	6 of 42 (14%)	< 0.001	4 of 14 (29%)	0.02 ^a
Time from baseline to last follow-up MRI scan [months]	35 (20-75)	25 (10-61)	0.18	24 (8-72)	0.45
Complete resolution on T2-images at last follow-up MRI scan	23 of 35 (66%)	0 of 42 (0%)	<0.001 ^a	2 of 14 (14%)	0.001 ^a
Complete resolution on T1-images at last-follow-up MRI scan	30 of 35 (86%)	13 of 42 (31%)	< 0.001	5 of 14 (36%)	< 0.001

^a Fisher's exact test

^bInfratentorial lesions involved: (1) the middle cerebellar peduncle: MOGAD (n=7, 16%), MS (n=4, 8%), and AQP4+NMOSD (n=1, 6%); (2) the medulla, pons, or midbrain: MOGAD (n=11, 26%), and AQP4+NMOSD (n=4, 25%, one of which extending to the middle cerebellar peduncle, hence also included above); (3) the cerebellum: MS (n=1, 2%), and AQP4+NMOSD (n=1, 6%).

^cA periventricular lesion detected in a AQP4+NMOSD patient also involved the splenium of the corpus callosum ("arch bridge pattern", Figure 2).

^dTumefactive lesions in the corticospinal tract usually extended to contiguous structures such as the thalamus (five MOGAD and two AQP4+NMOSD), and the midbrain (one MOGAD and one AQP4+NMOSD).

^eHippocampus in one MOGAD patient.

^fRing enhancement included: (1) closed ring enhancement: MOGAD (n=1, 2%), MS (n=6, 12.0%), and AQP4+NMOSD (n=1, 6%); and (2) open ring enhancement: MS (n=12, 24%).

¹All categorical values and percentages are out of this denominator unless specified.

Abbreviations: MOGAD=Myelin-oligodendrocyte-glycoprotein-IgG-associated disease; MS=multiple sclerosis; MRI=magnetic resonance imaging; AQP4+NMOSD=aquaporin-4-IgG positive neuromyelitis optica spectrum disorders; DWI=diffusion-weighted imaging.

Comparison of MRI features of the tumefactive index lesion (Table 6.2.2).

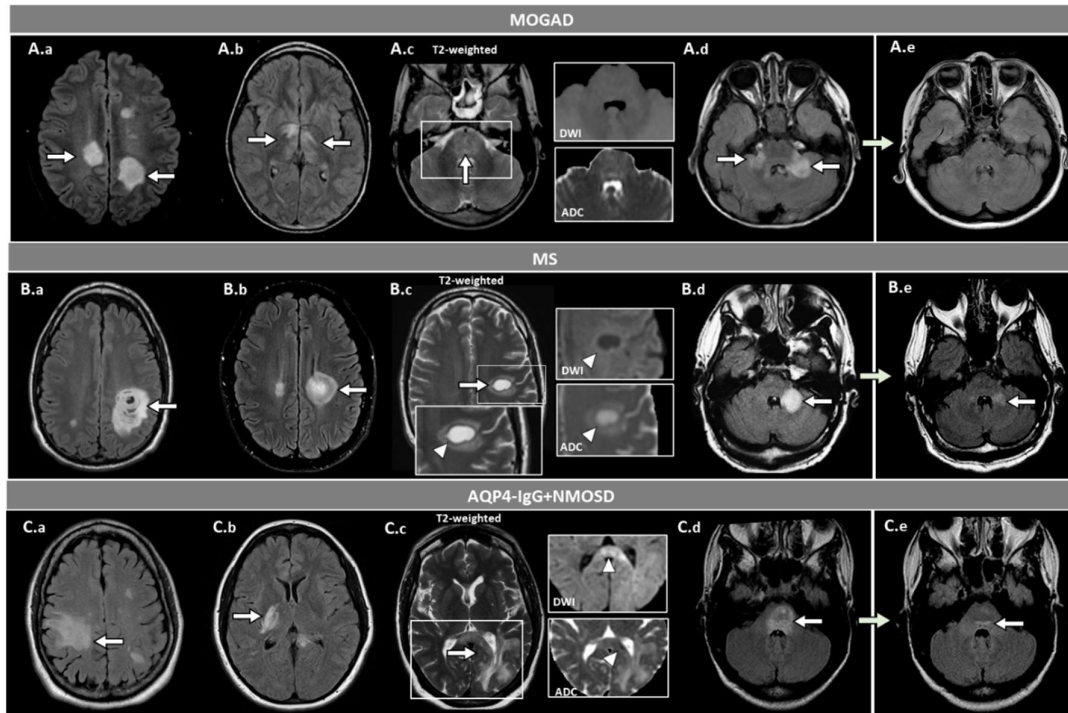
Overall, we evaluated 481 MRI scans of whom 108 were acquired at the time of the first tumefactive lesion attack, and 373 acquired at follow-up. The location, characteristics and resolution of the index lesions are compared in **Table 6.2.2**.

The MRI features of tumefactive lesions in the three diseases with key elements for the differential diagnosis are shown in **Figure 6.2.3**.

Figure 6.2.3. Examples of tumefactive brain lesions and relevant MRI features for the differential diagnosis of patients with MOGAD, MS, and AQP4+NMOSD.

Unless otherwise specified, lesions are shown on axial T2-fluid-attenuated inversion recovery (T2-FLAIR). Tumefactive lesions are indicated by white arrows, while specific features are indicated by arrowheads. Panel A (MOGAD): tumefactive lesions in the bilateral hemispheric white matter (A.a, arrows); bilateral tumefactive lesions in the corticospinal tract and thalami (A.b, arrows); tumefactive lesion involving the entire pons (A.c, arrow) without evidence of T2-hypointense rim, diffusion restriction (i.e., no DWI hyperintensity), and no ADC map hypointensity (A.c); bilateral tumefactive lesions in the middle cerebellar peduncles (A.d, arrows), with complete resolution at follow-up MRI (A.e). Panel B (MS): Balo'-like tumefactive lesions in the hemispheric white matter (B.a, arrow) and periventricular white matter (B.b, arrow); tumefactive lesion located in the hemispheric white matter, showing a complete T2-hypointense rim (arrowhead) with a corresponding ring of peripheral diffusion restriction as indicated by the hyperintensity in DWI (arrowhead) and hypointensity on ADC map (arrowhead) (B.c); tumefactive lesion in the left middle cerebellar peduncle (B.d, arrow) undergoing volumetric reduction, but still present at follow-up MRI (B.e, arrow). Panel C (AQP4+NMOSD): tumefactive lesions in the hemispheric white matter (C.a, arrow), corticospinal tract (C.b, arrow); tumefactive periventricular lesion extensively involving the splenium of the

corpus callosum in an “arc-bridge” pattern (C.c, arrow); the lesion does not show any T2-hypointense rim and is characterized by DWI hyperintensity of the splenium (arrowhead) with focal diffusion restriction (i.e., corresponding hypointensity on the ADC map, arrowhead); tumefactive lesion involving the entire pons (C.d, arrow), showing residual mild hyperintensity near the fourth ventricle (C.e, arrow).



Abbreviations: MOGAD=Myelin-oligodendrocyte-glycoprotein-IgG-associated disease; MS=multiple sclerosis; AQP4+NMOSD=aquaporin-4-IgG positive neuromyelitis optica spectrum disorders; ADC=apparent diffusion coefficient map; DWI=diffusion-weighted images.

Index lesion location. Compared to MS, MOGAD patients had a higher frequency of infratentorial tumefactive lesions, while periventricular and other white matter hemispheric lesions were less frequent. The localization of the index lesion in the deep grey matter (23%), corticospinal tract (14%), and corpus callosum (5%) was noted in MOGAD and AQP4+NMOSD (19%, 31%, and 19%, respectively), but not in MS.

Index lesion characteristics. Attributes of the index lesion favoring MS over MOGAD included: a T2-hypointense rim, T1-hypointensity, DWI restriction (particularly when in an arc pattern), Balo-like appearance and a cystic component, open or closed rings of enhancement. DWI restriction was also more common in AQP4+NMOSD compared to MOGAD patients. Mass effect did not differ between groups and cloud-like enhancement was rare across all groups (**Table 6.2.2**).

Lesion evolution. Follow-up MRIs were available in 35 of 43 MOGAD (81%), 42 of 49 MS (86%), and 14 of 16 (88%) AQP4+NMOSD. The median number (range) of scans per patient was 3 (1-12) for MOGAD, 3 (1-19) for MS, and 2 (1-9) for AQP4+NMOSD. It was similar between MOGAD and MS ($p=0.58$), but lower in AQP4+NMOSD compared to MOGAD ($p=0.03$). At first follow-up, details regarding ongoing treatment were available for all but two patients with MOGAD. Of these, disease-modifying medications or oral steroids were administered to 14 of 33 patients with MOGAD (42%), 27 of 42 patients with MS (64%), and 11 of 14 (79%) patients with AQP4+NMOSD. In those off of oral steroids, median (interquartile range) time to oral steroid discontinuation was 2.5 (2-8) months in MOGAD and 18 (1-38) months in AQP4+NMOSD, respectively. Complete resolution of the index tumefactive lesions on T2-weighted images was observed in 19 of 35 (54%) MOGAD patients, but not in the other groups (**Table 6.2.2**, **Figure 6.2.3**). Residual T1-hypointensity on follow-up MRI was rare in MOGAD, but common with MS and AQP4+NMOSD. Similar results were observed at the last follow-up MRI scan.

Distinguishing MOGAD tumefactive lesions from other demyelinating etiologies using clinical and MRI features (**Table 6.2.3**).

Results of the univariable binary logistic regression models assessing associations between clinical or MRI variables and MOGAD diagnosis are reported in the **Supplementary Table 6.2.3**.

To avoid separation, the following variables were merged, based on their similarity: (1) presence of somnolence or headache; (2) concomitant involvement of other CNS sites (e.g., optic neuritis or myelitis); (3) lesion location in brain regions not found in MS patients (deep grey matter, corticospinal tract, corpus callosum; this feature was not

included in the model MOGAD vs. MS); (4) Balo'-like or cystic component appearance; (5) complete resolution on T2- or T1-weighted images. A T2-hypointense rim was not encountered in AQP4+NMOSD, so this feature was not included in the model of MOGAD vs. AQP4+NMOSD.

Since the availability of CSF samples, optic nerve MRI, and spinal cord MRI was limited, these variables were not included in the final model. However, the presence of positive oligoclonal bands favored MS, while CSF white blood cell elevation, longitudinally-extensive spinal cord lesions, especially if involving the conus and centrally located, were associated with MOGAD (**Supplementary Table 6.2.3**).

Independent predictors of MOGAD diagnosis over the other demyelinating disorders were the presence of somnolence or headache, and absence of T2-hypointense rim, T1-hypointensity or DWI restriction (Nagelkerke R Squared=0.67).

The presence of somnolence or headache, the absence of periventricular location, T2-hypointense rim, and any type or arc peripheral DWI restriction supported MOGAD over MS (Nagelkerke R Squared=0.86), while the presence of somnolence or headache and the absence of DWI restriction favored MOGAD over AQP4+NMOSD (Nagelkerke R Squared=0.29).

When the complete resolution of the index tumefactive lesions on T2- or T1-weighted images at first follow-up MRI scan was included, the performance of all models improved in differentiating MOGAD from the other diseases (**Table 6.2.3**). We did not consider lesion resolution at the last follow-up MRI scan in our model, since it would be less useful in the acute clinical setting.

Table 6.2.3. Multivariable binary logistic regression analysis between clinical/MRI variables and MOGAD diagnosis. Data are presented as beta coefficient (standard error) and odds ratio (95% confidence interval).

MOGAD vs. Other demyelinating disorders	B (SE)	OR (95% CI)	p	Nagelkerke R Squared	+ Complete resolution on T1- or T2-images
Somnolence or headache	1.5 (0.7)	4.51 (1.12; 18.04)	0.03	0.67	0.73
T2-hypointense rim	-3.4 (1.4)	0.03 (0.00; 0.49)	0.01		
T1-hypointensity	-1.7 (0.7)	0.19 (0.05; 0.77)	0.02		
DWI restriction	-2.5 (0.6)	0.09 (0.03; 0.29)	<0.001		

MOGAD vs. MS	B (SE)	OR (95% CI)	p	Nagelkerke R Squared	+ Complete resolution on T1- or T2-images
Somnolence or headache	2.4 (1.3)	11.04 (0.82; 148.41)	0.07	0.86	0.96
Periventricular lesions	-2.11 (1.1)	0.12 (0.01; 1.07)	0.06		
T2-hypointense rim	-3.26 (1.5)	0.04 (0.00; 0.80)	0.03		
DWI restriction	-2.90 (1.3)	0.06 (0.00; 0.75)	0.03		
Arc peripheral DWI restriction	-3.13 (1.5)	0.04 (0.00; 0.78)	0.03		
MOGAD vs. AQP4+NMOSD	B (SE)	OR (95% CI)	p	Nagelkerke R Squared	+ Complete resolution on T1- or T2-images
Somnolence or headache	1.69 (0.9)	5.39 (1.01; 28.78)	0.049	0.29	0.44
DWI restriction	-1.65 (0.7)	0.19 (0.05; 0.73)	0.02		

Abbreviations: MOGAD=Myelin-oligodendrocyte-glycoprotein-IgG-associated disease; MS=multiple sclerosis; AQP4+NMOSD=aquaporin-4-IgG positive neuromyelitis optica spectrum disorders; DWI=diffusion-weighted imaging.

Comparison of subsequent tumefactive lesions (Table 6.2.4). The rate of subsequent tumefactive lesions across the three groups was similar: six of 35 MOGAD patients (17%), five of 42 MS (12%, *p vs. MOGAD*=0.74), and two of 14 AQP4+NMOSD (14%, *p vs. MOGAD*>0.99). In total, we observed 20 recurrent tumefactive attacks (eleven in MOGAD, seven in MS, and two in AQP4+NMOSD) and the features of the subsequent tumefactive lesions when compared to the baseline lesions are summarized in **Table 6.2.4** and examples shown in **Supplementary Figure 6.2.1**.

Table 6.2.4. MRI features of subsequent tumefactive demyelination across the three groups. Data refer to the index lesion of each tumefactive attack. To improve readability, if the proportion of subsequent tumefactive lesions a certain feature already present at the first tumefactive attack was at least 80%, this was highlighted in bold.

	Subsequent tumefactive lesions	Proportion of subsequent tumefactive lesions with the feature present also at first tumefactive attack

	MOGAD (n=11)	MS (n=7)	AQP4+NMO SD (n=2)	MOGAD	MS	AQP4+NMO SD
Location of index lesion						
Infratentorial	4 (36%)	2 (29%)	2 (100%)	1 of 4 (25%)	1 of 2 (50%)	1 of 2 (50%)
Deep grey matter	1 (9%)	0 (0%)	0 (0%)	1 of 1 (100%)	Not applicable	Not applicable
Periventricular	1 (9%)	2 (29%)	0 (0%)	0 of 1 (0%)	1 of 2 (50%)	Not applicable
Corticospinal tract ^a	2 (18%)	0 (0%)	1 (50%)	0 of 2 (0%)	Not applicable	1 of 1 (100%)
Corpus callosum	1 (9%)	0 (0%)	0 (0%)	0 of 1 (0%)	Not applicable	Not applicable
Hemispheric	4 (36%)	3 (43%)	0 (0%)	0 of 4 (0%)	3 of 3 (100%)	Not applicable
Index lesion MRI characteristics						
Mass effect	1 (9%)	5 (71%)	1 (50%)	0 of 1 (0%)	2 of 5 (40%)	1 of 1 (100%)
Balò-like	0 (0%)	0 (0%)	0 (0%)	Not applicable	Not applicable	Not applicable
Cystic component	0 (0%)	2 (29%)	0 (0%)	Not applicable	2 of 2 (100%)	Not applicable
Poorly demarcated borders	10 (91%)	2 (29%)	1 (50%)	8 of 10 (80%)	1 of 2 (50%)	1 of 2 (50%)
T2-hypointense rim	0 (0%)	5 (71%)	0 (0%)	Not applicable	4 of 5 (80%)	Not applicable
T1-hypointensity	9 (82%)	7 (100%)	2 (100%)	8 of 9 (89%)	6 of 7 (86%)	1 of 2 (50%)
DWI restriction	1 (9%)	6 (86%)	2 (100%)	0 of 1 (0%)	6 of 6 (100%)	2 of 2 (100%)
Arc peripheral DWI restriction	0 (0%)	5 (71%)	0 (0%)	Not applicable	2 of 5 (40%)	Not applicable
Contrast enhancement	9 (82%)	6 (86%)	2 (100%)	6 of 9 (67%)	3 of 3^b (100%)	0 of 2 (0%)
Ring	0 (0%)	3 (43%)	0 (0%)	Not applicable	1 of 1¹ (100%)	Not applicable
Cloud-like	3 (27%)	0 (0%)	1 (50%)	1 of 3 (33%)	Not applicable	0 of 1 (0%)
Follow-up evolution of the index lesion						
Complete resolution on T2-images at first follow-up MRI scan	5 of 10 (50%)	0 of 6 (0%)	0 of 1 (0%)	4 of 5 (80%)	Not applicable	Not applicable
Complete resolution on T1-images at first follow-up MRI scan	6 of 10 (60%)	0 of 6 (0%)	0 of 1 (0%)	6 of 6 (100%)	Not applicable	Not applicable

Complete resolution on T2-images at last follow-up MRI scan	5 of 10 (50%)	0 of 6 (0%)	0 of 1 (0%)	4 of 5 (80%)	Not applicable	Not applicable
Complete resolution on T1-images at last-follow-up MRI scan	7 of 10 (70%)	0 of 6 (0%)	0 of 1 (0%)	7 of 7 (100%)	Not applicable	Not applicable

^aTumefactive lesions in the corticospinal tract usually extended to contiguous structures such as the thalamus (one MOGAD), and the midbrain (one MOGAD and one AQP4+NMOSD)

^bGadolinium not administered at the time of the first tumefactive attack in a patient with multiple tumefactive attacks.

Abbreviations: MOGAD=Myelin-oligodendrocyte-glycoprotein-IgG-associated disease; MS=multiple sclerosis; MRI=magnetic resonance imaging; AQP4+NMOSD=aquaporin-4-IgG positive neuromyelitis optica spectrum disorders; DWI=diffusion-weighted imaging.

Discussion

In this study, we found tumefactive lesions were frequent in MOGAD but did not convey an increased risk of relapse or worse outcome. The clinical manifestations, MRI, and CSF features of MOGAD patients with tumefactive lesions had many differences from MS but were similar to AQP4+NMOSD.

Tumefactive lesions occurred in 22% of MOGAD patients, which was greater than in AQP4+NMOSD (5% in this study and 0-3.4% in prior studies) (Cacciaguerra et al., 2019b, Fereidan-Esfahani et al., 2022). Although our search criteria precluded analysis of the frequency of tumefactive demyelination in MS, a prior population-based study at our facility reported it in 1.9% of MS patients (Fereidan-Esfahani et al., 2022) and in studies from other centers it has ranged from 0.1 to 2.1% of MS patients (Poser, Luer et al., 1992, Sanchez, Meca-Lallana et al., 2017). Notably, tumefactive lesions were detected in almost 50% of MOGAD patients with brain attacks, and thus tumefactive brain lesions account for a far higher proportion of brain lesions in MOGAD than MS and AQP4+NMOSD. Therefore, in the presence of an inflammatory appearing tumefactive lesion, MOG-IgG testing should be considered, although we must keep in mind that the overall incidence of MS far exceeds MOGAD. Indeed, given MOGAD

brain MRI changes can take time to develop (noted in one patient in this study) or be subtle (e.g., cerebral cortical encephalitis), MOG-IgG testing early on can be especially helpful when the initial radiologic picture is uncertain. Tumefactive lesions in MOGAD sometimes needed intensive care unit admission and ventilatory support, as previously reported (Zhao-Fleming, Valencia Sanchez et al., 2021). However, despite the severe clinical features acutely our study shows that in MOGAD the presence of tumefactive demyelination, was not associated with a greater risk of relapse or long-term physical disability (Lopez-Chiriboga, Sechi et al., 2020).

In terms of clinical presentation, features of encephalopathy, especially somnolence, were more common among patients with MOGAD than MS and AQP4+NMOSD, in line with the higher prevalence of acute disseminated encephalomyelitis phenotype observed in this disease, particularly during childhood (Marignier et al., 2021). In our cohort the clinical presentation of tumefactive demyelination of patients with MS was polysymptomatic in approximately one third. Although not standard in typical MS, similar findings were found in other cohorts of tumefactive MS (Lin, Yu et al., 2017, Lucchinetti et al., 2008), and may reflect the high degree of inflammatory activity spreading to other regions such as the optic nerve or spinal cord. It is also notable that tumefactive demyelination usually occurred in the first two years from onset, earlier in patients with MOGAD and MS than AQP4+NMOSD, although a small proportion developed attacks with tumefactive lesions later on. Possible explanations for this include early use of more effective disease modifying treatments in those with aggressive inflammatory activity at onset and the first attack being recognized to be the most severe in MOGAD (Jurynczyk, Messina et al., 2017b).

In our tumefactive MS cohort the frequency of oligoclonal bands (70%) was slightly lower what typically observed in MS (approximately 88%),(Dobson, Ramagopalan et al., 2013) but it was still useful in discriminating from MOGAD. The reasons for the lower frequency of CSF oligoclonal bands in our tumefactive MS cohort is uncertain but in line with previous studies on tumefactive MS (52-66%) (Algahtani, Shirah et al., 2017, Fereidan-Esfahani et al., 2022). The presence of other clinical and radiologic features consistent with MS, pathological confirmation of demyelination in some, and absence of alternative diagnoses in longitudinal follow-up, further supported an MS diagnosis in these cases.

In our cohort, the differentiation between tumefactive lesions due to MS rather than MOGAD was feasible with conventional MRI sequences. Compared to MS, tumefactive lesions in MOGAD were preferentially located in the posterior fossa and deep grey matter, while were less frequently found in the periventricular and hemispheric white matter. Infratentorial involvement is considered a well-established radiological finding in MOGAD, where lesions can have poorly demarcated borders (i.e., “fluffy appearance”) (Filippi et al., 2019) and extensively involve the middle cerebellar peduncles, or, less frequently, the medulla, pons, and midbrain (Banks et al., 2020). Conversely, MS lesions have a tropism for the deep medullary veins running perpendicular to the outline of the ventricular system (Filippi et al., 2019).

We identified a number of MRI features which were frequent in MS and rarely observed in MOGAD, including the presence of a T2-hypointense rim, DWI restriction (especially when arc-shaped), ring enhancement, and T1-hypointensity.

A T2-hypointense rim has been observed in 45% of tumefactive lesions with pathological evidence of confluent inflammatory demyelination consistent with MS (Lucchinetti et al., 2008) and in around 9% of MS patients, irrespective of lesion dimension. (Llufriu et al., 2010) Studies also suggest a certain degree of association between the hypointense rim and the presence of ring enhancement, although both can occur in isolation as well (Llufriu et al., 2010, Lucchinetti et al., 2008). Prior pathology studies revealed that an iron-rich macrophage layer surrounding pattern I and II active demyelinating lesions represents the pathological correlate of the T2-hypointense rim (Bruck, Bitsch et al., 1997, Metz, Gavrilova et al., 2021). In addition, although macrophage densities is similar across immunopatterns of early active demyelinating lesions, macrophages in pattern II lesions are characterized by a higher expression of the heavy subunit of the iron-storage protein ferritin, and by internal iron accumulation (Tham, Frischer et al., 2021). The colocalization of iron with the peripheral border of macrophages could therefore locally reduce the T2-relaxation time, leading to the identification of a corresponding area of T2-hypointense signal (Ordidge, Gorell et al., 1994).

Discriminating between MOGAD and AQP4+NMOSD was more challenging, and a large overlap of clinical and radiological manifestations was noticed, in line with previous findings (Jurynczyk et al., 2017a, Marignier et al., 2021). However, lesions in MOGAD showed a lower rate of restricted diffusion, which was the only significant MRI

discriminant from AQP4+NMOSD at baseline. In agreement with the relatively benign course of MOGAD, a previous study suggested that the presence of restricted diffusion, likely due to altered fiber tract organization or cellular infiltrates, might reflect a more severe degree of tissue damage (Abou Zeid et al., 2012). A lower degree of tissue damage might also explain the numerically lower rate of T1-hypointensity (Bruck et al., 1997) in MOGAD, whose absence favored MOGAD diagnosis over the other demyelinating disorders.

This also aligns with the observation of complete resolution of tumefactive T2-hyperintense lesions in around 54% of MOGAD patients at first follow-up MRI, as opposed to none of the patients with AQP4+IgG+NMOSD and MS. Similar results were found in other studies, showing lesion resolution in 72% of MOGAD cases, but uncommon (5-24%) lesion resolution in AQP4+NMOSD or MS (Kim, Huh et al., 2014, Sechi et al., 2021c). When we included this feature as an explanatory variable for MOGAD identification, all model performances improved, especially when considering the differential diagnosis with AQP4+NMOSD, emphasizing its clinical usefulness when available. Nonetheless, when evaluating tumefactive lesions at onset the information on lesion resolution will not be available and this makes radiologic discrimination between these diseases more challenging at the initial presentation.

In patients with subsequent tumefactive attacks the presence of those features already identified as the most relevant for the differential diagnosis (i.e., T2-hypointense rim, DWI restriction, T1-hypointensity, and lesion resolution), were generally concordant in different episodes, strengthening their utility in clinical practice.

In terms of limitations, we acknowledge the retrospective design, the relatively small sample-size (especially for the AQP4+NMOSD cohort), and the lack of biopsy characterization of all lesions.

However, since biopsy is invasive with potential for neurologic morbidity, it is usually performed only in cases of greatest diagnostic uncertainty with atypical elements, and inclusion of all tumefactive cases regardless of biopsy may better reflect the spectrum of tumefactive lesions encountered in clinical practice. Also, in those biopsied from this study we did not focus on their pathology features which we have reported these in detail previously (Hoftberger et al., 2020, Lucchinetti et al., 2002, Lucchinetti, Popescu et al., 2011, Metz et al., 2021). The absence of a non-inflammatory control group, is an

additional limitation, but discriminators from alternative etiologies of large lesions can still be extrapolated from our study. For example, the presence of mass effect and avid contrast enhancement would favor tumor over MOGAD (Lin et al., 2017), while ring enhancement and a core of restricted diffusion would favor abscesses over MOGAD (Abou Zeid et al., 2012).

In addition, caution should be applied to the interpretation of longitudinal data (i.e., the rate of lesion resolution and recurrent tumefactive lesions) since MRI timing and frequency was not standardized, and different scanners were used at onset and follow-up, as expected in a clinical setting.

However, all this considered, our study provides several clinical and MRI features (i.e., the presence of somnolence, the absence of periventricular location, T2-hypointense rim, T1-hypointensity and any-shape or arc-peripheral DWI restriction) which might assist in correct identification of tumefactive lesions due to MOGAD rather than MS and, to a lesser extent, AQP4+NMOSD. The recognition of different MRI patterns of inflammatory tumefactive demyelination emphasizes the distinct pathophysiology of each disorder, and might contrast with the concept of pseudotumoral demyelination as a separate entity (Lassmann, 2022). Future studies, exploring the pathological correlates of tumefactive lesions in different demyelinating diseases will help clarify this. Also, future lines of research could assess double seronegative NMOSD, which are a more heterogeneous group of disorders and not a focus of this study.

Finally, this study furtherly underlines the importance of follow-up MRI when the diagnosis is uncertain, since the complete resolution of lesions was confirmed, once again, as a reliable hallmark of MOGAD.

Supplementary material

Supplementary Table 6.2.1. Demographic, clinical and cerebrospinal fluid attributes of tumefactive demyelination in MOGAD patients with adult- and pediatric-onset.

Unless otherwise specified, quantitative variables are presented as median (interquartile range) and p values refer to two-way Kruskal Wallis test, while categorical variables are reported as number (percentage) and p values refer to Pearson's Chi squared test.

	Adult-onset MOGAD (n=22)¹	Pediatric-onset MOGAD (n=21)¹	p value
Age [years]	37 (25-53)	8 (5-10)	<0.001
Females	13 (59%)	10 (48%)	0.45
Brain biopsy	1 (5%)	3 (14%)	0.35 ^a
Cerebrospinal fluid findings			
Positive oligoclonal bands	2 of 20 (10%)	0 of 17 (0%)	0.49 ^a
White blood cell count [cells/ μ l] ^b	52 (0-890)	24 (0-392)	0.63
Elevated white blood cells	15 of 20 (75%)	17 of 20 (85%)	0.43
Protein [mg/dl] ^b	72 (26-126)	36 (13-90)	0.002
Glucose [mg/dl] ^b	60 (45-87)	55 (38-68)	0.14
Disease duration [months] prior to initial tumefactive lesion detection	1 (0-5)	1 (0-8)	0.76
Tumefactive lesion at onset	13 (59%)	13 (62%)	0.85
Tumefactive attack severity			
EDSS at nadir	4.0 (3.0-7.0)	3.0 (2.0-4.0)	0.02
ICU admission	2 (9%)	1 (5%)	>0.99 ^a
Mechanical ventilation	1 (5%)	1 (5%)	>0.99 ^a
Clinical features			
Asymptomatic	3 (14%)	1 (5%)	0.61 ^a
Symptoms/signs referable to brainstem or cerebellum	6 (27%)	6 (29%)	0.92
Hemiparesis/monoparesis/quadruparesis	2 (9%)	3 (14%)	0.48 ^a
Aphasia	0 (0%)	1 (5%)	0.49 ^a

Seizures	0 (0%)	4 (19%)	0.048^a
Somnolence	2 (9%)	10 (48%)	0.007^a
Vomiting or nausea	4 (18%)	8 (38%)	0.15
Headache	9 (41%)	9 (43%)	0.90
Concomitant involvement of other CNS sites			
Optic neuritis	4 (18%)	4 (19%)	0.94
Myelitis	10 (45%)	6 (29%)	0.25

^aFisher's exact test

^bData reported as median (range)

¹All categorical values and percentages are out of this denominator unless specified.

Abbreviations: MOGAD=Myelin-oligodendrocyte-glycoprotein-IgG-associated disease; CNS=central nervous system.

Supplementary Table 6.2.2. MRI features of tumefactive demyelination in MOGAD patients with adult- and pediatric-onset. Unless otherwise specified, quantitative variables are presented as median (interquartile range) and p values refer to two-way Kruskal Wallis test, while categorical variables are reported as number (percentage) and p values refer to Pearson's Chi squared test.

	Adult-onset MOGAD (n=22)¹	Pediatric-onset MOGAD (n=21)¹	p value
Total number of T2-hyperintense lesions	8 (4-16)	4 (3-9)	0.06
Total number of enhancing lesions	1 (0-2)	1 (0-3)	0.40
Concomitant multiple tumefactive lesions	5 (23%)	12 (57%)	0.02
Total number of concomitant tumefactive lesions	1 (0-1)	1 (0-2)	0.39
Diameters of the index lesion			
Longitudinal [cm]	2.5 (2.2-3.0)	3.2 (2.4-4.6)	0.04
Cross-sectional [cm]	1.7 (1.0- 2.0)	1.5 (1.2-2.9)	0.41
Location of the index lesion			
Infratentorial	12 (55%)	6 (29%)	0.08

Deep grey matter	4 (18%)	6 (29%)	0.49 ^a
Periventricular	2 (9%)	2 (10%)	>0.99 ^a
Corticospinal tract	3 (14%)	3 (14%)	>0.99 ^a
Corpus callosum	0 (0%)	2 (10%)	0.23 ^a
Hemispheric	3 (14%)	5 (24%)	0.46 ^a
Other locations	1 (5%)	0 (0%)	>0.99 ^a
Index lesion characteristics			
Mass effect	4 (18%)	8 (38%)	0.19 ^a
Balò-like	1 (5%)	0 (0%)	>0.99 ^a
Cystic component	1 (5%)	1 (5%)	>0.99 ^a
Poorly demarcated borders	15 (68%)	15 (71%)	0.82
T2-hypointense rim	0 (0%)	1 (5%)	0.49 ^a
T1-hypointensity	10 (45%)	11 (52%)	0.65
DWI restriction	7 (32%)	4 of 20 (20%)	0.49 ^a
Arc peripheral DWI restriction	1 (5%)	1 of 20 (5%)	>0.99 ^a
Contrast enhancement	12 (55%)	11 (52%)	0.89
Ring	1 (5%)	0 (0%)	>0.99 ^a
Cloud-like	2 (9%)	1 (5%)	>0.99 ^a
Follow-up evolution			
Follow-up duration in months	7.3 (4-11)	6.2 (5-21)	0.90
Complete resolution on T2-images	7 of 16 (44%)	12 of 19 (63%)	0.25
Complete resolution on T1-images	9 of 16 (56%)	15 of 19 (79%)	0.15
Subsequent attacks with tumefactive lesions	4 of 16 (25%)	2 of 19 (11%)	0.39 ^a

^aFisher's exact test.

¹All categorical values and percentages are out of this denominator unless specified.

Abbreviations: MOGAD=Myelin-oligodendrocyte-glycoprotein-IgG-associated disease;

DWI=diffusion-weighted imaging.

Supplementary Table 6.2.3. Univariable binary logistic regression analysis between clinical/MRI variables and MOGAD diagnosis. Data are presented as odds ratio (95% confidence interval), models were not run when a feature was absent in at least one of the two groups.

MOGAD vs.	Other demyelinating disorders	MS	AQP4+NMOSD
Cerebrospinal fluid findings			
Oligoclonal bands	0.04 (0.01-0.19)***	0.03 (0.01-0.12)***	0.51 (0.04-6.33)
Elevated white blood cells ^a	3.17 (1.19-8.45)*	3.36 (1.27-9.93)*	2.0 (0.41-9.79)
Elevated proteins ^b	1.38 (0.55-3.48)	1.44 (0.55-3.78)	1.15 (0.23-5.65)
Reduced glucose ^c	2.45 (0.21-28.32)	2.07 (0.18-23.94)	Not applicable
Clinical symptoms			
Asymptomatic	0.64 (0.18-2.22)	0.74 (0.19-2.80)	0.44 (0.09-2.25)
Brainstem/cerebellar	0.91 (0.38; 2.17)	1.03 (0.42; 2.57)	0.60 (0.14; 2.47)
Hemiparesis/monoparesis	0.48 (0.16; 1.45)	0.46 (0.14; 1.43)	0.57 (0.12; 2.72)
Aphasia	0.12 (0.02; 0.94)*	0.09 (0.01; 0.76)*	0.36 (0.02; 6.08)
Seizures	0.73 (0.21; 2.60)	0.74 (0.19; 2.80)	0.72 (0.12; 4.36)
Somnolence	12.19 (2.57; 57.88)**	9.10 (1.90; 43.47)**	Not applicable
Vomiting or nausea	2.13 (0.83; 5.49)	2.77 (0.94; 8.20)	1.16 (0.31; 4.32)
Headache	3.18 (1.33; 7.60)**	2.81 (1.12; 7.06)*	5.04 (1.02; 24.98)*
Concomitant involvement of other CNS sites			
Optic neuritis	4.72 (1.18; 18.97)*	3.51 (0.87; 14.18)	Not applicable
Myelitis	2.16 (0.92; 5.08)	2.63 (1.02; 6.82)*	1.30 (0.38; 4.44)
Location of index lesion			
Infratentorial	3.96 (1.60; 9.80)*	6.34 (2.10; 19.14)**	1.47 (0.47; 5.36)
Deep grey matter	6.26 (1.61; 24.34)**	Not applicable	1.31 (0.31; 5.55)
Periventricular	0.14 (0.05; 0.45)**	0.12 (0.04; 0.37)***	0.31 (0.07; 1.42)
Corticospinal tract	1.95 (0.55; 6.83)	Not applicable	0.36 (0.09; 1.40)
Corpus callosum	1.00 (0.16; 6.30)	Not applicable	0.21 (0.03; 1.41)
Hemispheric	0.45 (0.18; 1.13)	0.31 (0.12; 0.79)*	3.43 (0.39; 29.88)
Other locations	Not applicable	Not applicable	Not applicable
Index lesion MRI characteristics			
Mass effect	1.18 (0.49; 2.84)	1.51 (0.58; 3.95)	0.65 (0.19; 2.17)
Balò-like	0.10 (0.01; 0.76)*	0.07 (0.01; 0.53)*	Not applicable
Cystic component	0.10 (0.02; 0.46)**	0.07 (0.01; 0.33)**	0.73 (0.06; 8.67)
Poorly demarcated borders	5.59 (2.41; 12.97)***	7.97 (3.13; 20.30)***	2.31 (0.71; 7.48)
T2-hypointense rim	0.03 (0.00; 0.19)***	0.01 (0.00; 0.10)***	Not applicable
T1-hypointensity	0.12 (0.04; 0.31)***	0.06 (0.02; 0.23)***	0.32 (0.09; 1.14)
DWI restriction	0.04 (0.01; 0.11)***	0.01 (0.00; 0.06)***	0.18 (0.05; 0.64)
Arc peripheral DWI restriction	0.03 (0.01; 0.15)***	0.01 (0.003; 0.07)***	0.70 (0.06; 8.33)
Contrast enhancement	0.27 (0.11; 0.65)**	0.11 (0.03; 0.35)***	1.15 (0.37; 3.63)

Ring	0.06 (0.00; 0.43)**	0.04 (0.01; 0.30)**	0.36 (0.02; 6.08)
Cloud	0.87 (0.20; 3.85)	0.91 (0.21; 5.77)	0.50 (0.08; 3.48)
Optic nerve MRI characteristics			
Optic nerve contrast enhancement	3.35 (0.79; 14.21)	3.81 (0.73; 19.98)	Not applicable
Optic nerve bilateral contrast enhancement	Not applicable	Not applicable	Not applicable
Contrast enhancement >50% of optic nerve length	6.56 (0.71; 60.87)	4.92 (0.53; 45.86)	Not applicable
Optic nerve sheath enhancement	Not applicable	Not applicable	Not applicable
Spinal cord MRI characteristics			
Presence of T2-hyperintense spinal cord lesion	1.00 (0.39; 2.61)	1.25 (0.46; 3.37)	0.36 (0.07; 2.05)
Presence of T2-hyperintense spinal cord lesion in the conus	6.53 (1.81; 23.60)**	6.88 (1.67; 28.26)**	5.50 (0.60; 50.44)
Multiple spinal cord lesions	1.01 (0.38; 2.68)	1.05 (0.38; 2.91)	0.88 (0.20; 3.90)
Longitudinally-extensive T2-hyperintense spinal cord lesion	3.21 (1.17; 8.81)*	11.14 (2.75; 45.14)**	0.23 (0.41; 1.30)
Spinal cord enhancement	1.51 (0.58; 3.93)	2.04 (0.73; 5.71)	0.53 (0.12; 2.33)
Central lesions	6.17 (1.55; 24.53)**	12.21 (2.10; 71.01)**	2.14 (0.38; 12.20)
Peripheral lesions	Not applicable	Not applicable	Not applicable
Mixed centro-peripheral lesions	1.48 (0.42; 5.16)	2.49 (0.61; 10.18)	0.47 (0.08; 2.66)
Follow-up			
Complete resolution on T1-images	10.04 (3.74; 26.97)***	13.09 (4.27; 40.16)***	5.46 (1.40; 21.29)*
Complete resolution on T2-images	Not applicable	Not applicable	Not applicable
Subsequent attacks with tumefactive lesions	1.37 (0.42; 4.47)	1.48 (0.41; 5.33)	1.10 (0.19; 6.29)

*p<0.05; **p≤0.01; ***p≤0.001.

^aWhite blood cell count >5 cells/μl

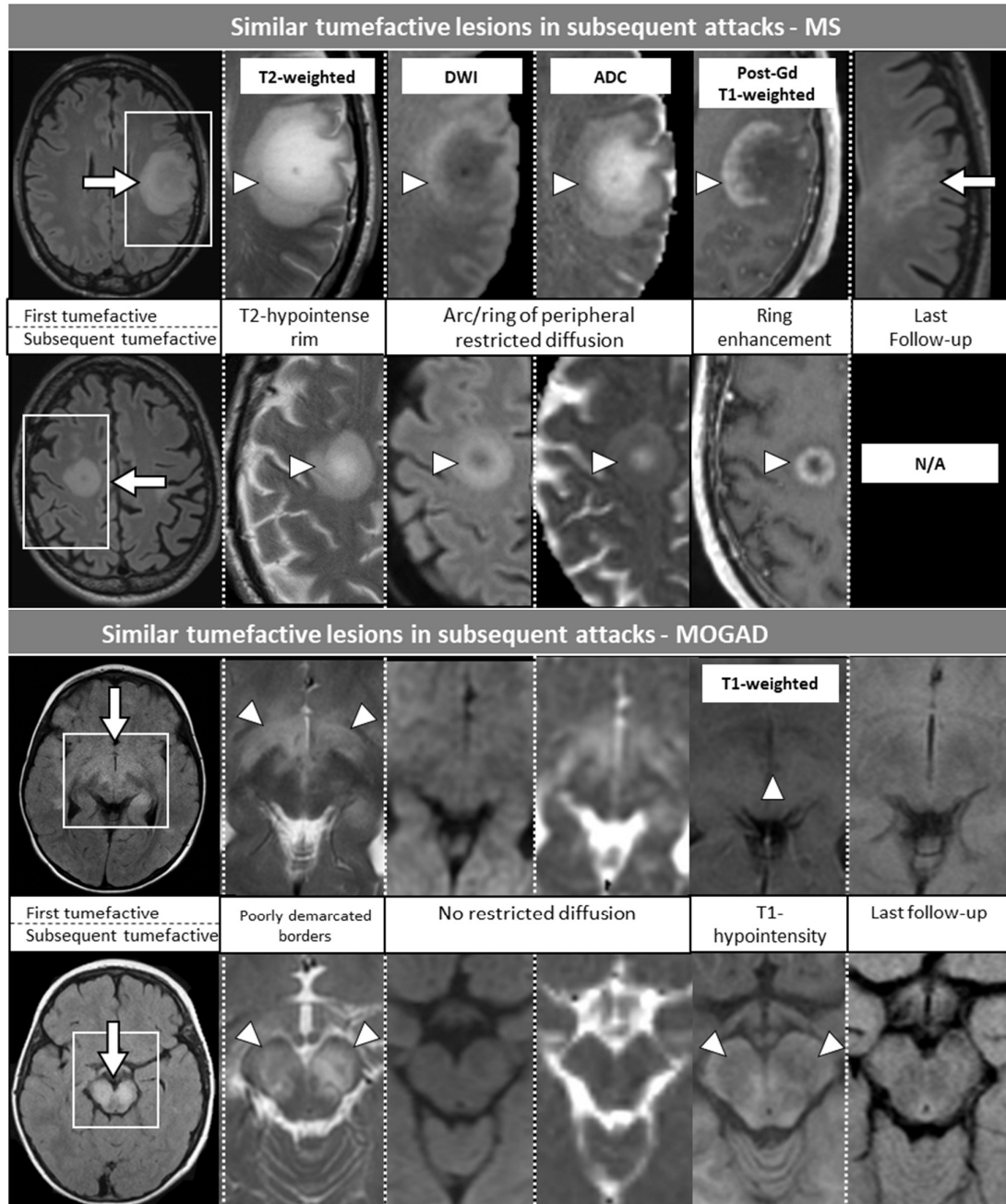
^bProtein levels >35 mg/dl

^cGlucose levels <40 mg/dl

Abbreviations: MOGAD=Myelin-oligodendrocyte-glycoprotein-IgG-associated disease; MS=multiple sclerosis; AQP4+NMOSD=aquaporin-4-IgG positive neuromyelitis optica spectrum disorders; DWI=diffusion-weighted imaging.

Supplementary Figure 6.2.1. Examples of tumefactive lesions with similar MRI features at first and subsequent tumefactive attacks. Lesions are shown by arrows and

displayed on axial T2-fluid-attenuated inversion recovery (T2-FLAIR, first picture on the left) and on the most appropriate sequence for the evaluation of each specific feature, indicated by an arrowhead. No further MRI follow-ups were available for the patient with MS and multiple tumefactive attacks.



Abbreviations: MOGAD=Myelin-oligodendrocyte-glycoprotein-IgG-associated disease; MS=multiple sclerosis; ADC=apparent diffusion coefficient map; DWI=diffusion-weighted images; Gd=gadolinium; N/A=not applicable.

6.3. Timing and Predictors of T2-Lesion Resolution in MOGAD

Cacciaguerra et al., unpublished data.

Abstract

Objectives. To determine the timing and predictors of T2-lesion resolution in myelin-oligodendrocyte-glycoprotein-antibody-associated disease (MOGAD).

Methods. Inclusion criteria were: 1) diagnosis of MOGAD; 2) ≥ 2 MRI scans ≥ 12 months apart; and 3) ≥ 1 brain or spinal cord T2-lesion. T2-lesion resolution or persistence was evaluated and predictors of it assessed with age-, sex- and T2-lesion size-adjusted generalized estimating equations.

Results. We studied 362 T2-lesions (brain, 291 [80%]; spinal cord, 71 [20%]), from 55 patients with a median follow-up of 54 months (interquartile range [IQR]: 17-74). At the last MRI, 268 T2-lesions (74%) resolved, with a median time to resolution of 4 months (IQR: 2-12). Acute steroid treatment favoured resolution (odds ratio [95% confidence interval] 1.75 [1.01; 3.03], $p=0.046$) but spontaneous T2-lesion resolution occurred in 17 of 35 untreated lesions (49%). Deep grey matter T2-lesions were more likely to resolve (2.94 [1.28; 6.75], $p=0.011$) while concomitant optic neuritis (0.39 [0.17; 0.90], $p=0.028$) or acute T1-hypointensity (0.30 [0.16; 0.55], $p<0.001$) reduced the likelihood of resolution.

Discussion. Most MOGAD T2-lesions resolve within 12 months. Spontaneous T2-lesion resolution in approximately 50% suggests that is part of MOGAD's natural history. The timing of T2-lesion resolution, promotion by corticosteroids and T1-hypointensity favoring persistence gives insight into the pathogenesis of T2-lesion resolution in MOGAD.

Introduction

MOGAD is an antibody-mediated demyelinating disorder affecting the CNS (Lopez-Chiriboga et al., 2018). Studies demonstrated that T2-hyperintense lesions in MOGAD can resolve over time with a frequency of 67-72% in the brain (Banks et al., 2020, Sechi et al., 2021c) and 79% in the spinal cord (Sechi et al., 2021c), differing from MS and AQP4+NMOSD in which T2-lesion resolution is rare occurring in 0-10% (Banks et al., 2020, Sechi et al., 2021c). It is not known if the high frequency of T2-lesion resolution reflects a treatment effect or the natural history of the disease. Moreover, studies assessing the timing and predictors of T2-lesion resolution are lacking but could guide follow-up MRI timing in MOGAD, determine if acute treatments help promote T2-lesion resolution, and improve our understanding of MOGAD pathophysiology. In this study, we aimed to determine the timing and predictors of T2-lesion resolution in MOGAD patients. We did this by analyzing the association with patient and lesional factors through retrospective evaluation of brain and spinal cord lesion dynamics in 55 patients from the Mayo Clinic database with a diagnosis of MOGAD (Lopez-Chiriboga et al., 2018).

Methods

Standard protocol approvals, registrations, and patient consents. The study was approved by Mayo Clinic's institutional review board. All participants consented to use of their medical records for research.

Data availability. Anonymized data from this study will be made available on request.

Inclusion criteria. Our inclusion criteria were: 1) MOGAD diagnosis (Lopez-Chiriboga et al., 2018); 2) availability of ≥ 2 MRI scans (at Mayo Clinic or outside facilities); 3) ≥ 1 brain or spinal cord T2-lesion of ≥ 1 cm; 4) clinical information available. A follow-up of at least 12 months without interval attacks in the same location was also required for the assessment of T2-lesion persistence or resolution.

We collected clinical and laboratory data (patient factors) from medical records, including age, sex, disease duration, phenotype, expanded disability status scale, MOG-IgG titer, evidence of CSF oligoclonal bands at any time, acute treatment within one

month of the attack (i.e., with steroids, intravenous immunoglobulins, or plasma exchange), and maintenance attack-prevention treatments.

We utilized the neuroradiology reports and a single rater with experience in neuroimaging (Laura Cacciaguerra), blinded to the clinical history to evaluate the following baseline MRI features of brain and spinal cord lesions (lesion factors): maximum transverse diameter (brain, on T2-FLAIR) or length (spine, on sagittal T2-weighted images), acute T1-hypointensity, gadolinium enhancement on T1-weighted post-gadolinium images. Complete resolution of T2-lesions was evaluated on all subsequent MRI scans.

Since each patient had multiple T2-lesions (median number of T2-lesions per patient 4, interquartile range [IQR] 1-7), hence outcomes being potentially correlated, the association between patient and lesion factors and T2-lesion resolution was assessed with age-, sex- and lesion size-adjusted generalized estimating equations with an exchangeable matrix.

Results

Details on the study population are reported in **Table 6.3.1**. A total of 362 lesions were studied, of whom 291 (80%) were in the brain and 71 (20%) in the spinal cord. Lesions were observed at the time of first attack in 149 cases (41%).

Table 6.3.1. Demographic and clinical features of the study population. Quantitative variables are reported as median (interquartile range), qualitative variables are reported as number (percentage).

	MOGAD with cerebral or spinal cord involvement (n=55)
Age in years	31 (15; 47)
Females	34 (62%)
Disease duration at first MRI [months]	1.4 (0.6; 3.4)
Pediatric onset	16 (29%)
Monophasic disease	26 (47%)
EDSS at first MRI scan	5.5 (3.5; 7.5)
Phenotype at onset*	
ADEM/multifocal	28 (51%)
Brainstem syndrome	0 (0%)
Optic neuritis	7 (13%)
Myelitis	15 (27%)

Cerebral cortical encephalitis	4 (6%)
High MOG-IgG titer ($\geq 1:100$)	40 (73%)
Oligoclonal bands in the CSF	4 (7%)

*Phenotype at onset was unknown in one patient.

Abbreviations: ADEM=acute disseminated encephalomyelitis; CSF=cerebrospinal fluid; EDSS=expanded disability status scale; MOG=myelin oligodendrocyte glycoprotein; MOGAD=myelin-oligodendrocyte antibody-associated disease.

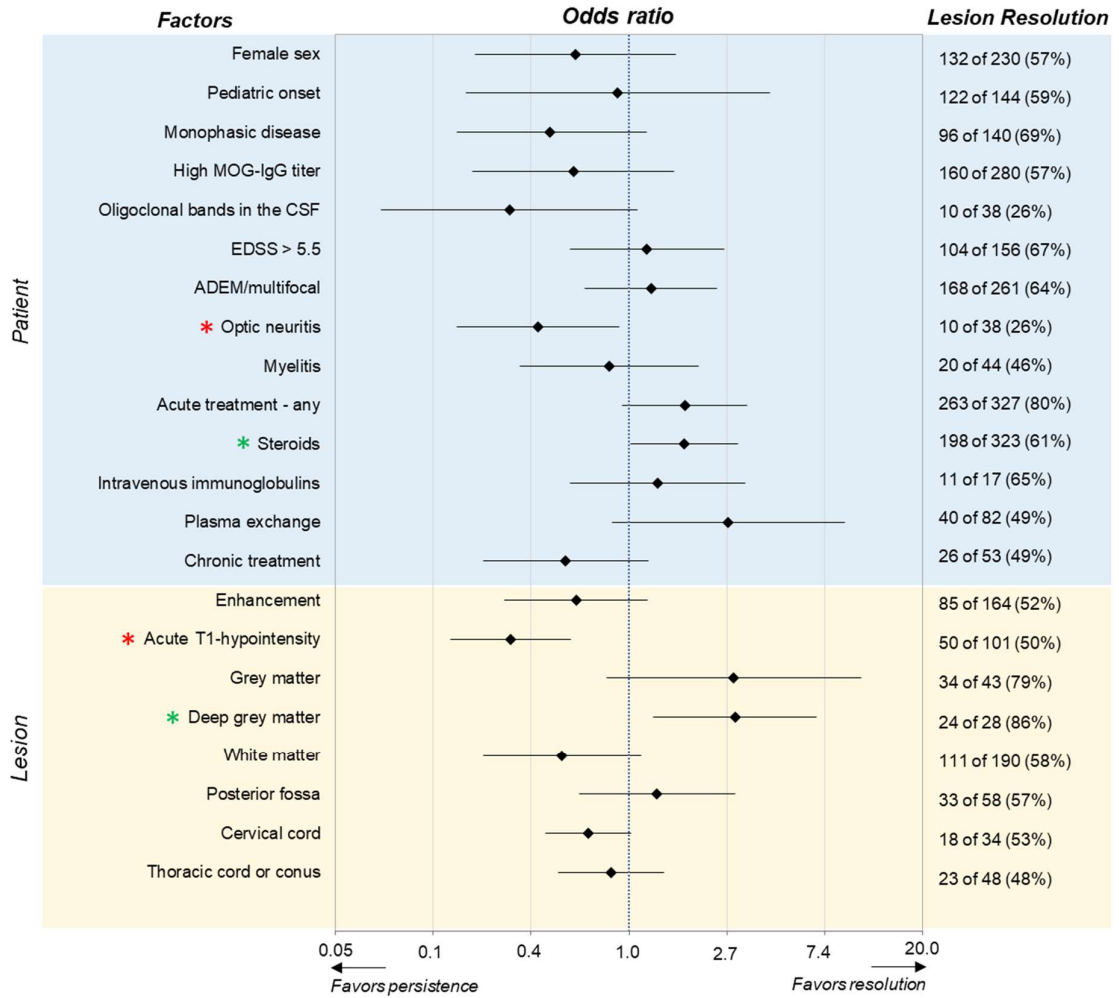
Timing and global frequency of lesion resolution. The median follow-up duration was 54 months (IQR: 17-74), with a median number of scans per patient of 5 (IQR: 3-8) in the brain and 4 (IQR: 2-8) in the spinal cord. At the last available MRI scan 268 of 362 T2-lesions (74%) resolved, with a median time to resolution of 4 (IQR: 2-12) months. The frequency of T2-lesion resolution was 217/291 (75%) in the brain, and 51/71 (72%) in the spinal cord.

Predictors of lesion resolution at 12 months (Figure 6.3.1). Concomitant optic neuritis was associated with a lower likelihood of T2-lesion resolution (odds ratio [95% confidence interval] 0.39 [0.17; 0.90]).

Among the treatments utilized, acute steroid treatment increased the likelihood of T2-lesion resolution (1.75 [1.01; 3.03], $p=0.046$) but other treatments had no significant effect (Figure 6.3.1). However, spontaneous T2-lesion resolution was observed in 17 of 35 lesions (49%) not undergoing any acute treatment. In these patients the median EDSS at the time of MRI was 3.5 (IQR: 2-5.5). Deep GM location increased the likelihood of T2-lesion resolution (2.94 [1.28; 6.75], $p=0.011$), while T1-hypointense lesions were less likely to resolve (0.30 [0.16; 0.55], $p<0.001$) (Figure 6.3.1).

Figure 6.3.1. Forest plot of patient and lesion factors associated with T2-lesion resolution at 12 months in MOGAD. Bars correspond to odds ratio and 95% intervals derived from age-, sex-, and lesion size-adjusted generalized estimating equations. The x axis is in logarithmic scale to improve readability. For lesion location, models were run separately for brain and spinal cord lesions. Significant results are highlighted with * (red for negative associations, green for positive associations). The total number of lesions

presenting a certain feature and the proportion resolved in 12 months is also specified in the column on the right.



Abbreviations: ADEM=acute disseminated encephalomyelitis; CSF=cerebrospinal fluid; EDSS=expanded disability status scale; MOG=myelin-oligodendrocyte glycoprotein.

Discussion

In MOGAD, T2-lesion resolution occurs in three quarters of MOGAD patients and usually occurs within one year. Acute corticosteroids increased the likelihood of T2-lesions disappearing while optic neuritis and T1-hypointensity reduced the likelihood of resolution. Notably, T2-lesions resolved in up to half of cases in the absence of any

treatment suggesting disappearance of T2-lesions in these patients is part of the natural history of MOGAD (Sechi et al., 2021c).

Prior studies have shown that MOGAD attacks often respond very favorably to acute corticosteroid treatment (Jarius et al., 2016) and thus it is not surprising that they increased the likelihood of T2-lesion resolution. Nonetheless, the finding that resolution of T2-lesions occurred in up to 50% without treatment suggest this is part of the natural history, and spontaneous resolution of T2-lesions has also been reported previously in case reports (Otani, Irioka et al., 2020, Takamatsu, Yamanaka et al., 2020) (Salama, Khan et al., 2020). This different behavior underlines the different pathophysiology from MS and AQP4+NMOSD in which lesion persistence is almost universal. While the use of maintenance attack prevention treatments and other acute treatments did not predict lesion resolution, this may reflect a selection bias with these treatments being administered in the more severe cases.

T2-lesions in the deep GM were more likely to resolve and fits with prior reports of acute disseminated encephalomyelitis (ADEM) in which thalamic lesions were noted to frequently resolve (up to 50% of ADEM cases are MOG-IgG positive and thus such cases may have represented MOGAD) (Tenenbaum, Chamoles et al., 2002). The greater remyelinating capacity of the GM than the WM was already outlined in patients with MS, although studies mainly focused on the cortex (Chang, Staugaitis et al., 2012). Another possibility is that T2-FLAIR lesions are more easily visualized in white than GM.

We found that with concomitant optic neuritis, the brain T2-lesions were less likely to resolve but the reasons are unclear. Increased CSF inflammatory markers in patients with optic neuritis and brain lesions versus optic neuritis alone could suggest a more aggressive disease in those patients (Sechi, Buciuc et al., 2021a). Also, acute T1-hypointensity, a biomarker of tissue disruption (Bruck et al., 1997), was the strongest predictor of lack of resolution.

Therefore, our study provides insight into the potential mechanisms of T2-lesion resolution. Firstly, steroids promoted lesion resolution which could suggest a role of myelin edema in this process. The presence of T1-hypointensity correlates with axonal damage on pathology (Bruck et al., 1997) and the absence of lesion resolution in those cases could suggest remyelination as being important, since a higher degree of axonal loss may overwhelm the capacity for tissue recovery and healing. Finally, the timing of

T2-lesion resolution might also fit with remyelination as isolated edema might be expected to resolve faster than a median of 4 months.

In terms of limitations, we acknowledge the retrospective design, and the lack of a standardized MRI protocol at regular time intervals, although this resembles clinical practice. In addition, we excluded lesions <1 cm which limited our assessment of smaller size as a predictor of lesion resolution and in our experience smaller lesions do often resolve. However, exclusion of smaller lesions <1 cm helped avoid the inclusion of small non-demyelinating T2-lesions that occur in 5% of young adults,(Hopkins, Beck et al., 2006) 38% of young adults with migraine (Messina, Rocca et al., 2013) and over 47% of aged 50 and older (Zhuang, Chen et al., 2018); the persistence of these non-demyelinating lesions over time could impede our ability to assess lesion resolution of MOGAD T2-lesions.

To conclude, this study demonstrates that T2-lesions in MOGAD usually resolve within one year even in the absence of acute treatment, and that a follow-up MRI at 6 to 12 months may help discriminate MOGAD from MS and AQP4+NMOSD as persistence of all lesions in follow-up strongly favors the latter two disorders.

7. DISCUSSION

This PhD project was focused on the study of NMOSD using MRI. For this purpose, we combined conventional and advanced MRI techniques to the newly available technological tools and biological resources such as artificial intelligence algorithms and transcriptomic atlases.

We started from the clinical observation of NMOSD patients, whose disease history is known to be characterized by a high frequency of severe motor or visual disability (Wingerchuk et al., 1999). The small rate of full recovery from an acute attack (Kleiter et al., 2016), the relatively high frequency of residual disability in patients with monophasic disease course (Wingerchuk et al., 1999), and the rarity of secondary disease progression (Wingerchuk et al., 2007) are elements supporting the notion that disability is attack-dependent.

However, more recent neuropsychological investigations also exposed a cognitive multidomain frailty in NMOSD (Oertel et al., 2019), which is hardly justifiable on the basis of acute clinical relapses, hence delineating a novel concept of attack-independent disability in this disease.

Physical and cognitive disability likely rely on different pathophysiological substrates. While the dependency between motor impairment and disease relapses supports the existence of a direct mechanism of damage due to focal inflammation, cognitive deficits suggest that primary mechanisms of neurodegeneration could also occur.

We chose the spinal cord as a model for the interplay between inflammation, neurodegeneration, and disability (Cacciaguerra et al., 2020). We studied lesions and atrophy location with a voxel-wise approach, hence being more specific in terms of spatial association between the two phenomena. Inflammatory spinal cord lesions generally colocalized with focal spinal cord atrophy, which in turn correlated with pyramidal and sensory EDSS functional scores, and disease duration. A group of AQP4+NMOSD patients without any spinal cord lesion or history of myelitis was also included, and their spinal cord volumes did not differ from HC. Altogether these findings suggest spinal that focal inflammatory damage is a necessary condition to the development of regional atrophy and disability. These results have been strengthened by the concomitant publication of similar findings obtained in an independent cohort of patients (Mariano,

Messina et al., 2021), where the Authors also found greater demyelination and axonal loss in within AQP4+NMOSD spinal cord lesions compared to MS and MOGAD, but no evidence of diffuse microstructural alterations in the segments never involved by an acute attack (Mariano et al., 2021). The burden of acute irreversible tissue damage likely explains the lack of clinical recovery, which in turns prevents focal processes of regional neurodegeneration to become clinically overt.

Regarding cognitive deficits, previous studies found an association with global atrophy in the hippocampus (Liu et al., 2015a), a structure that should be theoretically spared by acute NMOSD-attacks. Therefore, we decided to investigate cognitive impairment in AQP4+NMOSD patients and their association with global and regional hippocampal volumes (Cacciaguerra et al., 2021c). Results confirmed the previous notion of hippocampal atrophy in NMOSD, with a specific involvement of several subfields. Patients with verbal and visual memory impairment had greater atrophy in the hubs of the hippocampal trisynaptic circuit (i.e., CA1, CA3, and DG), but yet this did not explain attentive and executive deficits, which were the most frequent in our AQP4+NMOSD cohort and according to others (Oertel et al., 2019).

Therefore, we moved towards the hypothesis that cognitive impairment may rely on more diffuse brain abnormalities rather than regional atrophy. Functional MRI and especially the analysis of connectivity dynamics (i.e., TVC) is particularly sensitive to the functional changes associated with mild or absent structural damage, such as at early disease stages or in the presence of mild symptoms (Valsasina et al., 2019). We selected a brain area involved in highly integrated cognitive tasks, the precuneus, as seed region for a RS FC study exploring both static and dynamic FC in AQP4+NMOSD patients (Cacciaguerra, Mistri et al., 2022b). TVC abnormalities were more diffuse than static; increased TVC in the postcentral gyrus was associated with poorer cognitive performance in most domains, including attention/IPS, while in the occipital cortex contributed to worse performance at verbal learning. The cognitive role of brain regions mainly deputed to sensorimotor and visual processing suggests a maladaptive cross-modal plasticity in AQP4+NMOSD, probably secondary to the direct damage of the sensorimotor and visual pathways occurring in the disease. However, the variance of cognitive performance explained by RS FC abnormalities alone was quite small (R^2 ranging between 0.13 and 0.35), so it is evident that other elements contribute to cognition in these patients. The secondary results

of other studies enclosed in this PhD project, such as the correlation between worse performance in tests challenging attention and IPS and increased microstructural and perivascular abnormalities in the WM (Cacciaguerra, Carotenuto et al., 2022a, Cacciaguerra et al., 2021a) indicate a role of WM structural damage as well.

All this considered, the pathophysiology of cognitive issues in this disease is likely complex. It may be due to cortical neurodegeneration (Saji et al., 2013), as suggested by the evidence of atrophy, but also to the microstructural and functional changes of brain integrity associated with AQP4 and astrocytes loss. Therefore, the complexity of cognitive issues probably better suits to a multimodal MRI approach.

In the second part of the PhD, I pursued the aim of translating the a priori knowledge of AQP4+NMOSD pathophysiology into MRI-detectable measures. In MS, the most studied inflammatory disorder of the CNS, MRI is sensitive to subclinical disease activity, but the underlying pathophysiology is unknown. In AQP4+NMOSD we are facing an opposite scenario, where the pathophysiological mechanism is known, tailored treatments are available, but we are not able to identify upcoming relapses before they become clinically overt and, therefore, disabling.

I started drawing my considerations based on differences in WM microstructural features between patients with AQP4+NMOSD and MS (Cacciaguerra et al., 2021a), expecting AQP4+NMOSD patients to be characterized by mild or no NAWM abnormalities. However, we found an interesting diffuse dissociation between DTI measures, with normal FA and increased MD values, which was different from what usually reported in demyelinating disorders (i.e., FA reduction and MD increase), but already described in an independent cohort of NMOSD patients (Liu et al., 2012b). Furthermore, AQP4+NMOSD patients also had a significant reduction in the T1/T2-w, a ratio between T1- and T2-signal intensity which should theoretically enhance myelin based on its signal property (Glasser & Van Essen, 2011). We considered possible alternative sources of isolated MD and T1/T2-w variations, and interpreted the results in the hypothesis of a subclinical increase in brain water content due to (i) astrocytes injury at the BBB potentially enhanced by (ii) reduced water reabsorption secondary to AQP4 loss or its downregulation as described in pathology (Lucchinetti et al., 2002). A second element of interest was that NAWM abnormalities appeared to be diffuse in the brain, possibly

reflecting the serological origin of AQP4-IgG. This finding was later confirmed at pathological level, where a recent investigation reported for the first time the existence of a diffuse astrocytopathy in NMOSD (Guo et al., 2022).

Nonetheless, DTI and T1/T2-w cannot be considered optimized techniques for the assessment of water content, so we decided to specifically test this hypothesis by measuring the T2rt (i.e., the constant of magnetization decay on the transverse plane), which is a proxy of water content (Bonnier et al., 2014) and can be easily calculated from the echo time of conventional brain dual echo sequences. Results confirmed what previously observed, and increased T2rt (i.e., water) was observed in both NAWM and GM of AQP4+NMOSD patients compared to HC (Cacciaguerra, Pagani et al., 2022c).

The main limitation of the study was the retrospective design. However, this allowed the collection of the date of the closest clinical attack before and after the MRI acquisition, so we could identify a group of AQP4+NMOSD patients with incipient or recent disease activity. These patients were characterized by increased T2rt compared to those clinically stable, suggesting that the burden of this brain alteration may be dynamic and higher close to relapses, even when occurring at remotes sites such as the optic nerve and the spinal cord (Cacciaguerra et al., 2022c).

Likewise, a recent study demonstrated that seral GFAP levels (i.e., marker of astrocytes damage) increase in the week preceding a clinical relapse, hence being referenced as a biomarker of disease activity in AQP4+NMOSD (Aktas et al., 2021). However, this measure is not yet available in most clinical and research facilities, so its direct application in clinical practice is still far. The longitudinal measurement of the T2rt will clarify its utility for disease monitoring, ideally with a concomitant measurement of GFAP as proof-of-concept.

Another possible consequence of astrocytes damage and AQP4 loss *in vivo* is the macrostructural or microstructural alteration of perivascular spaces, which are delimited by the astrocytes (Wuerfel et al., 2008). Water diffusivity along these structures (i.e., DTI-ALPS index) was suggested as a proxy for glymphatic functioning (Taoka et al., 2017), a brain clearance system promoted by CSF flux that experimental models attribute to an AQP4-dependent mechanism (Iliff & Nedergaard, 2013).

We explored this using conventional MRI and DTI, and found significant perivascular enlargement and reduced diffusivity along perivascular spaces in patients compared to

controls. DTI-ALPS index reduction resulted independently associated with NMOSD diagnosis (Cacciaguerra et al., 2022a). However, it is worth to mention that a similar reduction of DTI-ALPS index was also observed in other neurological disorders (Carotenuto et al., 2021, Chen et al., 2021, Taoka et al., 2017, Yokota et al., 2019), so its applicability in terms of differential diagnosis is probably low. It also resulted associated with worse clinical disability independent of disease duration, supporting the idea that this alteration is the epiphenomenon of the pathophysiological mechanism of the disease, hence being associated with its severity but present since the onset.

The results obtained so far suggest a strong association between AQP4+NMOSD pathophysiology and altered water diffusivity in the brain (Cacciaguerra et al., 2022a, Cacciaguerra et al., 2022c, Cacciaguerra et al., 2021a), similarly to what already known for lesions, which usually occur in areas of high AQP4 expression (Pittock et al., 2006). This was less clear when we analyzed GM atrophy and functional reorganization (Cacciaguerra et al., 2022b, Cacciaguerra et al., 2021c), although it is known that AQP4 is also highly expressed in the cortex (Aoyama, Kakita et al., 2012) and hippocampus (Sjostedt, Zhong et al., 2020), and is associated with cortical neuronal loss in NMOSD (Saji et al., 2013).

To better investigate the association between brain damage and underlying biological processes we combined lesion, atrophy, and WM microstructural abnormalities maps with the AHBA, a gene expression atlas of the brain (*Section 5.4, unpublished data*). Results confirmed the association between pathophysiologically-specific processes such as complement activation, neutrophil degranulation, interferon gamma signaling, and TRAF6-NF-KB activation, with brain lesions and increased MD. Complement activation was also relevant for GM atrophy, although its location mainly in the visual pathway, and the heterogeneity of the associated biological processes, indicate that it is likely multifactorial and only in part attributable to a direct effect of AQP4-associated damage. The match between this type of imaging analysis and the established knowledge of AQP4+NMOSD supports the application of this approach for the study of other antibody-mediated CNS disorders, where it might potentially help with the identification of the most relevant biological processes, when unknown.

In the final part of the PhD we focused on the seronegative side of NMO. As already mentioned, this section is at least in part already outdated, since it is now established that patients with positive MOG-IgG testing and NMOSD-like phenotype should be diagnosed with MOGAD (Lopez-Chiriboga et al., 2018).

Seronegative-NMOSD is an acceptable diagnosis according to the latest available NMOSD diagnostic criteria (Wingerchuk et al., 2015), but their inclusion was debated from the beginning and several International Panel members were concerned about their heterogeneity (Fujihara, 2019). Literature is also controversial, and both increased or normal levels of astrocyte damage biomarkers (i.e., GFAP and S100B) have been reported in double-seronegative NMOSD patients (Alves Do Rego & Collongues, 2018, Hyun, Kim et al., 2022, Wei et al., 2018), fueling the disagreement regarding their pathogenesis. Beside the within-group heterogeneity of seronegative-NMOSD, differences in literature may also be attributed to inter-center variability in (i) applying the diagnostic criteria in clinical practice, (ii) type and timing of antibody-testing.

This issue is far from being solved, and was not unraveled during this PhD. However, our DL algorithm classified these double-seronegative NMOSD patients and double-seronegative patients with idiopathic recurrent myelitis and optic neuritis as extremely similar to AQP4+NMOSD, at least from a structural conventional imaging perspective. We also demonstrated that 3 of 27 (11%) double-seronegative patients actually had an antibody-mediated disorder, but the diagnostic test initially resulted negative (Cacciaguerra et al., 2022d). Factors affecting antibody detectability, such as steroid treatment, plasma exchange and others should be assessed in a systematic way to provide guidance to clinicians and improve patients clinical care. One double-seronegative patient had MS, and this gives credit to the heterogeneity and the possible misdiagnosis of double-seronegative patients.

Overall, my opinion is that updated diagnostic criteria for NMOSD and MOGAD are now needed, and should rely on antibody detection and clinical features, in order to improve diagnostic reliability and ensure an optimized treatment. On the other hand, I also believe that the scientific community should not scotomize the issue of double-seronegative NMOSD but encourage studies pursuing a systematic assessment of its heterogeneity. These patients represent a relatively common clinical challenge and probably do not receive optimal treatment given the uncertainty of their diagnosis and pathophysiology.

From my personal standpoint, I consider valuable the idea of applying artificial intelligence to get hints or learn something new about disease pathophysiology, rather than teaching to a DL algorithm an established knowledge, but the algorithm should probably be trained on a broader spectrum of differential diagnoses (including other antibody-mediated disorders such as GFAP astrocytopathy) and allow a multi-class rather than binary classification.

The potential of artificial intelligence for the understanding of seronegative patients was demonstrated by the ability of the DL algorithm of considering MOGAD patients different from both MS and AQP4+NMOSD (Cacciaguerra et al., 2022d) despite the limited sample-size, highlighting another strength of artificial intelligence which is its single-patient applicability.

This sensitivity to radiological differences between antibody-mediated disorders achieved by the DL algorithm is not obvious, because most prior studies applying MRI-based criteria (Cai, Zheng et al., 2021, Jurynczyk et al., 2017a) and even ML (Jurynczyk et al., 2017a) failed in discriminating AQP4+NMOSD and MOGAD from a single MRI scan.

During the final year of my PhD course, I had the chance to join the Mayo Clinic group and deepen the study of a group of patients previously included in the seronegative NMO spectrum, now known as MOGAD.

In that occasion I also observed an extensive clinical, laboratory, and radiological overlap between AQP4+NMOSD and MOGAD patients with tumefactive demyelination (*Section 6.2, unpublished data*). MRI features between the two antibody-mediated disorders were broadly similar, except for a higher rate of DWI restriction and a tendency towards a higher frequency of T1-hypointense lesions in AQP4+NMOSD patients, possibly indicating more severe acute tissue damage.

This study highlighted that follow-up imaging can be extremely useful for the differential diagnosis of antibody-mediated demyelinating diseases, because lesion resolution strongly favors MOGAD, as already demonstrated by the Mayo group (Banks et al., 2020, Sechi et al., 2021c) and reported by others (Jurynczyk et al., 2017a).

This peculiar behavior of T2-hyperintense lesions was reported in 67 to 72% of brain lesions and 79% of spinal cord lesions in MOGAD, while it is rarely encountered in

AQP4+NMOSD patients (0-10%) (Banks et al., 2020, Sechi et al., 2021c), likely reflecting the different pathogenesis of the two diseases.

We explored this aspect in the final project included in my PhD course, where we examined the timing and predictors of lesion resolution in over 350 lesions in patients with MOGAD. Findings suggest that resolution usually occurs early, with a median time of four months from lesion formation (*Section 6.3, unpublished data*).

Lesions in the deep GM are more likely to resolve (maybe because of the greater remyelinating capacity (Chang et al., 2012)) while those associated with T1-hypointensity usually persist; steroids favor lesion resolution but are not a necessary condition. Therefore, we hypothesized that lesion resolution in MOGAD may rely on both myelin edema reabsorption and remyelination, since the first is fast and promoted by steroids, while the second occurs later and may be hampered in case of severe tissue disruption as in T1-hypointense lesions (Bruck et al., 1997).

8. CONCLUSIONS

To conclude, in this PhD project we were able to identify different MRI correlates of attack-dependent (i.e., motor) and attack-independent (i.e., cognitive) disability in AQP4+NMOSD, likely reflecting the different underlying mechanism.

Then, we used advanced MRI techniques to reconstruct the elements of NMOSD pathophysiology in vivo and identified brain water content (here estimated with T2rt) as a possible indirect biomarker of disease activity, potentially useful for disease monitoring. Finally, we highlighted the potential of artificial intelligence for the differential diagnosis and understanding of inflammatory CNS disorders and found that lesion resolution is a key element for the discrimination between AQP4+NMOSD and the newly defined disease entity of MOGAD, as per different pathophysiology.

However, my personal opinion is that the novelty of this PhD project is not to be found in the results, but in the use of NMOSD as a model for tailored imaging analysis. We looked for specific pathophysiological correlates of the disease such as water unbalance or glymphatic impairment, based on the a priori knowledge of the pathogenetic antibody. Also, we demonstrated that a joint analysis of quantitative MRI and gene expression atlases could be a tool for the understanding of antibody-associated disorders. In fact, it was able to identify complement activation as the most relevant biological process associated with brain damage in AQP4+NMOSD, which was never shown before.

This type of approach is likely to become increasingly useful in the future because new technologies are speeding antibody discovery (Larman, Zhao et al., 2011) but the understanding of their pathophysiology is challenging, and their monitoring unclear.

For instance, despite the optimization of MOG-IgG testing with a cell-based assay expressing full-length native-conformation human MOG dates back several years ago (Waters, Woodhall et al., 2015), the pathophysiology of MOGAD is still a topic of intense scientific debate (Keller, Lopez et al., 2021, Keller, Lopez et al., 2022, McCombe, Flanagan et al., 2022) and, like NMOSD, the conventional use of inter-attack MRI for disease surveillance is questionable (S, Chen et al., 2022).

Future investigations will clarify the translational power of this approach, but this PhD project paved the way.

9. ADDITIONAL PUBLICATIONS OF THE PHD COURSE

Original Research

1. B Syc-Mazurek S, Chen JJ, Morris P, Sechi E, Mandrekar J, Tillema JM, Lopez-Chiriboga AS, Lucchinetti CF, Zaleski N, **Cacciaguerra L**, Buciuc M, Krecke KN, Messina SA, Bhatti MT, Pittock SJ, Flanagan EP. Frequency of New or Enlarging Lesions on MRI Outside of Clinical Attacks in Patients With MOG-Antibody-Associated Disease. *Neurology*. 2022 Sep 29;10.1212/WNL.0000000000201263. doi: 10.1212/WNL.0000000000201263. Epub ahead of print. PMID: 36175150.
2. Carnero Contentti E, Rojas JI, Criniti J, Lopez PA, Daccach Marques V, Soto de Castillo I, Tkachuk V, Marrodan M, Correale J, Farez MF, Kim HJ, Hyun JW, Messina S, Mariano R, Rocca MA, **Cacciaguerra L**, Filippi M, Palace J, Juryńczyk M. Towards imaging criteria that best differentiate MS from NMOSD and MOGAD: Large multi-ethnic population and different clinical scenarios. *Mult Scler Relat Disord*. 2022 Mar 27;61:103778. doi: 10.1016/j.msard.2022.103778. Epub ahead of print. PMID: 35452969.
3. Mistri D, **Cacciaguerra L**, Storelli L, Meani A, Cordani C, Rocca MA, Filippi M. The association between cognition and motor performance is beyond structural damage in relapsing-remitting multiple sclerosis. *J Neurol*. 2022 Mar 12. doi: 10.1007/s00415-022-11044-8. Epub ahead of print. PMID: 35278104.
4. Carotenuto A, Valsasina P, Hidalgo de la Cruz M, **Cacciaguerra L**, Preziosa P, Marchesi O, Filippi M, Rocca MA. Divergent time-varying connectivity of thalamic sub-regions characterizes clinical phenotypes and cognitive status in multiple sclerosis. *Mol Psychiatry*. 2022 Jan 7. doi: 10.1038/s41380-021-01401-w. Epub ahead of print. PMID: 34992237.
5. Carotenuto A, **Cacciaguerra L**, Pagani E, Preziosa P, Filippi M, Rocca MA. Glymphatic system impairment in multiple sclerosis: relation with brain damage and

disability. *Brain*. 2021 Dec 17;awab454. doi: 10.1093/brain/awab454. Epub ahead of print. PMID: 34919648.

6. Preziosa P, Pagani E, Bonacchi R, **Cacciaguerra L**, Falini A, Rocca MA, Filippi M. In vivo detection of damage in multiple sclerosis cortex and cortical lesions using NODDI. *J Neurol Neurosurg Psychiatry*. 2021 Nov 19;jnnp-2021-327803. doi: 10.1136/jnnp-2021-327803. Epub ahead of print. PMID: 34799405.

7. Rocca MA, Anzalone N, Storelli L, Del Poggio A, **Cacciaguerra L**, Manfredi AA, Meani A, Filippi M. Deep Learning on Conventional Magnetic Resonance Imaging Improves the Diagnosis of Multiple Sclerosis Mimics. *Invest Radiol*. 2021 Apr 1;56(4):252-260. doi: 10.1097/RLI.0000000000000735. PMID: 33109920.

8. Marchesi O, Bonacchi R, Valsasina P, Preziosa P, Pagani E, **Cacciaguerra L**, Meani A, Conti L, Mistri D, Rocca MA, Filippi M. Functional and structural MRI correlates of executive functions in multiple sclerosis. *Mult Scler*. 2022 Apr;28(5):742-756. doi: 10.1177/13524585211033184. Epub 2021 Aug 13. PMID: 34387534.

Reviews

1. **Cacciaguerra L**, Sechi E, Rocca MA, Filippi M, Pittock SJ, Flanagan EP. Neuroimaging features in inflammatory myelopathies: A review. *Front Neurol*. 2022 Oct 18;13:993645. doi: 10.3389/fneur.2022.993645. PMCID: PMC9623025.

2. Fadda G, Flanagan EP, **Cacciaguerra L**, Jitprapaikulsan J, Solla P, Zara P, Sechi E. Myelitis Features and Outcomes in CNS Demyelinating Disorders: Comparison between multiple sclerosis, MOGAD, and AQP4-IgG-positive NMOSD. *Front Neurol*. 2022 – Accepted, ahead of publication. doi: 10.3389/fneur.2022.1011579

3. Sechi E, **Cacciaguerra L**, Chen JJ, Mariotto S, Fadda G, Dinoto A, Lopez-Chiriboga AS, Pittock SJ, Flanagan EP. Myelin Oligodendrocyte Glycoprotein Antibody-Associated Disease (MOGAD): A Review of Clinical and MRI Features, Diagnosis, and

Management. *Front Neurol.* 2022 Jun 17;13:885218. doi: 10.3389/fneur.2022.885218. PMID: 35785363; PMCID: PMC9247462.

4. **Cacciaguerra L**, Tortorella P, Rocca MA, Filippi M. Targeting Neuromyelitis Optica Pathogenesis: Results from Randomized Controlled Trials of Biologics. *Neurotherapeutics.* 2021 Apr 28. doi: 10.1007/s13311-021-01055-0. Epub ahead of print. PMID: 33909234.

5. Rocca MA, **Cacciaguerra L**, Filippi M. Moving beyond anti-aquaporin-4 antibodies: emerging biomarkers in the spectrum of neuromyelitis optica. *Expert Rev Neurother.* 2020;20(6):601-618. doi:10.1080/14737175.2020.1764352

Editorials and Commentaries

1. **Cacciaguerra L**, Flanagan EP. Improving myelopathy diagnosis now and into the future. *J Neurol Sci.* 2022 Oct 1;442:120424. doi: 10.1016/j.jns.2022.120424. Epub ahead of print. PMID: 36201962.

2. Zanon A, **Cacciaguerra L**, Martelli G, Filippi M. Neurosensory dysphagia in a COVID-19 patient. *J Neurol.* 2021 Apr 19:1–3. doi: 10.1007/s00415-021-10541-6. Epub ahead of print. PMID: 33876325; PMCID: PMC8055053.

3. Giordano A, Schwarz G, **Cacciaguerra L**, et al. COVID-19: can we learn from encephalitis lethargica?. *Lancet Neurol.* 2020;19(7):570. doi:10.1016/S1474-4422(20)30189-7

Book chapters

1. **Cacciaguerra L**, Storelli L, Rocca MA, Filippi M. Chapter 6 - Current and future applications of artificial intelligence in multiple sclerosis, Editor(s): Anitha S. Pillai, Bindu Menon, “Augmenting Neurological Disorder Prediction and Rehabilitation Using Artificial Intelligence”, Academic Press, 2022, Pages 107-144, ISBN 9780323900379, <https://doi.org/10.1016/B978-0-323-90037-9.00012-6>.

10. REFERENCES

Abdul-Rahman HS, Gdeisat MA, Burton DR, Lalor MJ, Lilley F, Moore CJ (2007) Fast and robust three-dimensional best path phase unwrapping algorithm. *Appl Opt* 46: 6623-35

Abou Zeid N, Pirko I, Erickson B, Weigand SD, Thomsen KM, Scheithauer B, Parisi JE, Giannini C, Linbo L, Lucchinetti CF (2012) Diffusion-weighted imaging characteristics of biopsy-proven demyelinating brain lesions. *Neurology* 78: 1655-62

Aboul-Enein F, Krssak M, Hoftberger R, Prayer D, Kristoferitsch W (2010) Diffuse white matter damage is absent in neuromyelitis optica. *AJNR Am J Neuroradiol* 31: 76-9

Aktas O, Smith MA, Rees WA, Bennett JL, She D, Katz E, Cree BAC, group NMs, the NMsi (2021) Serum Glial Fibrillary Acidic Protein: A Neuromyelitis Optica Spectrum Disorder Biomarker. *Ann Neurol* 89: 895-910

Alexander DC, Pierpaoli C, Basser PJ, Gee JC (2001) Spatial transformations of diffusion tensor magnetic resonance images. *IEEE transactions on medical imaging* 20: 1131-9

Algahtani H, Shirah B, Alassiri A (2017) Tumefactive demyelinating lesions: A comprehensive review. *Mult Scler Relat Disord* 14: 72-79

Allali G, Assal F, Kressig RW, Dubost V, Herrmann FR, Beauchet O (2008) Impact of impaired executive function on gait stability. *Dement Geriatr Cogn Disord* 26: 364-9

Altermatt A, Gaetano L, Magon S, Haring DA, Tomic D, Wuerfel J, Radue EW, Kappos L, Sprenger T (2018) Clinical Correlations of Brain Lesion Location in Multiple Sclerosis: Voxel-Based Analysis of a Large Clinical Trial Dataset. *Brain topography* 31: 886-894

Alvarenga MP, Alvarenga RM, Alvarenga MP, Santos AM, Thuler LC (2012) Anti-AQP(4) antibody in idiopathic acute transverse myelitis with recurrent clinical course: frequency of positivity and influence in prognosis. *The journal of spinal cord medicine* 35: 251-5

- Alves Do Rego C, Collongues N (2018) Neuromyelitis optica spectrum disorders: Features of aquaporin-4, myelin oligodendrocyte glycoprotein and double-seronegative-mediated subtypes. *Revue neurologique* 174: 458-470
- Amato MP, Portaccio E, Goretti B, Zipoli V, Ricchiuti L, De Caro MF, Patti F, Vecchio R, Sorbi S, Trojano M (2006) The Rao's Brief Repeatable Battery and Stroop Test: normative values with age, education and gender corrections in an Italian population. *Mult Scler* 12: 787-93
- Andersson JLR, Graham MS, Drobnyak I, Zhang H, Filippini N, Bastiani M (2017) Towards a comprehensive framework for movement and distortion correction of diffusion MR images: Within volume movement. *Neuroimage* 152: 450-466
- Aoyama M, Kakita H, Kato S, Tomita M, Asai K (2012) Region-specific expression of a water channel protein, aquaporin 4, on brain astrocytes. *J Neurosci Res* 90: 2272-80
- Arnatkeviciute A, Fulcher BD, Fornito A (2019) A practical guide to linking brain-wide gene expression and neuroimaging data. *Neuroimage* 189: 353-367
- Asgari N, Skejoe HP, Lillevang ST, Steenstrup T, Stenager E, Kyvik KO (2013) Modifications of longitudinally extensive transverse myelitis and brainstem lesions in the course of neuromyelitis optica (NMO): a population-based, descriptive study. *BMC Neurol* 13: 33
- Ashburner J (2007) A fast diffeomorphic image registration algorithm. *Neuroimage* 38: 95-113
- Backner Y, Ben-Shalom I, Kuchling J, Siebert N, Scheel M, Ruprecht K, Brandt A, Paul F, Levin N (2020) Cortical topological network changes following optic neuritis. *Neurology(R) neuroimmunology & neuroinflammation* 7
- Badaut J, Ashwal S, Adami A, Tone B, Recker R, Spagnoli D, Ternon B, Obenaus A (2011) Brain water mobility decreases after astrocytic aquaporin-4 inhibition using RNA interference. *Journal of cerebral blood flow and metabolism : official journal of the International Society of Cerebral Blood Flow and Metabolism* 31: 819-31

Bailly M, Destrieux C, Hommet C, Mondon K, Cottier JP, Beaufils E, Vierron E, Vercouillie J, Ibazizene M, Voisin T, Payoux P, Barre L, Camus V, Guilloteau D, Ribeiro MJ (2015) Precuneus and Cingulate Cortex Atrophy and Hypometabolism in Patients with Alzheimer's Disease and Mild Cognitive Impairment: MRI and (18)F-FDG PET Quantitative Analysis Using FreeSurfer. *Biomed Res Int* 2015: 583931

Balint B, Vincent A, Meinck HM, Irani SR, Bhatia KP (2018) Movement disorders with neuronal antibodies: syndromic approach, genetic parallels and pathophysiology. *Brain* 141: 13-36

Banks SA, Morris PP, Chen JJ, Pittock SJ, Sechi E, Kunchok A, Tillema JM, Fryer JP, Weinshenker BG, Krecke KN, Lopez-Chiriboga AS, Nguyen A, Greenwood TM, Lucchinetti CF, Zalewski NL, Messina SA, Flanagan EP (2020) Brainstem and cerebellar involvement in MOG-IgG-associated disorder versus aquaporin-4-IgG and MS. *J Neurol Neurosurg Psychiatry*

Bansal R, Hao X, Liu F, Xu D, Liu J, Peterson BS (2013) The effects of changing water content, relaxation times, and tissue contrast on tissue segmentation and measures of cortical anatomy in MR images. *Magnetic resonance imaging* 31: 1709-30

Basser PJ, Mattiello J, LeBihan D (1994a) Estimation of the effective self-diffusion tensor from the NMR spin echo. *Journal of magnetic resonance Series B* 103: 247-54

Basser PJ, Mattiello J, LeBihan D (1994b) MR diffusion tensor spectroscopy and imaging. *Biophys J* 66: 259-67

Battaglini M, Jenkinson M, De Stefano N (2012) Evaluating and reducing the impact of white matter lesions on brain volume measurements. *Hum Brain Mapp* 33: 2062-71

Battaglini M, Smith SM, Brogi S, De Stefano N (2008) Enhanced brain extraction improves the accuracy of brain atrophy estimation. *Neuroimage* 40: 583-9

Beck AT, Steer RA (1987) *Manual for the Revised Beck Depression Inventory*. Psychological Corporation, San Antonio, TX

- Beck AT, Ward CH, Mendelson M, Mock J, Erbaugh J (1961) An inventory for measuring depression. *Arch Gen Psychiatry* 4: 561-71
- Beer A, Biberacher V, Schmidt P, Righart R, Buck D, Berthele A, Kirschke J, Zimmer C, Hemmer B, Muhlau M (2016) Tissue damage within normal appearing white matter in early multiple sclerosis: assessment by the ratio of T1- and T2-weighted MR image intensity. *Journal of neurology* 263: 1495-502
- Bermel RA, Bakshi R (2006) The measurement and clinical relevance of brain atrophy in multiple sclerosis. *The Lancet Neurology* 5: 158-70
- Bigaut K, Achard S, Hemmert C, Baloglu S, Kremer L, Collongues N, De Seze J, Kremer S (2019) Resting-state functional MRI demonstrates brain network reorganization in neuromyelitis optica spectrum disorder (NMOSD). *PLoS One* 14: e0211465
- Bigler ED, Mortensen S, Neeley ES, Ozonoff S, Krasny L, Johnson M, Lu J, Provencal SL, McMahon W, Lainhart JE (2007) Superior temporal gyrus, language function, and autism. *Dev Neuropsychol* 31: 217-38
- Bilbao D, Luciani L, Johannesson B, Piszczek A, Rosenthal N (2014) Insulin-like growth factor-1 stimulates regulatory T cells and suppresses autoimmune disease. *EMBO Mol Med* 6: 1423-35
- Bjornsson HT, Benjamin JS, Zhang L, Weissman J, Gerber EE, Chen YC, Vaurio RG, Potter MC, Hansen KD, Dietz HC (2014) Histone deacetylase inhibition rescues structural and functional brain deficits in a mouse model of Kabuki syndrome. *Sci Transl Med* 6: 256ra135
- Blanc F, Noblet V, Jung B, Rousseau F, Renard F, Bourre B, Longato N, Cremel N, Di Bitonto L, Kleitz C, Collongues N, Foucher J, Kremer S, Armspach JP, de Seze J (2012) White matter atrophy and cognitive dysfunctions in neuromyelitis optica. *PLoS One* 7: e33878
- Boisgontier J, Tacchella JM, Lemaitre H, Lehman N, Saitovitch A, Gatinois V, Boursier G, Sanchez E, Rechtman E, Fillon L, Lyonnet S, Le Quang Sang KH, Baujat G, Rio M, Boute O, Faivre L, Schaefer E, Sanlaville D, Zilbovicius M, Grevent D et al. (2019)

Anatomical and functional abnormalities on MRI in kabuki syndrome. *Neuroimage Clin* 21: 101610

Bonnier G, Roche A, Romascano D, Simioni S, Meskaldji D, Rotzinger D, Lin YC, Menegaz G, Schlupe M, Du Pasquier R, Sumpf TJ, Frahm J, Thiran JP, Krueger G, Granziera C (2014) Advanced MRI unravels the nature of tissue alterations in early multiple sclerosis. *Ann Clin Transl Neurol* 1: 423-32

Brown JW, Pardini M, Brownlee WJ, Fernando K, Samson RS, Prados Carrasco F, Ourselin S, Gandini Wheeler-Kingshott CA, Miller DH, Chard DT (2017) An abnormal periventricular magnetization transfer ratio gradient occurs early in multiple sclerosis. *Brain* 140: 387-398

Bruck W, Bitsch A, Kolenda H, Bruck Y, Stiefel M, Lassmann H (1997) Inflammatory central nervous system demyelination: correlation of magnetic resonance imaging findings with lesion pathology. *Ann Neurol* 42: 783-93

Buckner RL, Krienen FM, Yeo BT (2013) Opportunities and limitations of intrinsic functional connectivity MRI. *Nat Neurosci* 16: 832-7

Cacciaguerra L, Carotenuto A, Pagani E, Mistri D, Radaelli M, Martinelli V, Filippi M, Rocca MA (2022a) Magnetic Resonance Imaging Evaluation of Perivascular Space Abnormalities in Neuromyelitis Optica. *Ann Neurol* 92: 173-183

Cacciaguerra L, Meani A, Mesaros S, Radaelli M, Palace J, Dujmovic-Basuroski I, Pagani E, Martinelli V, Matthews L, Drulovic J, Leite MI, Comi G, Filippi M, Rocca MA (2019a) Brain and cord imaging features in neuromyelitis optica spectrum disorders. *Annals of neurology*

Cacciaguerra L, Meani A, Mesaros S, Radaelli M, Palace J, Dujmovic-Basuroski I, Pagani E, Martinelli V, Matthews L, Drulovic J, Leite MI, Comi G, Filippi M, Rocca MA (2019b) Brain and cord imaging features in neuromyelitis optica spectrum disorders. *Ann Neurol* 85: 371-384

- Cacciaguerra L, Mistri D, Valsasina P, Martinelli V, Filippi M, Rocca MA (2022b) Time-varying connectivity of the precuneus and its association with cognition and depressive symptoms in neuromyelitis optica: A pilot MRI study. *Mult Scler* 28: 2057-2069
- Cacciaguerra L, Pagani E, Radaelli M, Mesaros S, Martinelli V, Ivanovic J, Drulovic J, Filippi M, Rocca MA (2022c) MR T2-relaxation time as an indirect measure of brain water content and disease activity in NMOSD. *J Neurol Neurosurg Psychiatry*
- Cacciaguerra L, Rocca MA, Storelli L, Radaelli M, Filippi M (2021a) Mapping white matter damage distribution in neuromyelitis optica spectrum disorders with a multimodal MRI approach. *Mult Scler* 27: 841-854
- Cacciaguerra L, Storelli L, Radaelli M, Mesaros S, Moiola L, Drulovic J, Filippi M, Rocca MA (2022d) Application of deep-learning to the seronegative side of the NMO spectrum. *J Neurol* 269: 1546-1556
- Cacciaguerra L, Tortorella P, Rocca MA, Filippi M (2021b) Targeting Neuromyelitis Optica Pathogenesis: Results from Randomized Controlled Trials of Biologics. *Neurotherapeutics* 18: 1623-1636
- Cacciaguerra L, Valsasina P, Meani A, Riccitelli GC, Radaelli M, Rocca MA, Filippi M (2021c) Volume of hippocampal subfields and cognitive deficits in neuromyelitis optica spectrum disorders. *Eur J Neurol* 28: 4167-4177
- Cacciaguerra L, Valsasina P, Mesaros S, Martinelli V, Drulovic J, Filippi M, Rocca MA (2020) Spinal Cord Atrophy in Neuromyelitis Optica Spectrum Disorders Is Spatially Related to Cord Lesions and Disability. *Radiology* 297: 154-163
- Cai MT, Zheng Y, Shen CH, Yang F, Fang W, Zhang YX, Ding MP (2021) Evaluation of brain and spinal cord lesion distribution criteria at disease onset in distinguishing NMOSD from MS and MOG antibody-associated disorder. *Mult Scler* 27: 871-882
- Calabrese M, Oh MS, Favaretto A, Rinaldi F, Poretto V, Alessio S, Lee BC, Yu KH, Ma HI, Perini P, Gallo P (2012) No MRI evidence of cortical lesions in neuromyelitis optica. *Neurology* 79: 1671-6

Camp SJ, Stevenson VL, Thompson AJ, Miller DH, Borrás C, Auriacombe S, Brochet B, Falautano M, Filippi M, Herisse-Dulo L, Montalban X, Parricira E, Polman CH, De Sa J, Langdon DW (1999) Cognitive function in primary progressive and transitional progressive multiple sclerosis: a controlled study with MRI correlates. *Brain* 122 (Pt 7): 1341-8

Carnero Contentti E, Hryb JP, Morales S, Gomez A, Chiganer E, Di Pace JL, Lessa C, Perassolo M (2017) Longitudinally extensive transverse myelitis immune-mediated in aquaporin-4 antibody negative patients: Disease heterogeneity. *Journal of the neurological sciences* 373: 134-137

Carnero Contentti E, Rojas JI, Criniti J, Lopez PA, Daccach Marques V, Soto de Castillo I, Tkachuk V, Marrodan M, Correale J, Farez MF, Kim HJ, Hyun JW, Messina S, Mariano R, Rocca MA, Cacciaguerra L, Filippi M, Palace J, Jurynczyk M (2022) Towards imaging criteria that best differentiate MS from NMOSD and MOGAD: Large multi-ethnic population and different clinical scenarios. *Mult Scler Relat Disord* 61: 103778

Carotenuto A, Cacciaguerra L, Pagani E, Preziosa P, Filippi M, Rocca MA (2021) Glymphatic system impairment in multiple sclerosis: relation with brain damage and disability. *Brain*

Carotenuto A, Valsasina P, Hidalgo de la Cruz M, Cacciaguerra L, Preziosa P, Marchesi O, Filippi M, Rocca MA (2022) Divergent time-varying connectivity of thalamic subregions characterizes clinical phenotypes and cognitive status in multiple sclerosis. *Mol Psychiatry*

Cassinotto C, Deramond H, Olindo S, Aveillan M, Smadja D, Cabre P (2009) MRI of the spinal cord in neuromyelitis optica and recurrent longitudinal extensive myelitis. *Journal of neuroradiology Journal de neuroradiologie* 36: 199-205

Castelvecchi D (2016) Can we open the black box of AI? *Nature* 538: 20-23

Cavanna AE, Trimble MR (2006) The precuneus: a review of its functional anatomy and behavioural correlates. *Brain* 129: 564-83

- Cercignani M, Gandini Wheeler-Kingshott C (2019) From micro- to macro-structures in multiple sclerosis: what is the added value of diffusion imaging. *NMR in biomedicine* 32: e3888
- Chang A, Staugaitis SM, Dutta R, Batt CE, Easley KE, Chomyk AM, Yong VW, Fox RJ, Kidd GJ, Trapp BD (2012) Cortical remyelination: a new target for repair therapies in multiple sclerosis. *Ann Neurol* 72: 918-26
- Chanson JB, Lamy J, Rousseau F, Blanc F, Collongues N, Fleury M, Armspach JP, Kremer S, de Seze J (2013) White matter volume is decreased in the brain of patients with neuromyelitis optica. *Eur J Neurol* 20: 361-7
- Chard DT, Jackson JS, Miller DH, Wheeler-Kingshott CA (2010) Reducing the impact of white matter lesions on automated measures of brain gray and white matter volumes. *J Magn Reson Imaging* 32: 223-8
- Chavarro VS, Mealy MA, Simpson A, Lacheta A, Pache F, Ruprecht K, Gold SM, Paul F, Brandt AU, Levy M (2016) Insufficient treatment of severe depression in neuromyelitis optica spectrum disorder. *Neurology(R) neuroimmunology & neuroinflammation* 3: e286
- Chen HL, Chen PC, Lu CH, Tsai NW, Yu CC, Chou KH, Lai YR, Taoka T, Lin WC (2021) Associations among Cognitive Functions, Plasma DNA, and Diffusion Tensor Image along the Perivascular Space (DTI-ALPS) in Patients with Parkinson's Disease. *Oxid Med Cell Longev* 2021: 4034509
- Cheng W, Rolls ET, Qiu J, Yang D, Ruan H, Wei D, Zhao L, Meng J, Xie P, Feng J (2018) Functional Connectivity of the Precuneus in Unmedicated Patients With Depression. *Biol Psychiatry Cogn Neurosci Neuroimaging* 3: 1040-1049
- Chien C, Scheel M, Schmitz-Hubsch T, Borisow N, Ruprecht K, Bellmann-Strobl J, Paul F, Brandt AU (2019) Spinal cord lesions and atrophy in NMOSD with AQP4-IgG and MOG-IgG associated autoimmunity. *Mult Scler* 25: 1926-1936

Cho EB, Han CE, Seo SW, Chin J, Shin JH, Cho HJ, Seok JM, Kim ST, Kim BJ, Na DL, Lee KH, Seong JK, Min JH (2018) White Matter Network Disruption and Cognitive Dysfunction in Neuromyelitis Optica Spectrum Disorder. *Front Neurol* 9: 1104

Choe AS, Nebel MB, Barber AD, Cohen JR, Xu Y, Pekar JJ, Caffo B, Lindquist MA (2017) Comparing test-retest reliability of dynamic functional connectivity methods. *NeuroImage* 158: 155-175

Chou IJ, Tanasescu R, Mouglin OE, Gowland PA, Tench CR, Whitehouse WP, Gran B, Nikfekar E, Sharrack B, Mazibrada G, Constantinescu CS (2019) Reduced Myelin Signal in Normal-appearing White Matter in Neuromyelitis Optica Measured by 7T Magnetic Resonance Imaging. *Scientific reports* 9: 14378

Ciccarelli O, Cohen JA, Reingold SC, Weinshenker BG, International Conference on Spinal Cord I, Imaging in Multiple S, Neuromyelitis Optica Spectrum D (2019) Spinal cord involvement in multiple sclerosis and neuromyelitis optica spectrum disorders. *The Lancet Neurology* 18: 185-197

Cobo-Calvo A, Ruiz A, Maillart E, Audoin B, Zephir H, Bourre B, Ciron J, Collongues N, Brassat D, Cotton F, Papeix C, Durand-Dubief F, Laplaud D, Deschamps R, Cohen M, Biotti D, Ayrignac X, Tilikete C, Thouvenot E, Brochet B et al. (2018) Clinical spectrum and prognostic value of CNS MOG autoimmunity in adults: The MOGADOR study. *Neurology* 90: e1858-e1869

Coras R, Pauli E, Li J, Schwarz M, Rossler K, Buchfelder M, Hamer H, Stefan H, Blumcke I (2014) Differential influence of hippocampal subfields to memory formation: insights from patients with temporal lobe epilepsy. *Brain* 137: 1945-57

Crawley AP, Henkelman RM (1987) Errors in T2 estimation using multislice multiple-echo imaging. *Magn Reson Med* 4: 34-47

Cree BAC, Lamb S, Morgan K, Chen A, Waubant E, Genain C (2005) An open label study of the effects of rituximab in neuromyelitis optica. *Neurology* 64: 1270-1272

d'Ambrosio A, Valsasina P, Gallo A, De Stefano N, Pareto D, Barkhof F, Ciccarelli O, Enzinger C, Tedeschi G, Stromillo ML, Arevalo MJ, Hulst HE, Muhlert N, Koini M,

Filippi M, Rocca MA (2020) Reduced dynamics of functional connectivity and cognitive impairment in multiple sclerosis. *Mult Scler* 26: 476-488

Darnai G, Nagy SA, Horvath R, Acs P, Perlaki G, Orsi G, Kovacs N, Altbacker A, Plozer E, Tenyi D, Weintraut R, Schwarcz A, John F, Varga E, Bereczkei T, Clemens Z, Komoly S, Janszky J (2017) Iron Concentration in Deep Gray Matter Structures is Associated with Worse Visual Memory Performance in Healthy Young Adults. *J Alzheimers Dis* 59: 675-681

De Leener B, Levy S, Dupont SM, Fonov VS, Stikov N, Louis Collins D, Callot V, Cohen-Adad J (2017) SCT: Spinal Cord Toolbox, an open-source software for processing spinal cord MRI data. *NeuroImage* 145: 24-43

de Seze J, Blanc F, Kremer S, Collongues N, Fleury M, Marcel C, Namer IJ (2010) Magnetic resonance spectroscopy evaluation in patients with neuromyelitis optica. *Journal of neurology, neurosurgery, and psychiatry* 81: 409-11

De Stefano N, Stromillo ML, Giorgio A, Bartolozzi ML, Battaglini M, Baldini M, Portaccio E, Amato MP, Sormani MP (2016) Establishing pathological cut-offs of brain atrophy rates in multiple sclerosis. *J Neurol Neurosurg Psychiatry* 87: 93-9

Deschamps R, Gueguen A, Lecler A, Lecouturier K, Lamirel C, Bensa C, Marignier R, Vignal C, Gout O (2018) Acute idiopathic optic neuritis: not always benign. *European journal of neurology* 25: 1378-1383

DeYoe EA, Bandettini P, Neitz J, Miller D, Winans P (1994) Functional magnetic resonance imaging (fMRI) of the human brain. *J Neurosci Methods* 54: 171-87

Diederik P. Kingma JB (2015) Adam: A Method for Stochastic Optimization. In 3rd International Conference for Learning Representations, arXiv:1412.6980 (ed) San Diego, USA:

Dobson R, Ramagopalan S, Davis A, Giovannoni G (2013) Cerebrospinal fluid oligoclonal bands in multiple sclerosis and clinically isolated syndromes: a meta-analysis of prevalence, prognosis and effect of latitude. *Journal of neurology, neurosurgery, and psychiatry* 84: 909-14

- Dorostkar MM, Zou C, Blazquez-Llorca L, Herms J (2015) Analyzing dendritic spine pathology in Alzheimer's disease: problems and opportunities. *Acta Neuropathol* 130: 1-19
- Duan Y, Liu Y, Liang P, Jia X, Ye J, Dong H, Li K (2014) White matter atrophy in brain of neuromyelitis optica: a voxel-based morphometry study. *Acta Radiol* 55: 589-93
- Duan Y, Liu Y, Liang P, Jia X, Yu C, Qin W, Sun H, Liao Z, Ye J, Li K (2012) Comparison of grey matter atrophy between patients with neuromyelitis optica and multiple sclerosis: a voxel-based morphometry study. *Eur J Radiol* 81: e110-4
- Eden D, Gros C, Badji A, Dupont SM, De Leener B, Maranzano J, Zhuoquiong R, Liu Y, Granberg T, Ouellette R, Stawiarz L, Hillert J, Talbott J, Bannier E, Kerbrat A, Edan G, Labauge P, Callot V, Pelletier J, Audoin B et al. (2019) Spatial distribution of multiple sclerosis lesions in the cervical spinal cord. *Brain : a journal of neurology* 142: 633-646
- Eshaghi A, Wottschel V, Cortese R, Calabrese M, Sahraian MA, Thompson AJ, Alexander DC, Ciccarelli O (2016) Gray matter MRI differentiates neuromyelitis optica from multiple sclerosis using random forest. *Neurology* 87: 2463-2470
- Fereidan-Esfahani M, Decker PA, Eckel Passow JE, Lucchinetti CF, Flanagan EP, Tobin WO (2022) Population-based incidence and clinico-radiological characteristics of tumefactive demyelination in Olmsted County, Minnesota, United States. *Eur J Neurol* 29: 782-789
- Filippi M, Preziosa P, Banwell BL, Barkhof F, Ciccarelli O, De Stefano N, Geurts JJG, Paul F, Reich DS, Toosy AT, Traboulsee A, Wattjes MP, Yousry TA, Gass A, Lubetzki C, Weinshenker BG, Rocca MA (2019) Assessment of lesions on magnetic resonance imaging in multiple sclerosis: practical guidelines. *Brain* 142: 1858-1875
- Filippi M, Rocca MA (2020) Neuromyelitis Optica Spectrum Disorders. In *White Matter Diseases : An Update for Neurologists*, pp 67-94. Cham: Springer International Publishing

- Filippi M, Rocca MA, Martino G, Horsfield MA, Comi G (1998) Magnetization transfer changes in the normal appearing white matter precede the appearance of enhancing lesions in patients with multiple sclerosis. *Ann Neurol* 43: 809-14
- Filippi M, Rocca MA, Muiola L, Martinelli V, Ghezzi A, Capra R, Salvi F, Comi G (1999) MRI and magnetization transfer imaging changes in the brain and cervical cord of patients with Devic's neuromyelitis optica. *Neurology* 53: 1705-10
- Finke C, Zimmermann H, Pache F, Oertel FC, Chavarro VS, Kramarenko Y, Bellmann-Strobl J, Ruprecht K, Brandt AU, Paul F (2018) Association of Visual Impairment in Neuromyelitis Optica Spectrum Disorder With Visual Network Reorganization. *JAMA neurology* 75: 296-303
- Flanagan EP, Hinson SR, Lennon VA, Fang B, Aksamit AJ, Morris PP, Basal E, Honorat JA, Alfugham NB, Linnoila JJ, Weinshenker BG, Pittock SJ, McKeon A (2017) Glial fibrillary acidic protein immunoglobulin G as biomarker of autoimmune astrocytopathy: Analysis of 102 patients. *Ann Neurol* 81: 298-309
- Flanagan EP, Weinshenker BG, Krecke KN, Lennon VA, Lucchinetti CF, McKeon A, Wingerchuk DM, Shuster EA, Jiao Y, Horta ES, Pittock SJ (2015a) Short myelitis lesions in aquaporin-4-IgG-positive neuromyelitis optica spectrum disorders. *JAMA neurology* 72: 81-7
- Flanagan EP, Weinshenker BG, Krecke KN, Pittock SJ (2015b) Asymptomatic myelitis in neuromyelitis optica and autoimmune aquaporin-4 channelopathy. *Neurology Clinical practice* 5: 175-177
- Friston KJ, Holmes A, Poline JB, Price CJ, Frith CD (1996) Detecting activations in PET and fMRI: levels of inference and power. *NeuroImage* 4: 223-35
- Fujihara K (2019) Neuromyelitis optica spectrum disorders: still evolving and broadening. *Curr Opin Neurol* 32: 385-394
- Fujihara K, Bennett JL, de Seze J, Haramura M, Kleiter I, Weinshenker BG, Kang D, Mughal T, Yamamura T (2020) Interleukin-6 in neuromyelitis optica spectrum disorder pathophysiology. *Neurology(R) neuroimmunology & neuroinflammation* 7

Ganzetti M, Wenderoth N, Mantini D (2014) Whole brain myelin mapping using T1- and T2-weighted MR imaging data. *Frontiers in human neuroscience* 8: 671

Garcia-Estrada J, Garcia-Segura LM, Torres-Aleman I (1992) Expression of insulin-like growth factor I by astrocytes in response to injury. *Brain Res* 592: 343-7

Gibbons E, Campgana G, O'Connell K, Yeo T, Whittam D, Karthikeyan V-m, Leite MI, Palace J, Jacob A, Huda S (2022) 070 What is seronegative neuromyelitis optica spectrum disorder? *Journal of Neurology, Neurosurgery & Psychiatry* 93: A34-A34

Gillespie M, Jassal B, Stephan R, Milacic M, Rothfels K, Senff-Ribeiro A, Griss J, Sevilla C, Matthews L, Gong C, Deng C, Varusai T, Ragueneau E, Haider Y, May B, Shamovsky V, Weiser J, Brunson T, Sanati N, Beckman L et al. (2022) The reactome pathway knowledgebase 2022. *Nucleic Acids Res* 50: D687-D692

Gilmore CP, DeLuca GC, Bo L, Owens T, Lowe J, Esiri MM, Evangelou N (2005) Spinal cord atrophy in multiple sclerosis caused by white matter volume loss. *Archives of neurology* 62: 1859-62

Giovannoni G, Tomic D, Bright JR, Havrdova E (2017) "No evident disease activity": The use of combined assessments in the management of patients with multiple sclerosis. *Mult Scler* 23: 1179-1187

Glasser MF, Van Essen DC (2011) Mapping human cortical areas in vivo based on myelin content as revealed by T1- and T2-weighted MRI. *The Journal of neuroscience : the official journal of the Society for Neuroscience* 31: 11597-616

Gouveia-Freitas K, Bastos-Leite AJ (2021) Perivascular spaces and brain waste clearance systems: relevance for neurodegenerative and cerebrovascular pathology. *Neuroradiology* 63: 1581-1597

Granberg T, Fan Q, Treaba CA, Ouellette R, Herranz E, Mangeat G, Louapre C, Cohen-Adad J, Klawiter EC, Sloane JA, Mainero C (2017) In vivo characterization of cortical and white matter neuroaxonal pathology in early multiple sclerosis. *Brain* 140: 2912-2926

- Grassiot B, Desgranges B, Eustache F, Defer G (2009) Quantification and clinical relevance of brain atrophy in multiple sclerosis: a review. *Journal of neurology* 256: 1397-412
- Graves J, Grandhe S, Weinfurter K, Krupp L, Belman A, Chitnis T, Ness J, Weinstock-Guttman B, Gorman M, Patterson M, Rodriguez M, Lotze T, Aaen G, Mowry EM, Rose JW, Simmons T, Casper TC, James J, Waubant E, Centers USNoPMS (2014) Protective environmental factors for neuromyelitis optica. *Neurology* 83: 1923-9
- Gu HWaX (2015) Max-Pooling Dropout for Regularization of Convolutional Neural Networks. In Department of Electronic Engineering FU, Shanghai 200433, China (ed)
- Guo Y, Lennon VA, Parisi JE, Popescu B, Vasquez C, Pittock SJ, Howe CL, Lucchinetti CF (2021) Spectrum of sublytic astrocytopathy in neuromyelitis optica. *Brain*
- Guo Y, Lennon VA, Parisi JE, Popescu B, Vasquez C, Pittock SJ, Howe CL, Lucchinetti CF (2022) Spectrum of sublytic astrocytopathy in neuromyelitis optica. *Brain* 145: 1379-1390
- Hamid SH, Elson L, Mutch K, Solomon T, Jacob A (2017) The impact of 2015 neuromyelitis optica spectrum disorders criteria on diagnostic rates. *Multiple sclerosis* 23: 228-233
- Han Y, Liu Y, Zeng C, Luo Q, Xiong H, Zhang X, Li Y (2020) Functional Connectivity Alterations in Neuromyelitis Optica Spectrum Disorder : Correlation with Disease Duration and Cognitive Impairment. *Clin Neuroradiol* 30: 559-568
- Hardy TA, Chataway J (2013) Tumefactive demyelination: an approach to diagnosis and management. *J Neurol Neurosurg Psychiatry* 84: 1047-53
- Hardy TA, Tobin WO, Lucchinetti CF (2016) Exploring the overlap between multiple sclerosis, tumefactive demyelination and Balo's concentric sclerosis. *Mult Scler* 22: 986-92

Harris J, Mahone EM, Bjornsson HT (2019) Molecularly confirmed Kabuki (Niikawa-Kuroki) syndrome patients demonstrate a specific cognitive profile with extensive visuospatial abnormalities. *Journal of intellectual disability research : JIDR* 63: 489-497

Hartmann JF (1966) High sodium content of cortical astrocytes. *Archives of neurology* 15: 633-42

Hasan-Olive MM, Enger R, Hansson HA, Nagelhus EA, Eide PK (2019) Loss of perivascular aquaporin-4 in idiopathic normal pressure hydrocephalus. *Glia* 67: 91-100

Hawrylycz MJ, Lein ES, Guillozet-Bongaarts AL, Shen EH, Ng L, Miller JA, van de Lagemaat LN, Smith KA, Ebbert A, Riley ZL, Abajian C, Beckmann CF, Bernard A, Bertagnoli D, Boe AF, Cartagena PM, Chakravarty MM, Chapin M, Chong J, Dalley RA et al. (2012) An anatomically comprehensive atlas of the adult human brain transcriptome. *Nature* 489: 391-399

Helm K, Viol K, Weiger TM, Tass PA, Grefkes C, Del Monte D, Schiepek G (2018) Neuronal connectivity in major depressive disorder: a systematic review. *Neuropsychiatr Dis Treat* 14: 2715-2737

Hinson SR, Romero MF, Popescu BF, Lucchinetti CF, Fryer JP, Wolburg H, Fallier-Becker P, Noell S, Lennon VA (2012) Molecular outcomes of neuromyelitis optica (NMO)-IgG binding to aquaporin-4 in astrocytes. *Proc Natl Acad Sci U S A* 109: 1245-50

Hinton VNaG (2010) Rectified Linear Units Improve Restricted Boltzmann Machines. In International Conference on Machine Learning, Haifa, Israel:

Hoftberger R, Guo Y, Flanagan EP, Lopez-Chiriboga AS, Endmayr V, Hochmeister S, Joldic D, Pittock SJ, Tillema JM, Gorman M, Lassmann H, Lucchinetti CF (2020) The pathology of central nervous system inflammatory demyelinating disease accompanying myelin oligodendrocyte glycoprotein autoantibody. *Acta neuropathologica* 139: 875-892

Hopkins RO, Beck CJ, Burnett DL, Weaver LK, Victoroff J, Bigler ED (2006) Prevalence of white matter hyperintensities in a young healthy population. *J Neuroimaging* 16: 243-51

Hor JY, Asgari N, Nakashima I, Broadley SA, Leite MI, Kissani N, Jacob A, Marignier R, Weinshenker BG, Paul F, Pittock SJ, Palace J, Wingerchuk DM, Behne JM, Yeaman MR, Fujihara K (2020) Epidemiology of Neuromyelitis Optica Spectrum Disorder and Its Prevalence and Incidence Worldwide. *Front Neurol* 11: 501

Horsfield MA, Sala S, Neema M, Absinta M, Bakshi A, Sormani MP, Rocca MA, Bakshi R, Filippi M (2010) Rapid semi-automatic segmentation of the spinal cord from magnetic resonance images: application in multiple sclerosis. *NeuroImage* 50: 446-55

Hubbard JA, Szu JI, Binder DK (2018) The role of aquaporin-4 in synaptic plasticity, memory and disease. *Brain Res Bull* 136: 118-129

Hyun JW, Jeong IH, Joung A, Kim SH, Kim HJ (2016) Evaluation of the 2015 diagnostic criteria for neuromyelitis optica spectrum disorder. *Neurology* 86: 1772-9

Hyun JW, Kim SH, Jeong IH, Lee SH, Kim HJ (2015) Bright spotty lesions on the spinal cord: an additional MRI indicator of neuromyelitis optica spectrum disorder? *J Neurol Neurosurg Psychiatry* 86: 1280-2

Hyun JW, Kim Y, Kim KH, Kim SH, Olesen MN, Asgari N, Siritho S, Paul F, Kim HJ (2022) CSF GFAP levels in double seronegative neuromyelitis optica spectrum disorder: no evidence of astrocyte damage. *J Neuroinflammation* 19: 86

Hyun JW, Park G, Kwak K, Jo HJ, Joung A, Kim JH, Lee SH, Kim S, Lee JM, Kim SH, Kim HJ (2017) Deep gray matter atrophy in neuromyelitis optica spectrum disorder and multiple sclerosis. *European journal of neurology* 24: 437-445

Iglesias JE, Augustinack JC, Nguyen K, Player CM, Player A, Wright M, Roy N, Frosch MP, McKee AC, Wald LL, Fischl B, Van Leemput K, Alzheimer's Disease Neuroimaging I (2015) A computational atlas of the hippocampal formation using ex vivo, ultra-high resolution MRI: Application to adaptive segmentation of in vivo MRI. *NeuroImage* 115: 117-37

Iliff JJ, Nedergaard M (2013) Is there a cerebral lymphatic system? *Stroke* 44: S93-5

Iliff JJ, Wang M, Liao Y, Plogg BA, Peng W, Gundersen GA, Benveniste H, Vates GE, Deane R, Goldman SA, Nagelhus EA, Nedergaard M (2012) A paravascular pathway facilitates CSF flow through the brain parenchyma and the clearance of interstitial solutes, including amyloid beta. *Sci Transl Med* 4: 147ra111

Iorio R, Damato V, Mirabella M, Evoli A, Marti A, Plantone D, Frisullo G, Batocchi AP (2013) Distinctive clinical and neuroimaging characteristics of longitudinally extensive transverse myelitis associated with aquaporin-4 autoantibodies. *Journal of neurology* 260: 2396-402

Ito S, Mori M, Makino T, Hayakawa S, Kuwabara S (2009) "Cloud-like enhancement" is a magnetic resonance imaging abnormality specific to neuromyelitis optica. *Ann Neurol* 66: 425-8

Jarius S, Paul F, Aktas O, Asgari N, Dale RC, de Seze J, Franciotta D, Fujihara K, Jacob A, Kim HJ, Kleiter I, Kumpfel T, Levy M, Palace J, Ruprecht K, Saiz A, Trebst C, Weinshenker BG, Wildemann B (2018) MOG encephalomyelitis: international recommendations on diagnosis and antibody testing. *Journal of neuroinflammation* 15: 134

Jarius S, Ruprecht K, Kleiter I, Borisow N, Asgari N, Pitarokoili K, Pache F, Stich O, Beume LA, Hummert MW, Ringelstein M, Trebst C, Winkelmann A, Schwarz A, Buttman M, Zimmermann H, Kuchling J, Franciotta D, Capobianco M, Siebert E et al. (2016) MOG-IgG in NMO and related disorders: a multicenter study of 50 patients. Part 2: Epidemiology, clinical presentation, radiological and laboratory features, treatment responses, and long-term outcome. *Journal of neuroinflammation* 13: 280

Jarius S, Ruprecht K, Wildemann B, Kuempfel T, Ringelstein M, Geis C, Kleiter I, Kleinschnitz C, Berthele A, Brettschneider J, Hellwig K, Hemmer B, Linker RA, Lauda F, Mayer CA, Tumani H, Melms A, Trebst C, Stangel M, Marziniak M et al. (2012) Contrasting disease patterns in seropositive and seronegative neuromyelitis optica: A multicentre study of 175 patients. *Journal of neuroinflammation* 9: 14

Jeantroux J, Kremer S, Lin XZ, Collongues N, Chanson JB, Bourre B, Fleury M, Blanc F, Dietemann JL, de Seze J (2012) Diffusion tensor imaging of normal-appearing white

matter in neuromyelitis optica. *Journal of neuroradiology Journal de neuroradiologie* 39: 295-300

Jeong IH, Kim SH, Hyun JW, Joung A, Cho HJ, Kim HJ (2015) Tumefactive demyelinating lesions as a first clinical event: Clinical, imaging, and follow-up observations. *Journal of the neurological sciences* 358: 118-24

Jessen NA, Munk AS, Lundgaard I, Nedergaard M (2015) The Glymphatic System: A Beginner's Guide. *Neurochem Res* 40: 2583-99

Jia X, Li Y, Li K, Liang P, Fu X (2018) Precuneus Dysfunction in Parkinson's Disease With Mild Cognitive Impairment. *Front Aging Neurosci* 10: 427

Jiao Y, Fryer JP, Lennon VA, Jenkins SM, Quek AM, Smith CY, McKeon A, Costanzi C, Iorio R, Weinshenker BG, Wingerchuk DM, Shuster EA, Lucchinetti CF, Pittock SJ (2013) Updated estimate of AQP4-IgG serostatus and disability outcome in neuromyelitis optica. *Neurology* 81: 1197-204

Jiao Y, Fryer JP, Lennon VA, McKeon A, Jenkins SM, Smith CY, Quek AM, Weinshenker BG, Wingerchuk DM, Shuster EA, Lucchinetti CF, Pittock SJ (2014) Aquaporin 4 IgG serostatus and outcome in recurrent longitudinally extensive transverse myelitis. *JAMA neurology* 71: 48-54

Jie B, Liu M, Shen D (2018) Integration of temporal and spatial properties of dynamic connectivity networks for automatic diagnosis of brain disease. *Med Image Anal* 47: 81-94

Johns TG, Bernard CC (1999) The structure and function of myelin oligodendrocyte glycoprotein. *J Neurochem* 72: 1-9

Jurynczyk M, Geraldles R, Probert F, Woodhall MR, Waters P, Tackley G, DeLuca G, Chandratre S, Leite MI, Vincent A, Palace J (2017a) Distinct brain imaging characteristics of autoantibody-mediated CNS conditions and multiple sclerosis. *Brain* 140: 617-627

Jurynczyk M, Messina S, Woodhall MR, Raza N, Everett R, Roca-Fernandez A, Tackley G, Hamid S, Sheard A, Reynolds G, Chandratre S, Hemingway C, Jacob A, Vincent A, Leite MI, Waters P, Palace J (2017b) Clinical presentation and prognosis in MOG-antibody disease: a UK study. *Brain* 140: 3128-3138

Jurynczyk M, Tackley G, Kong Y, Geraldles R, Matthews L, Woodhall M, Waters P, Kuker W, Craner M, Weir A, DeLuca GC, Kremer S, Leite MI, Vincent A, Jacob A, de Seze J, Palace J (2017c) Brain lesion distribution criteria distinguish MS from AQP4-antibody NMOSD and MOG-antibody disease. *Journal of neurology, neurosurgery, and psychiatry* 88: 132-136

Kaiming H. XZ, Shaoqing R., Jian S. (2016) Deep Residual Learning for Image Recognition. *IEEE Conference on Computer Vision and Pattern Recognition (CVPR)*

Kaiser RH, Whitfield-Gabrieli S, Dillon DG, Goer F, Beltzer M, Minkel J, Smoski M, Dichter G, Pizzagalli DA (2016) Dynamic Resting-State Functional Connectivity in Major Depression. *Neuropsychopharmacology* 41: 1822-30

Keaney J, Campbell M (2015) The dynamic blood-brain barrier. *The FEBS journal* 282: 4067-79

Keller CW, Lopez JA, Wendel EM, Ramanathan S, Gross CC, Klotz L, Reindl M, Dale RC, Wiendl H, Rostasy K, Brilot F, Lunemann JD (2021) Complement Activation Is a Prominent Feature of MOGAD. *Ann Neurol* 90: 976-982

Keller CW, Lopez JA, Wendel EM, Ramanathan S, Gross CC, Klotz L, Reindl M, Dale RC, Wiendl H, Rostasy K, Brilot F, Lunemann JD (2022) Reply to "Investigating the Immunopathogenic Mechanisms Underlying MOGAD". *Ann Neurol* 91: 300-301

Kim HJ, Paul F, Lana-Peixoto MA, Tenenbaum S, Asgari N, Palace J, Klawiter EC, Sato DK, de Seze J, Wuerfel J, Banwell BL, Villoslada P, Saiz A, Fujihara K, Kim SH, Guthy-Jackson Charitable Foundation NMOICC, Biorepository (2015) MRI characteristics of neuromyelitis optica spectrum disorder: an international update. *Neurology* 84: 1165-73

Kim SH, Huh SY, Hyun JW, Jeong IH, Lee SH, Joung A, Kim HJ (2014) A longitudinal brain magnetic resonance imaging study of neuromyelitis optica spectrum disorder. *PLoS One* 9: e108320

Kimura MC, Doring TM, Rueda FC, Tukamoto G, Gasparetto EL (2014) In vivo assessment of white matter damage in neuromyelitis optica: a diffusion tensor and diffusion kurtosis MR imaging study. *Journal of the neurological sciences* 345: 172-5

Kleiter I, Gahlen A, Borisow N, Fischer K, Wernecke KD, Wegner B, Hellwig K, Pache F, Ruprecht K, Havla J, Krumbholz M, Kumpfel T, Aktas O, Hartung HP, Ringelstein M, Geis C, Kleinschnitz C, Berthele A, Hemmer B, Angstwurm K et al. (2016) Neuromyelitis optica: Evaluation of 871 attacks and 1,153 treatment courses. *Ann Neurol* 79: 206-16

Knecht S, Dräger B, Deppe M, Bobe L, Lohmann H, Floel A, Ringelstein EB, Henningsen H (2000) Handedness and hemispheric language dominance in healthy humans. *Brain* 123 Pt 12: 2512-8

Kong BS, Kim Y, Kim GY, Hyun JW, Kim SH, Jeong A, Kim HJ (2017) Increased frequency of IL-6-producing non-classical monocytes in neuromyelitis optica spectrum disorder. *Journal of neuroinflammation* 14: 191

Krampla W, Aboul-Enein F, Jecel J, Lang W, Fertl E, Hruby W, Kristoferitsch W (2009) Spinal cord lesions in patients with neuromyelitis optica: a retrospective long-term MRI follow-up study. *Eur Radiol* 19: 2535-43

Kumral E, Bayam FE, Ozdemir HN (2021) Cognitive and Behavioral Disorders in Patients with Precuneal Infarcts. *Eur Neurol* 84: 157-167

Kurtzke JF (1983) Rating neurologic impairment in multiple sclerosis: an expanded disability status scale (EDSS). *Neurology* 33: 1444-52

Larman HB, Zhao Z, Laserson U, Li MZ, Ciccio A, Gakidis MA, Church GM, Kesari S, Leproust EM, Solimini NL, Elledge SJ (2011) Autoantigen discovery with a synthetic human peptidome. *Nat Biotechnol* 29: 535-41

Lassmann H (2022) Tumefactive multiple sclerosis or inflammatory demyelinating disease with large lesions? *European journal of neurology* 29: 687-688

LeBien TW, Tedder TF (2008) B lymphocytes: how they develop and function. *Blood* 112: 1570-80

LeCun Y, Bengio Y, Hinton G (2015) Deep learning. *Nature* 521: 436-44

Lee MY, Yong KP, Hyun JW, Kim SH, Lee SH, Kim HJ (2020) Incidence of interattack asymptomatic brain lesions in NMO spectrum disorder. *Neurology* 95: e3124-e3128

Lennon VA, Kryzer TJ, Pittock SJ, Verkman AS, Hinson SR (2005) IgG marker of optic-spinal multiple sclerosis binds to the aquaporin-4 water channel. *J Exp Med* 202: 473-7

Lennon VA, Wingerchuk DM, Kryzer TJ, Pittock SJ, Lucchinetti CF, Fujihara K, Nakashima I, Weinshenker BG (2004) A serum autoantibody marker of neuromyelitis optica: distinction from multiple sclerosis. *Lancet* 364: 2106-12

Levy M, Mealy MA (2021) B-Cell Targeted Treatments for Neuromyelitis Optica Spectrum Disorder: A Focus on CD19 and CD20. *Immunotargets Ther* 10: 325-331

Lierse W, Horstmann E (1965) Quantitative anatomy of the cerebral vascular bed with especial emphasis on homogeneity and inhomogeneity in small parts of the gray and white matter. *Acta Neurol Scand Suppl* 14: 15-9

Lin X, Yu WY, Liauw L, Chander RJ, Soon WE, Lee HY, Tan K (2017) Clinicoradiologic features distinguish tumefactive multiple sclerosis from CNS neoplasms. *Neurol Clin Pract* 7: 53-64

Lindberg O, Walterfang M, Looi JC, Malykhin N, Ostberg P, Zandbelt B, Styner M, Paniagua B, Velakoulis D, Orndahl E, Wahlund LO (2012) Hippocampal shape analysis in Alzheimer's disease and frontotemporal lobar degeneration subtypes. *Journal of Alzheimer's disease : JAD* 30: 355-65

Liu Y, Duan Y, He Y, Wang J, Xia M, Yu C, Dong H, Ye J, Butzkueven H, Li K, Shu N (2012a) Altered topological organization of white matter structural networks in patients with neuromyelitis optica. *PLoS One* 7: e48846

Liu Y, Duan Y, He Y, Yu C, Wang J, Huang J, Ye J, Butzkueven H, Li K, Shu N (2012b) A tract-based diffusion study of cerebral white matter in neuromyelitis optica reveals widespread pathological alterations. *Mult Scler* 18: 1013-21

Liu Y, Duan Y, Huang J, Ren Z, Liu Z, Dong H, Weiler F, Hahn HK, Shi FD, Butzkueven H, Barkhof F, Li K (2018) Different patterns of longitudinal brain and spinal cord changes and their associations with disability progression in NMO and MS. *European radiology* 28: 96-103

Liu Y, Fu Y, Schoonheim MM, Zhang N, Fan M, Su L, Shen Y, Yan Y, Yang L, Wang Q, Zhang N, Yu C, Barkhof F, Shi FD (2015a) Structural MRI substrates of cognitive impairment in neuromyelitis optica. *Neurology* 85: 1491-9

Liu Y, Wang J, Daams M, Weiler F, Hahn HK, Duan Y, Huang J, Ren Z, Ye J, Dong H, Vrenken H, Wattjes MP, Shi FD, Li K, Barkhof F (2015b) Differential patterns of spinal cord and brain atrophy in NMO and MS. *Neurology* 84: 1465-72

Liu Y, Xie T, He Y, Duan Y, Huang J, Ren Z, Gong G, Wang J, Ye J, Dong H, Butzkueven H, Shi FD, Shu N, Li K (2014) Cortical thinning correlates with cognitive change in multiple sclerosis but not in neuromyelitis optica. *Eur Radiol* 24: 2334-43

Liu Z, Pardini M, Yaldizli O, Sethi V, Muhlert N, Wheeler-Kingshott CA, Samson RS, Miller DH, Chard DT (2015c) Magnetization transfer ratio measures in normal-appearing white matter show periventricular gradient abnormalities in multiple sclerosis. *Brain : a journal of neurology* 138: 1239-46

Llufriu S, Pujol T, Blanco Y, Hankiewicz K, Squarcia M, Berenguer J, Villoslada P, Graus F, Saiz A (2010) T2 hypointense rims and ring-enhancing lesions in MS. *Mult Scler* 16: 1317-25

Lopez-Chiriboga AS, Majed M, Fryer J, Dubey D, McKeon A, Flanagan EP, Jitraprakulsan J, Kothapalli N, Tillema JM, Chen J, Weinshenker B, Wingerchuk D,

Sagen J, Gadoth A, Lennon VA, Keegan BM, Lucchinetti C, Pittock SJ (2018) Association of MOG-IgG Serostatus With Relapse After Acute Disseminated Encephalomyelitis and Proposed Diagnostic Criteria for MOG-IgG-Associated Disorders. *JAMA Neurol* 75: 1355-1363

Lopez-Chiriboga AS, Sechi E, Buciu M, Chen JJ, Pittock SJ, Lucchinetti CF, Flanagan EP (2020) Long-term Outcomes in Patients With Myelin Oligodendrocyte Glycoprotein Immunoglobulin G-Associated Disorder. *JAMA neurology* 77: 1575-1577

Lu L, Zhang H, Dauphars DJ, He YW (2021) A Potential Role of Interleukin 10 in COVID-19 Pathogenesis. *Trends Immunol* 42: 3-5

Lucchinetti CF, Gavrilova RH, Metz I, Parisi JE, Scheithauer BW, Weigand S, Thomsen K, Mandrekar J, Altintas A, Erickson BJ, Konig F, Giannini C, Lassmann H, Linbo L, Pittock SJ, Bruck W (2008) Clinical and radiographic spectrum of pathologically confirmed tumefactive multiple sclerosis. *Brain* 131: 1759-75

Lucchinetti CF, Guo Y, Popescu BF, Fujihara K, Itoyama Y, Misu T (2014) The pathology of an autoimmune astrocytopathy: lessons learned from neuromyelitis optica. *Brain Pathol* 24: 83-97

Lucchinetti CF, Mandler RN, McGavern D, Bruck W, Gleich G, Ransohoff RM, Trebst C, Weinshenker B, Wingerchuk D, Parisi JE, Lassmann H (2002) A role for humoral mechanisms in the pathogenesis of Devic's neuromyelitis optica. *Brain* 125: 1450-61

Lucchinetti CF, Popescu BF, Bunyan RF, Moll NM, Roemer SF, Lassmann H, Bruck W, Parisi JE, Scheithauer BW, Giannini C, Weigand SD, Mandrekar J, Ransohoff RM (2011) Inflammatory cortical demyelination in early multiple sclerosis. *N Engl J Med* 365: 2188-97

Magana SM, Matiello M, Pittock SJ, McKeon A, Lennon VA, Rabinstein AA, Shuster E, Kantarci OH, Lucchinetti CF, Weinshenker BG (2009) Posterior reversible encephalopathy syndrome in neuromyelitis optica spectrum disorders. *Neurology* 72: 712-7

- Mainero C, Louapre C, Govindarajan ST, Gianni C, Nielsen AS, Cohen-Adad J, Sloane J, Kinkel RP (2015) A gradient in cortical pathology in multiple sclerosis by in vivo quantitative 7 T imaging. *Brain* 138: 932-45
- Majed M, Fryer JP, McKeon A, Lennon VA, Pittock SJ (2016) Clinical utility of testing AQP4-IgG in CSF: Guidance for physicians. *Neurology(R) neuroimmunology & neuroinflammation* 3: e231
- Majumdar S, Orphanoudakis SC, Gmitro A, O'Donnell M, Gore JC (1986) Errors in the measurements of T2 using multiple-echo MRI techniques. I. Effects of radiofrequency pulse imperfections. *Magn Reson Med* 3: 397-417
- Mariano R, Messina S, Roca-Fernandez A, Leite MI, Kong Y, Palace JA (2021) Quantitative spinal cord MRI in MOG-antibody disease, neuromyelitis optica and multiple sclerosis. *Brain* 144: 198-212
- Marignier R, Bernard-Valnet R, Giraudon P, Collongues N, Papeix C, Zephir H, Cavillon G, Rogemond V, Casey R, Frangoulis B, De Seze J, Vukusic S, Honnorat J, Confavreux C, Group NS (2013) Aquaporin-4 antibody-negative neuromyelitis optica: distinct assay sensitivity-dependent entity. *Neurology* 80: 2194-200
- Marignier R, Hacohen Y, Cobo-Calvo A, Probstel AK, Aktas O, Alexopoulos H, Amato MP, Asgari N, Banwell B, Bennett J, Brilot F, Capobianco M, Chitnis T, Ciccarelli O, Deiva K, De Seze J, Fujihara K, Jacob A, Kim HJ, Kleiter I et al. (2021) Myelin-oligodendrocyte glycoprotein antibody-associated disease. *Lancet Neurol* 20: 762-772
- Masaki K, Suzuki SO, Matsushita T, Matsuoka T, Imamura S, Yamasaki R, Suzuki M, Suenaga T, Iwaki T, Kira J (2013) Connexin 43 astrocytopathy linked to rapidly progressive multiple sclerosis and neuromyelitis optica. *PLoS One* 8: e72919
- Mason JL, Xuan S, Dragatsis I, Efstratiadis A, Goldman JE (2003) Insulin-like growth factor (IGF) signaling through type 1 IGF receptor plays an important role in remyelination. *The Journal of neuroscience : the official journal of the Society for Neuroscience* 23: 7710-8

Masuda H, Mori M, Hirano S, Uzawa A, Uchida T, Muto M, Ohtani R, Aoki R, Kuwabara S (2022) Silent progression of brain atrophy in aquaporin-4 antibody-positive neuromyelitis optica spectrum disorder. *J Neurol Neurosurg Psychiatry* 93: 32-40

Matiello M, Schaefer-Klein J, Sun D, Weinshenker BG (2013) Aquaporin 4 expression and tissue susceptibility to neuromyelitis optica. *JAMA neurology* 70: 1118-25

Matthews L, Kolind S, Brazier A, Leite MI, Brooks J, Traboulsee A, Jenkinson M, Johansen-Berg H, Palace J (2015) Imaging Surrogates of Disease Activity in Neuromyelitis Optica Allow Distinction from Multiple Sclerosis. *PLoS One* 10: e0137715

Matthews L, Marasco R, Jenkinson M, Kuker W, Luppe S, Leite MI, Giorgio A, De Stefano N, Robertson N, Johansen-Berg H, Evangelou N, Palace J (2013a) Distinction of seropositive NMO spectrum disorder and MS brain lesion distribution. *Neurology* 80: 1330-1337

Matthews L, Marasco R, Jenkinson M, Kuker W, Luppe S, Leite MI, Giorgio A, De Stefano N, Robertson N, Johansen-Berg H, Evangelou N, Palace J (2013b) Distinction of seropositive NMO spectrum disorder and MS brain lesion distribution. *Neurology* 80: 1330-7

McBee MP, Awan OA, Colucci AT, Ghobadi CW, Kadom N, Kansagra AP, Tridandapani S, Auffermann WF (2018) Deep Learning in Radiology. *Academic radiology* 25: 1472-1480

McCombe JA, Flanagan EP, Chen JJ, Zekeridou A, Lucchinetti CF, Pittock SJ (2022) Investigating the Immunopathogenic Mechanisms Underlying MOGAD. *Ann Neurol* 91: 299-300

McKeon A, Pittock SJ (2011) Paraneoplastic encephalomyelopathies: pathology and mechanisms. *Acta neuropathologica* 122: 381-400

McNamara LA, Topaz N, Wang X, Hariri S, Fox L, MacNeil JR (2017) High Risk for Invasive Meningococcal Disease Among Patients Receiving Eculizumab (Soliris)

Despite Receipt of Meningococcal Vaccine. *MMWR Morbidity and mortality weekly report* 66: 734-737

Mealy MA, Kim SH, Schmidt F, Lopez R, Jimenez Arango JA, Paul F, Wingerchuk DM, Greenberg BM, Kim HJ, Levy M (2018) Aquaporin-4 serostatus does not predict response to immunotherapy in neuromyelitis optica spectrum disorders. *Multiple sclerosis* 24: 1737-1742

Mealy MA, Shin K, John G, Levy M (2015) Bevacizumab is safe in acute relapses of neuromyelitis optica. *Clin Exp Neuroimmunol* 6: 413-418

Meng H, Xu J, Pan C, Cheng J, Hu Y, Hong Y, Shen Y, Dai H (2017) Cognitive dysfunction in adult patients with neuromyelitis optica: a systematic review and meta-analysis. *Journal of neurology* 264: 1549-1558

Messina R, Rocca MA, Colombo B, Valsasina P, Horsfield MA, Copetti M, Falini A, Comi G, Filippi M (2013) Cortical abnormalities in patients with migraine: a surface-based analysis. *Radiology* 268: 170-80

Metz I, Gavrilova RH, Weigand SD, Frischer JM, Popescu BF, Guo Y, Gloth M, Tobin WO, Zalewski NL, Lassmann H, Tillema JM, Erickson BJ, Parisi JE, Becker S, Konig FB, Bruck W, Lucchinetti CF (2021) Magnetic Resonance Imaging Correlates of Multiple Sclerosis Immunopathological Patterns. *Ann Neurol* 90: 440-454

Mistri D, Cacciaguerra L, Storelli L, Meani A, Cordani C, Rocca MA, Filippi M (2022) The association between cognition and motor performance is beyond structural damage in relapsing-remitting multiple sclerosis. *J Neurol*

Muthukrishnan N, Maleki F, Ovens K, Reinhold C, Forghani B, Forghani R (2020) Brief History of Artificial Intelligence. *Neuroimaging Clin N Am* 30: 393-399

Nagelhus EA, Veruki ML, Torp R, Haug FM, Laake JH, Nielsen S, Agre P, Ottersen OP (1998) Aquaporin-4 water channel protein in the rat retina and optic nerve: polarized expression in Muller cells and fibrous astrocytes. *The Journal of neuroscience : the official journal of the Society for Neuroscience* 18: 2506-19

Nakamura K, Brown RA, Araujo D, Narayanan S, Arnold DL (2014) Correlation between brain volume change and T2 relaxation time induced by dehydration and rehydration: implications for monitoring atrophy in clinical studies. *Neuroimage Clin* 6: 166-70

Nakamura K, Chen JT, Ontaneda D, Fox RJ, Trapp BD (2017) T1-/T2-weighted ratio differs in demyelinated cortex in multiple sclerosis. *Annals of neurology* 82: 635-639

Nakamura M, Miyazawa I, Fujihara K, Nakashima I, Misu T, Watanabe S, Takahashi T, Itoyama Y (2008) Preferential spinal central gray matter involvement in neuromyelitis optica. An MRI study. *Journal of neurology* 255: 163-70

Nielsen S, Nagelhus EA, Amiry-Moghaddam M, Bourque C, Agre P, Ottersen OP (1997) Specialized membrane domains for water transport in glial cells: high-resolution immunogold cytochemistry of aquaporin-4 in rat brain. *The Journal of neuroscience : the official journal of the Society for Neuroscience* 17: 171-80

Nitish Srivastava GH, Alex Krizhevsky, Ilya Sutskever, Ruslan Salakhutdinov (2014) Dropout: A Simple Way to Prevent Neural Networks from Overfitting. *Journal of Machine Learning Research* 15: 1929-1958

Nobis L, Manohar SG, Smith SM, Alfaro-Almagro F, Jenkinson M, Mackay CE, Husain M (2019) Hippocampal volume across age: Nomograms derived from over 19,700 people in UK Biobank. *Neuroimage Clin* 23: 101904

Noble KG, Grieve SM, Korgaonkar MS, Engelhardt LE, Griffith EY, Williams LM, Brickman AM (2012) Hippocampal volume varies with educational attainment across the life-span. *Front Hum Neurosci* 6: 307

Novelli G, Papagno C, Capitani E, Laiacona M, Vallar G, Cappa S (1986) Tre test clinici di ricerca e produzione lessicale. Taratura su soggetti normal. *Archivio di Psicologia, Neurologia e Psichiatria* 47: 477-506

O'Donnell LJ, Westin CF (2011) An introduction to diffusion tensor image analysis. *Neurosurg Clin N Am* 22: 185-96, viii

- Obata T, Kershaw J, Tachibana Y, Miyauchi T, Abe Y, Shibata S, Kawaguchi H, Ikoma Y, Takuwa H, Aoki I, Yasui M (2018) Comparison of diffusion-weighted MRI and anti-Stokes Raman scattering (CARS) measurements of the inter-compartmental exchange-time of water in expression-controlled aquaporin-4 cells. *Scientific reports* 8: 17954
- Ochoa D, Hercules A, Carmona M, Suveges D, Gonzalez-Uriarte A, Malangone C, Miranda A, Fumis L, Carvalho-Silva D, Spitzer M, Baker J, Ferrer J, Raies A, Razuvayevskaya O, Faulconbridge A, Petsalaki E, Mutowo P, Machlitt-Northen S, Peat G, McAuley E et al. (2021) Open Targets Platform: supporting systematic drug-target identification and prioritisation. *Nucleic Acids Res* 49: D1302-D1310
- Oertel FC, Schliesseit J, Brandt AU, Paul F (2019) Cognitive Impairment in Neuromyelitis Optica Spectrum Disorders: A Review of Clinical and Neuroradiological Features. *Frontiers in neurology* 10: 608
- Ohene Y, Harrison IF, Nahavandi P, Ismail O, Bird EV, Ottersen OP, Nagelhus EA, Thomas DL, Lythgoe MF, Wells JA (2019) Non-invasive MRI of brain clearance pathways using multiple echo time arterial spin labelling: an aquaporin-4 study. *Neuroimage* 188: 515-523
- Okłinski MK, Skowronski MT, Skowronska A, Rutzler M, Norgaard K, Nieland JD, Kwon TH, Nielsen S (2016) Aquaporins in the Spinal Cord. *International journal of molecular sciences* 17
- Ordidge RJ, Gorell JM, Deniau JC, Knight RA, Helpert JA (1994) Assessment of relative brain iron concentrations using T2-weighted and T2*-weighted MRI at 3 Tesla. *Magn Reson Med* 32: 335-41
- Oshio K, Binder DK, Yang B, Schechter S, Verkman AS, Manley GT (2004) Expression of aquaporin water channels in mouse spinal cord. *Neuroscience* 127: 685-93
- Otani T, Irioka T, Igarashi S, Kaneko K, Takahashi T, Yokota T (2020) Self-remitting cerebral cortical encephalitis associated with myelin oligodendrocyte glycoprotein antibody mimicking acute viral encephalitis: A case report. *Mult Scler Relat Disord* 41: 102033

Otero DC, Anzelon AN, Rickert RC (2003) CD19 function in early and late B cell development: I. Maintenance of follicular and marginal zone B cells requires CD19-dependent survival signals. *Journal of immunology* 170: 73-83

Padurariu M, Ciobica A, Mavroudis I, Fotiou D, Baloyannis S (2012) Hippocampal neuronal loss in the CA1 and CA3 areas of Alzheimer's disease patients. *Psychiatr Danub* 24: 152-8

Papadopoulos MC, Manley GT, Krishna S, Verkman AS (2004) Aquaporin-4 facilitates reabsorption of excess fluid in vasogenic brain edema. *FASEB journal : official publication of the Federation of American Societies for Experimental Biology* 18: 1291-3

Papadopoulos MC, Verkman AS (2012) Aquaporin 4 and neuromyelitis optica. *The Lancet Neurology* 11: 535-44

Pardini M, Gualco L, Bommarito G, Roccatagliata L, Schiavi S, Solaro C, Mancardi G, Uccelli A, Capello E, Inglese M (2019) CSF oligoclonal bands and normal appearing white matter periventricular damage in patients with clinically isolated syndrome suggestive of MS. *Multiple sclerosis and related disorders* 31: 93-96

Patenaude B, Smith SM, Kennedy DN, Jenkinson M (2011) A Bayesian model of shape and appearance for subcortical brain segmentation. *Neuroimage* 56: 907-22

Pekcevik Y, Mitchell CH, Mealy MA, Orman G, Lee IH, Newsome SD, Thompson CB, Pardo CA, Calabresi PA, Levy M, Izbudak I (2016) Differentiating neuromyelitis optica from other causes of longitudinally extensive transverse myelitis on spinal magnetic resonance imaging. *Multiple sclerosis* 22: 302-11

Petzold A, Woodhall M, Khaleeli Z, Tobin WO, Pittock SJ, Weinshenker BG, Vincent A, Waters P, Plant GT (2019) Aquaporin-4 and myelin oligodendrocyte glycoprotein antibodies in immune-mediated optic neuritis at long-term follow-up. *Journal of neurology, neurosurgery, and psychiatry* 90: 1021-1026

Pfefferbaum A, Mathalon DH, Sullivan EV, Rawles JM, Zipursky RB, Lim KO (1994) A Quantitative Magnetic Resonance Imaging Study of Changes in Brain Morphology From Infancy to Late Adulthood. *Archives of neurology* 51: 874-887

Pichiecchio A, Tavazzi E, Poloni G, Ponzio M, Palesi F, Pasin M, Piccolo L, Tosello D, Romani A, Bergamaschi R, Piccolo G, Bastianello S (2012) Advanced magnetic resonance imaging of neuromyelitis optica: a multiparametric approach. *Multiple sclerosis* 18: 817-24

Pittock SJ, Barnet M, Bennett JL, Berthele A, de Sèze J, Levy M, Nakashima I, Oreja-Guevara C, Palace J, Paul F, Pozzilli C, Allen K, Mashhoon Y, Yountz M, Kim HJ (2022) Efficacy subgroup analyses from the phase 3 CHAMPION-NMOSD trial in adults with anti-aquaporin-4 antibody-positive neuromyelitis optica spectrum disorder. *Multiple Sclerosis Journal* 28: 130-691

Pittock SJ, Berthele A, Fujihara K, Kim HJ, Levy M, Palace J, Nakashima I, Terzi M, Totolyan N, Viswanathan S, Wang KC, Pace A, Fujita KP, Armstrong R, Wingerchuk DM (2019) Eculizumab in Aquaporin-4-Positive Neuromyelitis Optica Spectrum Disorder. *N Engl J Med* 381: 614-625

Pittock SJ, Weinshenker BG, Lucchinetti CF, Wingerchuk DM, Corboy JR, Lennon VA (2006) Neuromyelitis optica brain lesions localized at sites of high aquaporin 4 expression. *Arch Neurol* 63: 964-8

Popescu BF, Lennon VA, Parisi JE, Howe CL, Weigand SD, Cabrera-Gomez JA, Newell K, Mandler RN, Pittock SJ, Weinshenker BG, Lucchinetti CF (2011) Neuromyelitis optica unique area postrema lesions: nausea, vomiting, and pathogenic implications. *Neurology* 76: 1229-37

Popescu BF, Parisi JE, Cabrera-Gomez JA, Newell K, Mandler RN, Pittock SJ, Lennon VA, Weinshenker BG, Lucchinetti CF (2010) Absence of cortical demyelination in neuromyelitis optica. *Neurology* 75: 2103-9

Portaccio E, Goretti B, Lori S, Zipoli V, Centorrino S, Ghezzi A, Patti F, Bianchi V, Comi G, Trojano M, Amato MP, Itali MSSG (2009) The brief neuropsychological battery for

children: a screening tool for cognitive impairment in childhood and juvenile multiple sclerosis. *Mult Scler J* 15: 620-626

Poser S, Luer W, Bruhn H, Frahm J, Bruck Y, Felgenhauer K (1992) Acute demyelinating disease. Classification and non-invasive diagnosis. *Acta Neurol Scand* 86: 579-85

Potter GM, Chappell FM, Morris Z, Wardlaw JM (2015) Cerebral perivascular spaces visible on magnetic resonance imaging: development of a qualitative rating scale and its observer reliability. *Cerebrovasc Dis* 39: 224-31

Prabhu D, Khan SM, Blackburn K, Marshall JP, Ashpole NM (2019) Loss of insulin-like growth factor-1 signaling in astrocytes disrupts glutamate handling. *J Neurochem* 151: 689-702

Preziosa P, Pagani E, Mesaros S, Riccitelli GC, Dackovic J, Drulovic J, Filippi M, Rocca MA (2017) Progression of regional atrophy in the left hemisphere contributes to clinical and cognitive deterioration in multiple sclerosis: A 5-year study. *Hum Brain Mapp* 38: 5648-5665

Prineas JW, Lee S (2019) Multiple Sclerosis: Destruction and Regeneration of Astrocytes in Acute Lesions. *J Neuropathol Exp Neurol* 78: 140-156

Ramezani M, Johnsrude I, Rasouljan A, Bosma R, Tong R, Hollenstein T, Harkness K, Abolmaesumi P (2014) Temporal-lobe morphology differs between healthy adolescents and those with early-onset of depression. *Neuroimage Clin* 6: 145-55

Ratelade J, Verkman AS (2012) Neuromyelitis optica: aquaporin-4 based pathogenesis mechanisms and new therapies. *The international journal of biochemistry & cell biology* 44: 1519-30

Raudvere U, Kolberg L, Kuzmin I, Arak T, Adler P, Peterson H, Vilo J (2019) g:Profiler: a web server for functional enrichment analysis and conversions of gene lists (2019 update). *Nucleic Acids Res* 47: W191-W198

Redenbaugh V, Montalvo M, Sechi E, Buciuic M, Fryer JP, McKeon A, Lennon VA, Mills JR, Weinshenker BG, Wingerchuk DM, Chen JJ, Tariq Bhatti M, Lopez Chiriboga

AS, Pittock SJ, Flanagan EP (2021) Diagnostic value of aquaporin-4-IgG live cell based assay in neuromyelitis optica spectrum disorders. *Mult Scler J Exp Transl Clin* 7: 20552173211052656

Reindl M, Waters P (2019) Myelin oligodendrocyte glycoprotein antibodies in neurological disease. *Nature reviews Neurology* 15: 89-102

Reulen HJ (1976) Vasogenic brain oedema. New aspects in its formation, resolution and therapy. *Br J Anaesth* 48: 741-52

Richard C, Ruiz A, Cavagna S, Bigotte M, Vukusic S, Masaki K, Suenaga T, Kira JI, Giraudon P, Marignier R (2020) Connexins in neuromyelitis optica: a link between astrocytopathy and demyelination. *Brain* 143: 2721-2732

Righart R, Biberacher V, Jonkman LE, Klaver R, Schmidt P, Buck D, Berthele A, Kirschke JS, Zimmer C, Hemmer B, Geurts JJG, Muhlau M (2017) Cortical pathology in multiple sclerosis detected by the T1/T2-weighted ratio from routine magnetic resonance imaging. *Annals of neurology* 82: 519-529

Ringstad G, Vatnehol SAS, Eide PK (2017) Glymphatic MRI in idiopathic normal pressure hydrocephalus. *Brain* 140: 2691-2705

Rizzo G, Veronese M, Expert P, Turkheimer FE, Bertoldo A (2016) MENGA: A New Comprehensive Tool for the Integration of Neuroimaging Data and the Allen Human Brain Transcriptome Atlas. *PLoS One* 11: e0148744

Rocca MA, Absinta M, Amato MP, Moiola L, Ghezzi A, Veggiotti P, Capra R, Portaccio E, Fiorino A, Pippolo L, Pera MC, Horsfield MA, Falini A, Comi G, Filippi M (2014) Posterior brain damage and cognitive impairment in pediatric multiple sclerosis. *Neurology* 82: 1314-21

Rocca MA, Agosta F, Mezzapesa DM, Martinelli V, Salvi F, Ghezzi A, Bergamaschi R, Comi G, Filippi M (2004) Magnetization transfer and diffusion tensor MRI show gray matter damage in neuromyelitis optica. *Neurology* 62: 476-478

Rocca MA, Anzalone N, Storelli L, Del Poggio A, Cacciaguerra L, Manfredi AA, Meani A, Filippi M (2021) Deep Learning on Conventional Magnetic Resonance Imaging Improves the Diagnosis of Multiple Sclerosis Mimics. *Invest Radiol* 56: 252-260

Rocca MA, Cacciaguerra L, Filippi M (2020a) Moving beyond anti-aquaporin-4 antibodies: emerging biomarkers in the spectrum of neuromyelitis optica. *Expert Rev Neurother* 20: 601-618

Rocca MA, Cercignani M, Iannucci G, Comi G, Filippi M (2000) Weekly diffusion-weighted imaging of normal-appearing white matter in MS. *Neurology* 55: 882-4

Rocca MA, Hidalgo de La Cruz M, Valsasina P, Mesaros S, Martinovic V, Ivanovic J, Drulovic J, Filippi M (2020b) Two-year dynamic functional network connectivity in clinically isolated syndrome. *Multiple sclerosis* 26: 645-658

Rocca MA, Savoldi F, Valsasina P, Radaelli M, Preziosa P, Comi G, Falini A, Filippi M (2019) Cross-modal plasticity among sensory networks in neuromyelitis optica spectrum disorders. *Mult Scler* 25: 968-979

Roemer SF, Parisi JE, Lennon VA, Benarroch EE, Lassmann H, Bruck W, Mandler RN, Weinshenker BG, Pittock SJ, Wingerchuk DM, Lucchinetti CF (2007) Pattern-specific loss of aquaporin-4 immunoreactivity distinguishes neuromyelitis optica from multiple sclerosis. *Brain* 130: 1194-205

Roosendaal SD, Hulst HE, Vrenken H, Feenstra HE, Castelijns JA, Pouwels PJ, Barkhof F, Geurts JJ (2010) Structural and functional hippocampal changes in multiple sclerosis patients with intact memory function. *Radiology* 255: 595-604

Roosendaal SD, Moraal B, Vrenken H, Castelijns JA, Pouwels PJ, Barkhof F, Geurts JJ (2008) In vivo MR imaging of hippocampal lesions in multiple sclerosis. *J Magn Reson Imaging* 27: 726-31

Rossi A, Ratelade J, Papadopoulos MC, Bennett JL, Verkman AS (2012) Neuromyelitis optica IgG does not alter aquaporin-4 water permeability, plasma membrane M1/M23 isoform content, or supramolecular assembly. *Glia* 60: 2027-39

Rueda Lopes FC, Doring T, Martins C, Cabral FC, Malfetano FR, Pereira VC, Alves-Leon S, Gasparetto EL (2012) The role of demyelination in neuromyelitis optica damage: diffusion-tensor MR imaging study. *Radiology* 263: 235-42

Russakovsky* O, Su H., Krause J., Satheesh S., Ma S., Huang Z., Karpathy A., Khosla A., Bernstein M., Berg A. C. and Fei-Fei L. (2015) ImageNet Large Scale Visual Recognition Challenge. *International Journal of Computer Vision* 115: 211-252

S BS-M, Chen JJ, Morris P, Sechi E, Mandrekar J, Tillema JM, Lopez-Chiriboga AS, Lucchinetti CF, Zalewski N, Cacciaguerra L, Buciu M, Krecke KN, Messina SA, Bhatti MT, Pittock SJ, Flanagan EP (2022) Frequency of New or Enlarging Lesions on MRI Outside of Clinical Attacks in Patients With MOG-Antibody-Associated Disease. *Neurology*

S.H. Shabbeer Basha SRD, Viswanath Pulabaigari, Snehasis Mukherjee (2019) Impact of Fully Connected Layers on Performance of Convolutional Neural Networks for Image Classification. *Neurocomputing Journal* arXiv:1902.02771

Saadoun S, Papadopoulos MC (2010) Aquaporin-4 in brain and spinal cord oedema. *Neuroscience* 168: 1036-46

Saji E, Arakawa M, Yanagawa K, Toyoshima Y, Yokoseki A, Okamoto K, Otsuki M, Akazawa K, Kakita A, Takahashi H, Nishizawa M, Kawachi I (2013) Cognitive impairment and cortical degeneration in neuromyelitis optica. *Ann Neurol* 73: 65-76

Salama S, Khan M, Shanechi A, Levy M, Izbudak I (2020) MRI differences between MOG antibody disease and AQP4 NMOSD. *Mult Scler* 26: 1854-1865

Sanchez P, Meca-Lallana V, Barbosa A, Manzanares R, Palmi I, Vivancos J (2017) Tumefactive demyelinating lesions of 15 patients: Clinico-radiological features, management and review of the literature. *Journal of the neurological sciences* 381: 32-38

Savoldi F, Rocca MA, Valsasina P, Riccitelli GC, Mesaros S, Drulovic J, Radaelli M, Filippi M (2020) Functional brain connectivity abnormalities and cognitive deficits in neuromyelitis optica spectrum disorder. *Mult Scler* 26: 795-805

Schaefer PW, Grant PE, Gonzalez RG (2000) Diffusion-weighted MR imaging of the brain. *Radiology* 217: 331-45

Scheuermann RH, Racila E (1995) CD19 antigen in leukemia and lymphoma diagnosis and immunotherapy. *Leukemia & lymphoma* 18: 385-97

Schubert JJ, Veronese M, Marchitelli L, Bodini B, Tonietto M, Stankoff B, Brooks DJ, Bertoldo A, Edison P, Turkheimer FE (2019) Dynamic (11)C-PiB PET Shows Cerebrospinal Fluid Flow Alterations in Alzheimer Disease and Multiple Sclerosis. *J Nucl Med* 60: 1452-1460

Sechi E, Buciu M, Flanagan EP, Pittock SJ, Banks SA, Lopez-Chiriboga AS, Bhatti MT, Chen JJ (2021a) Variability of cerebrospinal fluid findings by attack phenotype in myelin oligodendrocyte glycoprotein-IgG-associated disorder. *Mult Scler Relat Disord* 47: 102638

Sechi E, Buciu M, Pittock SJ, Chen JJ, Fryer JP, Jenkins SM, Budhram A, Weinshenker BG, Lopez-Chiriboga AS, Tillema JM, McKeon A, Mills JR, Tobin WO, Flanagan EP (2021b) Positive Predictive Value of Myelin Oligodendrocyte Glycoprotein Autoantibody Testing. *JAMA neurology* 78: 741-746

Sechi E, Cacciaguerra L, Chen JJ, Mariotto S, Fadda G, Dinoto A, Lopez-Chiriboga AS, Pittock SJ, Flanagan EP (2022) Myelin Oligodendrocyte Glycoprotein Antibody-Associated Disease (MOGAD): A Review of Clinical and MRI Features, Diagnosis, and Management. *Front Neurol* 13: 885218

Sechi E, Krecke KN, Messina SA, Buciu M, Pittock SJ, Chen JJ, Weinshenker BG, Lopez-Chiriboga AS, Lucchinetti CF, Zalewski NL, Tillema JM, Kunchok A, Monaco S, Morris PP, Fryer JP, Nguyen A, Greenwood T, Syc-Mazurek SB, Keegan BM, Flanagan EP (2021c) Comparison of MRI Lesion Evolution in Different Central Nervous System Demyelinating Disorders. *Neurology* 97: e1097-e1109

Seewann A, Enzinger C, Filippi M, Barkhof F, Rovira A, Gass A, Miller D, Montalban X, Thompson A, Yousry T, Tintore M, de Stefano N, Palace J, Rovaris M, Polman C, Fazekas F, network M (2008) MRI characteristics of atypical idiopathic inflammatory

demyelinating lesions of the brain : A review of reported findings. *Journal of neurology* 255: 1-10

Sepehrband F, Cabeen RP, Choupan J, Barisano G, Law M, Toga AW, Alzheimer's Disease Neuroimaging I (2019) Perivascular space fluid contributes to diffusion tensor imaging changes in white matter. *Neuroimage* 197: 243-254

Shah SS, Morris P, Buciu M, Tajfirouz D, Wingerchuk DM, Weinshenker BG, Eggenberger ER, Di Nome M, Pittock SJ, Flanagan EP, Bhatti MT, Chen JJ (2022) Frequency of Asymptomatic Optic Nerve Enhancement in a Large Retrospective Cohort of Patients With Aquaporin-4+ NMOSD. *Neurology* 99: e851-e857

Shannon P, Markiel A, Ozier O, Baliga NS, Wang JT, Ramage D, Amin N, Schwikowski B, Ideker T (2003) Cytoscape: a software environment for integrated models of biomolecular interaction networks. *Genome Res* 13: 2498-504

Shen EH, Overly CC, Jones AR (2012) The Allen Human Brain Atlas: comprehensive gene expression mapping of the human brain. *Trends Neurosci* 35: 711-4

Shimizu F, Sano Y, Takahashi T, Haruki H, Saito K, Koga M, Kanda T (2012) Sera from neuromyelitis optica patients disrupt the blood-brain barrier. *Journal of neurology, neurosurgery, and psychiatry* 83: 288-97

Shu Y, Long Y, Wang S, Hu W, Zhou J, Xu H, Chen C, Ou Y, Lu Z, Lau AY, Yu X, Kermod AG, Qiu W (2019) Brain histopathological study and prognosis in MOG antibody-associated demyelinating pseudotumor. *Ann Clin Transl Neurol* 6: 392-396

Sicotte NL, Kern KC, Giesser BS, Arshanapalli A, Schultz A, Montag M, Wang H, Bookheimer SY (2008) Regional hippocampal atrophy in multiple sclerosis. *Brain* 131: 1134-41

Simon KC, Schmidt H, Loud S, Ascherio A (2015) Risk factors for multiple sclerosis, neuromyelitis optica and transverse myelitis. *Mult Scler* 21: 703-9

Sinha S, Banwell B, Tucker A, Storm PB, Huh J, Lang SS (2022) Hemicraniectomy and externalized ventricular drain placement in a pediatric patient with myelin

oligodendrocyte glycoprotein-associated tumefactive demyelinating disease. *Childs Nerv Syst* 38: 185-189

Sjostedt E, Zhong W, Fagerberg L, Karlsson M, Mitsios N, Adori C, Oksvold P, Edfors F, Limiszewska A, Hikmet F, Huang J, Du Y, Lin L, Dong Z, Yang L, Liu X, Jiang H, Xu X, Wang J, Yang H et al. (2020) An atlas of the protein-coding genes in the human, pig, and mouse brain. *Science* 367

Skucas VA, Mathews IB, Yang J, Cheng Q, Treister A, Duffy AM, Verkman AS, Hempstead BL, Wood MA, Binder DK, Scharfman HE (2011) Impairment of select forms of spatial memory and neurotrophin-dependent synaptic plasticity by deletion of glial aquaporin-4. *The Journal of neuroscience : the official journal of the Society for Neuroscience* 31: 6392-7

Smith SM, Jenkinson M, Johansen-Berg H, Rueckert D, Nichols TE, Mackay CE, Watkins KE, Ciccarelli O, Cader MZ, Matthews PM, Behrens TE (2006) Tract-based spatial statistics: voxelwise analysis of multi-subject diffusion data. *Neuroimage* 31: 1487-505

Smith SM, Zhang Y, Jenkinson M, Chen J, Matthews PM, Federico A, De Stefano N (2002) Accurate, robust, and automated longitudinal and cross-sectional brain change analysis. *NeuroImage* 17: 479-89

Solomon AJ, Bourdette DN, Cross AH, Applebee A, Skidd PM, Howard DB, Spain RI, Cameron MH, Kim E, Mass MK, Yadav V, Whitham RH, Longbrake EE, Naismith RT, Wu GF, Parks BJ, Wingerchuk DM, Rabin BL, Toledano M, Tobin WO et al. (2016) The contemporary spectrum of multiple sclerosis misdiagnosis: A multicenter study. *Neurology* 87: 1393-9

Solomon JM, Paul F, Chien C, Oh J, Rotstein DL (2021) A window into the future? MRI for evaluation of neuromyelitis optica spectrum disorder throughout the disease course. *The Adv Neurol Disord* 14: 17562864211014389

Sormani MP, Bruzzi P (2013) MRI lesions as a surrogate for relapses in multiple sclerosis: a meta-analysis of randomised trials. *The Lancet Neurology* 12: 669-76

- Stepan J, Dine J, Eder M (2015) Functional optical probing of the hippocampal trisynaptic circuit in vitro: network dynamics, filter properties, and polysynaptic induction of CA1 LTP. *Frontiers in neuroscience* 9: 160
- Stokum JA, Mehta RI, Ivanova S, Yu E, Gerzanich V, Simard JM (2015) Heterogeneity of aquaporin-4 localization and expression after focal cerebral ischemia underlies differences in white versus grey matter swelling. *Acta Neuropathol Commun* 3: 61
- Stoodley CJ, Schmähmann JD (2009) Functional topography in the human cerebellum: a meta-analysis of neuroimaging studies. *NeuroImage* 44: 489-501
- Sumowski JF, Benedict R, Enzinger C, Filippi M, Geurts JJ, Hamalainen P, Hulst H, Inglese M, Leavitt VM, Rocca MA, Rosti-Otajarvi EM, Rao S (2018) Cognition in multiple sclerosis: State of the field and priorities for the future. *Neurology* 90: 278-288
- Sun H, Wilman AH (2014) Background field removal using spherical mean value filtering and Tikhonov regularization. *Magn Reson Med* 71: 1151-7
- Sun J, Sun X, Zhang N, Wang Q, Cai H, Qi Y, Li T, Qin W, Yu C (2017) Analysis of brain and spinal cord lesions to occult brain damage in seropositive and seronegative neuromyelitis optica. *European journal of radiology* 94: 25-30
- Szu JI, Binder DK (2016) The Role of Astrocytic Aquaporin-4 in Synaptic Plasticity and Learning and Memory. *Front Integr Neurosci* 10: 8
- Takahashi-Fujigasaki J, Takagi S, Sakamoto T, Inoue K (2009) Spinal cord biopsy findings of anti-aquaporin-4 antibody-negative recurrent longitudinal myelitis in a patient with sicca symptoms and hepatitis C viral infection. *Neuropathology : official journal of the Japanese Society of Neuropathology* 29: 472-9
- Takai Y, Misu T, Kaneko K, Chihara N, Narikawa K, Tsuchida S, Nishida H, Komori T, Seki M, Komatsu T, Nakamagoe K, Ikeda T, Yoshida M, Takahashi T, Ono H, Nishiyama S, Kuroda H, Nakashima I, Suzuki H, Bradl M et al. (2020) Myelin oligodendrocyte glycoprotein antibody-associated disease: an immunopathological study. *Brain* 143: 1431-1446

Takamatsu T, Yamanaka G, Uryu H, Takeshita M, Morishita N, Morichi S, Ishida Y, Oana S, Terashi H, Shichino H, Sakuma H, Kawashima H (2020) Improvement in recurrent anti-myelin oligodendrocyte glycoprotein antibody - positive cerebral cortical encephalitis not requiring anti - inflammatory therapy following the decrease in cytokine/chemokine levels. *Mult Scler Relat Disord* 43: 102168

Takano R, Misu T, Takahashi T, Sato S, Fujihara K, Itoyama Y (2010) Astrocytic damage is far more severe than demyelination in NMO: a clinical CSF biomarker study. *Neurology* 75: 208-16

Taoka T, Ito R, Nakamichi R, Kamagata K, Sakai M, Kawai H, Nakane T, Abe T, Ichikawa K, Kikuta J, Aoki S, Naganawa S (2021) Reproducibility of diffusion tensor image analysis along the perivascular space (DTI-ALPS) for evaluating interstitial fluid diffusivity and glymphatic function: CHanges in Alps index on Multiple condition acqUisition eXperiment (CHAMONIX) study. *Jpn J Radiol*

Taoka T, Masutani Y, Kawai H, Nakane T, Matsuoka K, Yasuno F, Kishimoto T, Naganawa S (2017) Evaluation of glymphatic system activity with the diffusion MR technique: diffusion tensor image analysis along the perivascular space (DTI-ALPS) in Alzheimer's disease cases. *Jpn J Radiol* 35: 172-178

Taso M, Girard OM, Duhamel G, Le Troter A, Feiweier T, Guye M, Ranjeva JP, Callot V (2016) Tract-specific and age-related variations of the spinal cord microstructure: a multi-parametric MRI study using diffusion tensor imaging (DTI) and inhomogeneous magnetization transfer (ihMT). *NMR in biomedicine* 29: 817-32

Tatekawa H, Sakamoto S, Hori M, Kaichi Y, Kunimatsu A, Akazawa K, Miyasaka T, Oba H, Okubo T, Hasuo K, Yamada K, Taoka T, Doishita S, Shimono T, Miki Y (2018) Imaging Differences between Neuromyelitis Optica Spectrum Disorders and Multiple Sclerosis: A Multi-Institutional Study in Japan. *AJNR American journal of neuroradiology* 39: 1239-1247

Tenembaum S, Chamoles N, Fejerman N (2002) Acute disseminated encephalomyelitis: a long-term follow-up study of 84 pediatric patients. *Neurology* 59: 1224-31

Tham M, Frischer JM, Weigand SD, Fitz-Gibbon PD, Webb SM, Guo Y, Adiele RC, Robinson CA, Bruck W, Lassmann H, Furber KL, Pushie MJ, Parisi JE, Lucchinetti CF, Popescu BF (2021) Iron Heterogeneity in Early Active Multiple Sclerosis Lesions. *Ann Neurol* 89: 498-510

Thomas R (2005) The TRAF6-NF kappa B signaling pathway in autoimmunity: not just inflammation. *Arthritis Res Ther* 7: 170-3

Thompson AJ, Banwell BL, Barkhof F, Carroll WM, Coetzee T, Comi G, Correale J, Fazekas F, Filippi M, Freedman MS, Fujihara K, Galetta SL, Hartung HP, Kappos L, Lublin FD, Marrie RA, Miller AE, Miller DH, Montalban X, Mowry EM et al. (2018) Diagnosis of multiple sclerosis: 2017 revisions of the McDonald criteria. *The Lancet Neurology* 17: 162-173

Thompson PM, Hayashi KM, de Zubicaray G, Janke AL, Rose SE, Semple J, Herman D, Hong MS, Dittmer SS, Doddrell DM, Toga AW (2003) Dynamics of gray matter loss in Alzheimer's disease. *The Journal of neuroscience : the official journal of the Society for Neuroscience* 23: 994-1005

Tian DC, Xiu Y, Wang X, Shi K, Fan M, Li T, Li H, Su L, Ma Y, Xu W, Song T, Liu Y, Shi FD, Zhang X (2020) Cortical Thinning and Ventricle Enlargement in Neuromyelitis Optica Spectrum Disorders. *Front Neurol* 11: 872

Tobin WO, Weinshenker BG, Lucchinetti CF (2014) Longitudinally extensive transverse myelitis. *Current opinion in neurology* 27: 279-89

Tomasello R, Wennekers T, Garagnani M, Pulvermuller F (2019) Visual cortex recruitment during language processing in blind individuals is explained by Hebbian learning. *Sci Rep* 9: 3579

Tozlu C, Jamison K, Gauthier SA, Kuceyeski A (2021) Dynamic Functional Connectivity Better Predicts Disability Than Structural and Static Functional Connectivity in People With Multiple Sclerosis. *Frontiers in neuroscience* 15: 763966

Traboulsee A, Greenberg BM, Bennett JL, Szczechowski L, Fox E, Shkrobot S, Yamamura T, Terada Y, Kawata Y, Wright P, Gianella-Borradori A, Garren H,

Weinshenker BG (2020) Safety and efficacy of satralizumab monotherapy in neuromyelitis optica spectrum disorder: a randomised, double-blind, multicentre, placebo-controlled phase 3 trial. *The Lancet Neurology* 19: 402-412

Transverse Myelitis Consortium Working G (2002) Proposed diagnostic criteria and nosology of acute transverse myelitis. *Neurology* 59: 499-505

Troili F, Cipollini V, Moci M, Morena E, Palotai M, Rinaldi V, Romano C, Ristori G, Giubilei F, Salvetti M, Orzi F, Guttmann CRG, Cavallari M (2020) Perivascular Unit: This Must Be the Place. The Anatomical Crossroad Between the Immune, Vascular and Nervous System. *Front Neuroanat* 14: 17

Tu TW, Williams RA, Lescher JD, Jikaria N, Turtzo LC, Frank JA (2016) Radiological-pathological correlation of diffusion tensor and magnetization transfer imaging in a closed head traumatic brain injury model. *Ann Neurol* 79: 907-20

Uddin MN, Figley TD, Solar KG, Shatil AS, Figley CR (2019) Comparisons between multi-component myelin water fraction, T1w/T2w ratio, and diffusion tensor imaging measures in healthy human brain structures. *Scientific reports* 9: 2500

Uzawa A, Mori M, Kuwabara S (2014) Cytokines and chemokines in neuromyelitis optica: pathogenetic and therapeutic implications. *Brain Pathol* 24: 67-73

Vakharia K, Kamal H, Atwal GS, Budny JL (2018) Transtentorial herniation from tumefactive multiple sclerosis mimicking primary brain tumor. *Surg Neurol Int* 9: 208

Valsasina P, Aboulwafa M, Preziosa P, Messina R, Falini A, Comi G, Filippi M, Rocca MA (2018) Cervical Cord T1-weighted Hypointense Lesions at MR Imaging in Multiple Sclerosis: Relationship to Cord Atrophy and Disability. *Radiology* 288: 234-244

Valsasina P, Hidalgo de la Cruz M, Filippi M, Rocca MA (2019) Characterizing Rapid Fluctuations of Resting State Functional Connectivity in Demyelinating, Neurodegenerative, and Psychiatric Conditions: From Static to Time-Varying Analysis. *Frontiers in neuroscience* 13: 618

- Valsasina P, Horsfield MA, Rocca MA, Absinta M, Comi G, Filippi M (2012) Spatial normalization and regional assessment of cord atrophy: voxel-based analysis of cervical cord 3D T1-weighted images. *AJNR American journal of neuroradiology* 33: 2195-200
- Valverde S, Cabezas M, Roura E, Gonzalez-Villa S, Pareto D, Vilanova JC, Ramio-Torrenta L, Rovira A, Oliver A, Llado X (2017) Improving automated multiple sclerosis lesion segmentation with a cascaded 3D convolutional neural network approach. *Neuroimage* 155: 159-168
- Van Petten C (2004) Relationship between hippocampal volume and memory ability in healthy individuals across the lifespan: review and meta-analysis. *Neuropsychologia* 42: 1394-413
- Varatharaj A, Liljeroth M, Darekar A, Larsson HBW, Galea I, Cramer SP (2019) Blood-brain barrier permeability measured using dynamic contrast-enhanced magnetic resonance imaging: a validation study. *J Physiol* 597: 699-709
- Vidaurre OG, Haines JD, Katz Sand I, Adula KP, Huynh JL, McGraw CA, Zhang F, Varghese M, Sotirchos E, Bhargava P, Bandaru VV, Pasinetti G, Zhang W, Inglese M, Calabresi PA, Wu G, Miller AE, Haughey NJ, Lublin FD, Casaccia P (2014) Cerebrospinal fluid ceramides from patients with multiple sclerosis impair neuronal bioenergetics. *Brain* 137: 2271-86
- Wang X, Chen X, Zhu C, Ma H, Wang F, Qin L, Li W (2018) A multi-facet comparative analysis of neuromyelitis optica spectrum disorders in patients with seropositive and seronegative AQP4-IgG. *Medicine* 97: e13100
- Wang X, Yi H, Liu J, Li M, Mao ZF, Xu L, Peng FH (2016) Anti-thyroid antibodies and thyroid function in neuromyelitis optica spectrum disorders. *Journal of the neurological sciences* 366: 3-7
- Wang Y, Wu A, Chen X, Zhang L, Lin Y, Sun S, Cai W, Zhang B, Kang Z, Qiu W, Hu X, Lu Z (2014) Comparison of clinical characteristics between neuromyelitis optica spectrum disorders with and without spinal cord atrophy. *BMC Neurol* 14: 246

Wardlaw JM, Benveniste H, Nedergaard M, Zlokovic BV, Mestre H, Lee H, Doubal FN, Brown R, Ramirez J, MacIntosh BJ, Tannenbaum A, Ballerini L, Rungta RL, Boido D, Sweeney M, Montagne A, Charpak S, Joutel A, Smith KJ, Black SE et al. (2020) Perivascular spaces in the brain: anatomy, physiology and pathology. *Nature reviews Neurology* 16: 137-153

Waschbisch A, Atiya M, Schaub C, Derfuss T, Schwab S, Lee DH, Muller M, Linker RA (2013) Aquaporin-4 antibody negative recurrent isolated optic neuritis: clinical evidence for disease heterogeneity. *Journal of the neurological sciences* 331: 72-5

Watanabe M, Nakamura Y, Michalak Z, Isobe N, Barro C, Leppert D, Matsushita T, Hayashi F, Yamasaki R, Kuhle J, Kira JI (2019) Serum GFAP and neurofilament light as biomarkers of disease activity and disability in NMOSD. *Neurology* 93: e1299-e1311

Waters P, Woodhall M, O'Connor KC, Reindl M, Lang B, Sato DK, Jurynczyk M, Tackley G, Rocha J, Takahashi T, Misu T, Nakashima I, Palace J, Fujihara K, Leite MI, Vincent A (2015) MOG cell-based assay detects non-MS patients with inflammatory neurologic disease. *Neurol Neuroimmunol Neuroinflamm* 2: e89

Waters PJ, McKeon A, Leite MI, Rajasekharan S, Lennon VA, Villalobos A, Palace J, Mandrekar JN, Vincent A, Bar-Or A, Pittock SJ (2012) Serologic diagnosis of NMO: a multicenter comparison of aquaporin-4-IgG assays. *Neurology* 78: 665-71; discussion 669

Wattjes MP, Steenwijk MD, Stangel M (2015) MRI in the Diagnosis and Monitoring of Multiple Sclerosis: An Update. *Clin Neuroradiol* 25 Suppl 2: 157-65

Wei Y, Chang H, Li X, Du L, Xu W, Cong H, Yao Y, Zhang X, Yin L (2018) CSF-S100B Is a Potential Candidate Biomarker for Neuromyelitis Optica Spectrum Disorders. *BioMed research international* 2018: 5381239

Whitwell JL (2009) Voxel-based morphometry: an automated technique for assessing structural changes in the brain. *The Journal of neuroscience : the official journal of the Society for Neuroscience* 29: 9661-4

Wingerchuk DM, Banwell B, Bennett JL, Cabre P, Carroll W, Chitnis T, de Seze J, Fujihara K, Greenberg B, Jacob A, Jarius S, Lana-Peixoto M, Levy M, Simon JH, Tenenbaum S, Traboulsee AL, Waters P, Wellik KE, Weinshenker BG, International Panel for NMOD (2015) International consensus diagnostic criteria for neuromyelitis optica spectrum disorders. *Neurology* 85: 177-89

Wingerchuk DM, Hogancamp WF, O'Brien PC, Weinshenker BG (1999) The clinical course of neuromyelitis optica (Devic's syndrome). *Neurology* 53: 1107-14

Wingerchuk DM, Pittock SJ, Lucchinetti CF, Lennon VA, Weinshenker BG (2007) A secondary progressive clinical course is uncommon in neuromyelitis optica. *Neurology* 68: 603-5

Wingerchuk DM, Weinshenker BG (2012) The emerging relationship between neuromyelitis optica and systemic rheumatologic autoimmune disease. *Mult Scler* 18: 5-10

Wingerchuk DM, Zhang I, Kielhorn A, Royston M, Levy M, Fujihara K, Nakashima I, Tanvir I, Paul F, Pittock SJ (2022) Network Meta-analysis of Food and Drug Administration-approved Treatment Options for Adults with Aquaporin-4 Immunoglobulin G-positive Neuromyelitis Optica Spectrum Disorder. *Neurol Ther* 11: 123-135

Wiseman SJ, Bastin ME, Jardine CL, Barclay G, Hamilton IF, Sandeman E, Hunt D, Amft EN, Thomson S, Belch JF, Ralston SH, Wardlaw JM (2016) Cerebral Small Vessel Disease Burden Is Increased in Systemic Lupus Erythematosus. *Stroke* 47: 2722-2728

Wolff SD, Balaban RS (1994) Magnetization transfer imaging: practical aspects and clinical applications. *Radiology* 192: 593-9

Wuerfel J, Haertle M, Waiczies H, Tysiak E, Bechmann I, Wernecke KD, Zipp F, Paul F (2008) Perivascular spaces--MRI marker of inflammatory activity in the brain? *Brain* 131: 2332-40

Y. Lecun LB, Y. Bengio, P. Haffner (1998) Gradient-based learning applied to document recognition. *Proceedings of the IEEE* 86: 2278 - 2324

Yamamura T, Kleiter I, Fujihara K, Palace J, Greenberg B, Zakrzewska-Pniewska B, Patti F, Tsai CP, Saiz A, Yamazaki H, Kawata Y, Wright P, De Seze J (2019) Trial of Satralizumab in Neuromyelitis Optica Spectrum Disorder. *The New England journal of medicine* 381: 2114-2124

Yan Z, Liu H, Chen X, Zheng Q, Zeng C, Zheng Y, Ding S, Peng Y, Li Y (2021) Quantitative Susceptibility Mapping-Derived Radiomic Features in Discriminating Multiple Sclerosis From Neuromyelitis Optica Spectrum Disorder. *Front Neurosci* 15: 765634

Yao Yuan LR, Andrea Caponnetto (2007) On Early Stopping in Gradient Descent Learning. *Constructive Approximation* 26: 289-315

Yokota H, Vijayasarithi A, Cekic M, Hirata Y, Linetsky M, Ho M, Kim W, Salamon N (2019) Diagnostic Performance of Glymphatic System Evaluation Using Diffusion Tensor Imaging in Idiopathic Normal Pressure Hydrocephalus and Mimickers. *Curr Gerontol Geriatr Res* 2019: 5675014

Yu C, Lin F, Li K, Jiang T, Qin W, Sun H, Chan P (2008) Pathogenesis of normal-appearing white matter damage in neuromyelitis optica: diffusion-tensor MR imaging. *Radiology* 246: 222-8

Yu CS, Lin FC, Li KC, Jiang TZ, Zhu CZ, Qin W, Sun H, Chan P (2006) Diffusion tensor imaging in the assessment of normal-appearing brain tissue damage in relapsing neuromyelitis optica. *AJNR Am J Neuroradiol* 27: 1009-15

Zhang Y, Brady M, Smith S (2001) Segmentation of brain MR images through a hidden Markov random field model and the expectation-maximization algorithm. *IEEE Trans Med Imaging* 20: 45-57

Zhang Z, Zhou H, Liu X, Liu L, Shu S, Fang F (2021) Identification of the clinical and neuroimaging characteristics in children with neuromyelitis optica spectrum disorders: a case series. *Transl Pediatr* 10: 2459-2466

Zhao-Fleming HH, Valencia Sanchez C, Sechi E, Inbarasu J, Wijdicks EF, Pittock SJ, Chen JJ, Wingerchuk DM, Weinshenker BG, Lopez-Chiriboga S, Dubey D, Tillema JM,

Toledano M, Yadav H, Flanagan EP (2021) CNS Demyelinating Attacks Requiring Ventilatory Support With Myelin Oligodendrocyte Glycoprotein or Aquaporin-4 Antibodies. *Neurology* 97: e1351-e1358

Zhao DD, Zhou HY, Wu QZ, Liu J, Chen XY, He D, He XF, Han WJ, Gong QY (2012) Diffusion tensor imaging characterization of occult brain damage in relapsing neuromyelitis optica using 3.0T magnetic resonance imaging techniques. *Neuroimage* 59: 3173-7

Zhuang FJ, Chen Y, He WB, Cai ZY (2018) Prevalence of white matter hyperintensities increases with age. *Neural Regen Res* 13: 2141-2146

Zoccarato M, Saggi MV, Serra G, Pelizza MF, Rosellini I, Peddone L, Ticca A, Giometto B, Zuliani L (2013) Aquaporin-4 antibody neuromyelitis optica following anti-NMDA receptor encephalitis. *Journal of neurology* 260: 3185-7

A handwritten signature or mark, possibly 'Hq', written in black ink.